SEISMIC IMAGING OF OCEANIC DETACHMENT FAULTING

by

Chisomaga Azubike Opara-Nestor

A thesis submitted to the University of Birmingham for the degree of

DOCTOR OF PHILOSOPHY

College of Life and Environmental Sciences

School of Geography, Earth and Environmental Science

June 2022

UNIVERSITY OF
BIRMINGHAM

University of Birmingham Research Archive

e-theses repository

This unpublished thesis/dissertation is copyright of the author and/or third parties. The intellectual property rights of the author or third parties in respect of this work are as defined by The Copyright Designs and Patents Act 1988 or as modified by any successor legislation.

Any use made of information contained in this thesis/dissertation must be in accordance with that legislation and must be properly acknowledged. Further distribution or reproduction in any format is prohibited without the permission of the copyright holder.

SEISMIC IMAGING OF OCEANIC DETACHMENT FAULTING

Abstract

We understand plate tectonics by understanding relative plate motion at the plate boundaries, and the processes occurring there. Diverging plate boundaries are classified according to their spreading rate, with two broad categories as fast or slow-spreading. While fast-spreading is considered dominantly a magmatic process, faulting is much more important during slow spreading, leading to a far rougher, more rugged and more three-dimensional seafloor morphology which together with the large acoustic impedance contrast between basement and seawater, presents a severe seismic imaging challenge, with scattering of energy by the rough seafloor, velocity distortions from the rugged seafloor and strong side-coming events from the three-dimensional topography. Overcoming these challenges is critical to determine the geometry, extent, and mechanics of the faults, including large offset normal faults, called oceanic detachment faults (ODFs). As their footwalls - known as oceanic core complexes (OCCs) - consist of plutonic gabbros and mantle rocks, the fault must root beneath the crust. Their dimensions in the spreading direction indicate large offset, together suggesting that ODFs locally take up much of the plate divergence, but key questions remain about their geometry, mechanics, and lateral extent. This thesis addresses these issues and the challenge of seismic imaging of slow-spread crust in the 13° N area of the Mid-Atlantic ridge through a study of two oceanic detachment faults (13°20' N and 13°30' N, shortened hereafter to 1320 and 1330). A processing scheme – consisting of downward continuation to collapse side-swipe diffractions, followed by amplitude muting to remove them, deconvolution and velocity filtering processes - was developed to allow 2D seismic data to resolve the fine structure of the detachments, to suppress side-coming events, to reveal the geometry of ODFs in depth, and to determine the lateral extent of the detachments and the interaction between neighbouring detachments. The fine structure of the ODF was resolved to be anastomosing subsurface features, consistent with the latest ideas for the origin of the corrugated surfaces. Depth imaging shows that ODF steepen smoothly downwards from the low-angle of the exposed OCC to dips of ~60° at depths of ~5km, projecting to the bands of micro-earthquakes observed, a geometry everywhere consistent with slip-angle allowed by rock mechanics. Finally, Imaging on four intersecting profiles outline the extent of the two ODFs (1320 and 1330) in the slip and isochron direction showing the 1320 ODF cuts across and deeper than the 1330, in agreement with micro-earthquake data that show it is active while 1330 is not but suggesting they could have been linked in the past.

Acknowledgements

I would wish to express my deep and sincere appreciation to my supervisors, Prof. Timothy Reston and Dr Stephen Jones, who have been instrumental to guiding and directing me in the last four plus years the research program has lasted and for making a dream of yesteryears come true. To Tim Reston most especially for his patience, understanding and indirect nudgings to ensure the knowledge gaps needed for the research were filled, and for his help editing this thesis and correcting my English, for permission to site in his classes and update my knowledge with his lectures. To the JC132 2016 research and acquisition team for making it possible to have the 2D seismic data used as that was the fulcrum of the research, including my main supervisor and the University of Birmingham for the permission to use it.

I am grateful to all my previous and current research colleagues who helped with answers to questions posed, their insightful feedbacks, including information on current issues relating to the research. These include Murray Hoggett, Gael Lymer, and Derren Cresswell whose advise in the early days positioned me on the right pedestal. I appreciate Murray particularly for encouraging me to take on python programming which really helped at a critical stage of the research. Also, the phase screen programme (written by Richard Hobbs and permitted for use) compilation and modelling shown in this thesis I owe to him. I appreciate all my Ph.D colleague who added fun to the journey.

I am deeply indebted to Globe Claritas (now Petrosys) support for the numerous responses, information, and advice while hands-on with their processing software. Especially Andy Juniper for being patient with my novice questions in the early days and taking the time to put me through all needed to understand seismic processing using Claritas. I would not forget Rob Hardy whom I was acquainted with in the latter days of the research via Steve Jones, his advice-cum-discussions on practical answers to some processing challenges.

I am highly grateful to my funders (Niger Delta Development Commission, NDDC) for the opportunity provided to realise a dream and providing the 3 years tuition fees.

My wife and children are mostly appreciated and acknowledged for their understanding, support, forbearance, love, distractions, and wonderfulness all these research times. I am highly honoured to have you by my side at those times of no research outcomes. I am especially humbled by the understanding of my wife, Jane Opara-Nestor.

THROUGH ALL VICISSITUDES VARIED I MADE MY WAY.

Contents

Abstract i

Acknowledgements iii

List of Figures ix

List of Table xxxi

Chapter 1 Introduction 1

1.1 Plate tectonics: 1

1.2 Spreading ridges 5

1.3 Slow spreading, oceanic detachment fault and oceanic core complexes 5

Chapter 2 Mid ocean slow spreading segments and the occurrence of oceanic core complexes (OCCs) 10

2.1 Melt production, lithospheric thickness, and faulting 13

2.2 Slow spreading segments: 19

2.3 Detachment faults 23

2.4 Features of OCCs 26

2.5 Origin of corrugations 28

2.6 Angle of detachment formation and slip 31

2.7 Area of study: 39

2.8 Outstanding questions and aims of the thesis 44

Chapter 3 Out of plane seismic noise and seismic imaging 45

3.1 Introduction: 45

3.2 Seismic reflection and scattering: 45

3.3 Seafloor Sideswipes: 47

3.4 Sideswipe characteristics: 49

3.5 Sideswipe velocities: 51

3.6 Attenuation of Scattered noise: 52

3.7 Velocity filtering: 54

3.8 f-k dip filtering: 55

3.9 Radon transforms: 57

3.10 Linear tau-p transform (Slant-stack): 59

3.11 Other Radon transforms: 60

3.12 Radon Transform (tau-p) application: 61

3.13 1500m/s migration and amplitude muting: 62

3.14 Conclusions: 66

Chapter 4 Seismic processing at 13˚20’N. 67

4.1 Introduction: 67

4.2 Seismic acquisition during JC132: 68

4.3 Hard seafloor noise: 71

4.4 Far field estimation: 75

4.5 Tau-p processing: 77

4.6 Interpolation and regularization (De-aliasing): 80

4.7 Velocity models and stacking: 81

4.8 Post-stack imaging: 85

  4.8.1 Cascaded migration: 85

  4.8.2 Depth migration: 90

4.9 Results and discussions: 93

  4.9.1 OCC footwall subseafloor: 93

  4.9.2 Impact of shot spacing: 94

4.10 Conclusions: 95

Chapter 5 Seismic Interpretation: 96
5.1 Introduction: 96
5.2 Prior knowledge of the study area: 97
5.3 Line 6.26 and the structure of the 1320 OCC 100
5.4 Result of processing other Lines: 106
5.4.1 Line 1-1: 106
5.4.2 Line 15a.17: 110
5.4.3 Line 7.23: 115
5.5 Conclusions: 120
Chapter 6 Discussion and Conclusions 121
6.1 Suppression of side-coming scattered energy to better image faulting. 122
6.2 Geometry of the detachment: 125
6.3 Detachment mechanics 126
6.4 Detachment internal structure: 130
6.5 Lateral continuity of oceanic detachment faults: 133
6.6 Conclusions and future work: 137
References 140
Appendix A: Python code for velocity model implementation and conversion to NETCDF file. 155
Appendix B: Digitised velocity values for velocity building 164
Appendix C: Claritas de-spiking values. 167

List of Figures

Figure 1.1: World map of plate boundaries indicating all plate types and the direction of motion (Duarte and Schellart, 2016).. 1

Figure 1.2: Cartoon depicting the three types of plate boundaries which are convergent plate, divergent and transform plate boundaries (Duarte and Schellart, 2016).. 2

Figure 1.3: Classical example of a fast-spreading ridge axis from Karson et al., (2006). The big arrow points to the upwelling of the partially molten mantle beneath a molten lens while the short arrows indicate a downward motion of magma from the lens.. 3

Figure 1.4: A-C: Bathymetric images of the East Pacific Rise near 18˚S (Cormier, M-H, https://www.gebco.net/about_us/presentations_and_publications/documents/cen_conf_abstract_cormier.pdf). A: from shipborne measurements, showing numerous axis-parallel faults and lines of volcanic seamounts formed off axis. B: zoom in on small rectangular patch indicated, showing limited resolution of A. C: same patch imaged by instrument operating 40 m above the seafloor. Note that on a scale well below 100m the seafloor is fairly smooth as lava flows have covered most fault offset (~straight lines parallel to axis), apart from a local feature running along the ridge crest (probably an ancient lava lake having a cooled, solidified roof which collapses when the lava drained away) and collapsed lava tubes flowing away from this lake to feed lobate flows. D: 2D seismic section (Vera et al., 1990) across the EPR at 10˚N, imaging the axial magma chamber and the Moho showing that seismic reflection can successfully image beneath fast-spreading ridges (AMC=axial magmatic chamber, M=Moho).. 4

Figure 1.5: the Chapman model for oceanic core complex formation at a slow-spreading ridge (Escartin et al., 2011).. 6

Figure 1.6: Seismic images of the Atlantis Massif oceanic core complex and associated detachment faulting at the Mid-Atlantic Ridge (location map is B; Canales et al., 2004). A: Flow-line profile Meg-10: the domal high is the Atlantis Massif. A small rider block is on the west side: the detachment should pass beneath this but is not imaged. No detachment can be traced to depth and beneath and little is seen below the “D reflection” interpreted as the base of the detachment zone. C: Axis parallel line passing north from the unroofed Atlantis Massif along its eastern flank where it is covered by a rider block. The detachment that forms the seafloor to the south may be tentatively traced in the subsurface as discontinuous reflection F. 7

Figure 2.1: World’s oceanic crust map by age (colour bar) away from the mid ocean ridge axis (modified after Muller et al., 2008). The spreading axis are the black lines with the coloured segments depicting the ultraslow (yellow), slow (green) and fast (blue) spreading segments of the oceanic ridges. Young crust resulting from decompressional melting (red-orange < 40 Ma) is widest for the fast-spreading ridges (e.g. E Pacific) and the narrower for the slow and ultraslow spreading segments (e.g. N Atlantic and SW Indian Ocean).. 10

Figure 2.2: Textbook view of seafloor spreading (Kearey, Klepeis and Vine, 2009, after Sinton and Detrick, 1992). Top: section across a fast-spreading ridge, with an axial high, underlain by an axial magma-chamber (AMC) that feeds the overlying pillow lavas via dikes that intrude other, older dikes forming a sheeted dike complex. Beneath the AMC are gabbros formed by the crystallisation of either deeper sill-like magma-chambers (Kelemen et al., 1997, Carbotte et al, 2013; Marjanovic et al., 2014) or as suggested here by downward and outward flow from the AMC (Henstock et al., 1993;

Phipps Morgan and Chen, 1993). Bottom: section across the middle of a slow-spreading segment. Magma injection is episodic. Inward-dipping normal faults cut into the lower crust, and both break up the magmatic crust and lift that up and out of the axial valley in the faults' footwalls. The total heaves (the horizontal offset) on the faults may contribute perhaps 10-25% of the spreading which remains dominantly magmatic. 11

Figure 2.3: The predicted (curves – for three different mantle potential temperatures) and observed (dots) thickness of the oceanic crust as a function of full spreading rates. Both the observations (from near the middle of segments) and the predictions (from numerical modelling) indicate little difference in magmatic thickness at full spreading rates above 20 mm/yr, but a sharp drop off in both predicted and observed thicknesses at lower spreading rates, particularly below ~10 mm/yr. Modified from Bown and White (1994)... 14

Figure 2.4: The effect of spreading rate on lithospheric thickness, seismicity and melt-lens depth and. a, b), Simplified thermal structure at slow (half rate 10 mm/yr - a) and fast (half-rate 50 mm/yr - b) spreading ridges (modified after Phipps Morgan et al., 1987). Purple box represents 6 km thick crust; thin lines are isotherms every 100˚C: the 600˚C contour marks the base of the shaded layer and the approximate minimum depth to which brittle faulting can penetrate. At a half spreading rate of 10 mm/yr (a), the 600C isotherm is beneath the Moho and faults can thus reach the mantle. At a half rate of 50 mm/yr, the brittle layer is restricted at the axis (left edge of models) to the top few km and so is within the crust: faults cannot reach the mantle. c) comparison (Phipps Morgan and Chen 1993) between base of mechanical lithosphere (inferred maximum depth of faulting from a) and b) with centroids (centre of an elliptical rupture) of teleseismic earthquakes (dot): the maximum centroid depth (dotted line) is half that of the maximum extent of faulting (green curve) and observed distribution of microearthquakes (coloured bars – Grevemeyer et al., 2019): earthquakes may extend slightly deeper than the 600˚C isotherm. Bars 1,4 microearthquake distribution from Grevemeyer et al. (2019) from SWIR and Cayman Trough; 2 SWIR 69-70˚E (Katsumata et al., 2001); 3, Gakkel Ridge at 85˚E (Korger and Schlindwein 2014); 5 MAR at 26˚N (deMartin et al., 2007), 6: Grevemeyer et al., 2013, Mid-Atlantic Ridge, various; 7 MAR at 13˚20'N (Parnell-Turner et al., 2017); 8 Wolfe et al., 1995; 9 Mid-Atlantic Ridge at 5˚S (Tilmann et al., 2004). d) comparison between predicted and observed depth of a steady-stake melt-lens or AMC (Phipps Morgan and Chen, 1993), emphasising that none is expected at half-rates below ~25 mm/yr (full rates <50mm/yr). 15

Figure 2.5: Along axis variations (Kearey, Klepeis and Vine 2009, modified from Cannat et al., 1995 and Sinton and Detrick, 1992), Top: Crustal thickness along axis of a typical fast-spreading ridge. Crustal thickness is almost constant from seafloor to the base of the oceanic lithosphere throughout the ridge with brittle deformation limited to top few km in the crust, thus restricting faulting to being minor and shallow. Bottom: Along-axis variation in crustal and lithospheric structure at slow-spreading ridges. The thickness of magmatic crust varies considerably: at the segment middles it can be thicker than average oceanic crust, but at the segment ends it is generally much thinner and in places absent. Both are expressions of focused magmatism at the segment middles. In contrast, the lithosphere is much thicker at the cooler segment ends than the segment middles, where magmatic addition increases the temperature and the geothermal gradient. The upshot is that faults can cut deep into the crust and even the mantle at segment ends, leading to the large-offset normal faults (oceanic detachment faults) that are investigated in this thesis. 17

Figure 2.6: Crustal velocity structure along profiles parallel to the spreading axis of the Mid-Atlantic Ridge (Planert et al., 2009). M marks the Moho, the base of the crust. The crust thins to < 5km at transforms and fracture zones (FZ) but reaches thickness of up to 10 km in the centre of the spreading segment. 18

Figure 2.7: Bathymetric map of the Mid-Atlantic slow spreading ridge. The boxes highlight some areas where oceanic core complexes are known to be present. 20

Figure 2.8: 3D block perspective view of the structure of a slow-spreading ridge near its intersection with a transform fault (modified from Tucholke and Lin, 1994). At the outside corner (OC), a complete if somewhat thin crustal section is cut by inward-dipping faults, but the facing inside corner exposes plutonic gabbros (green) and serpentinized mantle (light orange) adjacent to the active transform. 21

Figure 2.9: 3D perspective (A) image of the Atlantis Massif constructed from swath-bathymetric data showing corrugations sub-parallel to the adjacent transform (Cann et al., 1997) and B: side-scan sonar image of part of the corrugated surface showing smaller-scale lineations/grooves oriented ~parallel to the adjacent Atlantis Transform and so in the likely slip direction (Cann et al., 1997). The slipped block (A) consists of upper crustal lavas and may be better described as a rafted block (Reston and Ranero, 2011; Reston, 2020). 22

Figure 2.10: Early ideas about the nature of the slip surface exposed as a corrugated surface. A: Cann et al. (1997) considered the slip surface might either (question marks in A) be the base of a shallow slope failure, emerging at the foot of the valley wall or a deeply rooted extensional fault, here steepening at depth. B, C: Mitchell et al. (1998) considered that it was an extensional fault either rooting steeply (B) or at low-angle (C). 23

Figure 2.11: 3D perspective diagram of a metamorphic core complex (Fossen, 2012). The same features (breakaway, corrugated and domal metamorphic core, faulted upper plate) are observed in oceanic core complexes, suggesting a similar mode of formation. 24

Figure 2.12: Bathymetric images of two inside corner massifs: Atlantis Massif at 30N and Kane massifs A and B at 23 30’N. Both show marked corrugations oriented parallel to the adjacent transform, indicating the presence of an exhumed slip surface, i.e., the footwall to a large offset extensional fault. Key features that can be seen include the breakaway or footwall surface-cutoff and the hanging wall surface-cutoff (HW cutoff) also known as the fault trace where the subsurface fault intersects the surface. 25

Figure 2.13: Numerical model of Lavier et al. (1999, here without vertical exaggeration) showing the development of an oceanic detachment fault. The detachment is active at depth at ~ 45° rather than as a low-angle fault, but when exhumed the footwall, and the corrugated surface, flexes to low-angle. Also note that in this amagmatic model, the active fault moves with the hanging wall across and beyond the ridge axis, schematically represented by the red line. 26

Figure 2.14: Detailed bathymetric data (Reston, unpublished) collected during cruise JC132 showing details of the 1320 OCC compared with seafloor observations of Escartin et al. (2017). A: Pimply texture to west of sharp ridges: pillow lavas of magmatic seafloor; the ridges are the breakaways of oceanic detachment faults. B: Chaotic, blocky region consists of highly faulted blocks of basalt/gabbro. The corrugated surface is exposed as a grooved polished surface, typical of major fault zones (C). Ridgeward of the corrugated surface are more pillow lavas (D). From A to C is a section through the oceanic crust pulled out from beneath the hanging wall lavas

(D) by slip on a major extensional fault, the 1320 the oceanic detachment fault. The corrugated surface alone has an extent of 6x6 km. 27

Figure 2.15: Formation of an anastomosing fault zone by initial strain weakening (left), causing strain to focus into the centre of a damage zone, followed by strain hardening when the fault core is abandoned and a new fault core develops in the damage zone (Faulkner et al., 2003)... 30

Figure 2.16: The Chapman model for oceanic core complex formation at a slow-spreading ridge (Escartin et al., 2011)... 32

Figure 2.17: Velocity profiles (left) and velocity difference profiles (right, both shown without vertical exaggeration) oriented in the spreading direction in the vicinity of the Rainbow hydrothermal complex (Dunn et al., 2017). The convex-up geometry of a series of faults can be identified by interpreting high velocities (blue colours on the right) as the high density and higher seismic velocity deep crustal rocks that have been partially exhumed in the footwall of flexing normal faults....................................... 33

Figure 2.18: A Flexure and exhumation of the footwall by slip on a large-offset normal fault (Reston and Ranero, 2011 modified from deMartin et al., 2007). Key features are the breakaway, the domal slip surface of the exhumed footwall and the downward-steepening root zone. b): interpretation of seismic velocity anomalies (blue = fast, red = slow) and microearthquake distribution in terms of a variety of possible detachment geometries. 34

Figure 2.19: Rolling hinge models (modified from Reston and Ranero, 2011). A: during slip a large offset normal, the footwall is pulled out from beneath the hanging wall and flexes. This flexure controls the geometry of the fault: if the fault remains active, a large expanse of the footwall (likely corrugated) is unroofed, bounded at its outer limit by the rotated breakaway, the original footwall cutoff. B: if the footwall flexes too much, the fault may become too low-angle for slip to continue and the fault locks up, for instance if the fault has high friction coefficient (i.e. is strong). In this case the shallow, flexed portion of the fault may lock and become inactive, while slip remains possible at depth. A new shortcut fault can then cut up from the deeper root zone, transferring a slice of the hanging wall to the footwall of the new fault. The slice (a fault block, underlain by a now inactive detachment) is then rafted up and out with the footwall. Repeating the process results in successive fault blocks overlying an inactive detachment. 35

Figure 2.20: Perspective view of the segment scale detachment model: showing two possible interpretations. In the top (Reston et al., 2010), the detachment continues laterally beneath small fault blocks between adjacent OCCs, which represent the places where the detachment breaks the surface. In the alternative model (lower diagram, Parnell-Turner et al., 2021), adjacent OCCs are unconnected, the two detachments are not linked and between them spreading is dominated by magmatism. 36

Figure 2.21: MacLeod et al. (2009) model for OCC formation: strain weakening concentrates deformation onto a single fault which accommodates more than half the total spreading, and so migrates toward and over the spreading axis, to be cut by renewed magmatism. Left: structural map; Middle: magnetic lineations; Right: schematic sections. 37

Figure 2.22: Bathymetry map of the arear of study with location on world map insert. The two OCCs in focus are shown including ridge axis zone line indicated based on Mallows and Searle, (2012) interpretation of the ridge axis and recent volcanic floor. The breakaways of the two oceanic detachment faults are also interpreted. 38

Figure 2.23: MacLeod et al., 2009 Oblique view of the 1320 OCC. Note corrugations and striations are not continuous but are of finite length, and the shape of HW cuttoff reflects the corrugated/domal shape and NVZ absent in front of toe of OCC. Also note the bright backscatter of the volcanics in the hanging wall but the gap in these volcanics near the OCC toe. 39

Figure 2.24: Searle et al., (2019) 6–km-wide swathe comparison. Bathymetry (a), side scan sonar composite map (b), and magnetization from inversion (c) along slip direction and over 1320 OCC. On the composite map backscatters are observed in the footwall area of the ODF before the breakaway all through to the hanging wall, which corresponds with both positive and negative magnetisation 40

Figure 2.25: MacLeod et al.'s (2009) possibilities for the subsurface geometry of the 1320 OCC and other adjacent faults. These possibilities are extrapolations from the seafloor morphology derived from bathymetry map and side scan sonar. 41

Figure 2.26: Simao et al.'s (2020) wide angle experiment vertical sections of the velocity structure in the slip direction (over 1320 and 1330), Parnell-Turner et al.'s (2021) aseismic zone and parallel to axis. The acquisition lines for these sections coincide closely with the JC132 lines used for this thesis. 42

Figure 2.27: Distribution of seismicity around the 1320 OCC (Parnell-Turner et al., 2017). A: map view of seismicity: note it occurs two distinct bands: that outlined in red is dominantly normal faulting, that in blue dominantly reverse faulting. B: cumulative seismic moment release within these two bands over 6 months of recording. C: representative focal mechanisms for the bands. D, E: cross-sections showing distribution of the reverse (blue) and normal mechanisms. 43

Figure 3.1: Marine acquisition profiles of two views of acquisition from shot to hydrophones. (a) the sectional view of data acquisition depicting the ray theory of waves from shot to reflector to receiver, (1. Source. 2. Midpoint of incident and reflected rays. 3. receivers. 4. Acquisition vessel). (b) plane view of data acquisition representing reflections scattered from out of and in-plane scatterers. (c) Sectional view of side-coming reflection. (Larner et al., 1983; Carlvert, 1997; and Sercel.com) 46

Figure 3.2: shot gathers from marine environment synthetic and real data indicating the presence of scattered reflections and their apex shifted nature (e.g., red arrows). (a) synthetic shot from scatterers at the sea surface (Larner et al., 1983). (b)) Real shot gather from the mid-ocean ridge near 13N (deep marine environs.). (c) Synthetic shot gather showing strictly sideswipes modelled from bathymetric data from the acquisition environs of (b) using Hobbs et al., 2006 phase-screen method. These shot gathers exhibit close to similar features from the scatterers........ 48

Figure 3.3: CMP gathers with scattered noises which shows that the CMP domain does not discriminate such noises. (a, (b), and (c) are CMP gathers of Figure 3.2a, 3.2b, and 3.2c and point to non-discrimination of such noise in the CMP domain especially for the real data. 51

Figure 3.4: Synthetics of sideswipe noise modelled from a high-resolution bathymetric map using the phase-screen method demonstrating their predominance on stacked (NMO with 1500m/s and approximate model rock velocity) and 1500m/s imaged data. (a) 1500m/s NMO corrected CMP stacked data. (b) Model velocity NMO corrected CMP stacked data. (c) 1500m/s Stolt migrated section of (a). (d) 1500m/s Stolt migrated section of (b). The synthetic data has a CMP interval of 25m which impacts the length of resulting stacked data diffraction noise tails when compared to the real data in Figure 3.8. 53

Figure 3.5: Seismic data mapped to the f-k domain for filtering (Herman et al., 2017). (a) Original data mapped to the frequency domain with varying primary frequency to wavenumber while linear noise exhibits constant frequency with varying wavenumber. (b) Diamond polygon defines a filtering boundary for linear noises prior to mapping back to the x-t domain. 56

Figure 3.6: τ-p domain mapping of seismic gathers from x-t domain (Modified from Dondurur, 2018). (a) schematics of the process from x-t to τ-p domain of a single reflection. 1-5 show linear projections of points (A-E) on the gather to time prior to mapping onto τ-p. (b) live gather with primary reflection and varying noises (D = direct reflection), S = seafloor primary reflection, M = multiple, R = refracted reflection) mapped from x-t to τ-p domain. Red polygon in the τ-p domain defined for velocity filtering of noises outside the boundary. 58

Figure 3.7: A typical τ-p gather prior to polygon definition. The red, yellow, and green boundaries are the far, mid and near offsets. A close observation shows reflections in the red region are well separated from those in the yellow and green region. The red region being were most of the noise (sublinear) are separated from the P-wave reflections (elliptical). 62

Figure 3.8: Stacked and 1480m/s Stolt sections showing the attenuation achieved applying the Stolt de-spiking process. (a) CMP Zero offset section after shot gather velocity filtering in the τ-p domain with observable residual noise. (b) 1480m/s Stolt migrated section of (a) resulting to the maximum amplitude of imaged noise and their collapse to point-scale size. (c) De-spiking process applied to (b) muting collapsed noise. The muting process also results to P-wave muting were such exists at the location of the noise. (d) Stack model of (c) using Madagascar™ to de-migrate the data, showing that most of the scattered noise has been suppressed. 65

Figure 4.1: Bathymetric map of the study area showing the location of the profiles. This chapter focuses on profile L6.6 and 6a.26: the first number gives the position of the profile in the order first shot, and the second number the order in which the profile was shot; this as well as several other profiles was shot twice, once with a 20s shot interval (~ 50m) and once with a 10s shot interval (~25m) to reduce spatial aliasing. (Reston and Peirce 2016). 67

Figure 4.2: The airgun array used in MCS acquisition during JC132. The total volume was 3100 in^3, requiring ~20s to fully pressurise, but for half the survey each sub-array (volume 1550 in^3) was shot separately at 10 s intervals. (Reston and Peirce 2016). 68

Figure 4.3: Comparison of the fk spectra of a receiver location gather with 20 s shooting (left) and 10s shooting (right). Given the presence of coherent energy up to 60Hz, it is apparent that reducing the shot spacing results in far less spatial aliasing (energy beneath the lower black line). Reston and Peirce 2016 69

Figure 4.4: Detail (purple shallow, red deep) of the 1320 detachment fault at the transition from a corrugated to a blocky surface, thought to mark the boundary between dolerites and gabbros (blocky) and serpentinized peridotites (corrugated). The black horizontal line marks profile L6a.26. B: stack image along this portion of the profile, showing numerous quasi-hyperbolic events, particularly towards the left -m the region of the blocky seafloor. C, D: colour-coded by angle reflection points producing those hyperbolae. Particularly where the seafloor is rough and blocky, side-coming events are very common and can originate more than 1 km off the line. Figure courtesy of Reston, pers comm. 70

Figure 4.5: Raw shot gathers from the data of 2016 vintage from the Mid-Atlantic ridge aimed to image the footwall of the detachment fault of the 1320 OCC. On these gathers apex shifted hyperbolae (apex not at the near offset) are observed as well as strong background linear and swell noises. 72

Figure 4.6: Basic processing (bandpass frequency filtering and spherical divergence correction applied to shot gathers) of central portion of line 6a.26. (a)1500 m/s NMO corrected CMP stacked section which shows the dominance of diffraction scatterers. On this section it is difficult to point to possible real reflections. Insert is the full length of the line. (b) CMP stack after NMO correction with full refraction-derived velocity model. Diffractions still dominate and diffraction tails are even clearer. (c) Finite difference time migrated (with model Vint- time) section of (b) with the seafloor over migrated. (a) and (b) indicate the noise present in data is not attenuated either with water velocity or possible velocity of the lithology. 74

Figure 4.7: Shot source signature (far-field wavelet and frequency) estimation stages used in the process of wavelet shaping prior to deconvolution step. Modelled wavelet (a) derived from the near trace plot of a shot gather and composite far-field wavelet (b) resulting from convolution of possible bubbles, anti-aliased filter, and receiver ghost reflections. (c) Resulting minimum phase equivalent of (b). (d) Minimum phase conversion filter derived from (c). The first half of each plot is the time – amplitude wavelet plot while the second half is the frequency – amplitude plot. ... 76

Figure 4.8: Application of velocity filtering via tail muting in the τ-p domain. (a) First Shot of line 6a.26 in the τ-p domain showing elliptical and non-elliptical reflections with low linear velocity. Defined (b) and applied (c) mute boundary on (a) muting out most of the low linear events at deep. Comparing the shot gathers (in the offset-time domain) before (d) and after (e) hyperbolic velocity filtering shows removal of most linear noise in (d) while unmasking weak reflections in (e). (f) Interpolated shot gather with first resulting shot numbered 2. 78

Figure 4.9: Line L15a.17 shot gather comparing the result of τ-p deconvolution and muting to the original shot gather. (a) shows the shot gather with bandpass filtering, swell noise and water refraction removal applied. The red arrows point to possible reverberations or bubbles in the data while the blue arrows point to possible diffraction tails. (b) and (c) are gather in (a) with deconvolution and deconvolution combined with velocity filtering (tail muting) in the τ-p domain. (c) shows removal of both events in (a) and (b). 80

Figure 4.10: Semblance plot of L6a.26 with an initial seed model velocity in an attempt for velocity analysis. The plot shows the stacked sections (left) of the line and the estimated semblance plot (right) at the location (blue line through stack) along the line. The red arrow points at the low velocity estimates of the semblance from the data. 82

Figure 4.11: $vint$ – depth (a) of Peirce et al. (2019) and resulting $vint$ – time of (a) for seismic reflection studies of slow-spreading Mid-Atlantic ridge. The three plots are the upper (max) and lower (min) bound of the velocities with the mid-range (ave.) added. It is noted that the velocity model is a band of the possible range of values from the minimum to the maximum that oceanic rocks in a mid-ocean ridge could have. Note it does not indicate there are reversal implying there are no low velocity zones. 82

Figure 4.12: $vrms$ – time model (a), built from $vint$ – time model plot Figure 4.8b of Peirce et al., (2019,) used for NMO correction prior to stacking. (b) Dix converted $vint$ – depth model built from the $vint$ – time plot. (c) Second $Vint$ - time model for cascaded FD migration. These models are built in python owing to the difficulty of running velocity analysis from the 2D dataset due to masking of P-waves by sideswipes, diffraction noise and other low velocities associated with it. The layering is not indicative of the geology, but the assumptions made prior to building the velocity model and this was smoothed out before use in imaging. The models are displayed in Madagascar and Claritas. 84

Figure 4.13: CMP stack section of line 1320 after velocity filtering of the shot-channel gathers and NMO correction of the resulting CMP gather with built $vrms$ - time model. Note that velocity filtering attenuates most of the left dipping diffraction tail when compared to the right dipping tails in Figure 4.6b. 85

Figure 4.14: $1480\mathrm{ms}$ Stolt migrated sections of line 6a.26 (25m shot interval) showing the impact of de-spiking a Stolt imaged data to suppress residual sideswipes after velocity filtering in the τ-p domain. (a) Section without de-spiking and (b) Section with de-spiking applied. Note the improvement to the image of the seafloor and the removal of noise bursts resulting from diffraction-collapse. (c) Enlarged view of red square in (b) 88

Figure 4.15: CMP imaged time and depth converted sections of line 6a.25. (a) The FD migrated time section image with the cascaded migration process applying $1480\mathrm{ms}$ Stolt de-spike to attenuate residual sideswipe noise. In this section the red arrow points to a strong reflection from the footwall of the detachment fault. FC=footwall cut-off, HC=hanging wall cut-off, between the FC and HC is the chaotic zone. (b) Depth converted section of (a). 89

Figure 4.16: A: stack image from Figure 4.13, showing sideswipe diffraction hyperbolae from the rough seafloor. B: De-migrated data section resulting from the $1480\mathrm{ms}$ Stolt de-spiked data. Residual noises prior in the original CMP data are better attenuated for depth imaging procedure implementation. 91

Figure 4.17: Post-stack Kirchhoff migrated (ImageK2D) sections of lines 6a.26 and 6.6. (a) Depth migration of 6a.26 with original acquisition geometry; the red arrow pointing to the footwall sub-bottom. (b) Depth section of line 6a.26 interpolated data. The red sphere highlights the difference and improvement in (b) when compared to (a), also the footwall reflection is more continuous. However, the interpolated data has more migration noise. (c) Line 6.6 (50m shot spacing) depth image with more migration noise. Key features of the imaging are visible in all sections however sections from 25m shot spacing has better resolution. 92

Figure 4.18: Earthquake (EQ) plot from the 1320 MAR showing calculated hypocentres of the microseismicity from the detachment fault. The dash line is the elastic-plastic model deviation of the footwall subsurface. Compared to Figure 4.17 the imaged footwall conforms to this calculation by Parnell-Turner et al., 2017. 93

Figure 5.1: Bathymetric map of the study area using data collected during JC132. Location of the lines discussed are shown. 96

Figure 5.2: TOBI side-scan sonar mosaic of the study area (Mallows and Searle, 2012). Dashed blue lines show the TOBI tracks spaced 6 km apart. Either side of each track the acoustic illumination (“insonification”) is outwards from the track and so alternates every 3 km between northward (north of the track) and southward (S of the track). OCCs are picked out in pale green, the approximate position of the spreading axis in yellow and in pale orange-pink is magnetic anomaly 2. Bright regions have high acoustic back-scatter and are a combination of hard, rough, or steep and give an idea of both the age of the seafloor (hardness, roughness: as the seafloor ages, it is buried under soft sediment reducing its backscatter) and its geological fabric (e.g., volcanics, corrugated surface). 97

Figure 5.3: Seafloor fabrics (Mallows and Searle, 2012) inferred from the side-scan sonar survey, interpreted in Figure 5.4. The interpretations and relative ages will aid interpretation of the seismic sections. 98

Figure 5.4: Comparison between the interpreted seafloor geology in the vicinity of the 1320 OCC (seafloor geology map: Mallows and Searle, 2012; seafloor photographs - Escartin et al., 2017) and the detailed bathymetric image. Location of Line 6.26 shown. 99

Figure 5.5: CMP stack, time and depth migrated section of line L6a.26. (a) Modelled CMP stack after de-spiking the 1480ms Stolt migrated data and de-migration. (b) Kirchhoff migrated section of the line of the second step migration applied. (c) Interpolated geometry depth migrated section. 101

Figure 5.6: Interpretation of the depth section along the axis of the 1320 OCC. Thin black lines show the dimensions of ridges/scoops along and across the corrugations discussed in the text and in Chapter 6. HC is the hanging wall cut-off, where the oceanic detachment fault dips below the seafloor. The detachment steepens smoothly downwards, reaching a dip of ~ 45 at a depth of 6 km below the sea surface, that is ~ 3 km below the seafloor where the image worsens beneath the spreading axis: a possible continuation is shown. The continuation to depth and implications of the detachment geometry is discussed further in Chapter 6. Yellow line on the map is the spreading axis of Mallows and Searle (2012)... 102

Figure 5.7: Detail of the depth image and of the corresponding bathymetry highlighting the oblique ridge within the apron giving rise to the appearance of an incipient rider block and the details of possible anastomosing patterns in the 1320 detachment of comparable size to the ridge and scoop highlighted in the bathymetry by the and horizontal (E-W along the corrugations) black lines. Also shown is a vertical line (N-S, across the corrugations), showing the typical dimensions of the larger corrugations. 104

Figure 5.8: Cascaded time migration of Profile 1.1. Top location relative to bathymetric features. B: uninterpreted, with overlay of the bathymetric profile along the line to highlight local 3D effects. C: Possible interpretation in which the 1330 oceanic detachment fault (green) rooted close to the current hanging wall cut-off; D: alternative interpretation in which the detachment (green) roots further east and has been intensely disrupted by faulting and magmatism as the spreading axis propagates across the tip of the OCC. 107

Figure 5.9: Detail of the possible anastomosing geometry of the 1330 oceanic detachment fault near the crest of the OCC dome. The length scale and thickness are similar to that observed along line 6.26 along the 1320 OCC. 108

Figure 5.10: Detail of Line 1.1 (B, C) just east of the corrugated surface, and of the corresponding bathymetry (A). Spreading axis of Mallows & Searle (2012) in red. Black box shows area of Figure 5.11 (Escartin et al., 2017). See text for discussion. 109

Figure 5.11: Detail of the bathymetry at the toe (hanging wall cutoff) of the 1330 OCC (Escartin et al., 2017) showing the same detached block tentatively identified on the seismic image in Figure 5.10. 110

Figure 5.12: Depth migrated image along the N-S profile 15-17. Top: bathymetry, showing that the profile crosses both the 1330 OCC (left) and the 1320 OCC, and thus can test whether the OCC are linked in some way. The profile crosses the corrugated surface of the 1330 OCC: weak reflections that do not parallel the top of the surface may be lenses within an anastomosing fault zone: some of the reflections correspond to steps in the seafloor expressed as corrugations. The profile crosses the blocky surface of the 1320 OCC. Reflections from the N flank of the 1320 OCC appear to pass below the S-dipping reflections coming from the S-flank of the 1330 OCC. .. 111

Figure 5.13: Details of the lenses tentatively identified within the footwall of detachments imaged on profile 15-17. These may be lenses within an anastomosing fault zone: some of the reflections correspond to steps in the seafloor expressed as corrugations. The lenses are short enough in the isochron direction (perpendicular to slip) for the largest to be clearly resolved and control the apparent step-like topography. As depth below the seafloor increases, the anastomosing become increasingly less clear. 112

Figure 5.14: Detail of N-S profile 15-17 showing the relationship between reflections from the 1330 OCC (dark green) and those from the 1320 OCC, both of which can be tentatively interpreted as anastomosing at depth. Reflections from the N flank of the 1320 OCC appear to pass below the S-dipping reflections coming from the S-flank of the 1330 OCC. One possible interpretation is that the younger 1320 ODF partly cut across the older 1330 ODF inactive and cut by later faults. However, the 3D geometry of the surface needs to be determined. 113

Figure 5.15: Line 7.23: A: bathymetry, B: uninterpreted time migration, with overlay of bathymetric profile to highlight regions of partly out-of-plane reflections. C: interpretation: key reflections marked by broken lines: those in blue are associated with the 1320 breakaway ridge. D: same general features identified on the stack section for correlation with features on line 15-17. 114

Figure 5.16: Correlation between profiles 7-23 and 15-17. The features associated with both the 1330 OCC (green colours, B) and the 1320 high (blue colours, C) correlate with gently-dipping to sub-horizontal features on the intersecting profile, suggesting that neither comes markedly from out of the plane of section and thus that the 1320 detachment cuts beneath and across the 1330 detachment as inferred previously. Grey lines on selected profile are the seafloor from the bathymetry. .. 117

Figure 5.17: Correlation between profiles 7-23 and 15-17. The features associated with both the 1330 OCC (B, green colours) and the 1320 high (C, blue colours) correlate with gently-dipping to sub-horizontal features on the intersecting profile, suggesting that neither comes markedly from out of the plane of section and thus that the 1320 detachment cuts beneath and across the 1330 detachment as inferred previously. Grey lines on selected profile are the seafloor from the bathymetry. ... 118

Figure 6.1: Key steps in seismic processing illustrated by profile 6.26. A: CMP stacked section, showing pronounced convex-up diffractive energy, much with apexes below the seafloor. Phase screen modelling of the acoustic response of the 2D seafloor showed that much of this energy comes from the seafloor out of the plane of section. B: migration with full Vrms of the stack in A produced smeared out migrations smiles from the side-coming seafloor diffractions, obscuring any real sub-surface features. C: migration of the stack with water velocity (1480 m/s) collapses the diffractions to localised energy bursts which could be suppressed with de-spiking (D). The processing sequence continues in Figure 6.2 123

Figure 6.2: Key steps in seismic processing illustrated by profile 6.26, continued. A: CMP stacked section, showing pronounced convex-up diffractive energy coming from the seafloor out of the plane of section. B: stack section produced by de-migration of de-spiked section in Figure 6.1D. Compared to the stack in A, the diffractive energy has been largely suppressed. C: Full time migration after de-spiking. The same result can be obtained by migrating the image in B using full Vrms velocities or by a cascaded migration of the section in Figure 6.1D using reduced velocities. D: Depth migration of B using Vrms velocities, revealing the true geometry of the 1320 oceanic detachment fault. 124

Figure 6.3: Geometry of an OCC as proposed by Cann et al., (1997), Mitchell et al., (1998) and depth imaged from 2D MCS from the MAR. The geometries of ODF have been suggested prior to now and this includes as a failed plane (A) and as a steep angled (B) or low angled (C) normal fault at depth. (D) Depth image of the 1320 ODF OCC superimposed on microearthquakes (Parnell-Turner et al., 2017)................ 127

Figure 6.4: Geometry of 1320 ODF vs lock-up angles from Reston (2020). The grey and black lines show the minimum angles at which faults with the specified properties can slip as a function of depth. These lock-up angles generally decrease upwards, except for those faults that might have a high cohesion (thick black solid, broken and dot-dash lines). The dip of the 1320 detachment as imaged on the seismic (red lines) increases from low to high angle with depth, and is to the right of (steeper than) the minimum slip angle for most faults (thin and grey lines), which that the 1320 detachment should be able to slip unless it has a cohesion more than 20% of the intact rock. Ci= cohesion of intact rock (50 MPa in the top figure, 20 MPa in the lower figure), Cf= cohesion of faulted rock. Unfaulted friction coefficient (μ)=0.75 which most strongly affects the lock-up angle below the horizontal line which marks a transition from Griffiths to Coulomb behaviour.. 128

Figure 6.5: 1320 ODF depth (a) and micro-earthquake sections (b, Parnell-Turner et al., 2021). Comparing (a) and (b) it is observed the micro-seismicity slip surface aligns with the OCC from the seafloor on the depth section though the micro-earthquake is deeper than the imaged ODF plane. (b) left is closest to line 6.26 while the right side is to the south. Thick red lines indicate the position of the ridge axis on imaged section and micro-earthquake data. 129

Figure 6.6: Perspective view (Parnell-Turner et al., 2018) and sections showing the internal structure of OCCs (1320 and 1330) pointing to anastomosis in the footwall. (a)

Core complex cartoon showing how footwall anastomosis play a role in the formation of observed corrugation on the slip surface. (b) and (c) Slip and axis direction of the fault veins of rock anastomosis. (d) and (e) Section through the anastomosing fault zones in the slip and strike direction respectively, expressed where exposed as corrugated surface. In the axis-parallel (strike) direction only lenses corresponding to the largest scale of corrugations are clearly resolved and control the apparent step-like topography. As depth below the seafloor increases, the anastomosing become increasingly less clear and may include some reverberations............................... 131

Figure 6.7: Perspective views of ODFs by (A) Escartín et al. (2008) and Reston & Ranero (2011) and (B) Parnell-Turner et al., (2021). (A) ODFs are considered as a large single geologic entity with a surface expression resulting in unroofing of deep oceanic or mantle rocks during slip to form OCCs. (B) ODFs are depicted as isolated geologic entities having an aseismic zone separation.. 134

Figure 6.8: Interpreted depth imaged section along axis direction aimed to substantiate if the closely position OCCs in the MAR are single unite of a very large ODF or if they are two distinct ODFs in close proximity. Our interpretation shows these ODFs are isolated as at present but could have been linked at some point in time. 135

Figure 6.9: Along axis micro-earthquake (top - Parnell-Turner et al., 2021) and imaged depth section (bottom - line 15.17) of the 1320 ODF footwall (OCC). Even though the two sections cross the two OCC at different longitudes (the micro-earthquake section ~along the spreading axis and the seismic line 15.17 ~ten km further west and thus over the OCCS in the footwall of the detachment they show similar geometries for 1320 detachment. 136

List of Table

Table 4.1: Processing sequence applied for sideswipe suppression and imaging of the JC132 data set. 73

Chapter 1 Introduction

1.1 Plate tectonics:

The lithosphere is the upper part of the Earth composed of the crust (oceanic or continental) and the uppermost mantle. This portion of the Earth is rigid at the rate the plates move but the underlying asthenosphere, although not molten as it transmits shear wave (S-waves), is fluid-like, weak and sufficiently ductile to flow at the rates that the plate move and also weak enough to convect. Heat transfer beneath the lithosphere is primarily by convection but that in the lithosphere is primarily by conduction. As a result, the lithosphere moves as rigid plates (Fig 1.1) above a weak, convecting mantle. Relative motion between plates leads to deformation at the plate boundaries.

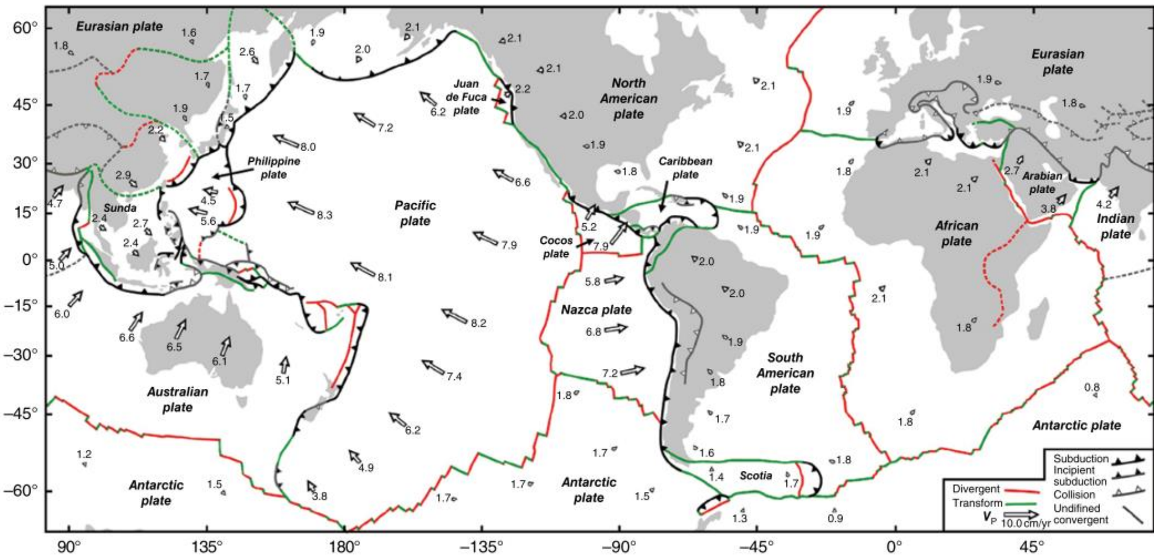
60°
45°
30°
15°
0°
−15°
−30°
−45°
−60°
90°
135°
180°
−135°
−90°
−45°
0°
45°
Eurasian plate
1.8
1.6
1.7
1.9
2.6
1.7
1.5
2.2
2.9
4.7
Sunda
2.4
2.7
2.4
5.0
6.0
6.6
6.5
6.1
5.1
Australian plate
1.2
Antarctic plate
1.5
3.8
4.9
6.2
1.9
2.0
2.1
Philippine plate
4.5
5.6
8.0
8.3
7.2
Pacific plate
8.1
8.2
7.4
7.9
6.6
Juan de Fuca plate
6.2
2.2
2.1
2.1
2.0
1.9
North American plate
1.8
Caribbean plate
Cocos plate
5.2
7.9
5.8
Nazca plate
6.8
7.2
1.8
1.7
1.7
1.7
Antarctic plate
1.5
2.1
2.1
1.9
1.9
2.0
2.0
1.9
South American plate
1.8
1.7
1.6
1.4
Scotia
1.7
1.3
0.9
1.8
1.9
1.8
1.9
2.1
2.1
1.8
African plate
1.8
Eurasian plate
1.9
1.8
2.1
2.7
Arabian plate
3.8
4.2
Indian plate
0.8
1.8
Antarctic plate
Divergent
Transform
V_P 10.0 cm/yr
Subduction
Incipient subduction
Collision
Undifined convergent

Figure 1.1: World map of plate boundaries indicating all plate types and the direction of motion (Duarte and Schellart, 2016).

Plate boundaries are classified by the motion at that boundary of one plate relative to the adjoining plate (Figure 1.2). Those boundaries where plates move towards each other are called “convergent boundaries” and – as one plate is destroyed through subduction – also “destructive boundaries”. Those where the plates moving away from each other are “divergent boundaries” and – as new lithosphere and oceanic crust is created there – also as “constructive boundaries”. And those boundaries where plates slide past each other lithosphere is neither created nor destroyed, but instead lithospheric volume is conserved and so are “conservative boundaries”. These conservative boundaries typically link other boundary types and so transform one deformation style into another and so are also called “transform boundaries” and their upper, brittle portion “transform faults”.

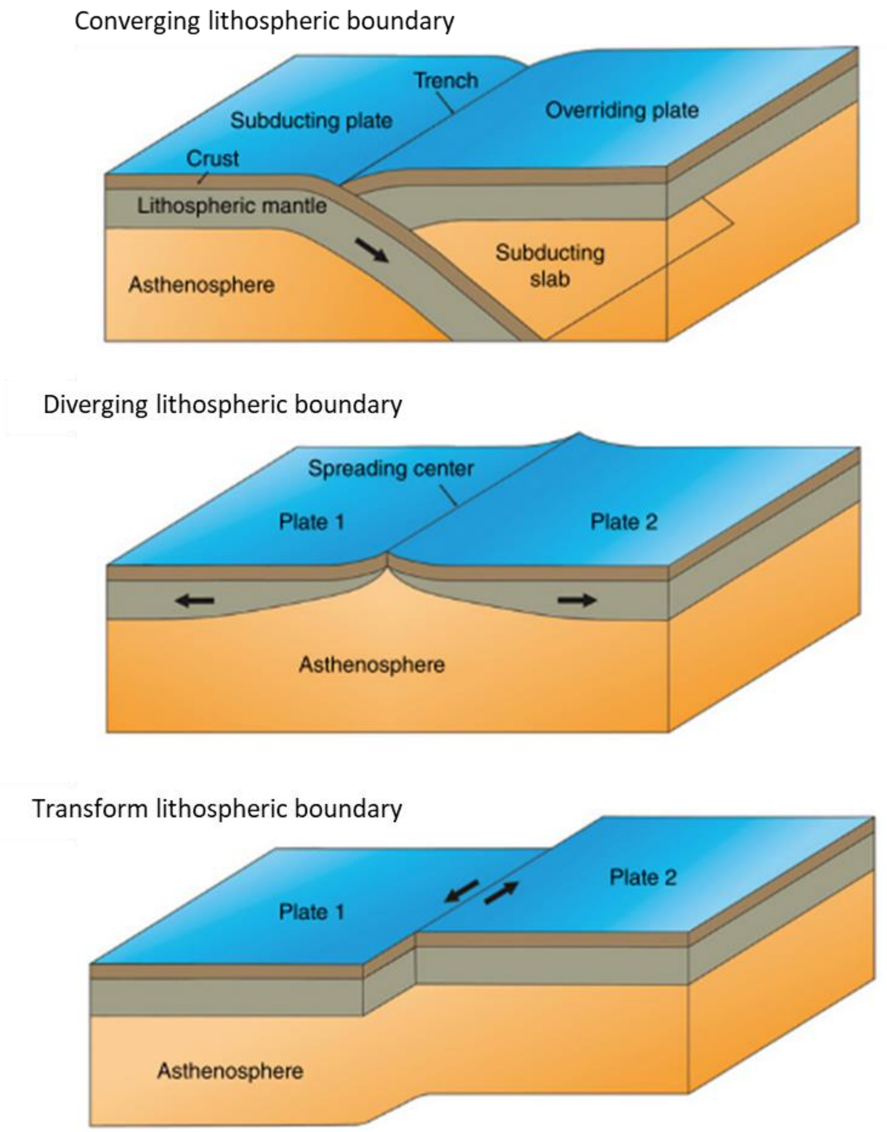
Converging lithospheric boundary
Trench
Subducting plate
Overriding plate
Crust
Lithospheric mantle
Subducting slab
Asthenosphere
Diverging lithospheric boundary
Spreading center
Plate 1
Plate 2
Asthenosphere
Transform lithospheric boundary
Plate 2
Plate 1
Asthenosphere

Figure 1.2: Cartoon depicting the three types of plate boundaries which are convergent plate, divergent and transform plate boundaries (Duarte and Schellart, 2016).

At divergent plate boundaries new oceanic crust and lithosphere is created by the upwelling of hot asthenosphere and its partial melting to generate the magma that rises to form the oceanic crust. As the newly formed lithosphere moves away from the spreading axis, it cools, thickens and subsides, so that the most elevated portion occurs at the spreading boundary. Thus, this is termed a “ridge”, even though some are marked by relatively narrow (~20 km across) axial valleys. As these ridges occur along the middle of some oceans, they are sometimes termed “mid-ocean ridges”, the best-known example being the Mid-Atlantic Ridge.

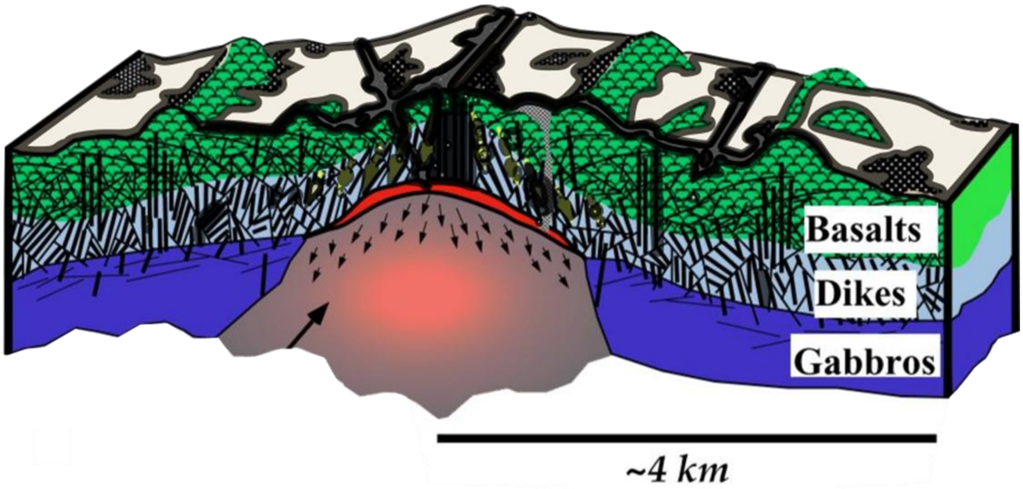

Figure 1.3: Classical example of a fast-spreading ridge axis from Karson et al., (2006). The big arrow points to the upwelling of the partially molten mantle beneath a molten lens while the short arrows indicate a downward motion of magma from the lens.

The rate at which diverging plates move apart controls the lithospheric temperature structure (Phipps Morgan et al., 1997) and hence affects the geological structure of the spreading ridge (e.g., Sinton and Detrick, 1992) leading to their classification as fast or slow with further subdivision in between. Spreading rate is calculated in mm per year (mm/yr) and considered in terms of full or half spreading rate: full rate is the relative motion between the two diverging plates; half rate is the motion of one plate away from the ridge axis. When plates diverge at the rate of more than $80\,mm/yr$ full

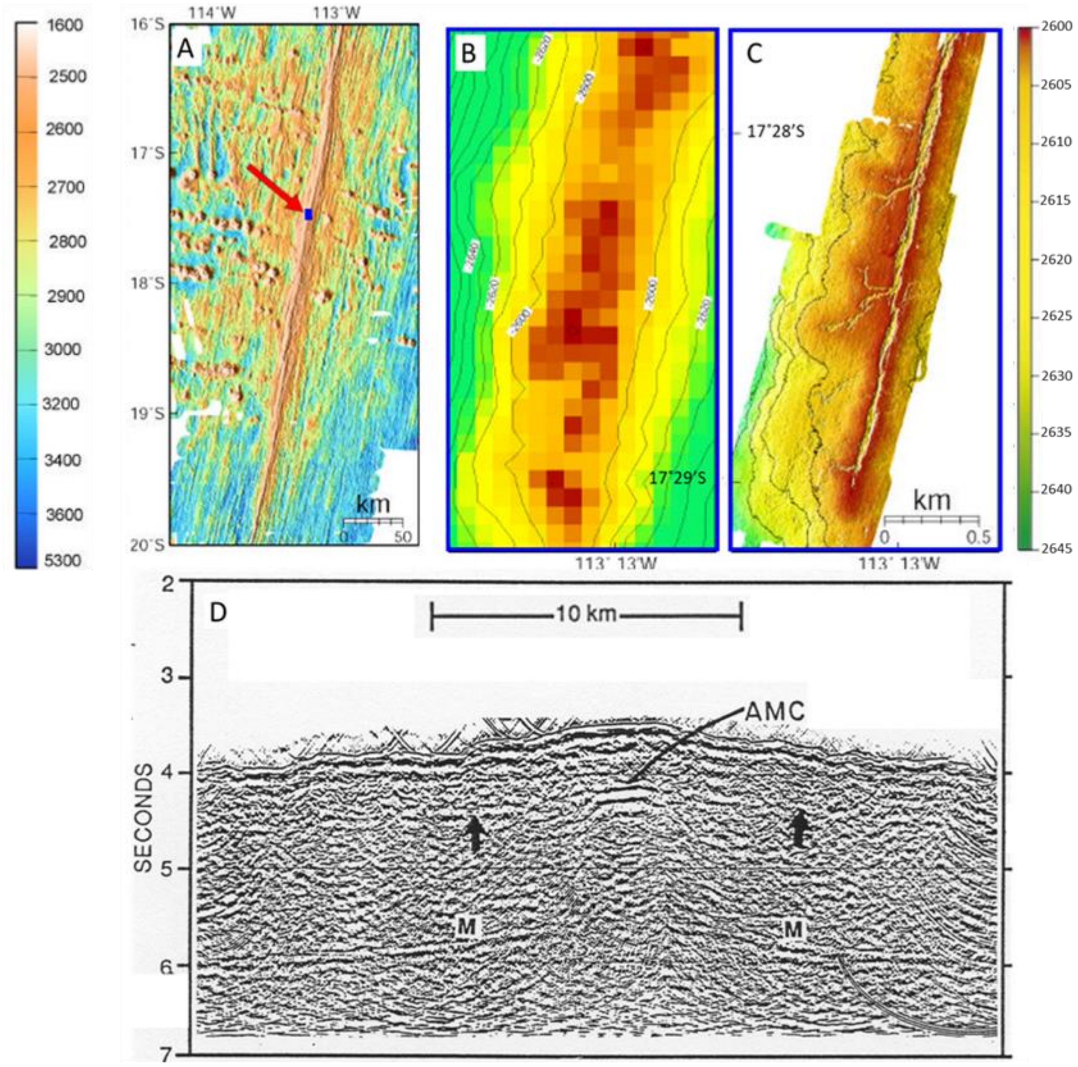
1600
2500
2600
2700
2800
2900
3000
3200
3400
3600
5300
114°W
113°W
16°S
17°S
18°S
19°S
20°S
A
km
0
50
B
17°29'S
113° 13'W
C
17°28'S
km
0
0.5
113° 13'W
2600
2605
2610
2615
2620
2625
2630
2635
2640
2645
D
10 km
AMC
M
M
SECONDS
2
3
4
5
6
7

Figure 1.4: A-C: Bathymetric images of the East Pacific Rise near 18˚S (Cormier, M-H, https://www.gebco.net/about_us/presentations_and_publications/documents/cen_conf_abstract_cormier.pdf). A: from shipborne measurements, showing numerous axis-parallel faults and lines of volcanic seamounts formed off axis. B: zoom in on small rectangular patch indicated, showing limited resolution of A. C: same patch imaged by instrument operating 40 m above the seafloor. Note that on a scale well below 100m the seafloor is fairly smooth as lava flows have covered most fault offset (~straight lines parallel to axis), apart from a local feature running along the ridge crest (probably an ancient lava lake having a cooled, solidified roof which collapses when the lava drained away) and collapsed lava tubes flowing away from this lake to feed lobate flows. D: 2D seismic section (Vera et al., 1990) across the EPR at 10˚N, imaging the axial magma chamber and the Moho showing that seismic reflection can successfully image beneath fast-spreading ridges (AMC=axial magmatic chamber, M=Moho).

rate the ridge is classified as a “fast-spreading” ridge, while any plate boundary spreading at less than $50\ mm/yr$ is a “slow spreading” ridge, and anything in between is considered “intermediate”.

1.2 Spreading ridges

The standard view of a spreading ridge best describes one that is fast-spreading (Figure 1.3), which is dominated by magmatism that, at least within the top few km, accommodate nearly all of the plate divergence, with only minor faulting (Philipps Morgan et al., 1987). The magmatic oceanic crust consists of extrusive basalt fed by a series of dikes that form an approximately continuous layer and are themselves underlain by several km of gabbros (Figure 1.3; Karson et al., 2006). An example of a fast-spreading ridge is the East Pacific Rise at 18˚S which owing to the high magmatic activities accommodates most of the plate divergence in the top few km via magmatism and minor faulting (Philipps Morgan et al., 1987). Images of the seafloor from the East Pacific Rise show the seafloor consists of basalt, in places covered by a thin layer of sediment (Figure 1.4; Karson et al., 2002), and thus “hard” – with an acoustic impedance more than five times that of the overlying ocean, and hence a very large reflection coefficient. However, at the EPR, the seafloor is mostly smooth, with faulting covered by lava flows, meaning that seismic reflection methods have successfully imaged the axial magma chamber.

1.3 Slow spreading, oceanic detachment fault and oceanic core complexes

Slow-spreading ridges are associated with larger earthquakes (Grevemeyer et al., 2019) which show that normal faulting is important, and contributes to the plate divergence. Most normal faults are of limited total slip but extend up to several km along strike, producing pronounced axis-parallel footwall uplifts, and based on the distribution of earthquakes (e.g., Mutter and Karson, 1992) cut deep into the crust and even the mantle. Some have several to many km of offset, are termed “oceanic detachment faults”, and are associated with the formation of domal massifs - termed “oceanic core complexes”- of plutonic gabbros and mantle rocks (Figure 1.5) and are the main subject of this thesis. Slow spreading ridges have been studied by geological sampling (by dredging, by manned and unmanned submersibles, and by drilling), by acoustic imagery, including high density bathymetry and side-scan sonar, by magnetic and gravity methods, and by seismic methods, both seismic and reflection. But despite the wealth of study, there remain unanswered questions, particularly about both the oceanic core complexes and the extent, geometry, and mechanics of the controlling oceanic detachment faults (Mitchell et al., 1998). These questions are detailed in Chapter 2.

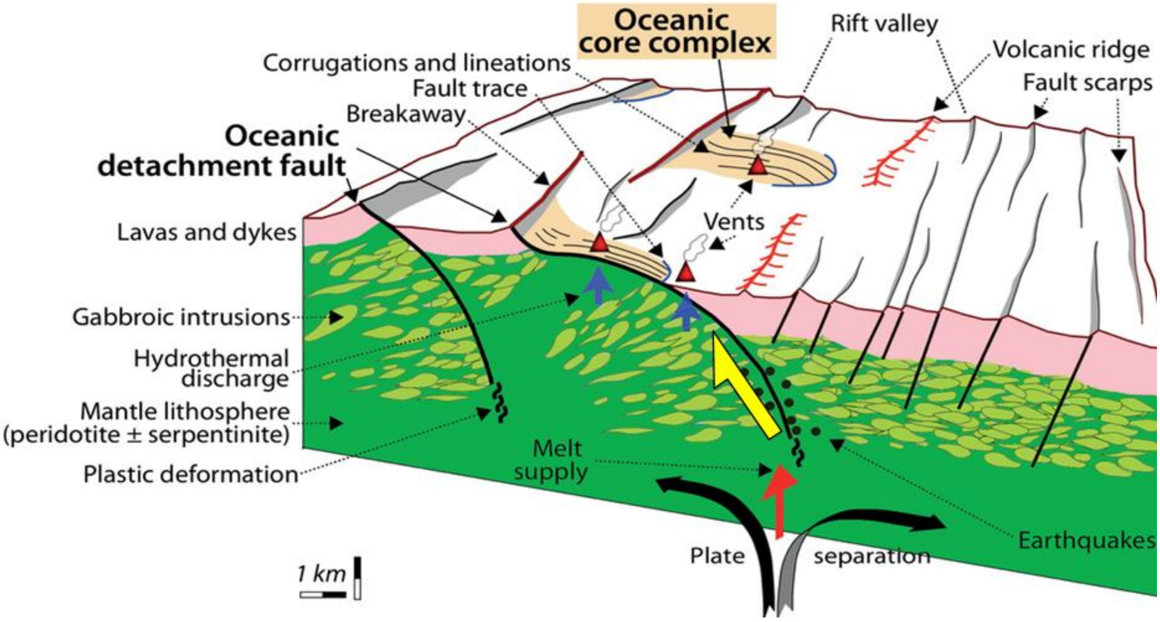
Oceanic core complex
Rift valley
Volcanic ridge
Fault scarps
Corrugations and lineations
Fault trace
Breakaway
Oceanic detachment fault
Lavas and dykes
Vents
Gabbroic intrusions
Hydrothermal discharge
Mantle lithosphere (peridotite ± serpentinite)
Plastic deformation
Melt supply
Earthquakes
Plate separation
1 km

Figure 1.5: the Chapman model for oceanic core complex formation at a slow-spreading ridge (Escartin et al., 2011).

One reason these questions remain is the lack of success of the seismic reflection method in imaging detachment fault geometry, extent, and structure beneath the

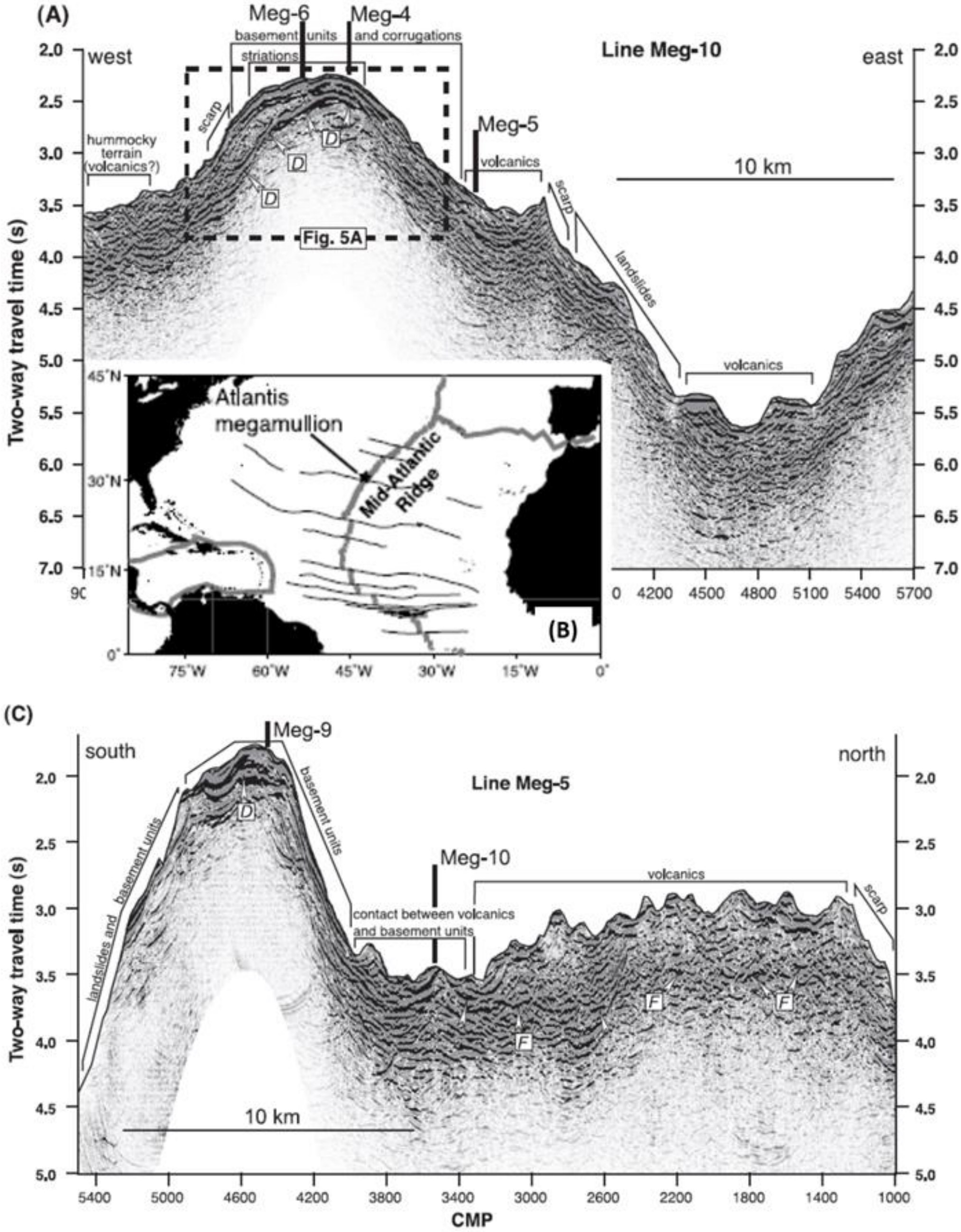

Figure 1.6: Seismic images of the Atlantis Massif oceanic core complex and associated detachment faulting at the Mid-Atlantic Ridge (location map is B; Canales et al., 2004). A: Flow-line profile Meg-10: the domal high is the Atlantis Massif. A small rider block is on the west side: the detachment should pass beneath this but is not imaged. No detachment can be traced to depth and beneath and little is seen below the "D reflection" interpreted as the base of the detachment zone. C: Axis parallel line passing north from the unroofed Atlantis Massif along its eastern flank where it is covered by a rider block. The detachment that forms the seafloor to the south may be tentatively traced in the subsurface as discontinuous reflection F.

seafloor (Figure 1.6). This stems from the physical nature of the seafloor at slow-spreading ridges: as at fast spreading ridges the seafloor is “hard” (Mutter and Karson, 1992 – hard in this context describing the large acoustic impedance contrast between basalts and water, as there is no sedimentary cover), but at slow spreading ridges it is also extremely rough, rugged, and three-dimensional (Calvert, 1997; Peirce et al. 2007). Together these characteristics present severe imaging challenges. Understanding the subsurface nature of such spreading ridges, and the extent, geometry and structure of oceanic detachment faults requires overcoming these challenges and thus the proper imaging of the subsurface nature of the faults.

This thesis presents a study of oceanic detachment fault at a slow spreading ridge, using seismic imaging techniques applied to overcome such imaging problems associated with a rough, hard rugged three-dimensional (3D) seafloor to outline the geometry and extent of such faults. In the following paragraphs a summary of the subsequent chapters is outlined aimed to address the key questions.

Chapter 2 develops further the main themes of this chapter, discussing the relevant aspects of our current understanding of seafloor spreading, pointing out the importance of spreading rate, and the processes of slow seafloor spreading, the formation of oceanic core complexes by slip on large offset oceanic detachment faults. This chapter poses the key questions to be addressed in this thesis.

Chapter 3 outlines the problems and challenges encountered in the seismic imaging of slow spreading processes, particularly when applied to address the questions posed in Chapter 2. These problems centre on the scattering of the seismic signal by the rough seafloor and the dominance of side-coming diffractions from rugged, 3D seafloor topography found at slow spreading ridges in particular. Possible noise attenuation methods via downward continuation methods and velocity filtering are proposed, to be developed, tested and applied in Chapter 4.

Chapter 4 details the application of the noise attenuation methods proposed in chapter 3. The data sets of choice are two dimensional (2D) seismic reflection data collected over the slow-spreading axis of the Mid-Atlantic Ridge in 2016. In this chapter the focus is on a single line, but the same methods have been applied to other profiles, discussed in Chapter 5.

Chapter 5 interprets the imaged results of the data sets using time and depth section. This interpretation compares the results obtained to previous works especially to the proposed source of corrugations observed on the exhumed footwalls of oceanic detachment faults and the earthquake results proposing the footwall geometry.

Finally, Chapter 6 summarises the main results to address the questions posed in Chapter 2 and 3 and emphasises the importance of the results for our understanding of oceanic detachment faulting at slow-spreading ridges.

Chapter 2 Mid ocean slow spreading segments and the occurrence of oceanic core complexes (OCCs)

At mid ocean ridges new material is added to each plate at rates in the range of ~7-60 mm per year, the half spreading rate, leading to the classification of mid ocean ridges into superfast, fast, intermediate, slow, and ultra-slow spreading ridges (Yu et al., 2013). The different spreading rates lead to different age distributions of oceanic crust formed at different ridges (Figure 2.1).

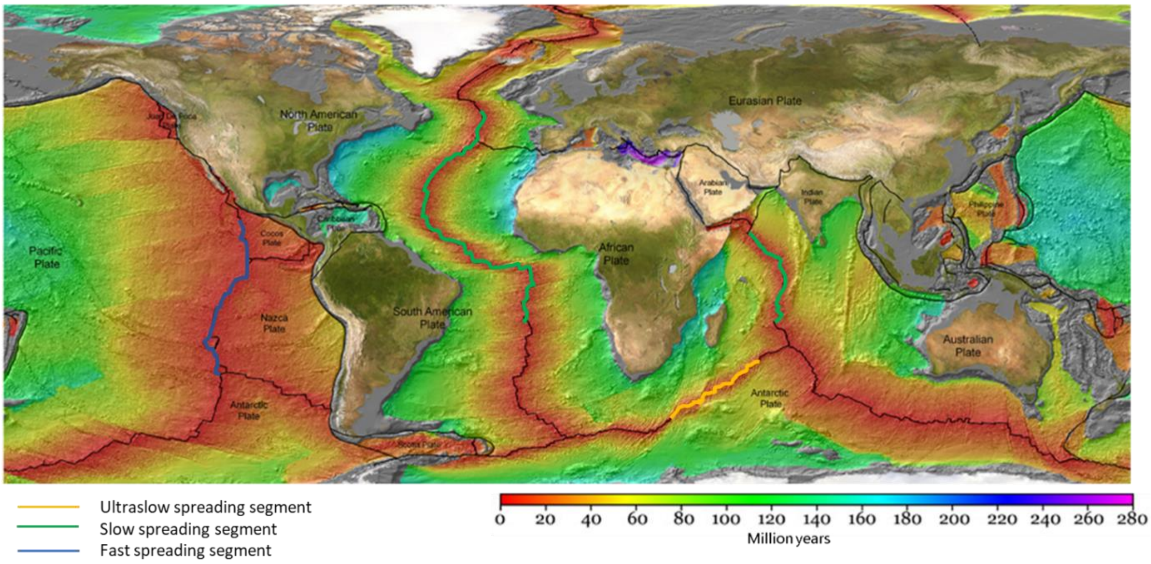
Juan de Fuca Plate
North American Plate
Eurasian Plate
Arabian Plate
Indian Plate
Philippine Plate
Caribbean Plate
Cocos Plate
Pacific Plate
African Plate
South American Plate
Nazca Plate
Australian Plate
Antarctic Plate
Antarctic Plate
Scotia Plate
Ultraslow spreading segment
Slow spreading segment
Fast spreading segment
0
20
40
60
80
100
120
140
160
180
200
220
240
260
280
Million years

Figure 2.1: World's oceanic crust map by age (colour bar) away from the mid ocean ridge axis (modified after Muller et al., 2008). The spreading axis are the black lines with the coloured segments depicting the ultraslow (yellow), slow (green) and fast (blue) spreading segments of the oceanic ridges. Young crust resulting from decompressional melting (red-orange < 40 Ma) is widest for the fast-spreading ridges (e.g. E Pacific) and the narrower for the slow and ultraslow spreading segments (e.g. N Atlantic and SW Indian Ocean).

The fast-spreading mid-ocean ridges such as the East Pacific Rise are the textbook examples where spreading is dominated by magmatic processes. As the plates move apart, the underlying asthenosphere rises to fill the gap and undergoes decompression melting. This implies, if upwelling is fast enough, the asthenosphere effectively rises adiabatically (without losing energy) and the geotherm (the temperature variation with

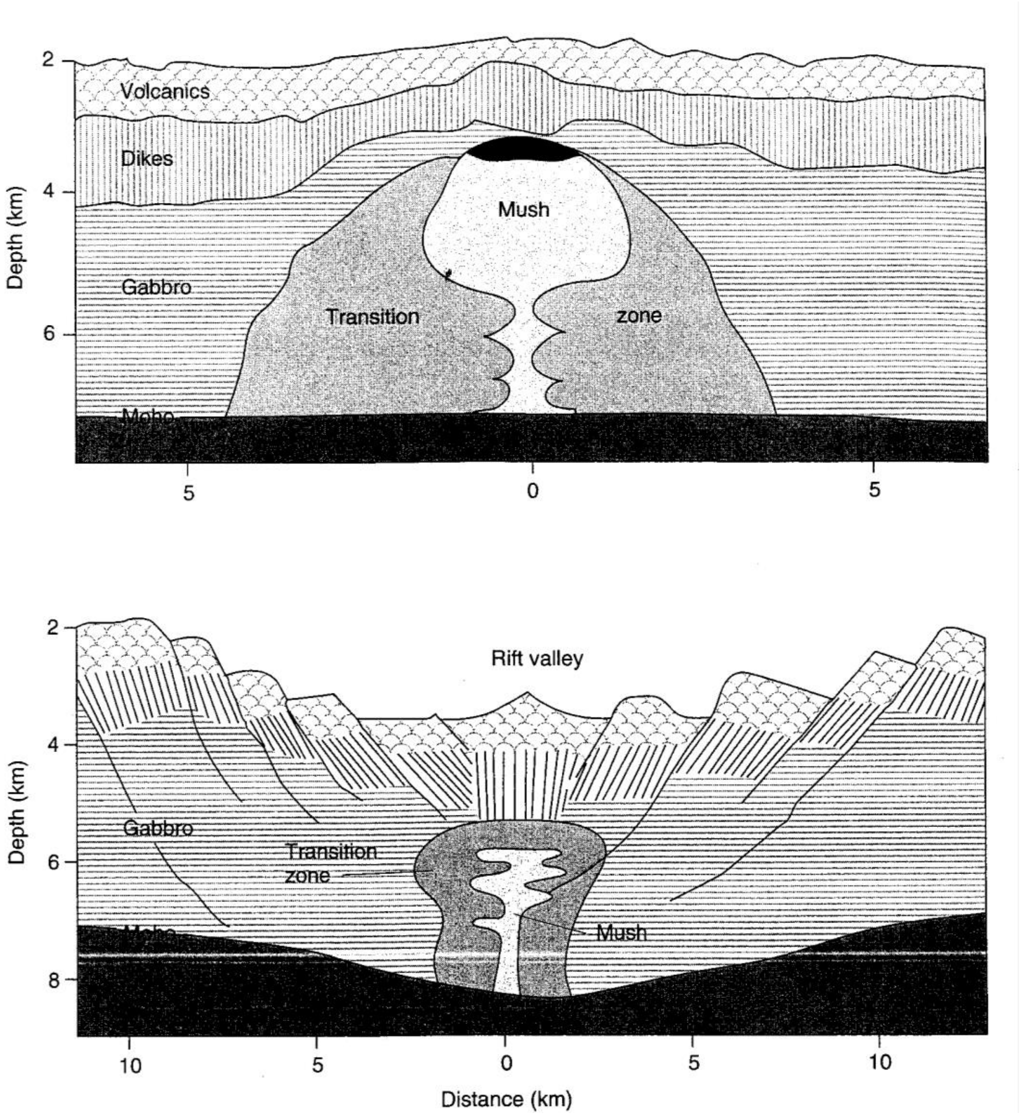
2
4
6
Depth (km)
Volcanics
Dikes
Mush
Gabbro
Transition
zone
Moho
5
0
5
2
4
6
8
Depth (km)
Rift valley
Gabbro
Transition
zone
Mush
Moho
10
5
0
5
10
Distance (km)

Figure 2.2: Textbook view of seafloor spreading (Kearey, Klepeis and Vine, 2009, after Sinton and Detrick, 1992). Top: section across a fast-spreading ridge, with an axial high, underlain by an axial magma-chamber (AMC) that feeds the overlying pillow lavas via dikes that intrude other, older dikes forming a sheeted dike complex. Beneath the AMC are gabbros formed by the crystallisation of either deeper sill-like magma-chambers (Kelemen et al., 1997, Carbotte et al, 2013; Marjanovic et al., 2014) or as suggested here by downward and outward flow from the AMC (Henstock et al., 1993; Phipps Morgan and Chen, 1993). Bottom: section across the middle of a slow-spreading segment. Magma injection is episodic. Inward-dipping normal faults cut into the lower crust, and both break up the magmatic crust and lift that up and out of the axial valley in the faults' footwalls. The total heaves (the horizontal offset) on the faults may contribute perhaps 10-25% of the spreading which remains dominantly magmatic.

depth) intersects the solidus, the temperature-depth function that marks when some of the mantle minerals (e.g., garnet and clinopyroxene) begin to melt (Sinton and Detrick, 1992). The resulting melt is broadly basaltic in composition with a lower density than the mantle and so rises rapidly towards the surface. The magma intrudes the diverging crust, forming gabbros at depth, topped by a small sill-like axial magma chamber (AMC) that in turn feeds dikes that transport the melt to the surface where it erupts as pillow lavas (Figure 2.2). The dikes intrude other older dikes which had intruded even older dikes, building up a thick sequence entirely consisting of dikes and known as a sheeted dike complex. Divergence is almost entirely magmatic, and tectonic extension by faulting is minor. The spreading axis is typically a high and fast-spreading ridges are commonly offset by widely spaced transforms and fracture zones (typically much larger than 100km apart) and the crust has “normal” oceanic crust thickness, which is between 6 and 7 km and fairly consistent in the along and cross axial direction. In short, such spreading is close to steady-state, uniform**,** magmatic and symmetric.

This model does however not apply at lower spreading rates. At slow spreading ridges (e.g., the Mid-Atlantic Ridge) where the opposing plates grow at between 10 mm/yr and 25 mm/yr (the half rate), the axis is marked by a deep axial valley ten or more km wide and bounded by inward-dipping normal faults (Sinton and Detrick, 1992; Carbotte et al., 2016). Although normal faults are generally viewed as allowing the subsidence of the hanging wall above the fault, it is perhaps easier to view the faults as allowing the footwall (the rocks beneath the fault, created by spreading processes) to be lifted up and out of the axial valley. At slow-spreading ridges, no steady-state axial magma-chamber has been imaged seismically: instead, magmatism is thought to be episodic with separate injections of magma into the crust (*Figure 2.2bottom*) and the magmatic layering is thought to be less continuous than at fast spreading ridges. There appear on the whole to be more transforms offsetting the slow-spreading ridge and dividing it into spreading segments (Figure 2.1), and in places - particularly at the ends of spreading segments - the crust formed on opposite sides of the spreading axis is not symmetrical as discussed more below. In the next section I consider why crustal and lithospheric spreading mechanism, and hence the geometry of the resulting ridge, varies so much with spreading rate before detailing the structure of oceanic crust formed at slow-spreading rates and in particular the role of large-offset normal faulting in slow spreading, the subject of this thesis.

2.1 Melt production, lithospheric thickness, and faulting

As the plates move apart, the upwelling mantle partially melts (decompressional melting) as it intersects the mantle solidus, the depth-dependent temperature at which minerals in the mantle begin to melt. As the mantle may rise more slowly beneath slow-spreading ridges, and thus have time to cool, it might be expected that the difference between fast and slow-spreading ridges is a result of different melt production: less melt might be expected where slow-spreading has given the rising mantle time to cool. It is known for instance that, in places, ultraslow spreading is effectively amagmatic (Sauter et al., 2013), accommodated entirely by successive large-offset normal (detachment) faults (Reston and McDermott, 2011; Reston, 2018). In comparing melt production with crustal thickness, it is useful to consider “magmatic thickness”, the thickness of the melt produced which will include any melt trapped in the mantle (not all the melt produced may rise high enough to reach the crust, and also to recognise that some apparent “crust” may be altered mantle – Lizzaralde et al., 2004).

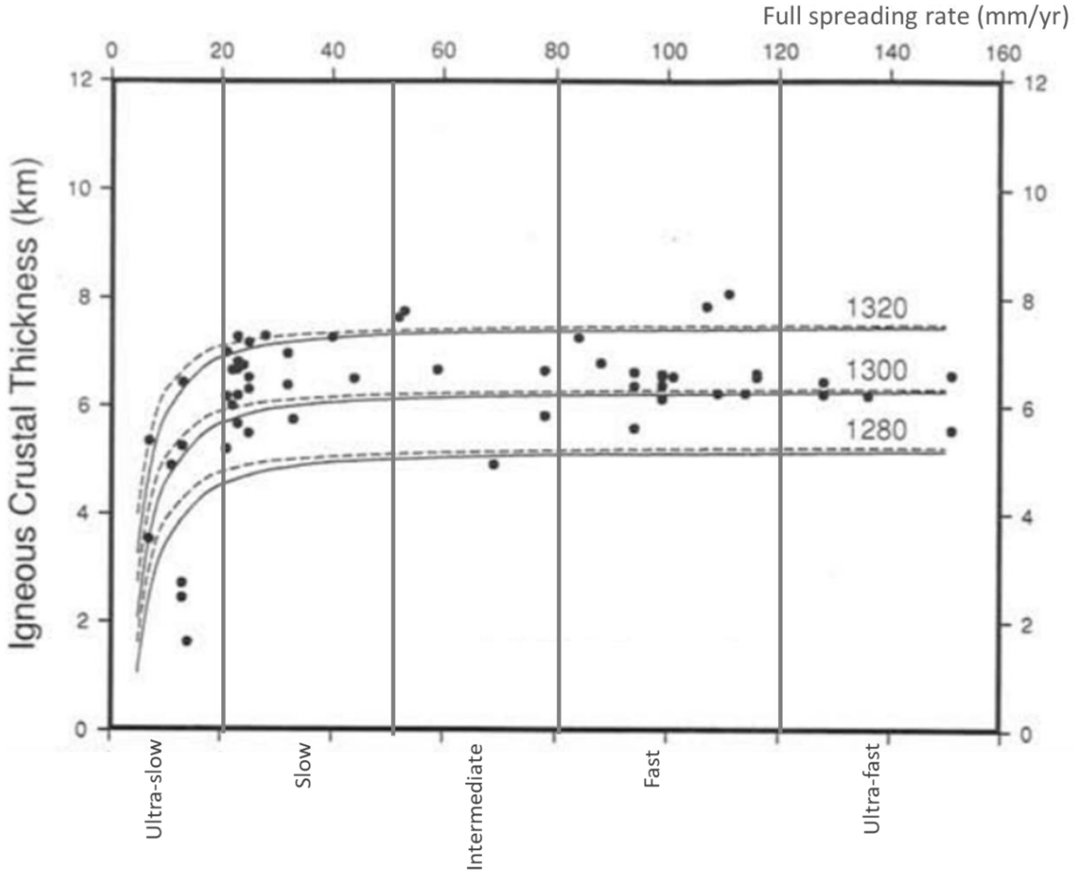

Figure 2.3: The predicted (curves – for three different mantle potential temperatures) and observed (dots) thickness of the oceanic crust as a function of full spreading rates. Both the observations (from near the middle of segments) and the predictions (from numerical modelling) indicate little difference in magmatic thickness at full spreading rates above 20 mm/yr, but a sharp drop off in both predicted and observed thicknesses at lower spreading rates, particularly below ~10 mm/yr. Modified from Bown and White (1994).

Although reduced melt production and thinner magmatic crust is observed below 20 mm/yr full rate (10 mm/yr half rate – Figure 2.3), above 20 mm/yr full rate, the amount of melt predicted and the thickness of magmatic crust observed is largely independent of the spreading rate (Figure 2.3 – Bown and White, 1994). Instead melt production should be more dependent on the “mantle potential temperature” (the temperature it would have if brought instantaneously and adiabatically to the surface).

The spreading rate does however strongly influence the ridge’s thermal structure in the top ~20 km (Figure 2.4) and hence the structure, thickness, and growth of the lithospheric plate. Numerical modelling (Phipps Morgan et al, 1987) suggests, that

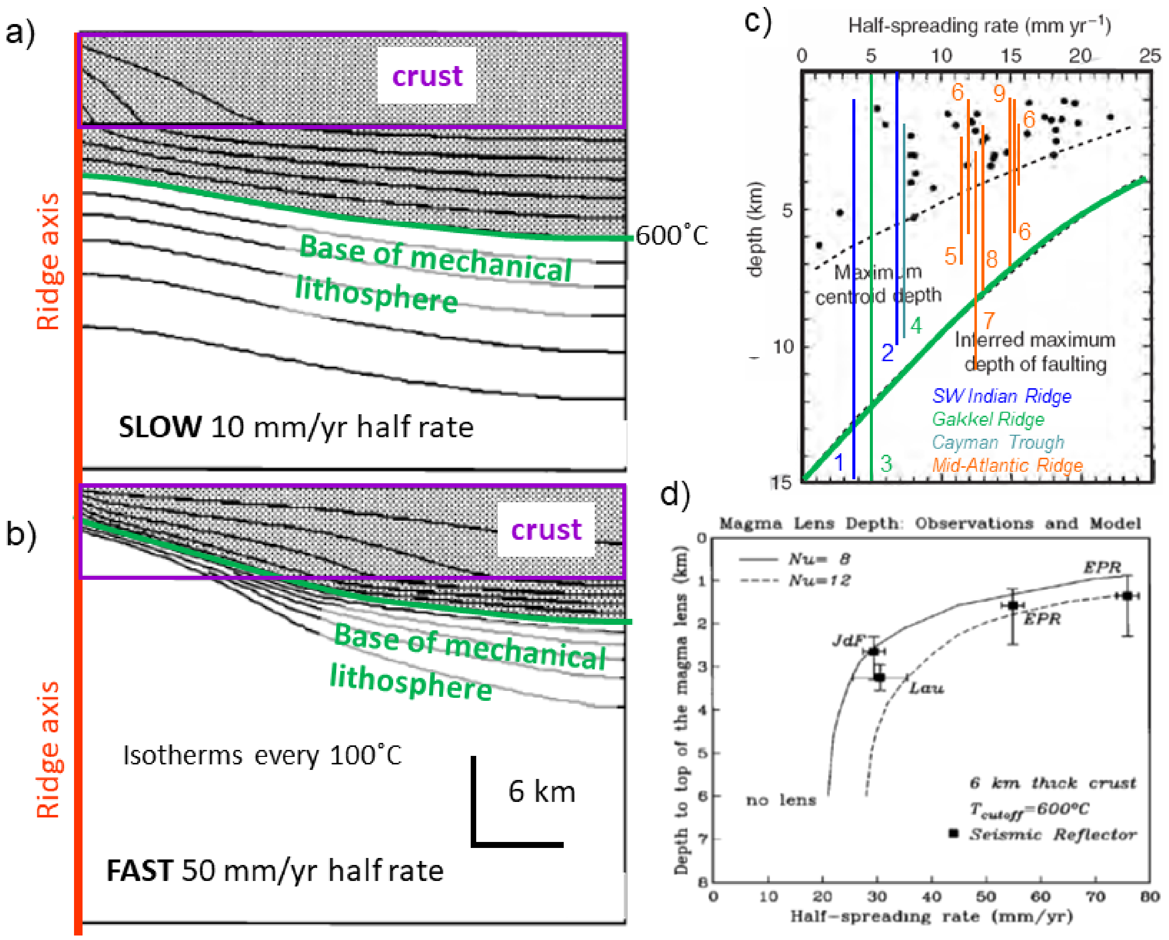

Figure 2.4: The effect of spreading rate on lithospheric thickness, seismicity and melt-lens depth and. a, b), Simplified thermal structure at slow (half rate 10 mm/yr - a) and fast (half-rate 50 mm/yr - b) spreading ridges (modified after Phipps Morgan et al., 1987). Purple box represents 6 km thick crust; thin lines are isotherms every 100˚C: the 600˚C contour marks the base of the shaded layer and the approximate minimum depth to which brittle faulting can penetrate. At a half spreading rate of 10 mm/yr (a), the 600C isotherm is beneath the Moho and faults can thus reach the mantle. At a half rate of 50 mm/yr, the brittle layer is restricted at the axis (left edge of models) to the top few km and so is within the crust: faults cannot reach the mantle. c) comparison (Phipps Morgan and Chen 1993) between base of mechanical lithosphere (inferred maximum depth of faulting from a) and b) with centroids (centre of an elliptical rupture) of teleseismic earthquakes (dot): the maximum centroid depth (dotted line) is half that of the maximum extent of faulting (green curve) and observed distribution of microearthquakes (coloured bars – Grevemeyer et al., 2019): earthquakes may extend slightly deeper than the 600˚C isotherm. Bars 1,4 microearthquake distribution from Grevemeyer et al. (2019) from SWIR and Cayman Trough; 2 SWIR 69-70˚E (Katsumata et al., 2001); 3, Gakkel Ridge at 85˚E (Korger and Schlindwein 2014); 5 MAR at 26˚N (deMartin et al., 2007), 6: Grevemeyer et al., 2013, Mid-Atlantic Ridge, various; 7 MAR at 13˚20'N (Parnell-Turner et al., 2017); 8 Wolfe et al., 1995; 9 Mid-Atlantic Ridge at 5˚S (Tilmann et al., 2004). d) comparison between predicted and observed depth of a steady-stake melt-lens or AMC (Phipps Morgan and Chen, 1993), emphasising that none is expected at half-rates below ~25 mm/yr (full rates <50mm/yr).

ignoring melt production at fast-spreading rates, the base of the thermal (~1300˚C) and mechanical (~600-750˚C) lithosphere occur within the top few km at the axis. Melt production reduces the temperature but conversely replaces mantle with weaker crustal rocks again meaning that the base of the lithosphere is within the crust. This prevents faults penetrating more than ~2 km and means that the spreading axis is marked by an axial high (Phipps Morgan et al., 1987). In contrast at slow-spreading rates (Figure 2.4a), the base of the mechanical lithosphere lies beneath the crust even at the spreading axis, allowing faults to cut down into the mantle. This is confirmed by both teleseismic and microseismicity studies (Figure 2.4c): the centroid of teleseismic earthquakes mark the centre of the rupture, about halfway between the surface and deepest extent of the rupture, so the maximum centroid depth should occur at half the depth of the brittle layer. This is observed, with the thickness of the brittle layer tracking the 600-750˚C isotherm (Phipps Morgan and Chen, 1993; Grevemeyer et al., 2019). The same result is found using microearthquakes: these small ruptures occur throughout the brittle layer and their maximum depth from a variety of detailed studies (Figure 2.4c) closely matches the predicted thickness of the brittle layer.

The thermal structure at the spreading axis also controls the depth at which an axial-magma chamber (AMC) can be long-lived or even steady-state (Phipps Morgan et al., 1993). As thermal structure in the relevant range (0-10 km) is closely related to spreading rate, again the spreading rate also correlates with AMC depth: at fast-spreading rates the AMC is both predicted (lines) and observed (error bars) to occur at ~ 2 km depth, but as spreading rate decreases, the depth to the AMC rapidly increases, until none is expected within the crust at slow-spreading ridges (half-rate < 25 mm/yr).

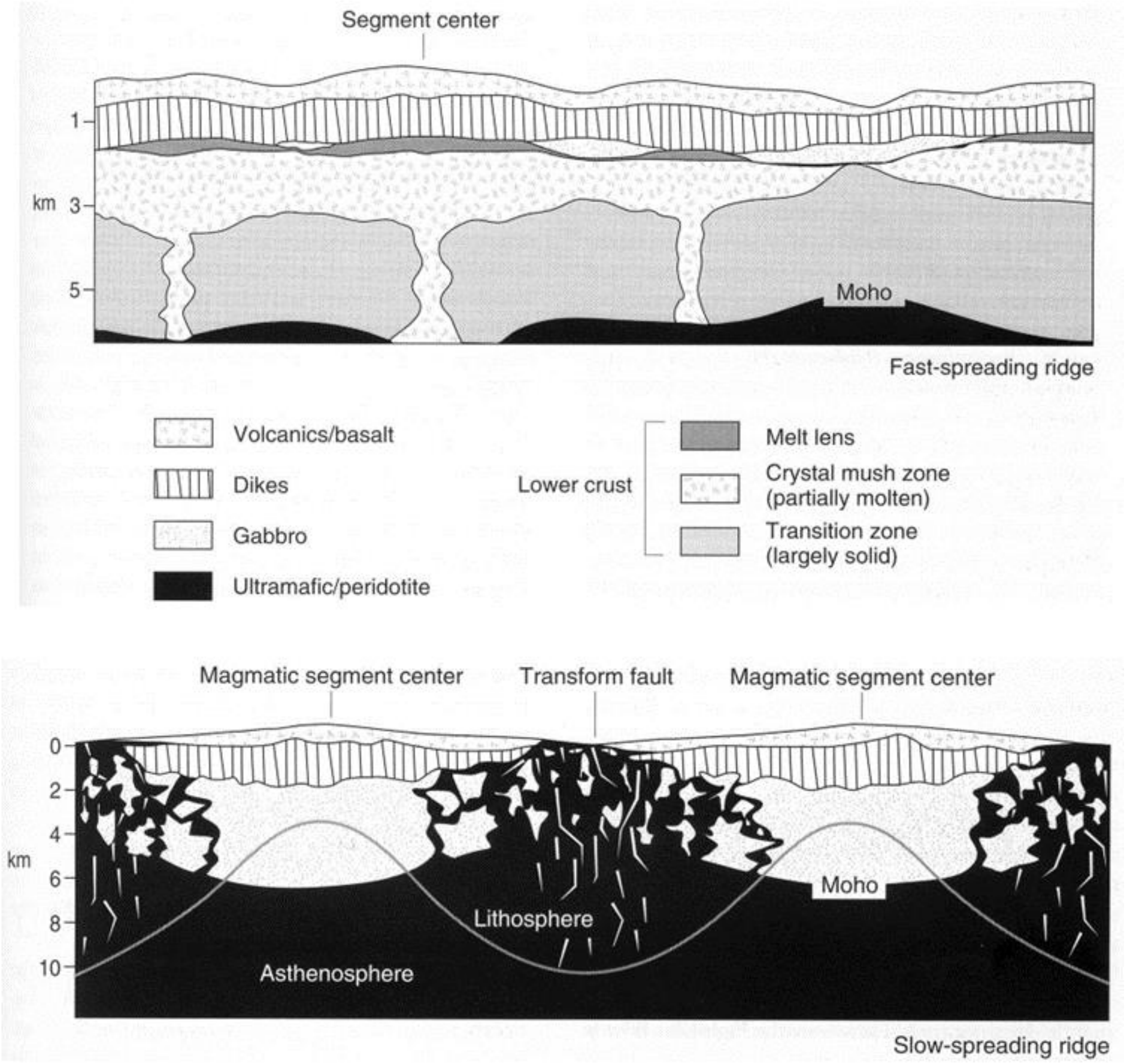
Segment center
1
km 3
5
Moho
Fast-spreading ridge
Volcanics/basalt
Dikes
Gabbro
Ultramafic/peridotite
Lower crust
Melt lens
Crystal mush zone (partially molten)
Transition zone (largely solid)
Magmatic segment center
Transform fault
Magmatic segment center
0
2
4
km
6
8
10
Moho
Lithosphere
Asthenosphere
Slow-spreading ridge

Figure 2.5: Along axis variations (Kearey, Klepeis and Vine 2009, modified from Cannat et al., 1995 and Sinton and Detrick, 1992), Top: Crustal thickness along axis of a typical fast-spreading ridge. Crustal thickness is almost constant from seafloor to the base of the oceanic lithosphere throughout the ridge with brittle deformation limited to top few km in the crust, thus restricting faulting to being minor and shallow. Bottom: Along-axis variation in crustal and lithospheric structure at slow-spreading ridges. The thickness of magmatic crust varies considerably: at the segment middles it can be thicker than average oceanic crust, but at the segment ends it is generally much thinner and in places absent. Both are expressions of focused magmatism at the segment middles. In contrast, the lithosphere is much thicker at the cooler segment ends than the segment middles, where magmatic addition increases the temperature and the geothermal gradient. The upshot is that faults can cut deep into the crust and even the mantle at segment ends, leading to the large-offset normal faults (oceanic detachment faults) that are investigated in this thesis.

The thermal structure also varies along the spreading axis (Figure 2.5), being cooler towards the segment end due to the cooling effect of the adjacent, older, colder, thicker lithosphere of the adjoining segment. For a given transform offset, the effect should be greater for slow-spreading rates as the same transform offset corresponds to a much greater age difference. The result is that towards the end of a slow-spreading segment, the temperature structure along the axis is cooler and the lithosphere is thicker (Figure 2.5b – Cannat et al., 1995). This has the effect of channelling and focusing the rising magma towards the middle of a spreading segment, producing thicker crust there and far thinner crust at the end of the segment (Figure 2.5b; 2.6). So, moving from the middle to the end of a slow-spreading segment the magmatic thickness decreases but the lithospheric thickness increases (Figure 2.5b), allowing faults to cut deeper there. In contrast, everywhere along a fast-spreading ridge the base of the lithosphere is thin enough to remain in the crust, the lower crust itself is

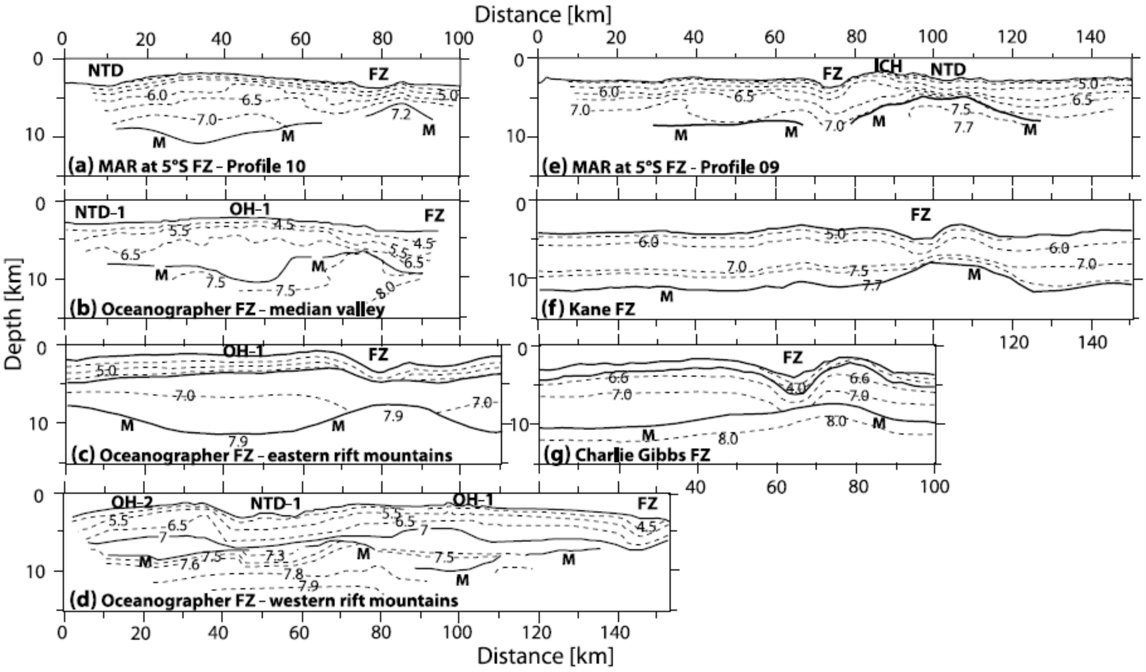

Figure 2.6: Crustal velocity structure along profiles parallel to the spreading axis of the Mid-Atlantic Ridge (Planert et al., 2009). M marks the Moho, the base of the crust. The crust thins to < 5km at transforms and fracture zones (FZ) but reaches thickness of up to 10 km in the centre of the spreading segment.

partly molten and/or hot enough to flow ductilely, and any melt focusing that occurs suppressed by along-axis flow within the crust, producing magmatic crust that is fairly constant in terms of thickness and structure (Figure 2.5a).

In conclusion, the key differences between fast and slow-spreading ridges (Figure 2.2) can all be explained by the differing thermal structure between 0 and 20 km. Note that it is fundamentally the thermal structure that controls these properties and processes, so that an unusually hot slow-spreading system (e.g., Reykjanes Ridge) might resemble a fast-spreading ridge and an unusually cold fast-spreading system might resemble a slow-spreading ridge (Phipps Morgan et al., 1987). The overall cooler lithosphere and hence thicker brittle layer resulting from slow-spreading allows faults to cut deeper, and, especially near segment ends, into the mantle. The geometry, mechanics and life-span of the largest of these faults, oceanic detachment faults, are the subject of this study.

2.2 Slow spreading segments:

Studies of slow spreading ridges (Tucholke and Lin, 1994; Cann et al., 1997; Mitchell et al., 1998; Reston et al., 2004; Canales et al., 2004; Peirce et al., 2007; deMartin et al., 2007; Escartin et al., 2008; Cann et al., 2015;) have focused on its variable morphology and the relationship between this morphology and the role of large offset extensional normal faults play in spreading. We have seen that the accretion of magmatic crust at fast spreading ridge segments is controlled by the steady supply of magma and thin lithosphere. At the other extreme, along parts of the ultraslow spreading, such as the Southwest Indian Ridge, spreading is accommodated mostly by extensional tectonic processes with little magmatic contribution (Reston and McDermott, 2011; Sauter et al., 2013; Reston 2018). At slow-spreading ridges the

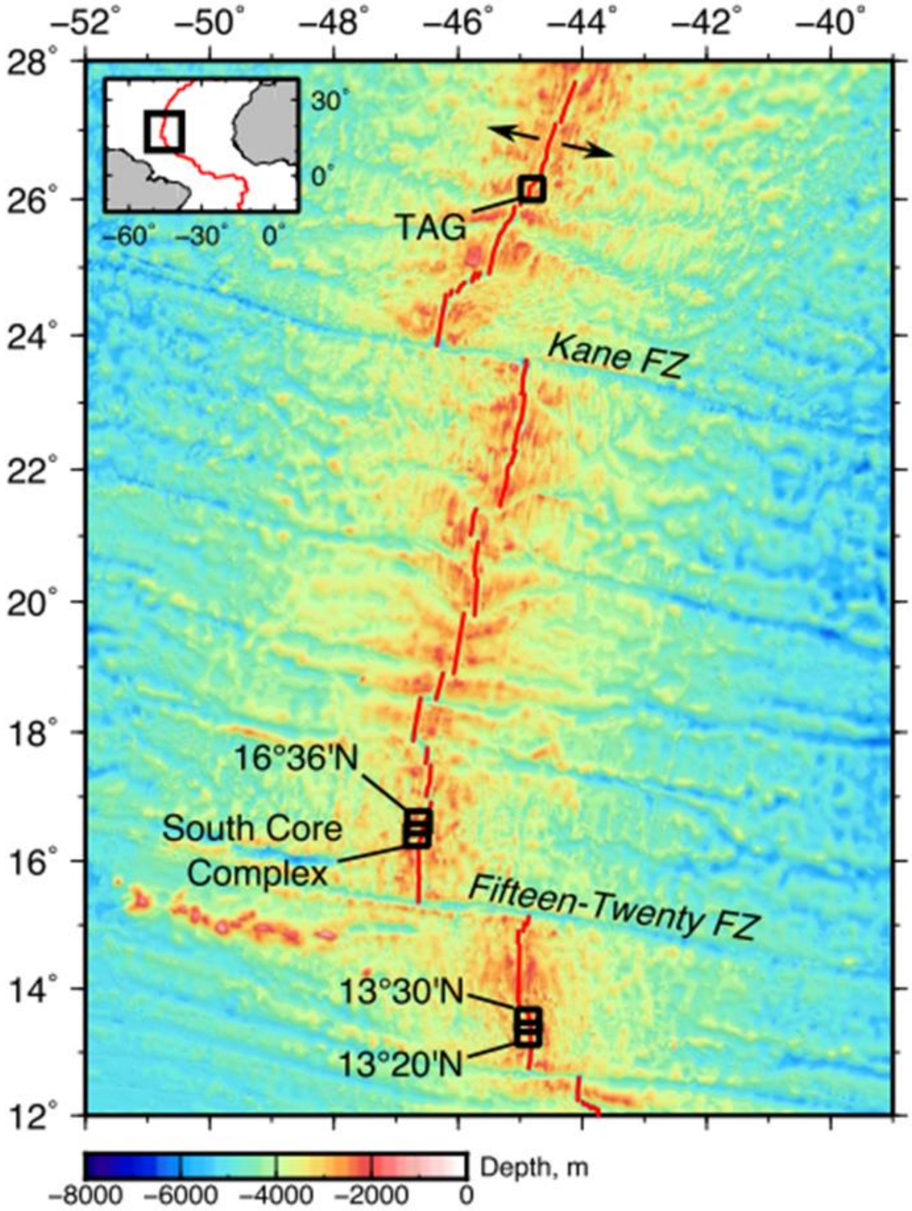

−52°
−50°
−48°
−46°
−44°
−42°
−40°
28°
26°
24°
22°
20°
18°
16°
14°
12°
30°
0°
−60°
−30°
0°
TAG
Kane FZ
16°36'N
South Core Complex
Fifteen-Twenty FZ
13°30'N
13°20'N
−8000
−6000
−4000
−2000
0
Depth, m

Figure 2.7: Bathymetric map of the Mid-Atlantic slow spreading ridge. The boxes highlight some areas where oceanic core complexes are known to be present.

magma supply is similar to that at fast-spreading ridges (Figure 2.3) but faults cut deep into the crust (Figure 2.2) and even into the mantle (Figure 2.4), so we expect both magmatism and faulting to control crustal accretion. Slow spreading ridge segments occur in both the Atlantic and Indian Oceans: I focus in on the better-known examples from the Mid-Atlantic ridge of the Central Atlantic between 12° N and 30° N (Figure 2.7).

Tucholke and Lin, (1994) used gravity, bathymetric and geological sampling data to identify a strong asymmetry towards the end of slow-spreading segments where the crust was thinner. At the “outside corner” adjacent to the inactive fracture zone the crust, although thin and somewhat deeper, resembled that towards the segment middle, with numerous moderate offset (~100m) inward-dipping normal faults offsetting oceanic upper crust (lavas and dikes). But at the corresponding “inside corner” adjacent to the active transform fault, they noted large highs or massifs, some convex-up and described as domal, rising up to 2km above the outside corner and up to 4 km above the adjacent transform, characterized by positive gravity anomalies and the presence of lower crustal gabbros and peridotites rather than lavas (Figure 2.8). They inferred that these massifs represented the footwall of very large offset normal faults.

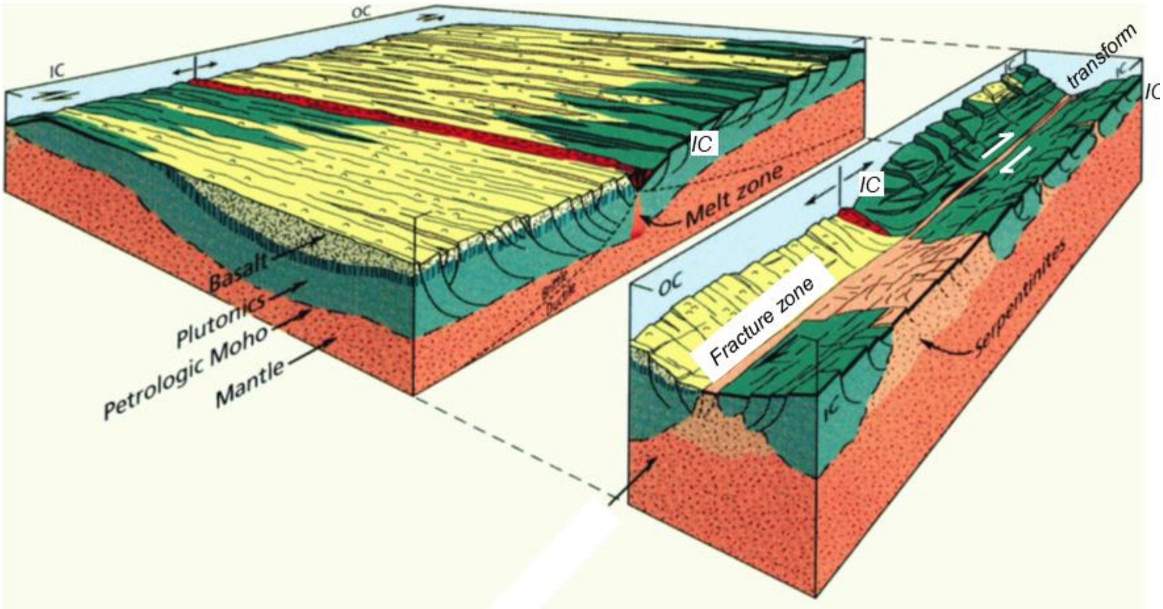

Figure 2.8: 3D block perspective view of the structure of a slow-spreading ridge near its intersection with a transform fault (modified from Tucholke and Lin, 1994). At the outside corner (OC), a complete if somewhat thin crustal section is cut by inward-dipping faults, but the facing inside corner exposes plutonic gabbros (green) and serpentinized mantle (light orange) adjacent to the active transform.

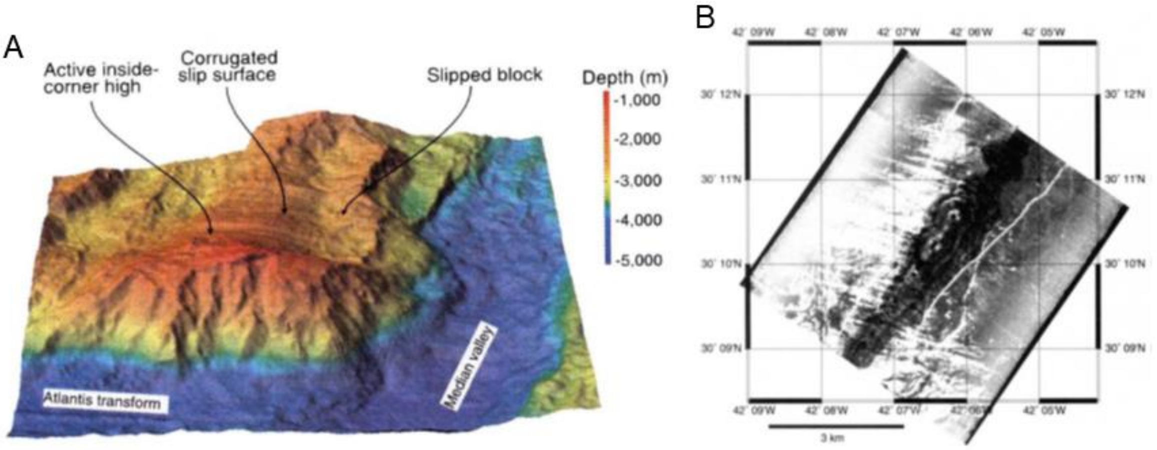
A
Active inside-corner high
Corrugated slip surface
Slipped block
Depth (m)
-1,000
-2,000
-3,000
-4,000
-5,000
Atlantis transform
Median valley
B
42' 09'W
42' 08'W
42' 07'W
42' 06'W
42' 05'W
30' 12'N
30' 11'N
30' 10'N
30' 09'N
3 km

Figure 2.9: 3D perspective (A) image of the Atlantis Massif constructed from swath-bathymetric data showing corrugations sub-parallel to the adjacent transform (Cann et al., 1997) and B: side-scan sonar image of part of the corrugated surface showing smaller-scale lineations/grooves oriented ~parallel to the adjacent Atlantis Transform and so in the likely slip direction (Cann et al., 1997). The slipped block (A) consists of upper crustal lavas and may be better described as a rafted block (Reston and Ranero, 2011; Reston, 2020).

Supporting evidence came from the observation from detailed study of the seafloor using bathymetric mapping and side-scan sonar imaging (Cann et al., 1997) that these highs were marked by corrugated and striated surfaces (both common features of exposed fault planes) where the corrugations are ~parallel to the adjacent transform and thus the expected slip direction (Figure 2.9). From the extent of the corrugated surface, described by Tucholke (1998) as "megamullions", fault offset is of the order of 10 km, sufficient to have exhumed plutonic gabbros from the oceanic lower crust and the underlying mantle peridotites, and the fault appears low-angle where its footwall is exposed at the surface. However, Cann et al. considered that the slip surface might be either the base of a shallow slope failure, emerging at the foot of the axial valley wall or a deeply rooted extensional fault (Figure 2.10). Mitchell et al. (1998) considered that the slip surfaces were extensional faults but pointed out that their geometry and depth, and hence their slip mechanics, were unknown (Figure 2.10).

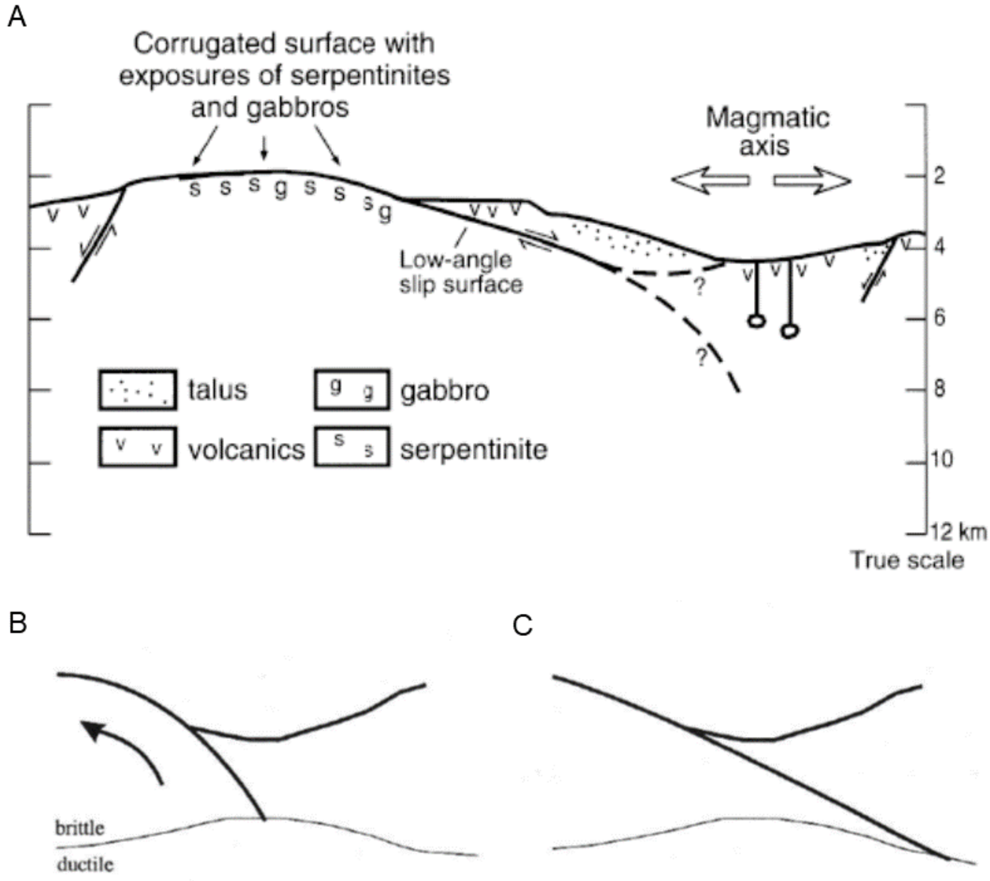

A
Corrugated surface with exposures of serpentinites and gabbros
s s s g s s s g
v v
v v v
Magmatic axis
Low-angle slip surface
?
?
v v v v
2
4
6
8
10
12 km
True scale
talus
gabbro
volcanics
serpentinite
B
C
brittle
ductile

Figure 2.10: Early ideas about the nature of the slip surface exposed as a corrugated surface. A: Cann et al. (1997) considered the slip surface might either (question marks in A) be the base of a shallow slope failure, emerging at the foot of the valley wall or a deeply rooted extensional fault, here steepening at depth. B, C: Mitchell et al. (1998) considered that it was an extensional fault either rooting steeply (B) or at low-angle (C).

2.3 Detachment faults

Domal massifs of deep crustal rocks exhumed by slip on large-offset normal faults dipping at allow-angle at the surface are also observed in highly extended continental regions. There "detachment faults" are laterally extensive (tens of km, e.g. Andreas fault), apparently low-angle normal faults (dipping <20˚ where exposed), separating a lower plate (footwall) of middle-lower crustal metamorphic and plutonic rocks from an overlying upper plate (hanging wall) of upper crustal, sedimentary or volcanic rocks, locally occurring as rider blocks above the footwall and flanking the footwall on all sides. The footwall is thus a high-grade metamorphic unit surrounded by upper crustal

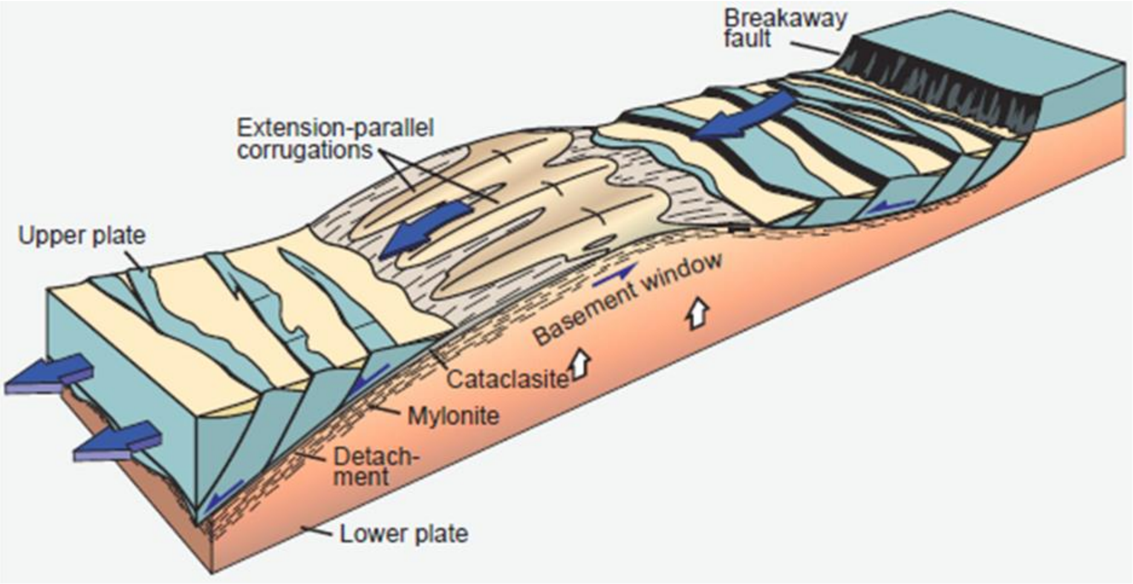

Figure 2.11: 3D perspective diagram of a metamorphic core complex (Fossen, 2012). The same features (breakaway, corrugated and domal metamorphic core, faulted upper plate) are observed in oceanic core complexes, suggesting a similar mode of formation.

rocks and is thus referred to as a “metamorphic core complex” (Figure 2.11). Initially considered to be associated with slope failure and thus emerging at the surface at the slide toe, Wernicke (1981) first proposed that continental detachment faults might represent major extensional faults rooting at depth (and perhaps cutting through the entire lithosphere), which were active at angles well below 30˚. The key debate (Collettini, 2011) has in the last twenty years focused on whether these faults formed at low-angle, formed as steeper structures but rotated to low-angle at which they continued to slip, or are steep faults which were passively rotated to low-angle once no longer active. Low-angle formation would be contrary to classical fault mechanics, but possible if the stress field were somehow rotated, or if the detachments reactivated older structures or fabric. Continued slip after rotation to low-angle is considerable easier as they might form at the 60˚ dip predicted from Mohr-Coulomb analysis for

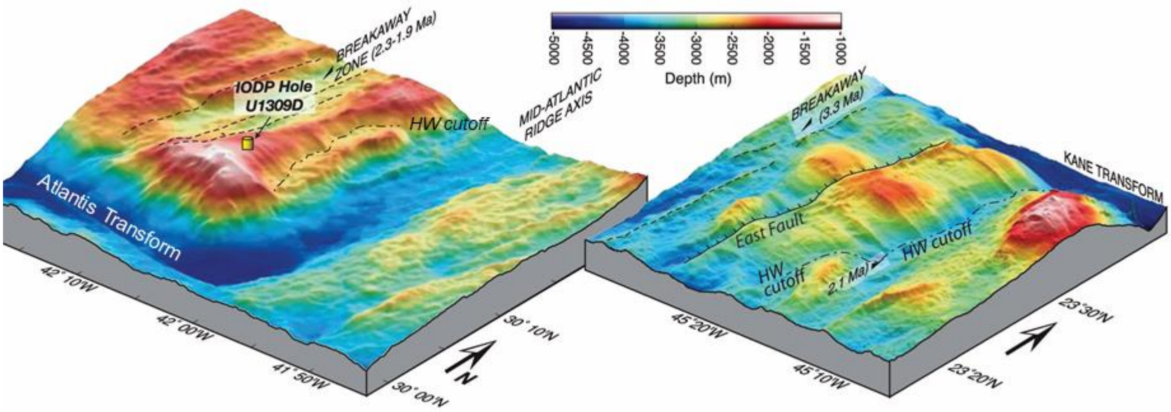
BREAKAWAY ZONE (2.3-1.9 Ma)
IODP Hole U1309D
HW cutoff
MID-ATLANTIC RIDGE AXIS
Atlantis Transform
42° 10'W
42° 00'W
41° 50'W
30° 10'N
30° 00'N
N
-5000
-4500
-4000
-3500
-3000
-2500
-2000
-1500
-1000
Depth (m)
BREAKAWAY (3.3 Ma)
KANE TRANSFORM
East Fault
HW cutoff
2.1 Ma)
HW cutoff
45°20'W
45°10'W
23°30'N
23°20'N

Figure 2.12: Bathymetric images of two inside corner massifs: Atlantis Massif at 30N and Kane massifs A and B at 23 30'N. Both show marked corrugations oriented parallel to the adjacent transform, indicating the presence of an exhumed slip surface, i.e., the footwall to a large offset extensional fault. Key features that can be seen include the breakaway or footwall surface-cutoff and the hanging wall surface-cutoff (HW cutoff) also known as the fault trace where the subsurface fault intersects the surface.

normal faults, but once formed able to remain active at non-optimum angles due to fault weakening (Reston, 2020).

Oceanic core complexes (OCC – Figures 2.12, 2.13) and oceanic detachment faults are considered analogous to their continental counterparts (Blackman et al., 1998; Tucholke et al., 1998). They comprise domal massifs of plutonic (gabbros) and mantle (partially serpentinized peridotites), topped by distinct corrugated and striated surfaces indicating slip ~parallel to adjoining transforms and are found mainly, but not entirely, at slow and ultra-slow spreading ridges. The key questions again concern whether they accommodate extension or slope failure (Cann et al., 1997), the geometry of the active fault (Mitchell et al., 1998), how they develop and are abandoned (MacLeod et al., 2009) the lateral extent of the structures at depth (Reston and Ranero, 2011) and the mechanics of slip (Olive et al., 2019; Reston, 2020).

2.4 Features of OCCs

Much of our current understanding of OCCs come from observations of their morphology and relationships at the seafloor (Figure 2.12), provided by seafloor imagery through side scan sonar and swath bathymetric mapping (e.g., Smith et al., 2008; MacLeod et al., 2009; Escartin et al, 2017), combined with control on the seafloor geology provided by sampling by dredging or submersible (manned or unmanned).

The primary feature of OCCs is a domal or gently-dipping massif marked by a grooved or corrugated surface with grooves oriented approximately parallel to the direction of plate separation, consistent with the exhumed footwall of a major normal fault (Figures 2.12, 2.14, 2.15). Sampling by dredging, by submersible, by Remotely Operated vehicles (ROVs) and by drilling has found that the domal massif consists of gabbros (probably lower oceanic crust) and serpentinized peridotites (upper mantle

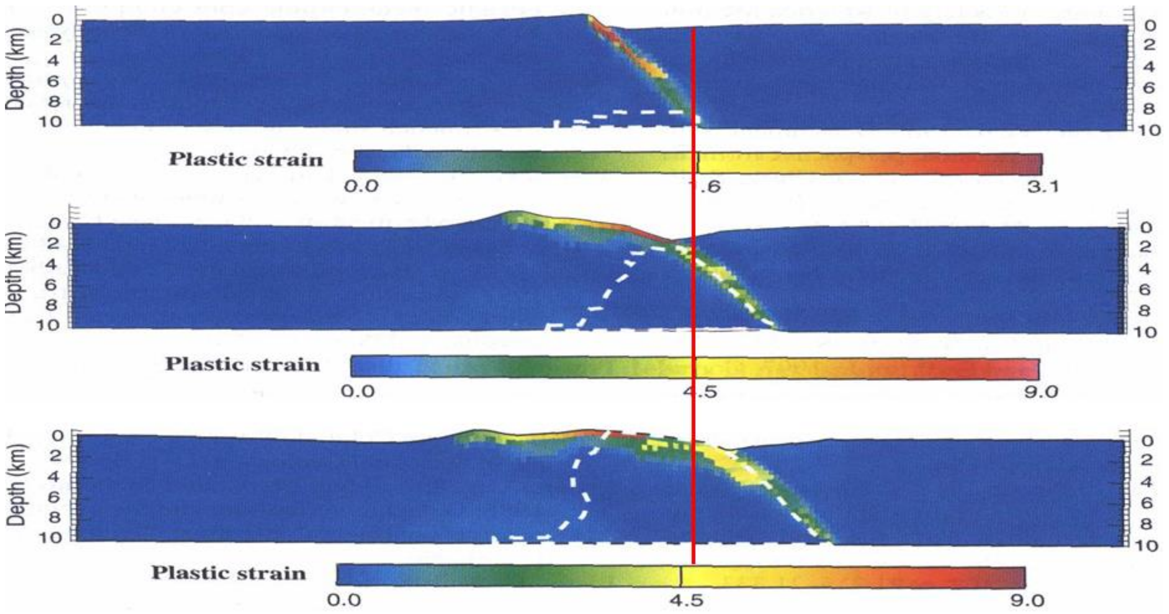

Figure 2.13: Numerical model of Lavier et al. (1999, here without vertical exaggeration) showing the development of an oceanic detachment fault. The detachment is active at depth at ~ 45˚ rather than as a low-angle fault, but when exhumed the footwall, and the corrugated surface, flexes to low-angle. Also note that in this amagmatic model, the active fault moves with the hanging wall across and beyond the ridge axis, schematically represented by the red line.

rocks), also consistent with exhumation along deeply penetrating normal faults. Associated features can include a sharp ridge on the far side of the OCC from the spreading axis, interpreted as the original top of the footwall, and referred to as the "*breakaway"* and a distinct ridgeward edge of the corrugated surface at what has been referred to as the "termination" although it is unclear what might be terminated there as if the corrugated surface does represent an exhumed slip surface, it would be expected to continue in the subsurface as a normal fault. This boundary is better –

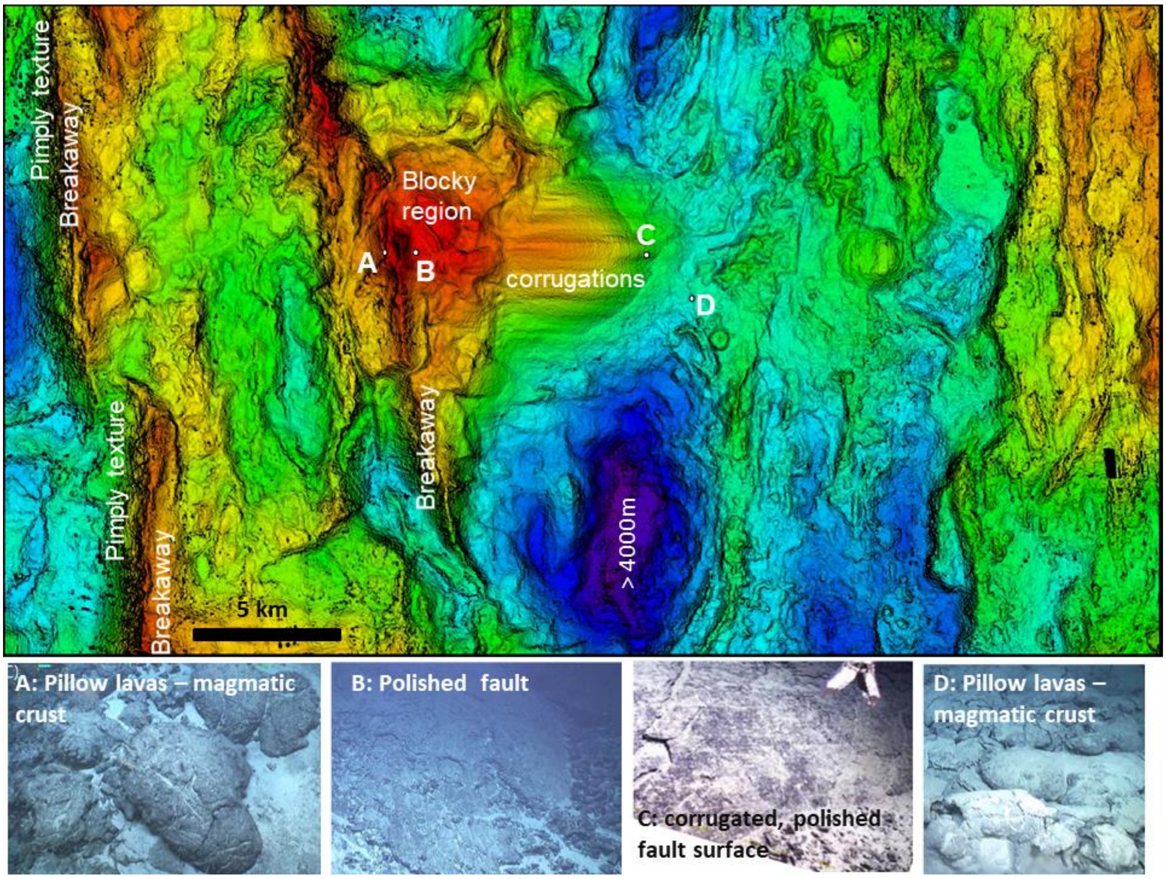
Pimply texture
Breakaway
Blocky region
A
B
C
corrugations
D
Pimply texture
Breakaway
Breakaway
> 4000m
5 km
A: Pillow lavas – magmatic crust
B: Polished fault
C: corrugated, polished fault surface
D: Pillow lavas – magmatic crust

Figure 2.14: Detailed bathymetric data (Reston, unpublished) collected during cruise JC132 showing details of the 1320 OCC compared with seafloor observations of Escartin et al. (2017). A: Pimply texture to west of sharp ridges: pillow lavas of magmatic seafloor; the ridges are the breakaways of oceanic detachment faults. B: Chaotic, blocky region consists of highly faulted blocks of basalt/gabbro. The corrugated surface is exposed as a grooved polished surface, typical of major fault zones (C). Ridgeward of the corrugated surface are more pillow lavas (D). From A to C is a section through the oceanic crust pulled out from beneath the hanging wall lavas (D) by slip on a major extensional fault, the 1320 the oceanic detachment fault. The corrugated surface alone has an extent of 6x6 km.

and below - described as the hanging wall cut-off, or the fault trace. In places (e.g., on the MAR at 13˚20'N – Escartin et al, 2008; 2017), the edge of the hanging wall is marked by an "apron" which partly mimics the expected shape of the underlying footwall and so is thought to be a very deformed, deformable and semi-detached part of the hanging wall that partly moves with the footwall, but exactly how is not yet fully known. Where sampled the apron consists of basaltic rubble: basaltic volcanic rocks (pillow lavas, volcanic cones) and diabase (dikes) dominate the regions surrounding the OCC. Beyond the apron, the hanging wall itself either appears largely undeformed, with well-preserved little rotated volcanic features, or to be broken into a series of blocks, each bounded by inward-dipping faults (e.g., Reston and Ranero, 2011). Thus, all the main features of the OCC are consistent with their interpretation as exhumed plutonic and mantle footwalls of major oceanic detachment faults.

2.5 Origin of corrugations

Although corrugated normal faults had been previously described, the widespread presence of corrugations at oceanic core complexes led to a renewed discussion of their mode of formation. Where originally observed in metamorphic core complexes, the corrugations were initially interpreted as a result of horizontal shortening perpendicular to the horizontal extension direction (Yin and Dunn, 1992; Mancktelow and Pavlis, 1994). However, in a mid-ocean ridge setting, cooling and contraction should lead to isochron parallel extension (Tucholke et al., 1998) and although such compression in a mid-ocean ridge setting might result from a change in spreading direction (Tucholke et al., 1998), the number and wide distribution of corrugated surfaces would make this interpretation unlikely. Other ideas (described in the following paragraph) include that corrugations are the shape of a strong hanging wall imprinted on a weaker footwall, that corrugations develop through the linkage of short initial fault segments, and that corrugations are the surface manifestation of an anastomosing fault zone.

The idea that corrugations are the imprint of hanging wall structure on a weaker footwall has two main forms. One is that corrugations are effectively mechanical abrasion features, mega-striations in effect, formed as the footwall is pulled out from beneath the volcanics of the hanging wall. But these volcanics are typically fragmented, faulted, and weak, and so unlikely to be able to consistently shape the footwall over hundreds of thousands of years / many km of displacement. A similar idea is that the imprint is a form of continuous-casting as hot, ductile footwall is pulled out from beneath a cooler, harder hanging wall, as proposed for the grooved extrusion of Sacsayhuamán, Peru (Spencer, 1999). This idea would require that the footwall is hot and ductile, and that the corrugated surface is a true surface, the interface between the footwall and the hanging wall, but examination of the corrugated surface suggests that the footwall is dominated by brittle deformation and that the corrugations also occur beneath the exhumed slip surface (Bonnemains et al. 2017; Escartin et al., 2017).

Another explanation arises from the way faults grow. Faults are known to start off as small, laterally restricted structures that grow and link into more continuous structures such as border faults (Cowie et al., 2005). Although this can make structures appear locally corrugated (Lapadat et al., 2017), it is hard to see how this could produce a corrugated surface with corrugations extending for many hundreds of m or even km, and hard to see why the corrugated surface appears to correspond to the dominance of plutonic and mantle rocks in the footwall rather than upper crustal rocks.

The observation that the individual slip surface that make up a corrugated surface may continue into the footwall suggests that the corrugated surface itself is the surface expression of an anastomosing fault zone comprising numerous slip surfaces separating lens-shaped lower strain zones (Parnell-Turner et al., 2018). Anastomosing fault zones may form through a combination of strain weakening (focusing the deformation in a wide damage zone into a narrow fault core) followed by strain hardening as grain size decreases causing the strain to localise elsewhere within the damage zone (Faulkner et al., 2003 – Figure 2.15). However, never have the anastomosing geometries been imaged beneath the corrugated surface on seismic. This topic will be revisited in Chapter 6.

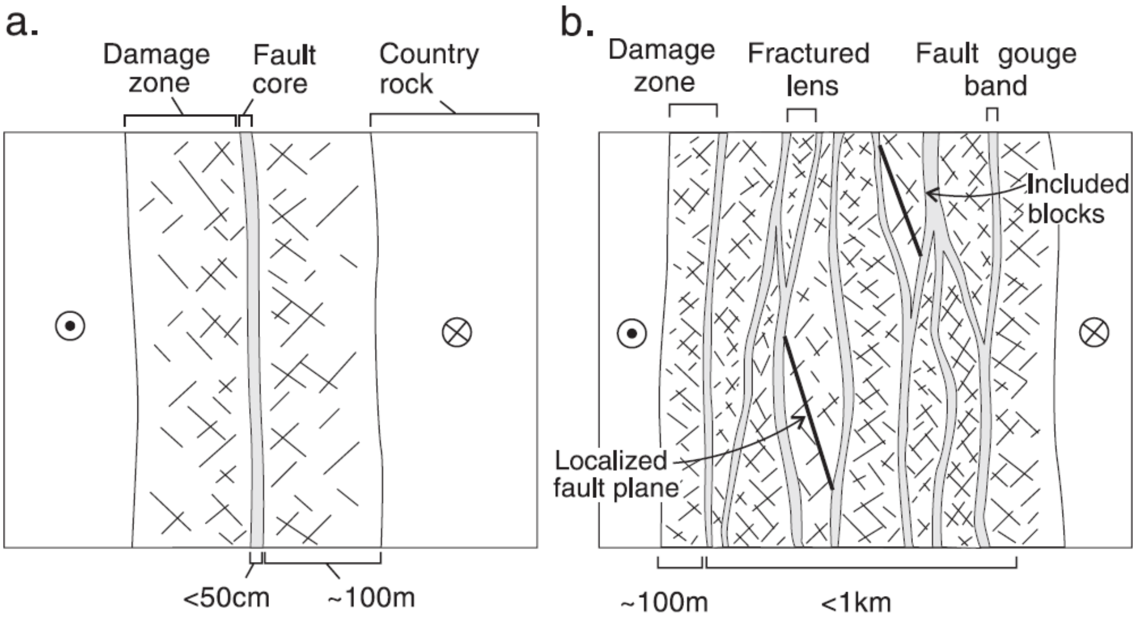
a.
Damage zone
Fault core
Country rock
<50cm
~100m
b.
Damage zone
Fractured lens
Fault gouge band
Included blocks
Localized fault plane
~100m
<1km

Figure 2.15: Formation of an anastomosing fault zone by initial strain weakening (left), causing strain to focus into the centre of a damage zone, followed by strain hardening when the fault core is abandoned and a new fault core develops in the damage zone (Faulkner et al., 2003).

2.6 Angle of detachment formation and slip

Normal faults are expected to form at steep angles (60-70˚) but rotate during ongoing extension. If the footwall can flex during unloading (Buck, 1988; Lavier et al., 1999) it can rotate much more than the hanging wall, so explaining OCCs as the domal massifs of exhumed footwall (Cann et al., 1997; Ranero and Reston, 1999; Lavier et al., 1999; Smith et al., 2008; Reston and Ranero 2011; Olive et al., 2019). Models in which the footwall of a steep normal fault flexurally rotates to low angle as it is pulled out from beneath a less-rotated hanging wall are called “rolling hinge” models (Buck, 1988; Lavier et al., 1999; Fig 2.13) and are widely applied to explain the formation of OCCs. The key questions concern the amount of footwall rotation, the angle of fault initiation, the geometry of the detachment at depth with implications for the mechanics of slip and the evolution of the detachment system in space and time.

Smith et al., 2008, pointed out the significance of the breakaway ridge as an indication of rotation during the formation and lifetime of detachment fault and used it as part of the identification of closely spaced oceanic core complexes in the 13N region (Figure 2.14). Between the breakaway and the spreading axis is a chaotic zone (Escartin et al. 2008; MacLeod et al., 2009) with numerous small faults and in places a blocky texture (Figure 2.14). The chaotic zone is thought to be a section through the upper crust (lavas and dikes) affected by secondary faults related to the bending and rotation of the footwall. If the breakaway has not been significantly affected by mass-wasting or secondary deformation, the angle there of the rotated top of the footwall indicates how much the footwall has rotated, and the angle between the top of the footwall and the fault can be used to infer the angle at which the fault initiated (Reston et al., 2004). Such analysis generally shows that the footwall has rotated by 45-60˚, consistent with values deduced from paleomagnetism (Garces and Gee, 2007; Morris et al., 2009) and which imply that the detachment fault initiated as a steep normal fault. Such results are consistent with numerical models of OCC formation in which the angle of initiation varies between 45˚ (Lavier et al., 1999) and ~60˚ (Tucholke et al., 2008), leading to the Chapman model for slow seafloor spreading (Figure 2.16).

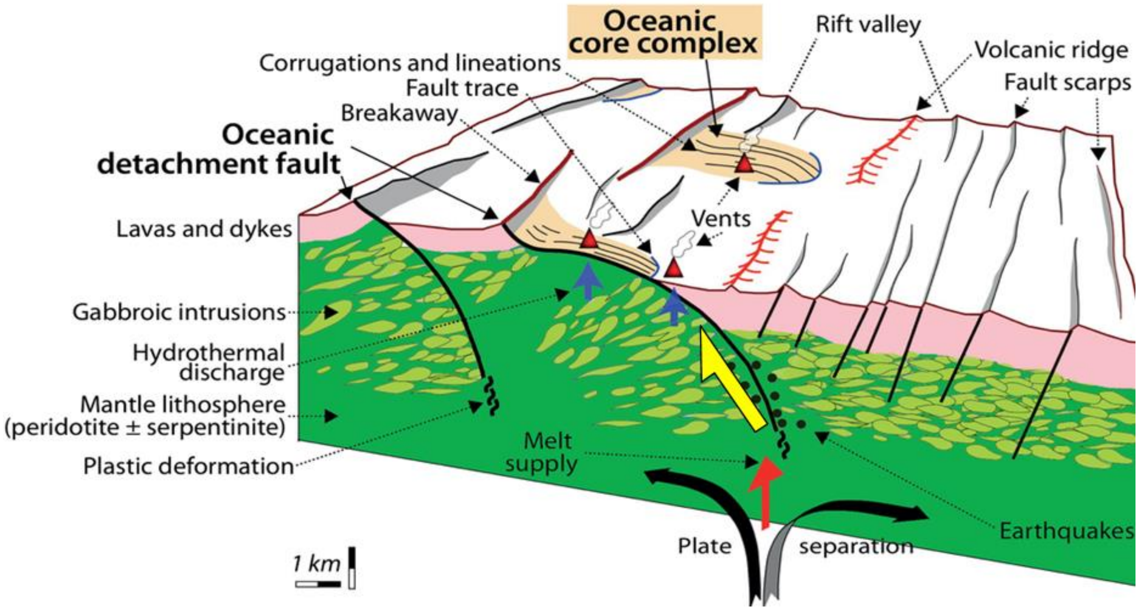
Oceanic core complex
Rift valley
Volcanic ridge
Fault scarps
Corrugations and lineations
Fault trace
Breakaway
Oceanic detachment fault
Lavas and dykes
Vents
Gabbroic intrusions
Hydrothermal discharge
Mantle lithosphere (peridotite ± serpentinite)
Plastic deformation
Melt supply
Earthquakes
Plate separation
1 km

Figure 2.16: The Chapman model for oceanic core complex formation at a slow-spreading ridge (Escartin et al., 2011).

There have however been few direct studies of detachment geometry at depth, a key question in understanding OCC formation (Mitchell et al., 1998). A variety of geophysical studies, (seismic refraction, microseismicity, reflection imagery) have been used to map the geometry of the detachment. Reston et al. (2004) and Reston and Ranero (2011) used depth images of possible Cretaceous OCCs buried beneath the Canary Basin to infer that the faults steepened to at least 45˚ at depth. Dunn and others (2017) used detailed velocity profiles to identify regions where seismic velocity was lower or higher velocity than expected, interpreting the high velocity zones as the deep crustal rocks partially exhumed in the footwall of large offset normal faults (Figure 2.17). DeMartin et al., 2007 used the velocity structure of the top few km to guide the

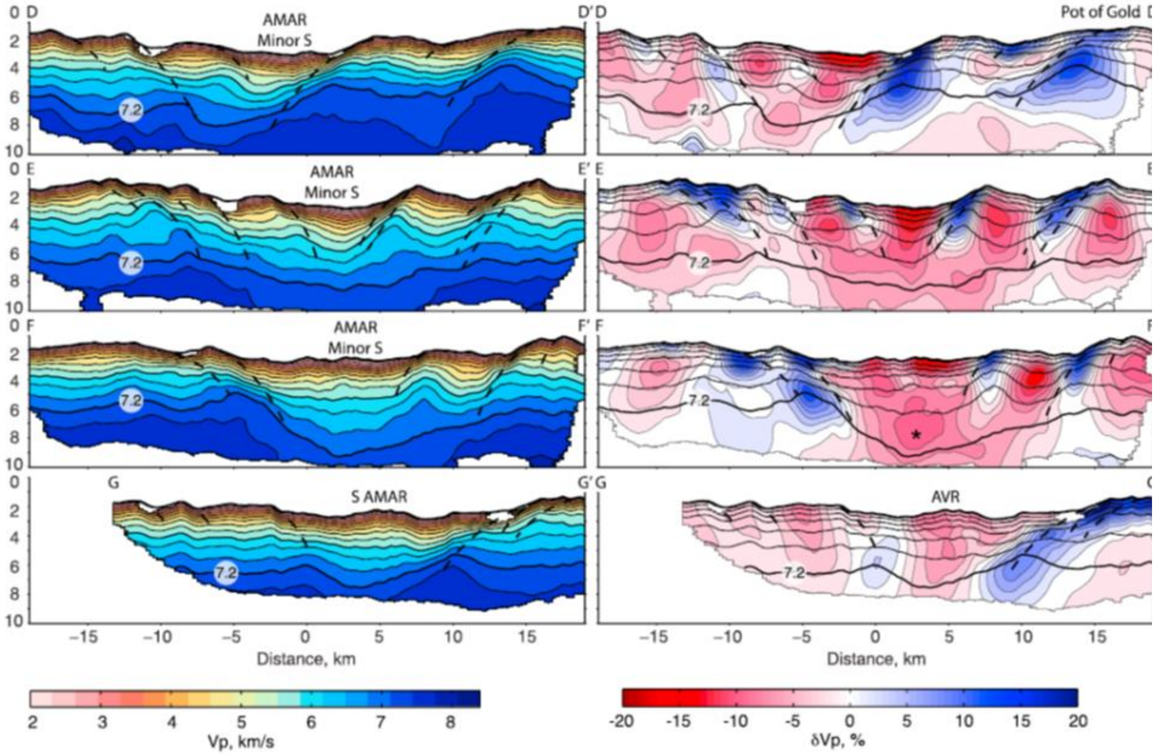

Figure 2.17: Velocity profiles (left) and velocity difference profiles (right, both shown without vertical exaggeration) oriented in the spreading direction in the vicinity of the Rainbow hydrothermal complex (Dunn et al., 2017). The convex-up geometry of a series of faults can be identified by interpreting high velocities (blue colours on the right) as the high density and higher seismic velocity deep crustal rocks that have been partially exhumed in the footwall of flexing normal faults.

interpolation of fault geometry between the surface (geometry of the OCC as it approached the HW cutoff) and a steeply dipping band of microearthquakes at depth (Figure 2.18) inferring that OCCs initiate at a high angle (~70°) prior to low angle rotation to ~20° of the exhumed footwalls during their life cycle. Parnell-Turner et al. (2017) and Simao et al., (2020) used the distribution of microearthquakes with a normal faulting mechanism to infer that the 1320 detachment rooted at depth at >70°.

The use of seismic velocity variations to identify the footwall is however risky as other variations in the deep crustal structure can cause variations in the seismic velocity. Canales et al., (2008) interpreted high velocities observed as refraction on long streamer data as gabbros and lower velocity regions as serpentinized mantle: if

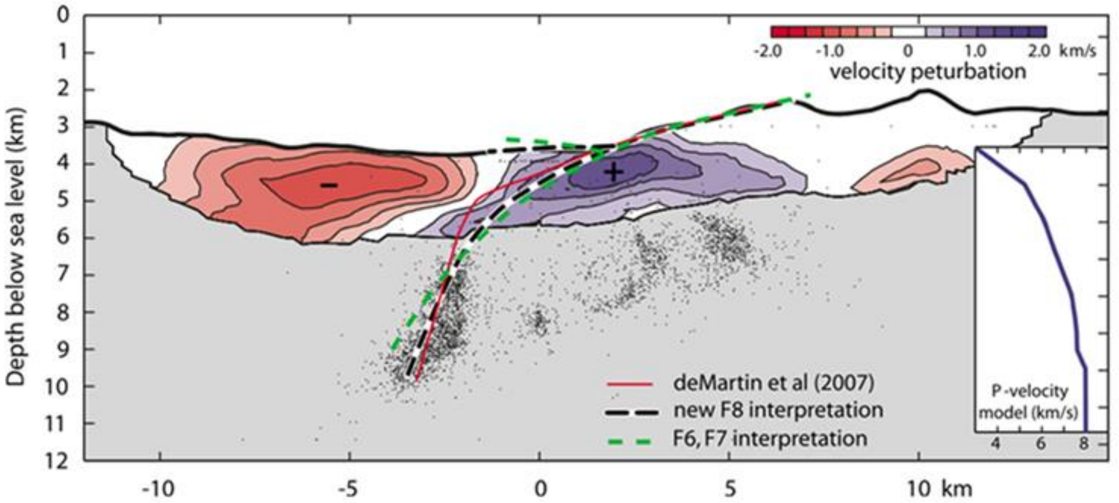

Figure 2.18: A Flexure and exhumation of the footwall by slip on a large-offset normal fault (Reston and Ranero, 2011 modified from deMartin et al., 2007). Key features are the breakaway, the domal slip surface of the exhumed footwall and the downward-steepening root zone. b): interpretation of seismic velocity anomalies (blue = fast, red = slow) and microearthquake distribution in terms of a variety of possible detachment geometries.

correct, the fault geometry may be misinterpreted if serpentinites form the footwall and gabbros the hanging wall to the faults. Furthermore, microearthquakes are not reliably located in the shallow subsurface (deMartin et al., 2007) meaning that there is considerable uncertainty about the geometry of the fault down to a few km depth.

The geometry of the detachment in the top few km is critical to understanding their mechanics. It is commonly thought that normal faults should lock-up once they reach angles as low as 30-40˚, but in the shallow subsurface, where detachments are flexing most rapidly to low angles slip can occur at lower angles (Choi and Buck, 2012; 2013; Reston, 2020; Figure 2.19). Shallow lock-up does not imply that the entire fault lock-up as a steep shortcut fault can cut up through the hanging wall from the still active deeper part of the flexing fault, transferring a slice of the hanging wall to the footwall of the new fault. This slice or fault block is then lifted up and out with the rest of the footwall (Figure 2.19), a process central to the first rolling hinge model proposed (Buck, 1988).

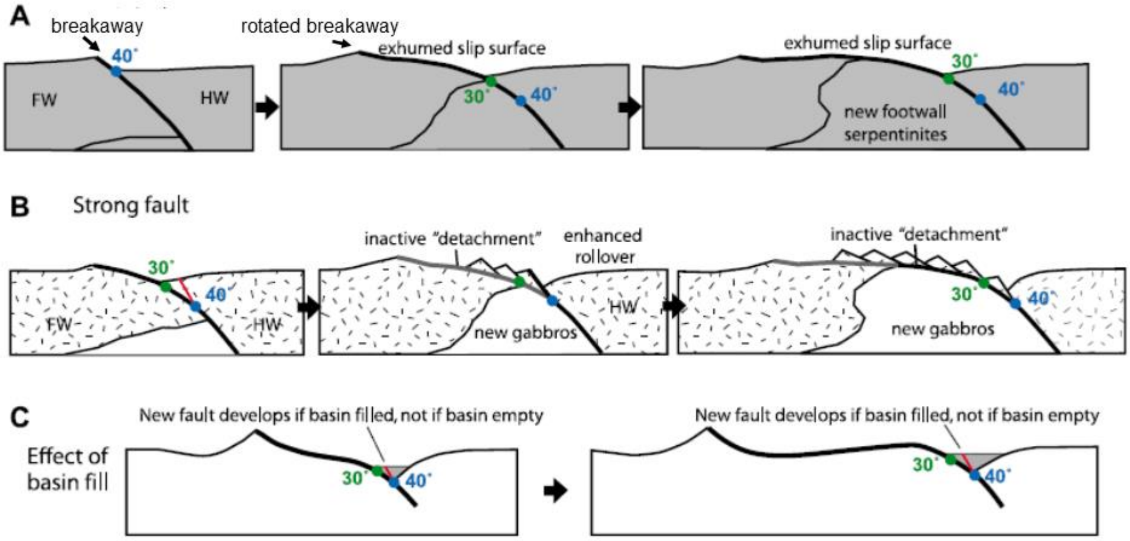
A
breakaway
40°
FW
HW
rotated breakaway
exhumed slip surface
30°
40°
exhumed slip surface
30°
40°
new footwall serpentinites
B
Strong fault
30°
40°
FW
HW
inactive "detachment"
enhanced rollover
HW
new gabbros
inactive "detachment"
30°
40°
new gabbros
C
Effect of basin fill
New fault develops if basin filled, not if basin empty
30°
40°
New fault develops if basin filled, not if basin empty
30°
40°

Figure 2.19: Rolling hinge models (modified from Reston and Ranero, 2011). A: during slip a large offset normal, the footwall is pulled out from beneath the hanging wall and flexes. This flexure controls the geometry of the fault: if the fault remains active, a large expanse of the footwall (likely corrugated) is unroofed, bounded at its outer limit by the rotated breakaway, the original footwall cutoff. B: if the footwall flexes too much, the fault may become too low-angle for slip to continue and the fault locks up, for instance if the fault has high friction coefficient (i.e. is strong). In this case the shallow, flexed portion of the fault may lock and become inactive, while slip remains possible at depth. A new shortcut fault can then cut up from the deeper root zone, transferring a slice of the hanging wall to the footwall of the new fault. The slice (a fault block, underlain by a now inactive detachment) is then rafted up and out with the footwall. Repeating the process results in successive fault blocks overlying an inactive detachment.

A flexing fault can lead to both the unroofing of the footwall as a domal, corrugated oceanic core complex, and to the development of a whole series of fault blocks resting on and moving with an inactive sub-horizontal “detachment” that was only ever active as a steep structure (Reston and Ranero, 2011). Choi and Buck (2012; 2013) and Reston (2020) built on this concept and explored the range of parameters separating the two different types of rolling hinge systems (Figure 2.19) and concluded that it is quite possible for a single fault to switch from one type to another through changes in fault properties or the amount of sedimentary or volcanic fill (Figure 2.19C). The implication is that the detachment footwall exposed as a domal detachment in an OCC might continue laterally beneath a series of rafted blocks. In such a model, oceanic detachments may be essentially continuous, long-lasting features active on a regional scale (Smith et al., 2008; Reston and Ranero, 2011; Escartin et al., 2008) and OCCs simply the places where a mega-detachment breaks surface, being covered in the intervening regions by thin-skinned rider blocks of volcanic seafloor (Figure 2.20). If so, as much as 50% of Mid-Atlantic Ridge (MAR) crust may be the result of asymmetric detachment faulting.

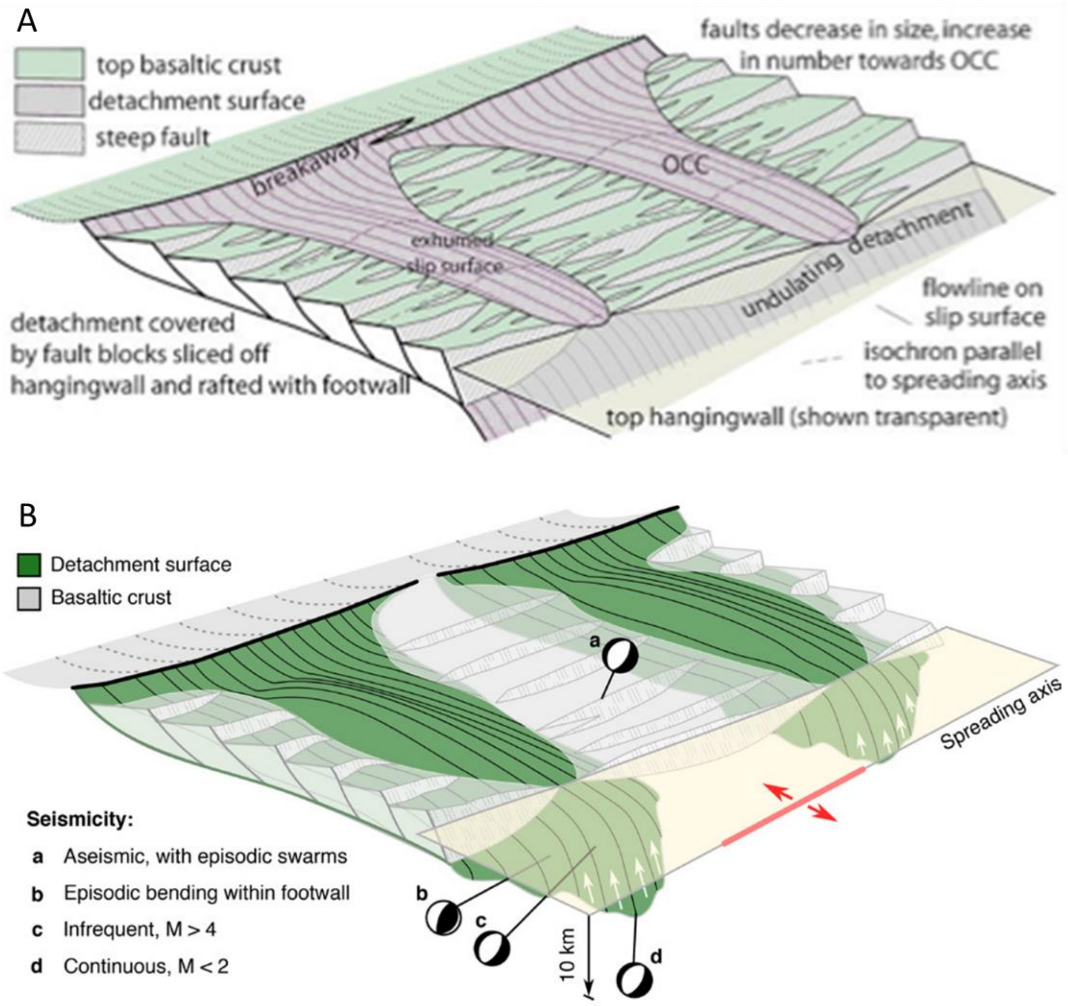
A
top basaltic crust
detachment surface
steep fault
faults decrease in size, increase in number towards OCC
breakaway
OCC
exhumed slip surface
undulating detachment
flowline on slip surface
isochron parallel to spreading axis
detachment covered by fault blocks sliced off hangingwall and rafted with footwall
top hangingwall (shown transparent)
B
Detachment surface
Basaltic crust
a
Spreading axis
Seismicity:
a Aseismic, with episodic swarms
b Episodic bending within footwall
c Infrequent, M > 4
d Continuous, M < 2
b
c
10 km
d

Figure 2.20: Perspective view of the segment scale detachment model: showing two possible interpretations. In the top (Reston et al., 2010), the detachment continues laterally beneath small fault blocks between adjacent OCCs, which represent the places where the detachment breaks the surface. In the alternative model (lower diagram, Parnell-Turner et al., 2021), adjacent OCCs are unconnected, the two detachments are not linked and between them spreading is dominated by magmatism.

Alternatively, MacLeod et al. (2009) see OCCs as spatially restricted, ephemeral features that are switched on and off by variations in local magma supply (Figure 2.21). In this model OCC detachments are ordinary valley wall faults on which slip continues because of the progressive waning of magma supply to below half that needed to accommodate plate divergence (Tucholke et al., 2008). Strain localisation would result in progressively more asymmetric plate separation, until more than half is partitioned onto the detachment itself.

If there is insufficient magmatism to accommodate half of the plate divergence (Tucholke et al., 2008) the detachment migrates towards and across the axial valley. Eventually either renewed magmatism is intruded into the detachment footwall and ultimately overwhelms it, or the detachment is cut by faults (Reston, 2008). During this process spreading becomes strongly asymmetric between a localised OCC and its immediate conjugate, but not across the whole of a spreading segment. The lateral change in spreading asymmetry and the limited dimensions of the detachment fault in this model require spatially restricted transfer zones (dominated by magmatism and ductile shear at depth and faulting near surface) to accommodate the along-strike variations in strain distribution (Figure 2.21).

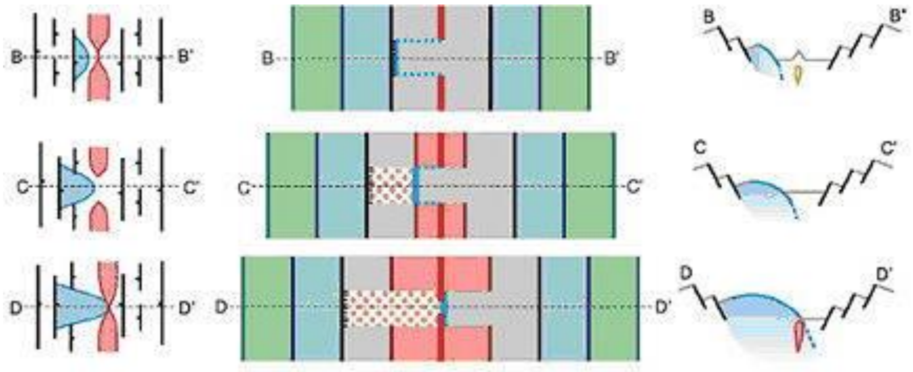

Figure 2.21: MacLeod et al. (2009) model for OCC formation: strain weakening concentrates deformation onto a single fault which accommodates more than half the total spreading, and so migrates toward and over the spreading axis, to be cut by renewed magmatism. Left: structural map; Middle: magnetic lineations; Right: schematic sections.

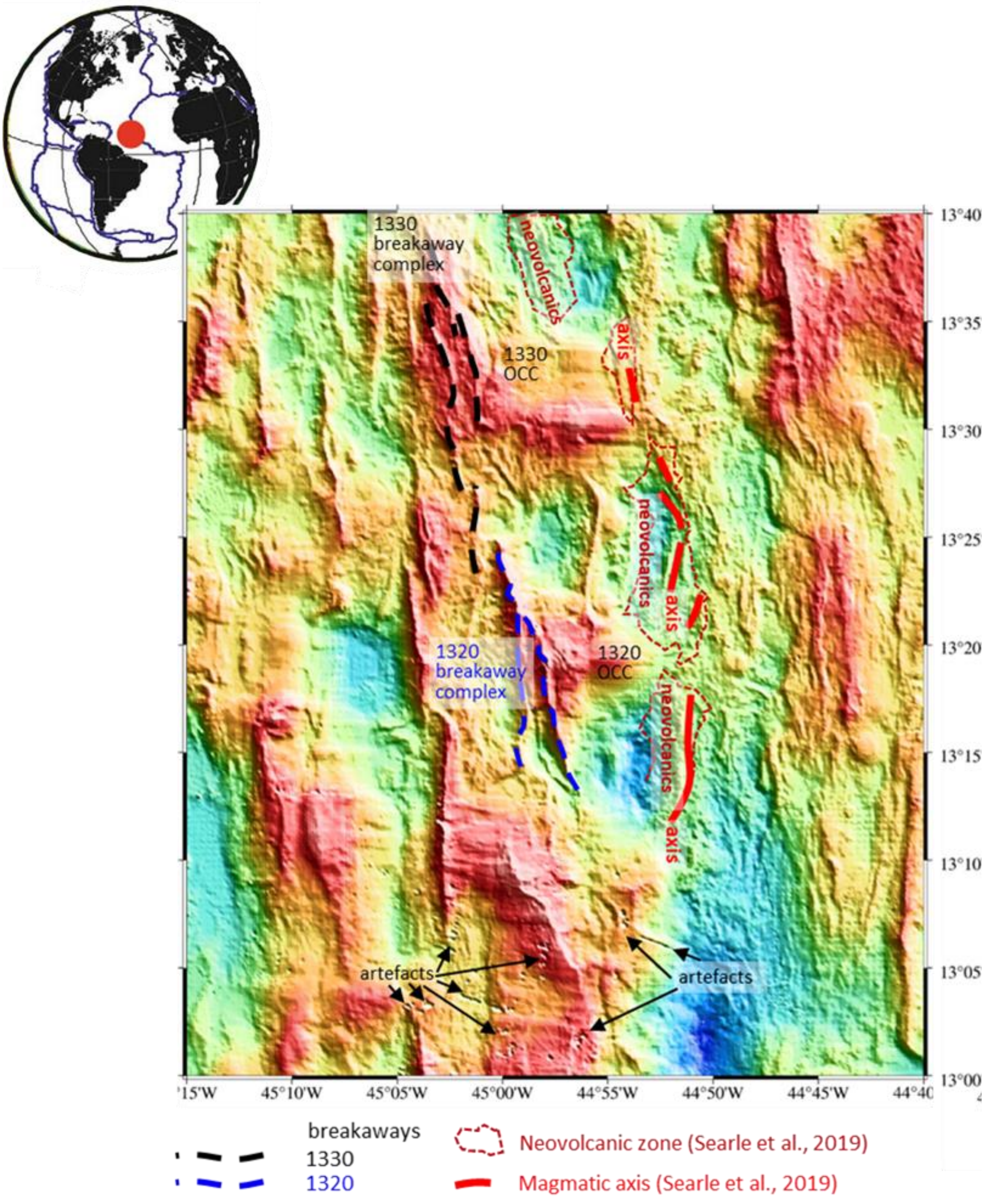
1330
breakaway
complex
neovolcanics
1330
OCC
axis
neovolcanics
axis
1320
breakaway
complex
1320
OCC
neovolcanics
axis
artefacts
artefacts
13°40
13°35
13°30
13°25
13°20
13°15
13°10
13°05
13°00
'15'W
45°10'W
45°05'W
45°00'W
44°55'W
44°50'W
44°45'W
44°40
breakaways
1330
1320
Neovolcanic zone (Searle et al., 2019)
Magmatic axis (Searle et al., 2019)

Figure 2.22: Bathymetry map of the arear of study with location on world map insert. The two OCCs in focus are shown including ridge axis zone line indicated based on Mallows and Searle, (2012) interpretation of the ridge axis and recent volcanic floor. The breakaways of the two oceanic detachment faults are also interpreted.

2.7 Area of study:

The study area (Figure 2.22) is located in part in the Mid-Atlantic ridge (from 13° - 13°40' N and 45°15' – 44°40') known as the 13° N and is a slow spreading (24 mm/yr) ridge (MacLeod et al, 2009; Escartin et al, 2017; Mallow and Searle, 2012) with numerous identified oceanic detachment faults via corrugated slip surface (numbering 24 including 1320 and 1330 N; Mallow and Searle, 2012) with their back rotated breakaway ridge. The area in the vicinity of the ridge axis has a young volcanic seafloor which Mallows and Searle identified from their backscatter while the general vicinity of the seafloor is rough (Figure 2.22) and consists of pillow lavas an indication of partial volcanism (Escartin et al, 2017). The rough seafloor including its volcanic materials are identified as the source of the noise inherent in seismic data sets

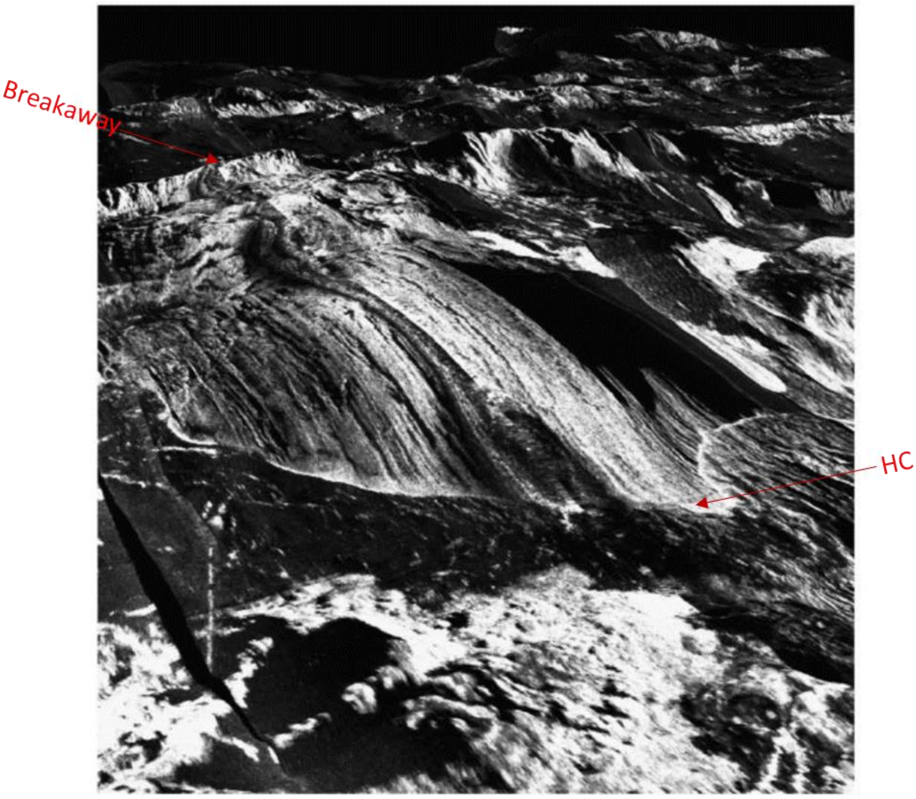

Figure 2.23: MacLeod et al., 2009 Oblique view of the 1320 OCC. Note corrugations and striations are not continuous but are of finite length, and the shape of HW cuttoff reflects the corrugated/domal shape and NVZ absent in front of toe of OCC. Also note the bright backscatter of the volcanics in the hanging wall but the gap in these volcanics near the OCC toe.

acquired from such area towards understanding the subsurface morphology of the area as shown by Peirce et al., 2007. Three of these identified OCCs have exhumed footwall in 10s of km offset with two of these, 1320 (Figure 2.23 and 2.24) and 1330, being our focus. A side scan sonar of the 1320 OCC (Figure 2.23) and bathymetry map (Figure 2.24a) show the footwalls of the ODFs are topographic highs with distinct surface features. These surface features include the characteristic corrugations and striations traceable to the hanging wall cutoff (Macleod et al, 2009; Escartin et al., 2017), which distinguish OCC from other topographic highs. Linear ridges (note not the spreading axis itself or the whole Mid-Atlantic Ridge) in the area are mostly back rotated fault scarps which points to the importance of normal faulting (Searle et al., 2012). Such ridges include those identified as breakaways of oceanic detachment faults which are very conspicuous in some cases as well as not so obvious in others (Figure 2.22). The proximity of the 1320 and 1330 OCC led to the idea that these

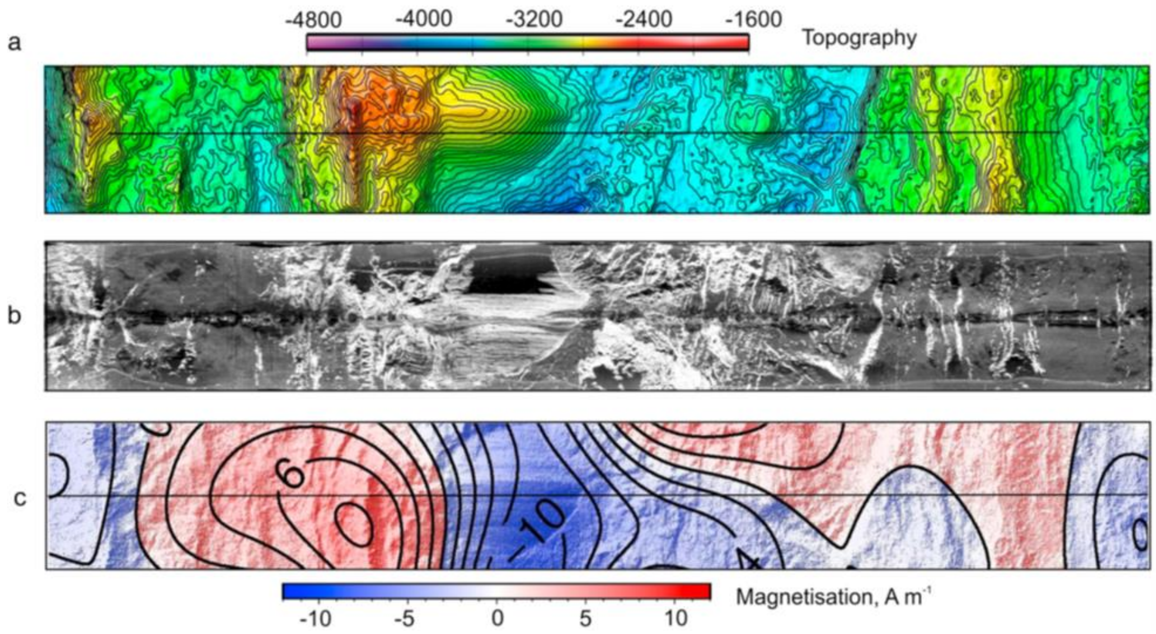

Figure 2.24: Searle et al., (2019) 6–km-wide swathe comparison. Bathymetry (a), side scan sonar composite map (b), and magnetization from inversion (c) along slip direction and over 1320 OCC. On the composite map backscatters are observed in the footwall area of the ODF before the breakaway all through to the hanging wall, which corresponds with both positive and negative magnetisation

might be the exposed portions of a larger detachment system, covered in the intervening region by small fault blocks (Fig 2.20A).

Following on from Cann et al., (1997) and Mitchell et al., (1998), MacLeod et al., (2009; Figure 2.25) attempted to infer the subsurface geological structure of the ODF (Figure 2.25) based on the seafloor geology. The key unknown was the curvature and extent of the detachment as it passes beneath the hanging wall. The velocity structure revealed by wide-angle seismic investigations (Peirce et al., 2019; Simao et al., 2020, Figure 2.26) provide some control: the velocity contours define a generally convex-up boundary where the fault might be expected, steepening downward beneath the ridge axis defined by Mallows and Searle (2012). These sections show a seafloor of velocity ~2 km/s which increases subsurface up to ~6 km/s with possible low velocity zones directly below the 1320 OCC and not the 1330. It also informs the oceanic crust below the OCC is thin here for the 1320 (and 1330 though with thicker crust than 1320) with mantle rocks close to the seafloor and thick elsewhere.

Sampling studies (e.g., MacLeod et al., 2009: Escartin et al., 2017) over the ODF footwalls shows the seafloor rocks are composed of deep crustal and upper mantle rocks (gabbros and peridotites, the latter having undergone some hydration to from serpentinites) while the hanging walls are predominantly young volcanics.

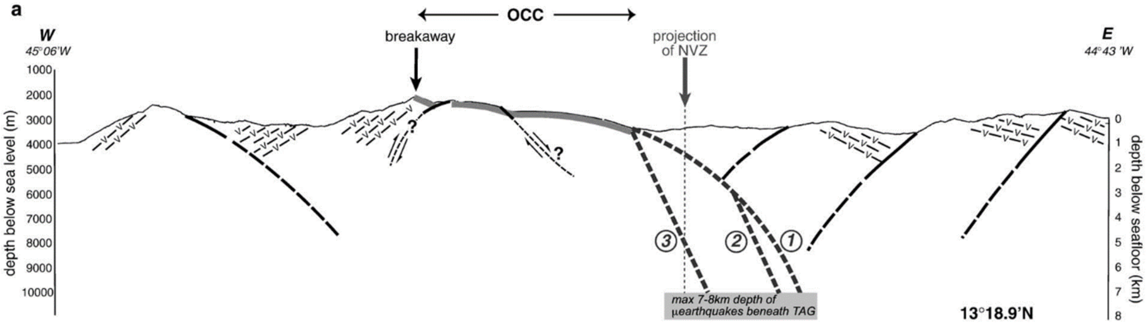
a
OCC
W
45°06'W
breakaway
projection of NVZ
E
44°43 'W
1000
2000
3000
4000
5000
6000
7000
8000
9000
10000
depth below sea level (m)
?
?
③
②
①
max 7-8km depth of μearthquakes beneath TAG
13°18.9'N
0
1
2
3
4
5
6
7
8
depth below seafloor (km)

Figure 2.25: MacLeod et al.'s (2009) possibilities for the subsurface geometry of the 1320 OCC and other adjacent faults. These possibilities are extrapolations from the seafloor morphology derived from bathymetry map and side scan sonar.

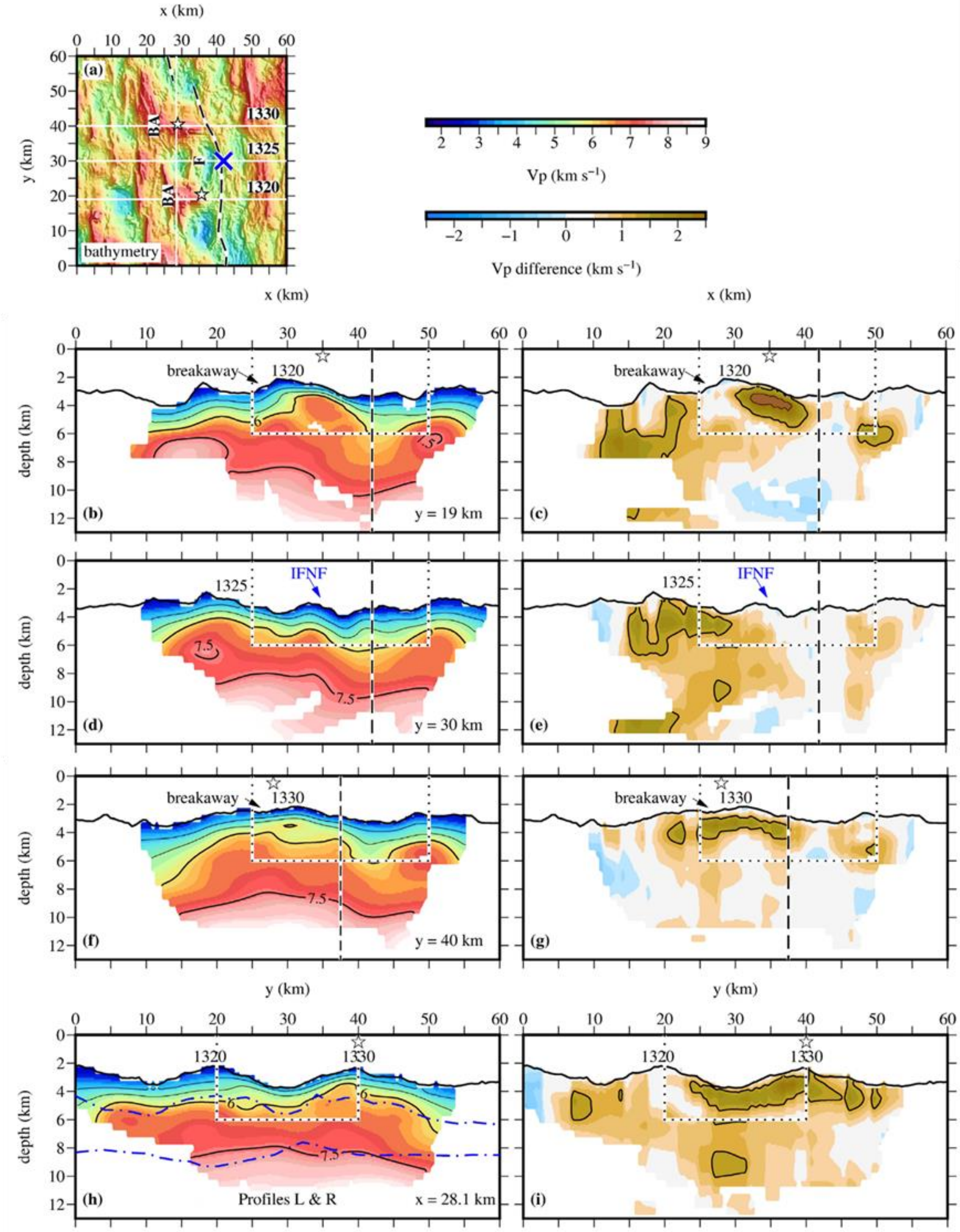

Figure 2.26: Simao et al.'s (2020) wide angle experiment vertical sections of the velocity structure in the slip direction (over 1320 and 1330), Parnell-Turner et al.'s (2021) aseismic zone and parallel to axis. The acquisition lines for these sections coincide closely with the JC132 lines used for this thesis.

The geometry of the ODF is also partially constrained by the distribution or microearthquakes (Parnell-Turner et al., 2017). These occur as a distinct steeply east-dipping (75) band of normal faulting earthquakes and a broader west-dipping cluster of compressional earthquakes (Figure 2.27). The former is interpreted as coming from the fault itself, the latter as the result of footwall flexure.

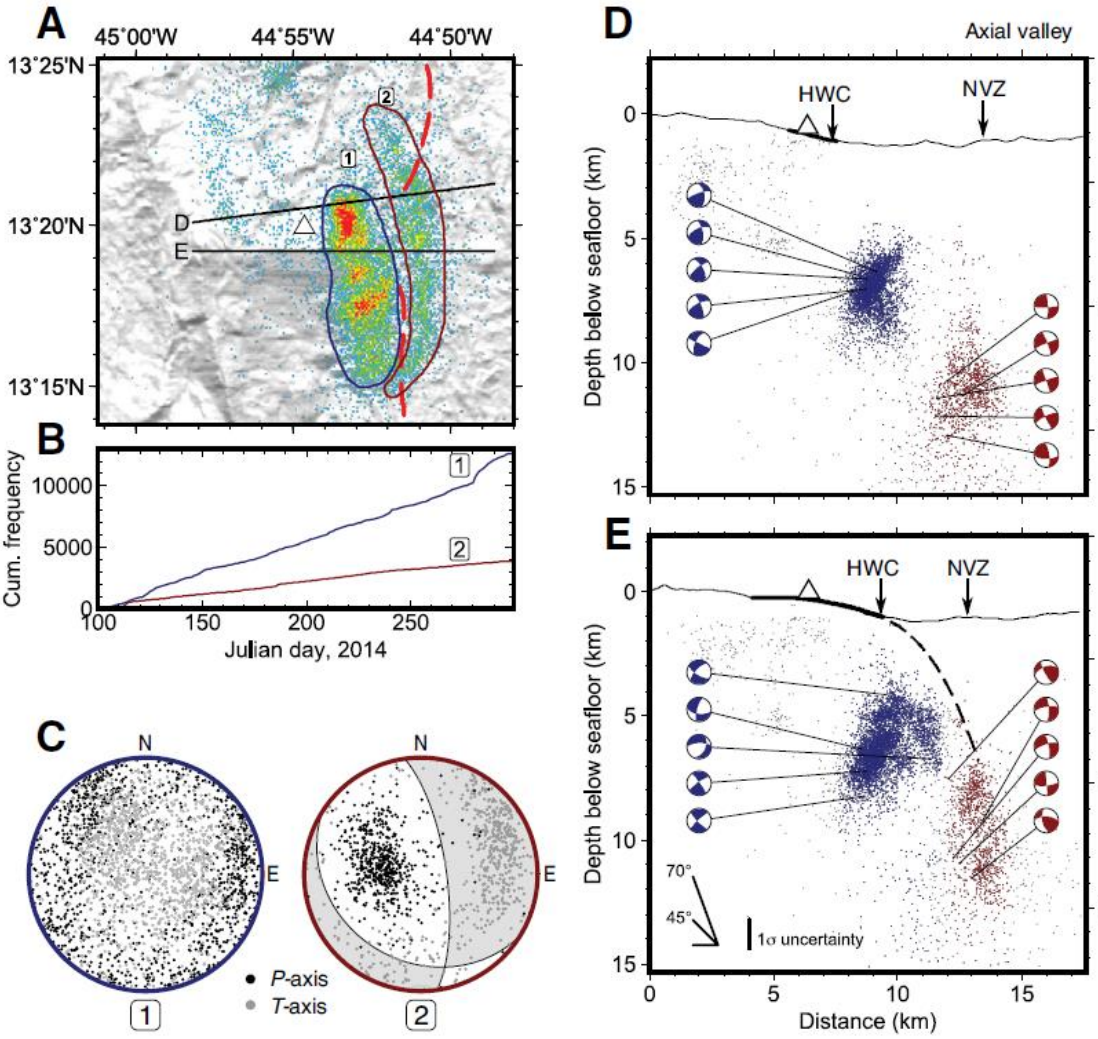

Figure 2.27: Distribution of seismicity around the 1320 OCC (Parnell-Turner et al., 2017). A: map view of seismicity: note it occurs two distinct bands: that outlined in red is dominantly normal faulting, that in blue dominantly reverse faulting. B: cumulative seismic moment release within these two bands over 6 months of recording. C: representative focal mechanisms for the bands. D, E: cross-sections showing distribution of the reverse (blue) and normal mechanisms.

The velocity models, the seafloor observations and the microearthquake distribution all provide constraints on the fault geometry but fail to resolve its precise geometry, particularly in the critical region between the hanging wall cutoff (where the OCC dips ~20°) and the steep band of normal fault earthquakes.

The quality of the pre-existing data, both geological and geophysical, the close proximity of the 1320 and 1330 OCCs and the belief that at least one (the 1320) detachment system is still active makes this area the ideal place to study OCC formation.

2.8 Outstanding questions and aims of the thesis

The key remaining questions concerning the formation of oceanic core complexes and the evolution of oceanic detachment faults are thus:

- What is the true geometry of the detachment from the surface (fault trace) to depth?
- What are the implications of this geometry for the properties of the fault?
- What is the internal structure of the detachment: does the corrugated surface represent the two-dimensional representation of a 3D anastomosing fault zone?
- What is the lateral extent of the detachment? Is the 1320 and 1330 detachments part of one undulating structure beneath a series of fault blocks or if not, how do they interact?

The aim of this thesis is to address these questions, leading to the answers summarised in Chapter 6.

Chapter 3 Out of plane seismic noise and seismic imaging

3.1 Introduction:

As outlined in the preceding chapter, slow-spreading segments of the mid-ocean ridge system have been studied using gravity, magnetic, seafloor imagery, microseismicity, refraction and reflection geophysical processes. However, seismic reflection, the technique that can provide the highest resolution images of the subsurface, encounters substantial problems when collected over the rough and/or complex 3D terrain of a slow-spreading ridge, largely a consequence of the imaging problems resulting from scattering and out-of-plane reflections on 2D seismic data. This chapter discusses the origin, appearance and properties of such noise, and discusses how they might be best suppressed or removed and thus provides the theoretical underpinning for Chapter 4 when the processing of 2D seismic data from the mid-Atlantic Ridge is discussed.

3.2 Seismic reflection and scattering:

In the 2D reflection method, the seismic waves generated by a source are reflected from underlying boundaries - obeying the law of reflection - and detected by a receiver, or more typically many receivers in a line. The method assumes all the recorded energy travels in the same vertical plane as the source and receiver (Figure 3.1). However, waves do not travel in a straight line but as wavefronts and can encounter scattering (Huygens' principle) in and out of this plane of reflection. Scattering is the reflection of energy by diffractors (point or linear scatters) or reflectors not in the plane of reflection (Figure 3.1b). In 2D seismic the recorded scattered energy that comes from well out of the plane of reflection is considered as noise and known as sideswipe or out-of-plane reflections (Dondurur, 2018).

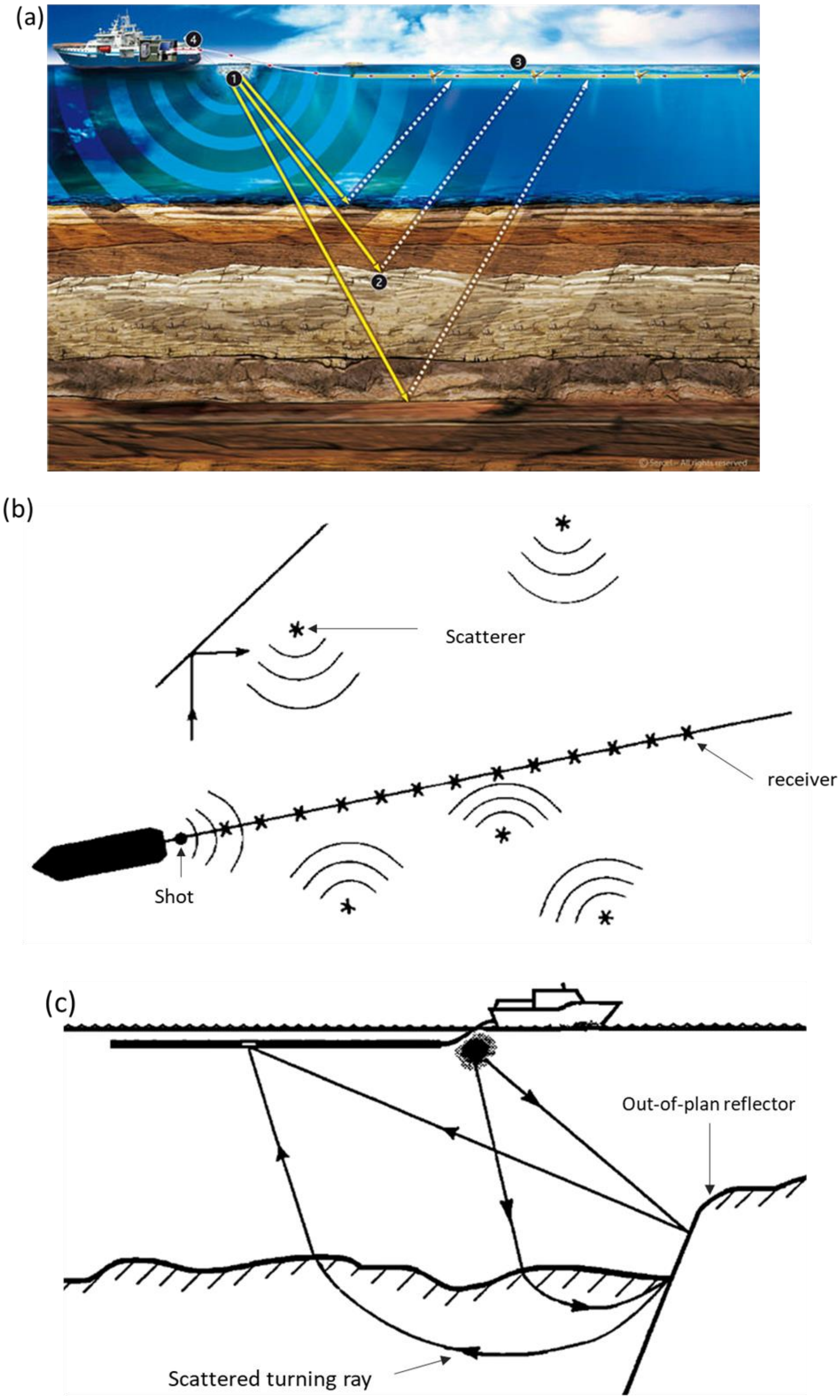
(a)
4
1
3
2
© Sercel – All rights reserved
(b)
Scatterer
receiver
Shot
(c)
Out-of-plan reflector
Scattered turning ray

Figure 3.1: Marine acquisition profiles of two views of acquisition from shot to hydrophones. (a) the sectional view of data acquisition depicting the ray theory of waves from shot to reflector to receiver, (1. Source. 2. Midpoint of incident and reflected rays. 3. receivers. 4. Acquisition vessel). (b) plane view of data acquisition representing reflections scattered from out of and in-plane scatterers. (c) Sectional view of side-coming reflection. (Larner et al., 1983; Carlvert, 1997; and Sercel.com)

3.3 Seafloor Sideswipes:

Sideswipes originate from any wavefront scatterer or reflector that is positioned outside the vertical plane, with regards to the acquisition line for a two dimensional seismic and includes reflected refractions or diffractions (Calvert 1997). Depending on the scale of the 3D roughness relative to wavelength, this noise is classified as, (a) generated from the roughness (point or linear scatters) of the surrounding seafloor, referred to as scattered energy/reflection and (b) the adjoining reliefs (three dimensional structures, 3D), referred to as side-coming reflections.

The key difference between point/linear scattered reflections and out-of-plane/side-coming reflections are hinged on the size of their Fresnel zone. For point/linear scatterers the associated Fresnel zone, R_{fz}, (the central area from which the dominant constructive reflected sound energy originates from a reflector, relating the depth, z, of the reflector and wavelength, λ, of such energy as $R_{fz} = \frac{\sqrt{z\lambda}}{2}$) has a reduced diameter compared to that of side-coming reflections (Lindsey, 1989). This noise is coherent as it is observable on seismic gathers as possible primary reflections (Larner et al., 1983: Tsai, 1984). The strongest and most problematic sideswipes come from large contrasts in acoustic impedance (product of seismic velocity and density), such as a rough seafloor (Larner et al., 1983), which is a particular problem when seismic profiles are acquired over a mid-ocean ridge. The newly formed ocean floor is both extremely rough (3D structure smaller than the seismic wavelength), hard (strong acoustic impedance contrast with the seawater), and three-dimensional on a larger scale as it is characterized by the presence of pillow lavas, volcanic and hydrothermal vents, seafloor weathering or mass wasting, compressional and extensional cavities, or feature such as abyssal ridges.

Another source of scattered reflected noise on seismic data are scattered turning waves (Calvert, 1997). These are turning waves backscattered or reflected from rugged basement, such as from fault surfaces, linear scarps, or other subsurface discontinuities, and have similar characteristics as surface scatterers (Calvert, 1997). However, modelling scattered noise on seismic acquired from 23°N Mid-Atlantic Ridge area Kim and Orcutt (1991) showed that such noise also originated from small voids on the seafloor as well as fault scarps and seamounts.

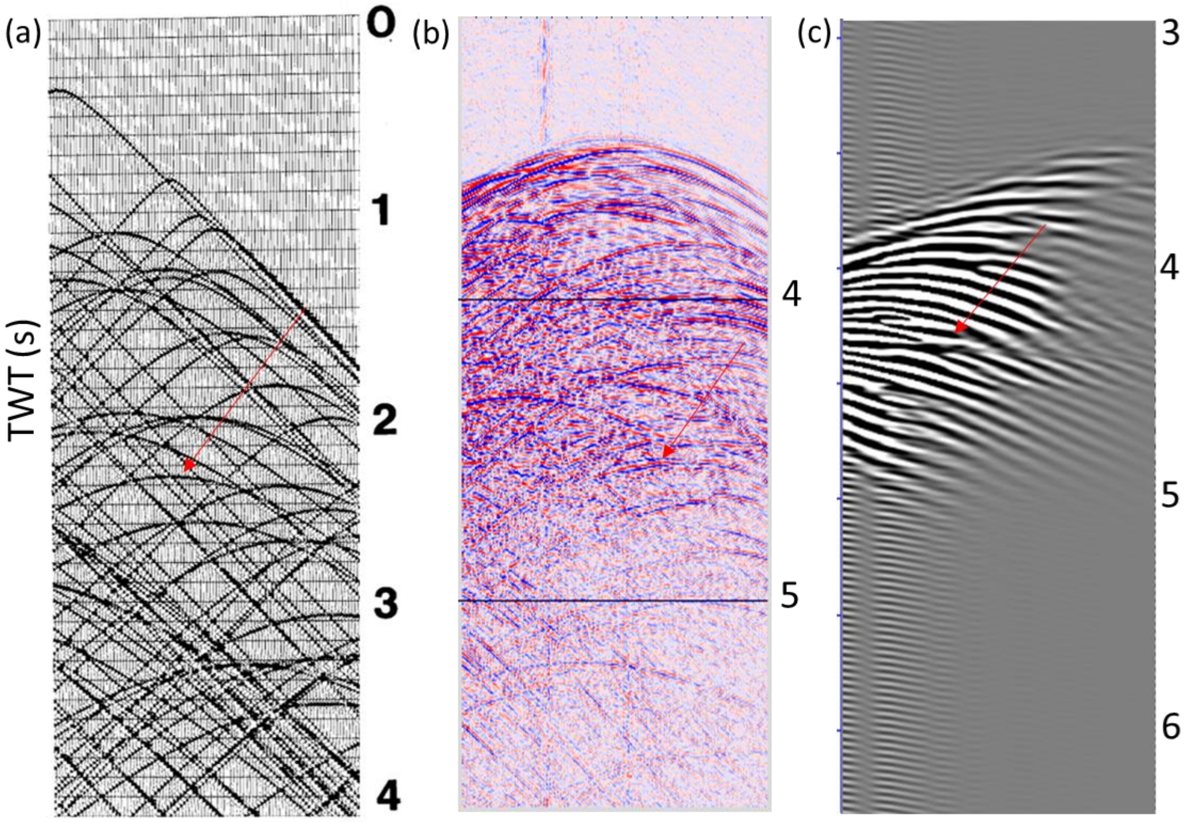

Figure 3.2: shot gathers from marine environment synthetic and real data indicating the presence of scattered reflections and their apex shifted nature (e.g., red arrows). (a) synthetic shot from scatterers at the sea surface (Larner et al., 1983). (b)) Real shot gather from the mid-ocean ridge near 13N (deep marine environs.). (c) Synthetic shot gather showing strictly sideswipes modelled from bathymetric data from the acquisition environs of (b) using Hobbs et al., 2006 phase-screen method. These shot gathers exhibit close to similar features from the scatterers.

3.4 Sideswipe characteristics:

Larner et al., (1983) and Tsai (1984) have extensively looked at the issue of sideswipe and how it relates to primary reflections on seismic data. They observed that side-scattered noises on a seismic record have the following distinguishing features from a primary inline reflection:

1. Their normal-moveout (the increase in travel time as a function of offset) depends on the angle of propagation (azimuth) and on record time and is tied to a range of values with a minimum/maximum at the largest/smallest azimuth. Tsai (1984) showed the largest angles were reflection angles situated out-of-plane from the line of acquisition while the smallest angles resulted from inline scatters either in front or behind the recorded line.
2. Their normal moveout (NMO) velocity (V_{nmo} – the velocity needed to optimally flatten reflection hyperbolae in the common-midpoint (CMP) domain before stacking which in an ideal layer cake world would equal the V_{rms}) could differ from the V_{rms} of the overburden and the primary velocity value at the record time.
3. In shot gathers they are apex-shifted, and only quasi-hyperbolic (Figure 3.2) unlike dipping reflections which are apex-shifted and hyperbolic.
4. Side-coming reflections typically have a range of V_{nmo} which increases with recording time, and which overlaps with that of inline primaries, meaning that the side-coming reflections stack-in.

The 3D nature of sideswipes (scattered and side-coming noise), including their characteristics in a 2D plane (for 2D seismic data) leads to a variety of problems. First, out of the plane of section energy scattered from a rough seafloor can appear below the seafloor on a 2D image and be misinterpreted. Second, 2D migration assumes that the energy is both zero-offset and from within the plane of section, so that out-of-plane reflections will not migrate properly. For 2D data acquired from a slow-spreading mid-ocean ridge, which includes such noises, migration introduces over/under migration artifacts as these noises do not collapse to their zero-offset location using the correct subsurface velocity model and as a consequence of the noise varied V_{rms} with time. These problems are evident on the JC132 data and pose processing and imaging challenges, Figure 3.2c.

The velocity distinction of primary reflections and noise is one of many bases on which a processing sequence is applied with aim at noise attenuation via velocity discrimination. With the propensity of scattered noise V_{nmo} approaching that of inline primary energy (Larner et al., 1983; Tsai, 1984; Hargreaves and Wombell, 2004) at a given two-way time (TWT), but not higher, a major processing challenge results as NMO correction followed by stacking will not adequately suppress the scattered noise. Recognition of this problem prompted the investigation into which seismic domain might provide the best possible opportunity to discriminate between reflections and scattered energy. The strong coherent nature of sideswipes and their close primary velocity value, therefore, renders most processing methods developed for other noises (such as multiples) ineffective in most seismic domains. This was shown by Larner et al. (1983) to result from the fixed nature of the scatterers, thus representing scattered noises as possible primary reflections. This shows why the primary reflections in a shot gather could be overwhelmed and obscured by numerous sideswipe reflections (Larner et al., 1983; Hargreaves and Wombell, 2004). Therefore, shot gathers from the mid-ocean ridge could be dominated by both primary and multiple diffractions, scattered and side-coming energy, obscuring the inline primary reflections. As the problem cannot be addressed during 2D acquisition, it poses a major processing challenge (Hargreaves and Wombell, 2004).

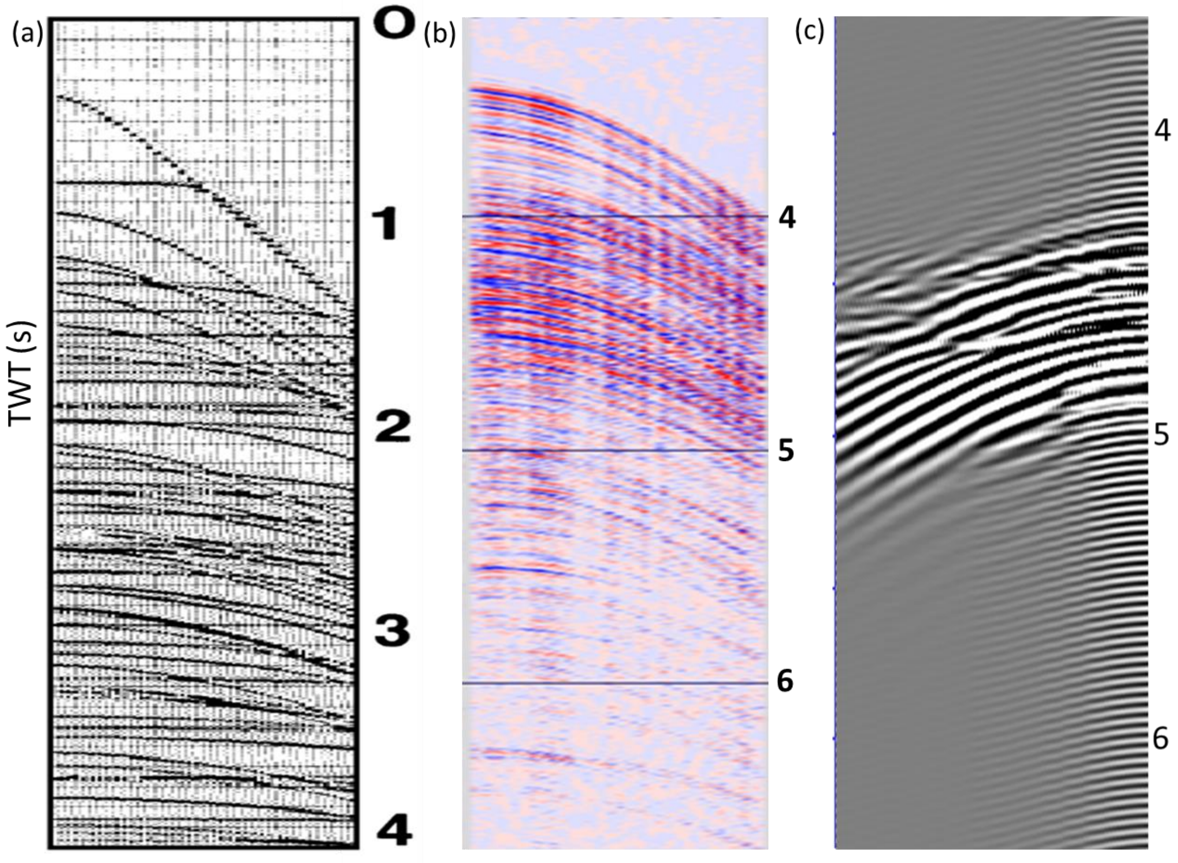

Figure 3.3: CMP gathers with scattered noises which shows that the CMP domain does not discriminate such noises. (a, (b), and (c) are CMP gathers of Figure 3.2a, 3.2b, and 3.2c and point to non-discrimination of such noise in the CMP domain especially for the real data.

3.5 Sideswipe velocities:

Sideswipes propagate at the velocity of seismic waves in the medium of travel, meaning that those travelling exclusively in the water column (sideswipes from the seafloor) travel at close to 1500 m/s (Larner et al., 1983; Tsai, 1984; Calvert, 1997) , whereas as those passing below the seafloor have travelled at a variety of velocities, partly that of the water column, partly that of the subsurface, and those passing to greater depth in shallow water might eventually travel at close to the basement velocity (Calvert, 1997). The key question then is how this propagation velocity appears in the various seismic domains.

Tsai, (1984), Calvert, (1997), and Peirce et al., (2007), have demonstrated that the stacking velocities of sideswipes vary from that of the water column overburden to basement under consideration, because of their record times. Their NMO values closely mirror that of primaries at near offsets and deviate to higher values due to their dip moveout at the far offsets, (Figure 3.3 CMP gathers from Hargreaves and Wombel, 2004). This enhances stacking of sideswipes leading to their over migration when primary interval velocities are applied for imaging.

3.6 Attenuation of Scattered noise:

To attenuate scattered noises Larner et al., (1983) and Tsai (1984) suggested the use of velocity filtering as a fundamental step aimed at propagations in water columns resulting from surface scatterers. Velocity filtering using frequency-wavenumber (fk) dip filters in the CMP domain was suggested.

Kent et al., (1996) suggested that using dip moveout (DMO) correction followed by dip filtering (velocity filtering), for deep water data could distinguish between side-coming and deep primary reflections; Reston et al. (1999) used this method to demonstrate such deep reflections genuinely came from the oceanic lower crust of the NW Pacific rather than from the side. However, Calvert et al., (1997) pointed out this method strictly only attenuates noise traveling in the water column after correcting the dip of such noise if it is higher or lower than the medium of travel, enabling the application of a filtering process such as velocity filters. Furthermore, in the shallow subsurface of rough oceanic crust, DMO followed by any other processing sequence would be inefficient as there is insufficient moveout difference between the noise and genuine shallow basement reflections, explaining the failure of DMO in removing sideswipes during processing (Peirce et al., 2007). Calvert (1997) therefore suggested

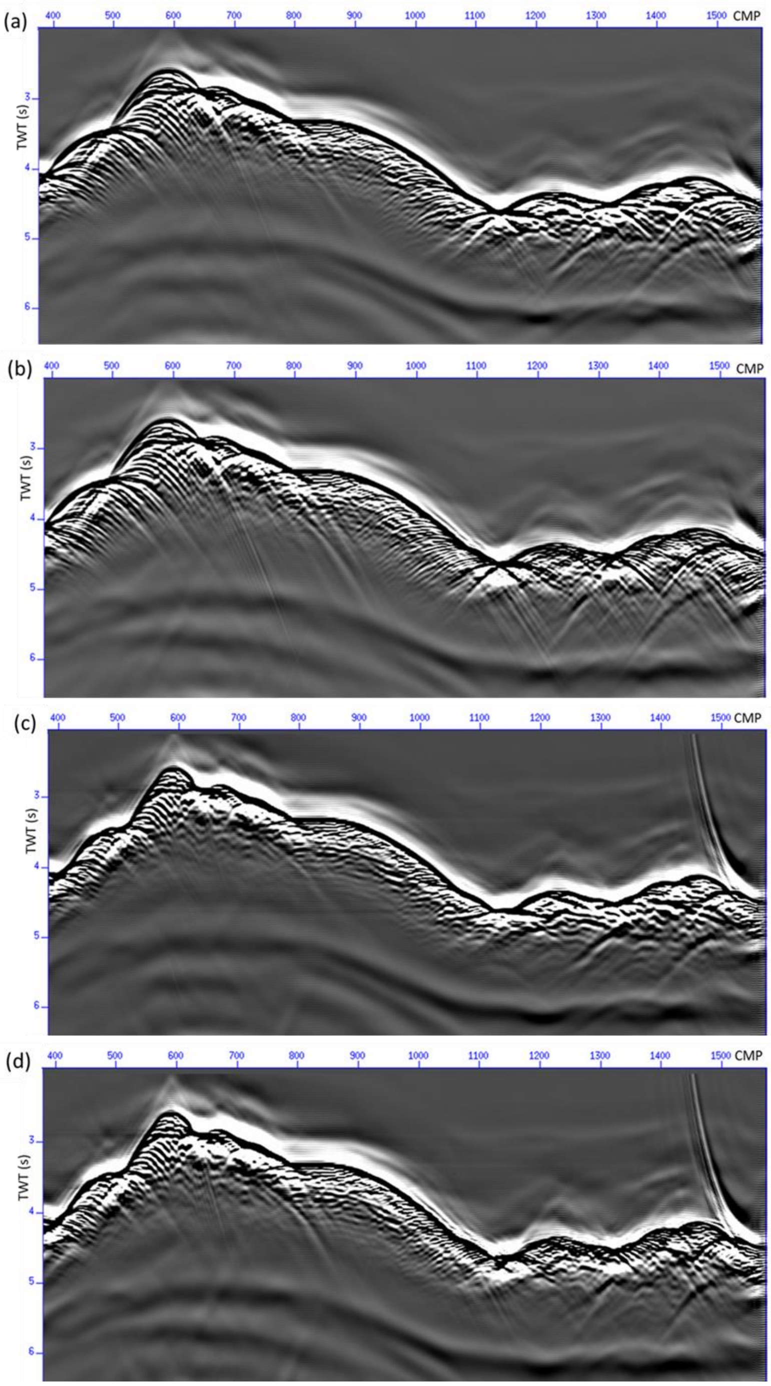

Figure 3.4: Synthetics of sideswipe noise modelled from a high-resolution bathymetric map using the phase-screen method demonstrating their predominance on stacked (NMO with 1500m/s and approximate model rock velocity) and 1500m/s imaged data. (a) 1500m/s NMO corrected CMP stacked data. (b) Model velocity NMO corrected CMP stacked data. (c) 1500m/s Stolt migrated section of (a). (d) 1500m/s Stolt migrated section of (b). The synthetic data has a CMP interval of 25m which impacts the length of resulting stacked data diffraction noise tails when compared to the real data in Figure 3.8.

such basement related scattered noise be suppressed in the CMP domain using generalised Radon transform velocity filters after DMO has been applied, and also showed radon velocity filtering after stacking attenuates sideswipes from most sources reasonably in a seismic profile.

Although most processing sequences of seismic profiles from slow-spreading mid-ocean ridges continued applying DMO as a basic step in various processing flows (Canales et al.,2004), Peirce et al., (2007) approached this differently by employing a modelling, muting and comparison method. This method involves synthetic modelling of the profile to reproduce the scattered source-generated noises from the seafloor via the phase screen (Figure 3.4) method - following a basic standard processing flow combined with constant velocity stacks (CVS) is first applied, but without velocity filtering. However, such modelling is extremely computer intensive, particularly if trying to replicate the acquisition geometry and frequency range of real seismic, requires extremely well resolved seafloor imagery, and navigation during acquisition to the ~10m scale. Because of all these issues, here we use phase screen modelling to identify the problem, but prefer other, more widely applicable methods to the actual suppression of the side-coming energy. This method uses velocity filtering as the foundation of the processing sequence combined with water velocity imaging and muting attenuation methods as described below.

3.7 Velocity filtering:

Velocity filtering is a method of signal segregation based on their apparent velocities (lateral, interval velocity or normal moveout [root-mean square]). Velocity filters are also called apparent velocity filters, fan filters, dip filters, frequency-wavenumber filters ($f-k$ filters) or pie-slice filters with dip and $f-k$ filtering being the most common names (Christie et al., 1983). As the names varies so does the methods through which it is implemented and used in seismic processing sequence, which are dependent on the seismic domain and the noise characteristics addressed.

Velocity filtering can be used to suppress most type of noise which travels at a distinct apparent velocity relative to the primary wave (P-wave) energy, because velocity (v) is associated with time (t), frequency (f), or offset (x) of travel (3.1).

$v = {}^{2x}/_{t}$ Two-way travel time (TWT) ……………………… (3.1a)

f = wave velocity (v) * wavenumber ……………………… (3.1a)

$v = {}^{dx}/_{dt}$ instantaneous velocity ……………………… (3.1c)

Velocity filtering methods include: the radon transform processes (linear, parabolic and hyperbolic), $f - k$ dip filtering, muting of normal moveout (NMO) corrected common midpoint (CMP) gather (Hasselgren and Clowes 1995), hyperbolic velocity filtering (Tatham 1984) all relating to the domain of application.

3.8 $\boldsymbol{f - k}$ dip filtering:

The frequency-wavenumber velocity or dip filtering applies in the frequency-wavenumber domain (Figure 5a) and uses the Fourier transform transforming signals from the distance – time $(x - t)$ to the frequency-wavenumber $(f - k)$ domain or spectrum via the following general equation:

Velocity = frequency/wavenumber

This yields an apparent or instantaneous velocity given by:

$$\frac{\partial f}{\partial k} = v \qquad \dots\dots\dots\dots\dots\dots\dots\dots\dots\dots\dots \text{(3.2)}$$

$$f = frequency, k = wavenumber\ and\ v = apparent\ velocity.$$

Equation 3.2 implies signals travelling at a given recorded instance of frequency and wavenumber would have values or slopes in the $f - k$ domain defined by radial contours of amplitude and phase (Hale and Claerbout, 1983). Therefore, velocity discrimination of noise is as an instantaneous velocity bandpass or $f - k$ mute (Figure 3.5b) based on the apparent dip or velocity difference of wave fronts recorded or related to their medium of travel before recording.

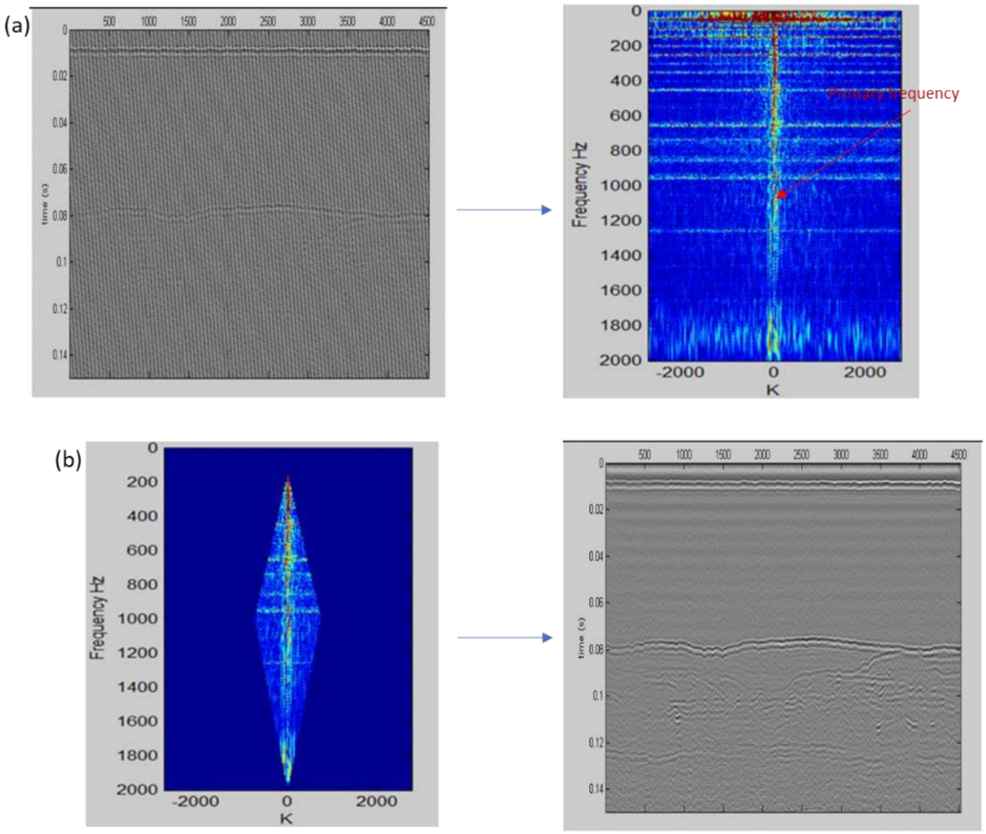

Figure 3.5: Seismic data mapped to the $f - k$ domain for filtering (Herman et al., 2017). (a) Original data mapped to the frequency domain with varying primary frequency to wavenumber while linear noise exhibits constant frequency with varying wavenumber. (b) Diamond polygon defines a filtering boundary for linear noises prior to mapping back to the $x - t$ domain.

Yilmaz (2001) points out $f - k$ dip filtering attenuates mostly coherent linear noise, such as ground roll, thus suggesting its use as proposed by Larner et al. (1983) to attenuate coherent non-linear noise, (as sideswipe) would be suboptimal. However, noises from oblique scatterers (such as fault scarps) to the profile line, could be attenuated (Calvert, 1995). Also, besides the seeming application to only coherent linear noise $f - k$ dip filtering is hampered in application with invariance of dip to time in the $f - k$ domain owing to the stationarity of the $^{k}/_{f}$ ratio corresponding to velocity in the space-time $(x - t)$ domain which is non-stationary (Hale and Claerbout, 1983).

3.9 Radon transforms:

Velocity filtering basically involves signal discrimination from noise based on their apparent or instantaneous velocity or dip. This implies processes or procedures relating to the velocity of recorded signals (primary wave and noise) presents a velocity filtering method. An example relating the linear velocity of propagation to the wavefront in a recorded signal is the Radon transform introduced by Radon (1917). Upon its development Radon transform has metamorphosed into different variants know by different names. Dunne and Beresford (1995) and Gu and Sacchi (2009) in their reviews note the transform is known as tau-p transform (and also as discrete or parabolic or hyperbolic radon transform, slant-stack [cartesian, corrected, cylindrical and proper slant-stack], plane-wave decomposition, velocity stack, back projection and beam forming depending on the field of study and precise application domains with varied application choices). They observed all Radon transform methods now find application in seismic signal processing under the generic name tau-p transform. Owing to the varied nomenclatures used in literature for Radon transform here the three most common names (tau-p, Radon or slant-stack transform) would be used interchangeably.

The tau-p transform is defined and shown (Figure 3.6) as a tool in seismic data processing which map signals from the distance-time domain (traditional profile

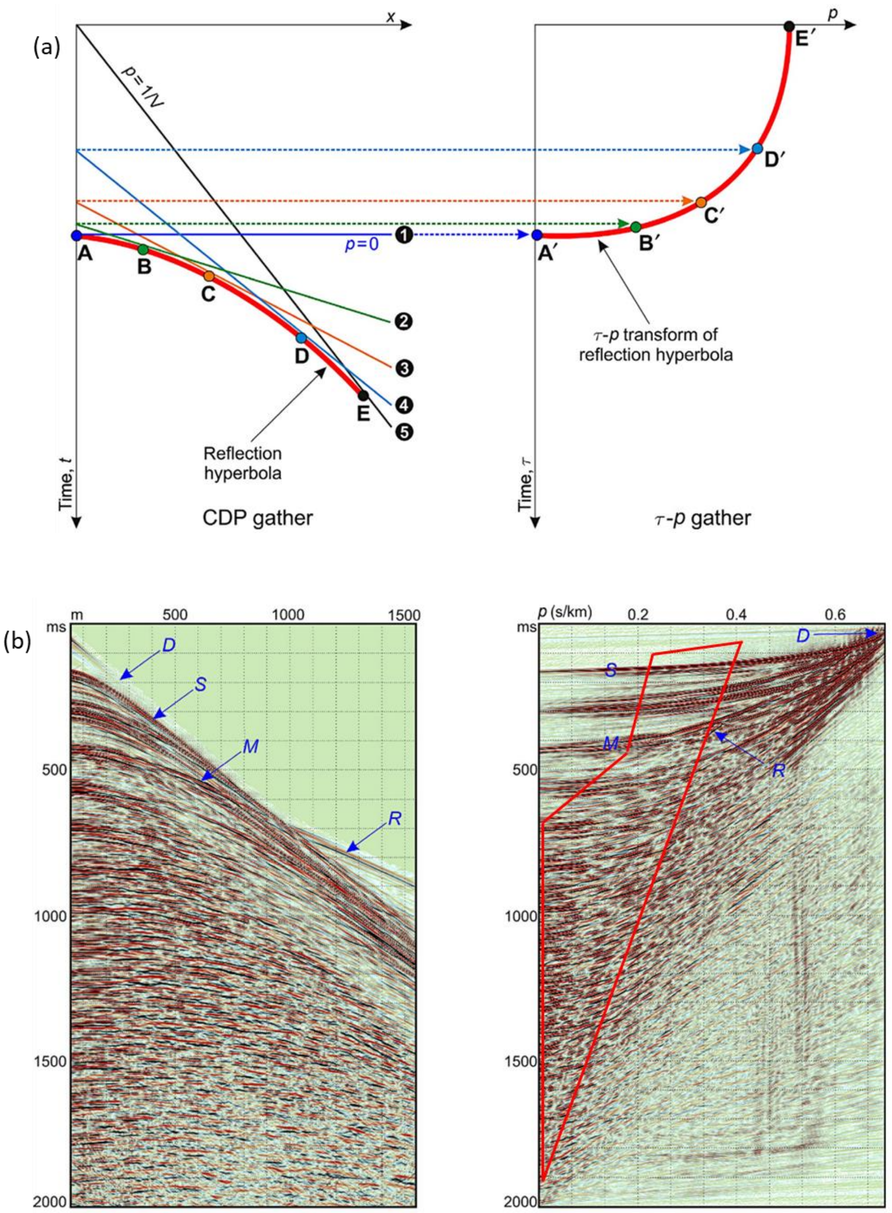
(a)
x
p=1/V
p=0
A
B
C
D
E
❶
❷
❸
❹
❺
Reflection hyperbola
Time, t
CDP gather
p
E′
D′
C′
B′
A′
τ-p transform of reflection hyperbola
Time, τ
τ-p gather
(b)
m
500
1000
1500
ms
500
1000
1500
2000
D
S
M
R
p (s/km)
0.2
0.4
0.6
ms
500
1000
1500
2000
D
S
M
R

Figure 3.6: $\tau - p$ domain mapping of seismic gathers from $x - t$ domain (Modified from Dondurur, 2018). (a) schematics of the process from $x - t$ to $\tau - p$ domain of a single reflection. 1-5 show linear projections of points (A-E) on the gather to time prior to mapping onto $\tau - p$. (b) live gather with primary reflection and varying noises (D = direct reflection), S = seafloor primary reflection, M = multiple, R = refracted reflection) mapped from $x - t$ to $\tau - p$ domain. Red polygon in the $\tau - p$ domain defined for velocity filtering of noises outside the boundary.

domain) to an intercept time (tau or τ) and slope (p) domain resulting from slopes and intercept of each $(x-t)$ pulse recorded (Dunne and Beresford (1995). Such mapping is implementable using the linear (cartesian), parabolic, hyperbolic, elliptical, or generalized domains or equations, resulting to the varied names mentioned such as linear tau-p transform.

3.10 Linear tau-p transform (Slant-stack):

This is the most generally used radon transform in exploration seismology imaging (Dunne and Beresford 1995; Gu and Sacchi 2009) based on amplitude summation (stacking) of computed slopes (s) for each event in the $x-t$ domain mapped to the tau-p domain (Dondurur, 2018) such that point events in the $x-t$ domain become lines and line events become points. It is aimed at decomposing any plane wave in its simplest ray characteristics. Generally, the linear Radon transform equation is,

$$R_{\psi} = [f(t,x)] = F(\tau,p) = \int_{-\infty}^{\infty} f(\tau+px,x)dx \qquad \ldots\ldots\ldots\ldots\ldots\ldots\ldots.. (3.3)$$

Where $t = \tau + px$ and $p = {dt}/{dx}$

with the $(x-t)$ domain amplitude given by $f(t,x)$ and the $(\tau-p)$ domain amplitude given by $F(\tau,p)$ is the plane wave decomposition of a cake model earth from a plane wave source (Chapman, 1981). In cartesian coordinates the above equation reduces to a summation over slopes as,

$$F(\tau_i,p_j) = \sum_{k=1}^{N} f(\tau_i + p_j x_k, x_k) \qquad \ldots\ldots\ldots\ldots\ldots\ldots\ldots\ldots\ldots (3.4)$$

N = number of traces, and i,j,k, are points in the $\tau-p$ and $x-t$ domains (Dunne and Beresford, 1995)

Stoffa (1981), Dunne and Beresford (1995), and Gu and Sacchi (2009) demonstrated the τ-p domain as an important domain like most other domains in exploration seismic imaging to which data could be mapped for velocity filtering (dip filtering), velocity analysis, multiple suppression and imaging with comparable or better outcomes, when such processes are applied to processing and imaging in the $x-t$ domain.

3.11 Other Radon transforms:

Other transform methods are aimed at the more natural nature of a propagating wave and its resulting recorded waveform in relation to given offset. When recorded reflections exhibit more of hyperbolic or parabolic moveout to offset then the preferred Radon process would be hyperbolic or parabolic Radon transform (Gu and Sacchi, 2009). Yilmaz (2001) pointed out linear Radon process is distinct from the other transforms by utilizing linear moveout, resulting in tau and ray parameter, while the parabolic and hyperbolic (velocity stack) transforms utilize hyperbolic moveout leading to tau-velocity domain meaning the mapping function is hyperbolic. This implies a hyperbolic event would naturally map onto a point in the parabolic or hyperbolic transform unlike a line to point mapping in the linear transform. Gu and Sacchi (2009) gave the general form of the Radon transform equation for the other two transforms as,

$\emptyset(\tau, \Delta, p) = \tau + p\Delta^2$ Parabolic Radon Transform ……. (3.5a)

$\emptyset(\tau, \Delta, p) = \sqrt{\tau + p\Delta^2}$ Hyperbolic Radon Transform (velocity stack) (3.5b)

Where Ø is a function which depends on tau, half offset Ø, and ray parameter p.

In terms of their moveout correction prior to mapping in the tau-p domain Yilmaz (2001) writes that these are given by,

$t^2 = \tau^2 + \frac{4h^2}{v^2}$ Hyperbolic moveout for hyperbolic Radon transform (3.6a)

$t_n = \tau + qh^2$ Parabolic moveout for parabolic Radon transform … (3.6b)

$t =$ two-way travel (TWT) time, $\tau(tau) =$ time in the tau-p domain or the TWT zero-offset time, $h =$ half-offset, $v =$ stacking velocity, $t_n =$ time after normal moveout (NMO) correction, $q =$ parabolic reflection parameter.

3.12 Radon Transform (tau-p) application:

Stoffa (1981), Kelamis and Mitchell (1989), Masoomzadeh et al., (2005) point to the linear Radon transform $(\tau - p)$ as a domain for frequency filtering, velocity filtering, demultipling, deconvolution, stacking and migration which still preserves the amplitude and phase of the data set as is in the $x - t$ domain.

For velocity filtering various authors, such as Tatham (1983), Nopoen and Keeney (1986), Kelamis and Mitchell (1989), Landa et al (1999), Spitzer at al., (2001), Yilmaz (2001), Masoomzadeh et al., (2005), show that performing such process gives an optimal output when compared to any other domain. Velocity filtering is implemented as an inside or outside mute polygon to the transform gathers. The mute creates a reject and accept zone for noise removal and signal preservation, thereby, attenuating coherent and non-coherent noises present in the data set (Mitchell and Kelamis, 2002). Such reject zone for noise informed the use and application of the tau-p process in noise removal and filtering of the JC132 data set from the Mid-Atlantic Ridge.

The tau-p transform is distinct from the $f - k$ transform owing to its tau (time) component (Yilmaz, 2001; Dondurur, 2018) which creates repeatability or periodicity for coherent and incoherent noise reflections. This is down to the decomposition of recorded signal to their plane waves. Yilmaz (2001) pointed out some recorded noises such as multiples are not always distinguishable in most signal processing domains as the $x - t$ domain which, therefore, makes it a little challenging to attenuate. The plane wave ‘decompositional’ nature of the linear Radon transforms implies each transformed reflection is characterised by a distinct ray parameter, thus making any transformed cojoined reflection separable. Deep water seismic profiles from slow-spreading ridge are inundated with mostly coherent noise not so easily attenuated in the $x - t$ domain, thus making the tau-p domain a possible domain to further explore the attenuation of observed coherent noises.

3.13 1500m/s migration and amplitude muting:

Any processing sequence is composed of different processing steps (including noise attenuation, geometry correction, waveform shaping, phase correction, stacking and imaging) aimed at inline reflected primary enhancement. Such steps as applied in the processing of the slow-spreading ridge data are discussed in the following chapter and here the focus is on the method following velocity filtering to further suppress sideswipes.

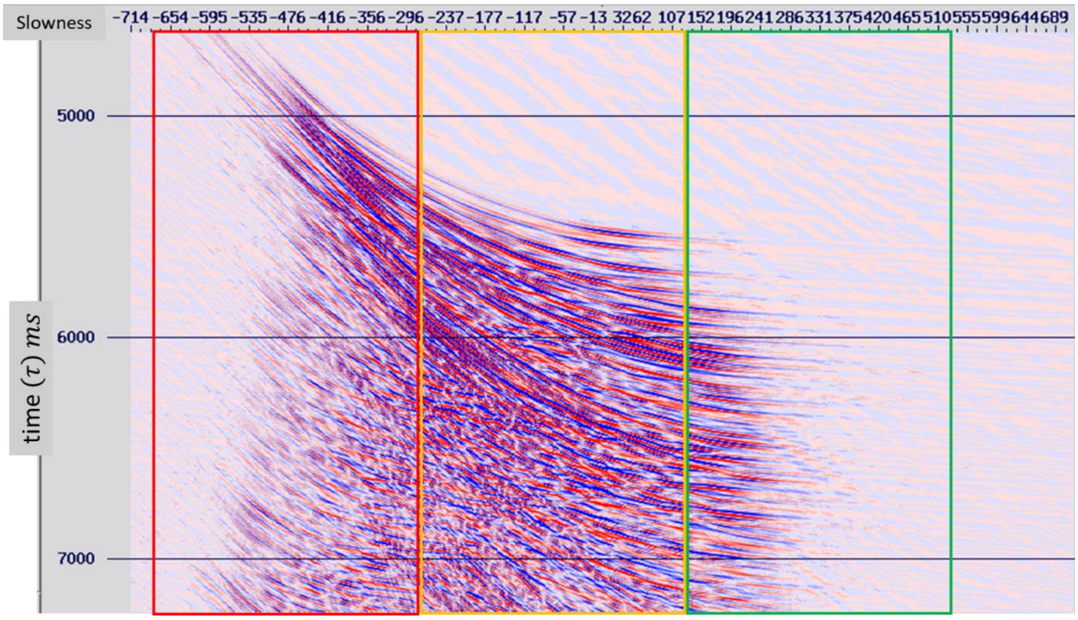

Figure 3.7: A typical $\tau - p$ gather prior to polygon definition. The red, yellow, and green boundaries are the far, mid and near offsets. A close observation shows reflections in the red region are well separated from those in the yellow and green region. The red region being were most of the noise (sublinear) are separated from the P-wave reflections (elliptical).

Owing to the nature of sideswipes described above (which are near basement velocity as P-wave inline reflection in most offset and quasi-hyperbolic shape) applying a $\tau - p$ velocity filter does not provide very optimal noise attenuation process as it leaves residual noises close to the seafloor afterwards. This results from the lateral velocity (slowness, $p = {}^{1}/_{v}$) of most sideswipes being very close, if not same, to those of possible primary inline reflections in the near (green band in Figure 3.7) and mid (yellow band in Figure 3.7) offsets data in the $\tau - p$ domain for possible optimal mute boundary definition for noise. Such closeness was observed especially for reflection in the first ~1000ms from the seafloor. It became necessary, therefore, to use a 1500m/s imaging process termed as “Stolt de-spiking” to further suppress residuals of such noises. Stolt de-spiking was informed by the relatively small size of the residual scatterers which collapse almost to a point upon imaging with water velocity when the diffractions are at zero offset (stacked), Figure 3.8.

Stacking is the summation of reflection amplitudes with a common origin or midpoint (Dondurur, 2018) aimed to enhance such amplitudes, therefore, a common method implemented prior to imaging. It attenuates some seismic noises such as multiples (Yilmaz, 2001; Dondurur 2018) but scattered noises are not attenuated and may be enhanced by stacking, so that subsequent migration of data is ineffective at anything other than water velocity, ~1500m/s, (Larner et al., 1983; Tsia, 1984; Calvert, 1997; Hargreaves and Wombell, 2004). We use this property to our advantage but following CMP stacking (to enhance amplitudes in the data) prior to “Stolt de-spiking”.

On stacking an assumption for reflection collapse during migration (imaging) of deep-water data is that all residual noises close to the seafloor travel at the velocity of water. Therefore, with amplitudes of scatterers enhanced an imaging process (Stolt migration) in their velocity of travel (~1500m/s) is implemented collapsing scattered diffractions virtually to a high amplitude localised energy burst. This can then be suppressed on the basis of its limited lateral continuity and high amplitude using an automated muting procedure known as de-spiking: an algorithm compares the amplitude in adjacent traces and mutes those where the lateral contrast exceeds a user-specified value within a user-specified window defining both vertical and horizontal dimensions. We dub this combination of water velocity Stolt migration followed by de-spiking the "Stolt de-spiking", which can be applied in the post-stack and pre-stack data domain, however, only the post-stack data domain process is shown in this work.

The Stolt de-spiking process yielded 1500m/s imaged sections with suppressed residual sideswipes when compared to 1500m/s sections with only velocity filtering, Figure 3.8a and 3.8d. Its success yields from collapsing noises in their speed (1500m/s) of travel prior to muting, thus properly discriminating such from all other inline reflections traveling at the speed of the target geology. The $\tau - p$ velocity filtering process could not attain this level of noise discrimination and attenuation especially for noise in the first ~500ms from the seafloor. Though the muting (de-spiking) process attenuated the noises, however, it left holes in the data and de-spiked bits of possible real reflections.

The results obtained of the two staged (velocity filtering and 1500m/s Stolt de-spiking) sideswipe attenuation processes employed is compared to the synthetics of the noise modelled from a high-resolution bathymetric map via the phase-screen process (Hobbs et al., 2006). In Figure 3.4a and 4b stacking was implemented after NMO using 1500m/s and modelled velocity from seismic refraction results. Compared to real data sections, Figure 3.8a and 3.8d, attenuation of sideswipes is observed as diffraction tails no longer predominate the real data. The synthetic Stolt migrated

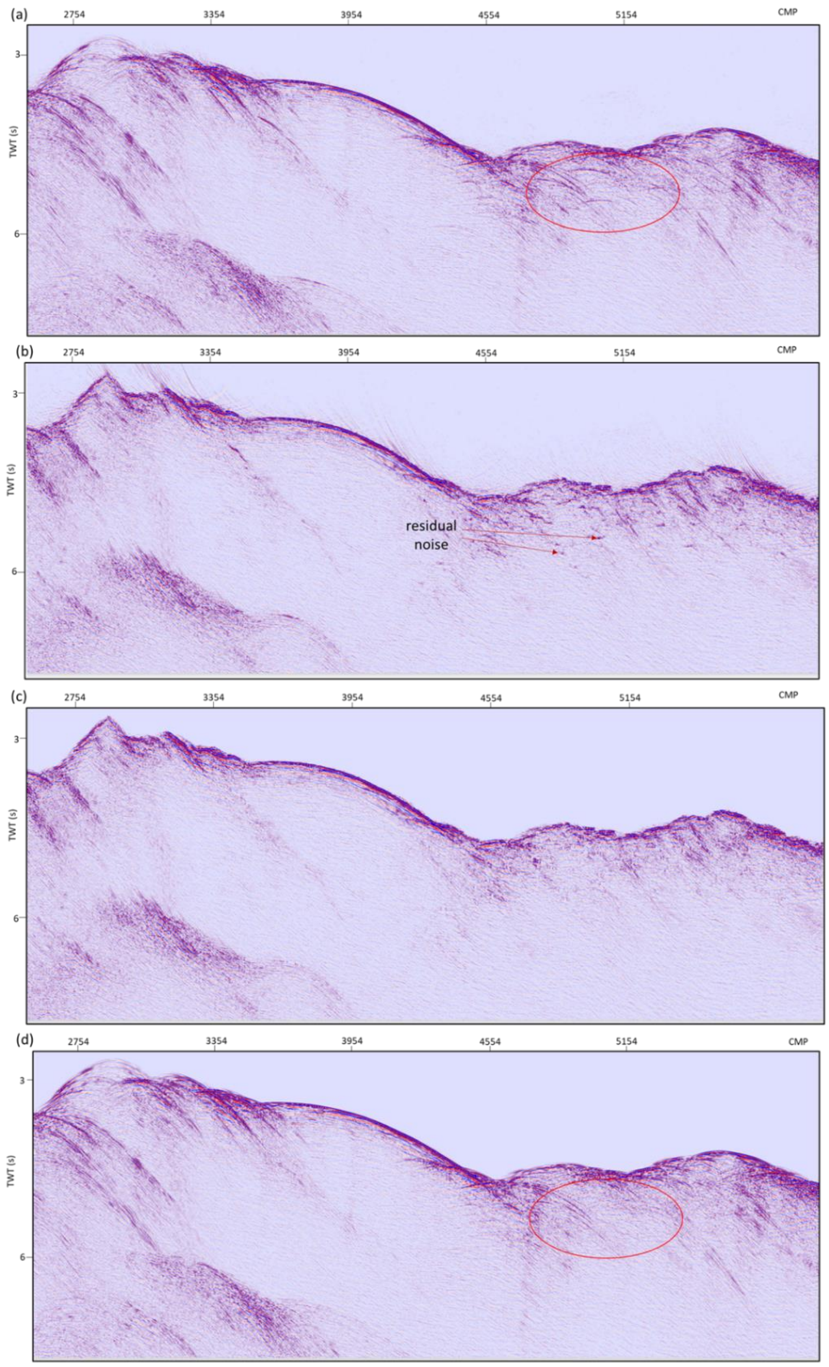

Figure 3.8: Stacked and 1480m/s Stolt sections showing the attenuation achieved applying the Stolt de-spiking process. (a) CMP Zero offset section after shot gather velocity filtering in the $\tau - p$ domain with observable residual noise. (b) 1480m/s Stolt migrated section of (a) resulting to the maximum amplitude of imaged noise and their collapse to point-scale size. (c) De-spiking process applied to (b) muting collapsed noise. The muting process also results to P-wave muting were such exists at the location of the noise. (d) Stack model of (c) using Madagascar™ to de-migrate the data, showing that most of the scattered noise has been suppressed.

sections Figure 3.4c and 3.4d do not replicate real data closely owing to the larger CMP spacing (25m) with which the synthetics was implemented. However, it shows the validity of the muting process applied to the 1500m/s Stolt imaged section with the dominance of point-scale collapsed reflections, Figure 3.4d.

The foregoing shows the importance of attenuating sideswipes from seismic reflection data set via a processing sequence aimed at eliminating or suppressing their impact such that the underlying inline P-waves are enhanced or preserved. Such process ensures the repeatability and validity of imaged results from data sets encumbered by such noise.

3.14 Conclusions:

The analysis here has shown that side-scattered energies from the rough seafloor are likely to present a major imaging problem at slow-spreading ridges, but that they can be suppressed through a combination of $\tau - p$ and similar filtering, and through constant water velocity migration to collapse the quasi-hyperbolae to local energy bursts followed by amplitude clipping to remove those bursts. The data can then be either further migrated (cascaded migration) with a variable velocity function or de-migrated (modelling) to recreate the stack section (without the scattering hyperbolae) and then further processed, e.g., through depth migration. These approaches will now be applied to the real reflection data from 13N in Chapter 4 and following to show possible outcomes.

Chapter 4 Seismic processing at 13˚20’N.

4.1 Introduction:

The data set presented here was acquired in 2016 during the JC132 expedition at the Mid-Atlantic ridge (MAR) between 13°10’N and 13°40’N (Figure 4.1) to better understand the process of slow seafloor spreading and in particular the role of oceanic detachment faulting in the formation of oceanic core complexes (OCCs) as discussed in Chapter 2. The data set was acquired over a hard, irregular, seafloor made of various magmatic rocks (basalts, dolerites, gabbros) and mantle serpentinites

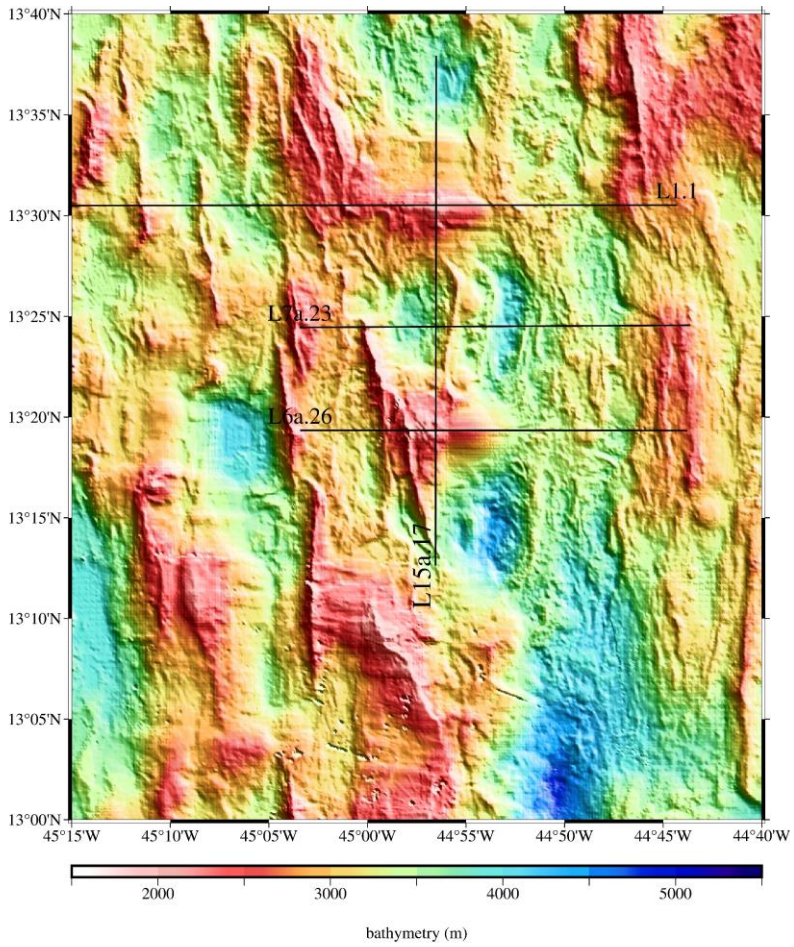
13°40'N
13°35'N
13°30'N
13°25'N
13°20'N
13°15'N
13°10'N
13°05'N
13°00'N
L1.1
L7a.23
L6a.26
L15a.17
45°15'W
45°10'W
45°05'W
45°00'W
44°55'W
44°50'W
44°45'W
44°40'W
2000
3000
4000
5000
bathymetry (m)

Figure 4.1: Bathymetric map of the study area showing the location of the profiles. This chapter focuses on profile L6.6 and 6a.26: the first number gives the position of the profile in the order first shot, and the second number the order in which the profile was shot; this as well as several other profiles was shot twice, once with a 20s shot interval (~ 50m) and once with a 10s shot interval (~25m) to reduce spatial aliasing. (Reston and Peirce 2016).

(MacLeod et al., 2009) that represent a strong acoustic impedance contrast with the overlying water column. The combination of seafloor roughness, hardness and three-dimensionality mean that the data is likely to be strongly affected by scattered noise from out of the plane of section, as discussed in Chapter 3, thus presenting significant processing challenges. Here we outline the processing scheme (Table 4.1) applied to suppress non-geological apparent velocity reflections and side-scatter from the rough seafloor using the sort of processes available through standard and open-source seismic processing software to present an imaging of the 1320 OCC in time and depth. I focus on one flowline transect along the centre of this OCC, shot twice in opposite directions and different acquisition parameters: lines L6.6 and L6a.26.

4.2 Seismic acquisition during JC132:

The JC132 data were acquired in 2016 by the RRS James Cook towing two strings of airguns ~5 m either side of a central 3000m-long 240 channel multichannel streamer. Seismic acquisition during cruise JC132 was into both an array of ocean bottom seismometers (Ourabah et al., 2015) and into a 3000m 240 channel streamer.

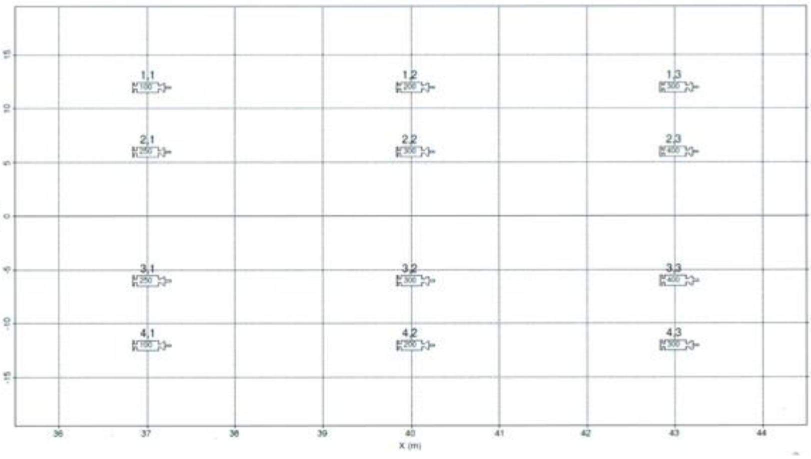

Figure 4.2: The airgun array used in MCS acquisition during JC132. The total volume was 3100 in^3, requiring ~20s to fully pressurise, but for half the survey each sub-array (volume 1550 in^3) was shot separately at 10 s intervals. (Reston and Peirce 2016).

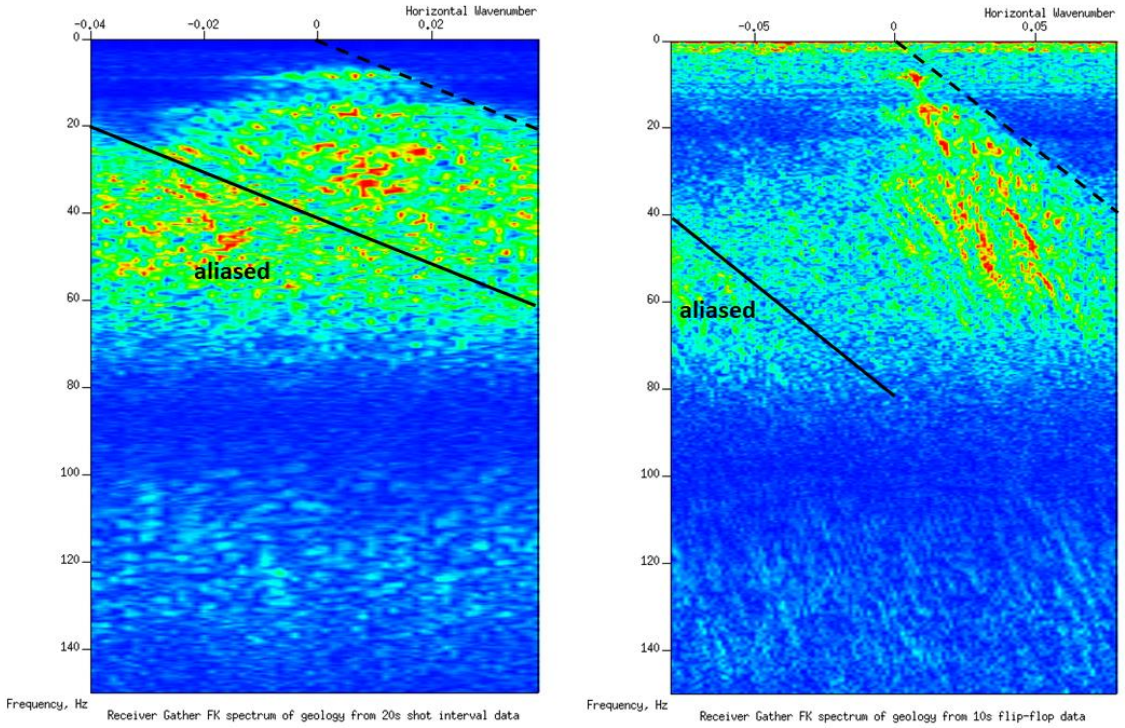

Figure 4.3: Comparison of the fk spectra of a receiver location gather with 20 s shooting (left) and 10s shooting (right). Given the presence of coherent energy up to 60Hz, it is apparent that reducing the shot spacing results in far less spatial aliasing (energy beneath the lower black line). Reston and Peirce 2016

To maximise signal strength and as the OBS recordings require a long shot interval to allow water-borne noise to disperse prior to the following shot, the initial profiles were shot using a moderately large array of 12 Bolt^{TM} airguns with a total volume of 3100 in^3 (Figure 4.2) that required >15s to fully pressurise and which was consequently fired every 20s (~50m at the shooting speed of 4-4.5 knots); navigation was not of sufficient quality to shoot strictly on distance and shooting on time simplifies OBS analysis. But while providing better data for wide-angle analysis, fk analysis (Figure 4.3) showed that at this shot interval the higher frequencies were spatially aliased on receiver gathers from the streamer data, limiting processing options. Consequently, during the second half of seismic acquisition, each half of the array was fired alternately with a shot interval of 10 s (~25m), shifting the spatial aliasing Nyquist frequency to higher

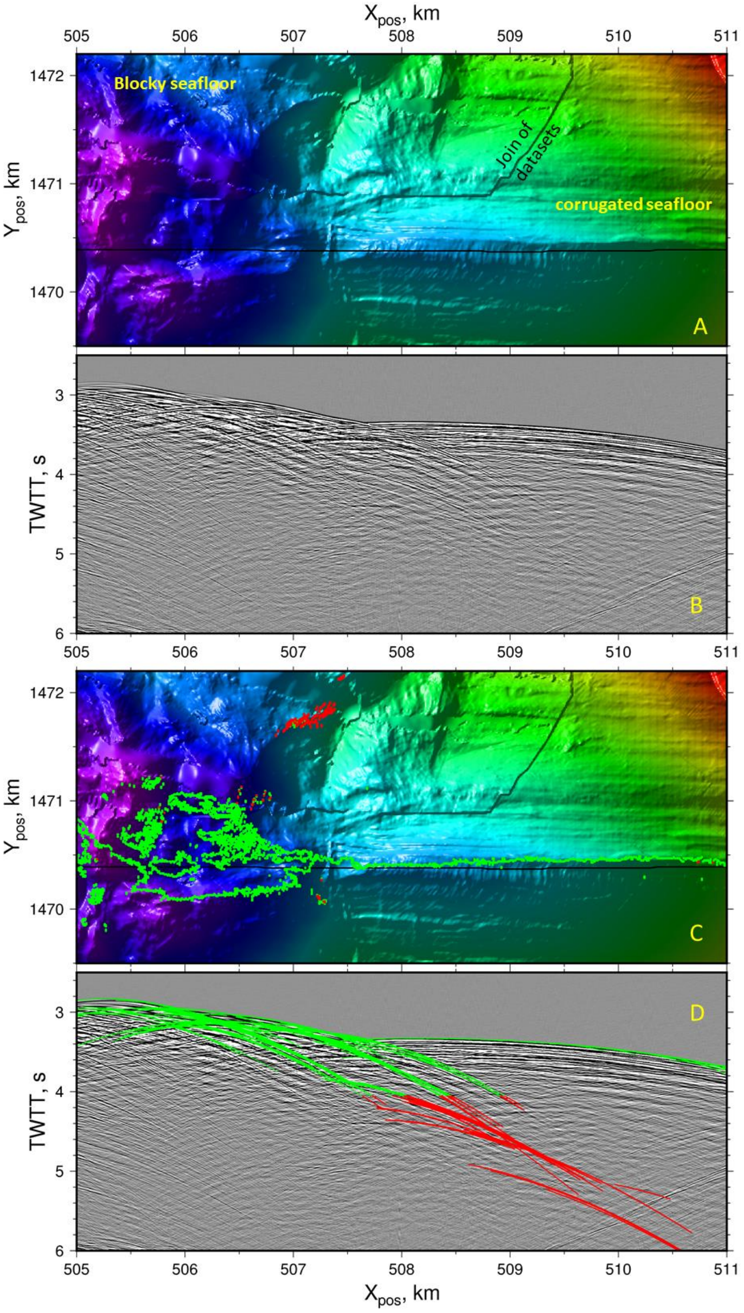

Xpos, km
505
506
507
508
509
510
511
Ypos, km
1472
1471
1470
Blocky seafloor
Join of datasets
corrugated seafloor
A
TWTT, s
3
4
5
6
B
C
D

Figure 4.4: Detail (purple shallow, red deep) of the 1320 detachment fault at the transition from a corrugated to a blocky surface, thought to mark the boundary between dolerites and gabbros (blocky) and serpentinized peridotites (corrugated). The black horizontal line marks profile L6a.26. B: stack image along this portion of the profile, showing numerous quasi-hyperbolic events, particularly towards the left -m the region of the blocky seafloor. C, D: colour-coded by angle reflection points producing those hyperbolae. Particularly where the seafloor is rough and blocky, side-coming events are very common and can originate more than 1 km off the line. Figure courtesy of Reston, pers comm.

values to allow higher resolution imaging. Changing the shot interval gave two data sets of 30 and 60 common midpoint (CMP) folds. Profiles were shot dominantly either E-W (or W-E) and N-S, that is in the direction of spreading (along flow-lines) or perpendicular to it (along lines of equal age, or isochrons) to image both structures associated with the spreading process, e.g. the orientation of oceanic detachment faults at depth (Cann et al., 1997; Mitchell et al., 1998), and to reveal their lateral continuity (Reston and Ranero, 2011). The profiles were collected over and around two well-developed oceanic core complexes located at 1320 (subsequently 1320) and 1330. This chapter focuses on the 1320 OCC, Figure 4.4, including the processing and imaging sequence applied (Table 4.1).

4.3 Hard seafloor noise:

Imaging deep oceanic structures, such as the mid-ocean ridge (MOR) system, via 2D seismic reflection has been shown in Chapter 3 to be compounded by out-of-plane reflections (during data acquisition) which considerably affect the quality and resolution of seismic signals recorded. This stems from the three-dimensionality, roughness, and hardness of the seafloor in proximity to the acquisition line which impact the quality of acquired data by exhibiting non-hyperbolic and apex shifted moveout reflections from surface scatterers, including inline reflections ahead or behind the shot and streamer combination (Larner et. al., 1983). Therefore, for data sets dominated by out-of-plane, there is a need to optimise the processing sequence to suppress unwanted scattered energy while preserving and enhancing desired inline primary reflections (P-wave) from subsurface geological boundaries and surfaces, such as faults.

Basic seismic reflection processing assumptions are mostly based on P-wave reflection hyperbolae generated from layered (cake model) subsurface rocks such as

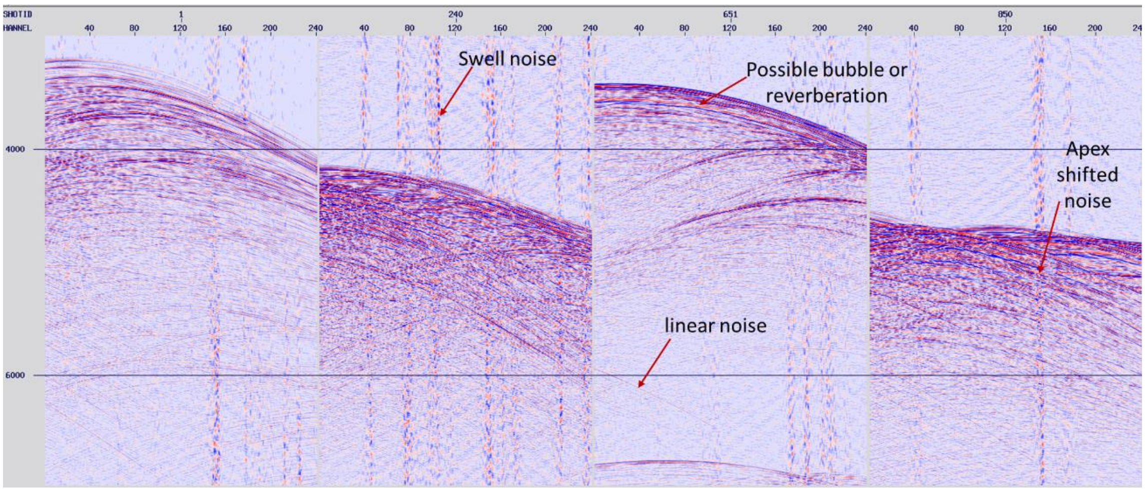

Figure 4.5: Raw shot gathers from the data of 2016 vintage from the Mid-Atlantic ridge aimed to image the footwall of the detachment fault of the 1320 OCC. On these gathers apex shifted hyperbolae (apex not at the near offset) are observed as well as strong background linear and swell noises.

a sedimentary sequence. Seismic data acquired over a hard seafloor setting, such as at the 13° north segment of the MAR (Figure 4.4) exhibit close to non-hyperbolic moveout on most of the recorded reflections (Figure 4.5), thus limiting the application of basic processing sequence to obtain interpretable images in time and depth. Due to the rough nature of the seafloor, noise suppression processes like frequency-wavenumber (fk) dip filtering, that are invariant in the time domain are less effective when applied in the common shot, common offset, and common mid-point (CMP) domains. As observed by Hargreaves and Wombell (2004), any dip filtering processes that are not efficient and effective in discriminating recorded reflections would attenuate both the targeted noise (sideswipes and diffraction scatterer) and the desired P-wave reflections needed to be preserved and enhanced. However, dip filtering processes that can vary in the time domain - such as the linear Radon transform process (tau-p or linear slantstack) – have been shown to be somewhat effective in suppressing side-wipes and dipping linear noises, consequently enhancing the inline P-wave dipping reflections (Dunne and Beresford, 1995) and improving

Table 4.1: Processing sequence applied for sideswipe suppression and imaging of the JC132 data set.

Read SegD and convert to hdf5 format
Trace editing for dead traces
Apply marine geometry (line dependent)
T^2 Amplitude correction
Minimum phase conversion (wavelet process application)
Far field (FFsig) estimation from data set near trace plot
Receiver ghost (Recghost) estimation (calculated with streamer depth
Debubble operator estimation (gap 24ms and length 480ms)
Convolution of FFsig, Recghost and debubble
Convolution of FFsig, Recghost, debubble and antialias filter
Minimum phase conversion
Minimum phase filter generation
Bandpass filter (5-70Hz minimum phase)
Swell noise attenuation (DUSWELL and FKmute)
Bandpass filter (5-70Hz minimum phase)
Regularization to 6.25m
Forward Taup (-1400m/s to 1400m/s linear velocity)
Hyperbolic velocity filtering (apply picked tail mute)
Weinner Deconvolution with 26msec gap
Bandpass filtering
Hyperbolic velocity filtering (apply picked tail mute)
Rho filter
Inverse Tau-p (-1400m/s to 1400m/s linear velocity)
Regularise to 3.125m
Antialias filter (Kfilter)
Interpolation (shot and/or group)
NMO and stack with modelled Vrms of subsurface
Time migration
Stolt migration with1480m/s (first time MIG)
De-spiking
Finite difference migration using modelled Vint (2nd time MIG)
Depth migration
Stolt migration with1480m/s
De-spiking
Stolt modelling with 1480m/s
Kirchhoff poststack depth migration with modelled interval velocity
Display

signal to noise ratio. Below we outline such methods applied to image this dataset as outlined in Table 4.1.

The unprocessed shot gathers (Figure 4.5) are affected by several types of noise, including low frequency swell noise, easily removed by low cut frequency filtering,

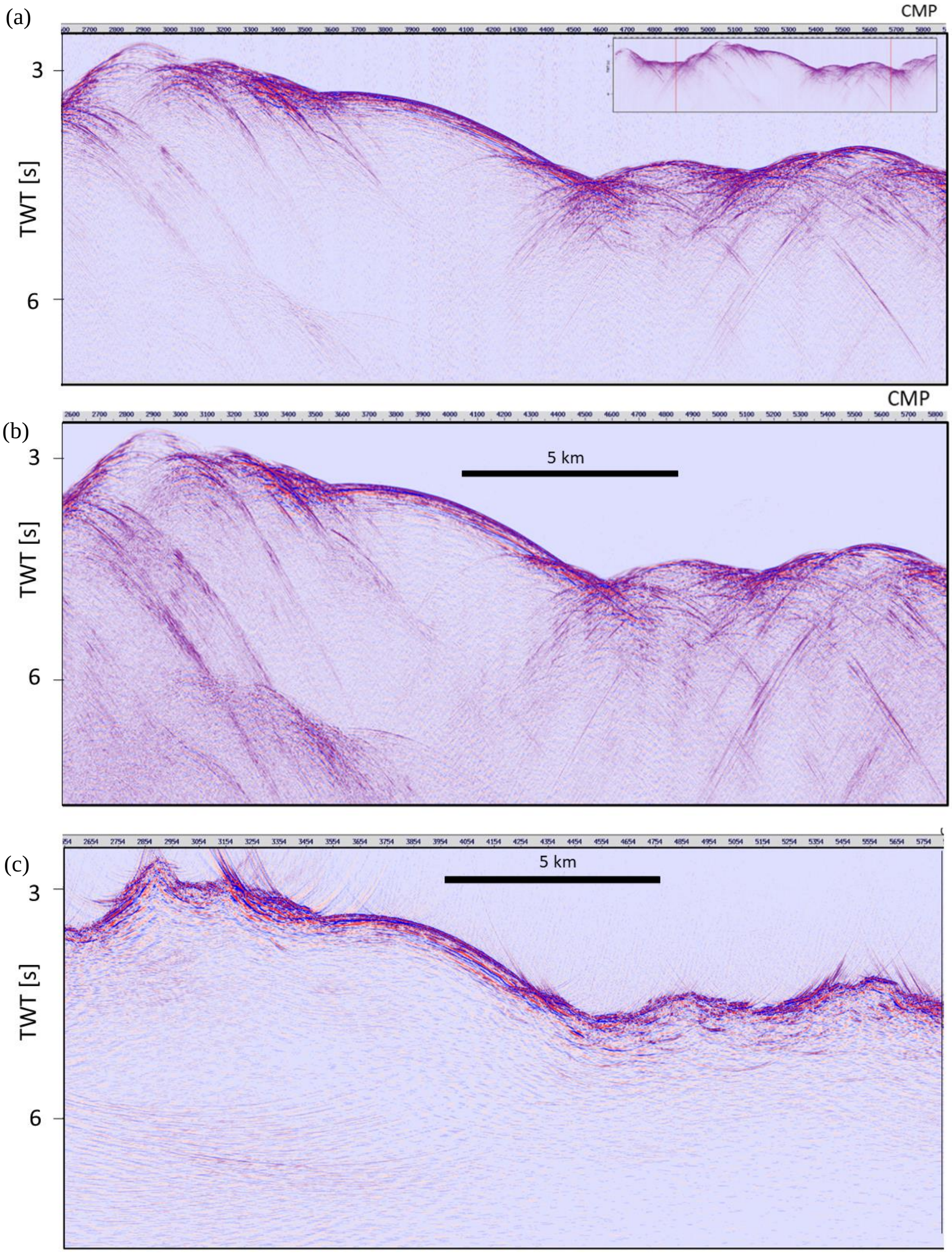

Figure 4.6: Basic processing (bandpass frequency filtering and spherical divergence correction applied to shot gathers) of central portion of line 6a.26. (a)1500 m/s NMO corrected CMP stacked section which shows the dominance of diffraction scatterers. On this section it is difficult to point to possible real reflections. Insert is the full length of the line. (b) CMP stack after NMO correction with full refraction-derived velocity model. Diffractions still dominate and diffraction tails are even clearer. (c) Finite difference time migrated (with model V_{int}- time) section of (b) with the seafloor over migrated. (a) and (b) indicate the noise present in data is not attenuated either with water velocity or possible velocity of the lithology.

likely reverberations, or bubble pulses, targeted by deterministic deconvolution, and possible out-of-plane apex-shifted reflections/diffractions. In CMP gathers the last in particular are less obvious, limiting the choice of processing flows applicable in the shot and CMP domain. Stacking and migrating such CMP gathers shows the line is dominated by diffraction scatterers (Figure 4.6a, b) which smear out on migration with a geologically reasonable velocity model to produce smiles on time migrated section of this stack (Figure 4.6c).

The approach adopted is a combination of pre-stack hyperbolic velocity filtering and deconvolution of the shot gathers; followed by normal-moveout correction and CMP stacking; followed using multi-step migration to suppress side-coming diffractions. The tau-p (slantstack) domain process suppressed diffraction tails for improved shape and resolution of the wavelet. This was combined with post-stack process of Stolt migration with a constant water velocity to collapse diffractions to small energy bursts and such bursts suppressed through applied de-spiking algorithm; followed by either cascaded time migration, or by water velocity modelling (de-migration) to revert to the stacked section with full velocity Kirchhoff depth migration afterwards. Most of these steps are easily implementable on any processing system. These processes are aimed to shape the wavelet of the dataset, remove low velocity travelling noise, further collapse outstanding residual noise - and subsequently– de-spike sideswipe diffractions unattenuated after 1480m/s Stolt migration prior to finite-difference and depth migration as explained in detail later.

4.4 Far field estimation:

Prior to tau-p processing (following water refraction muting and swell noise attenuation as in Table. 4.1) the dataset was converted to minimum phase using a

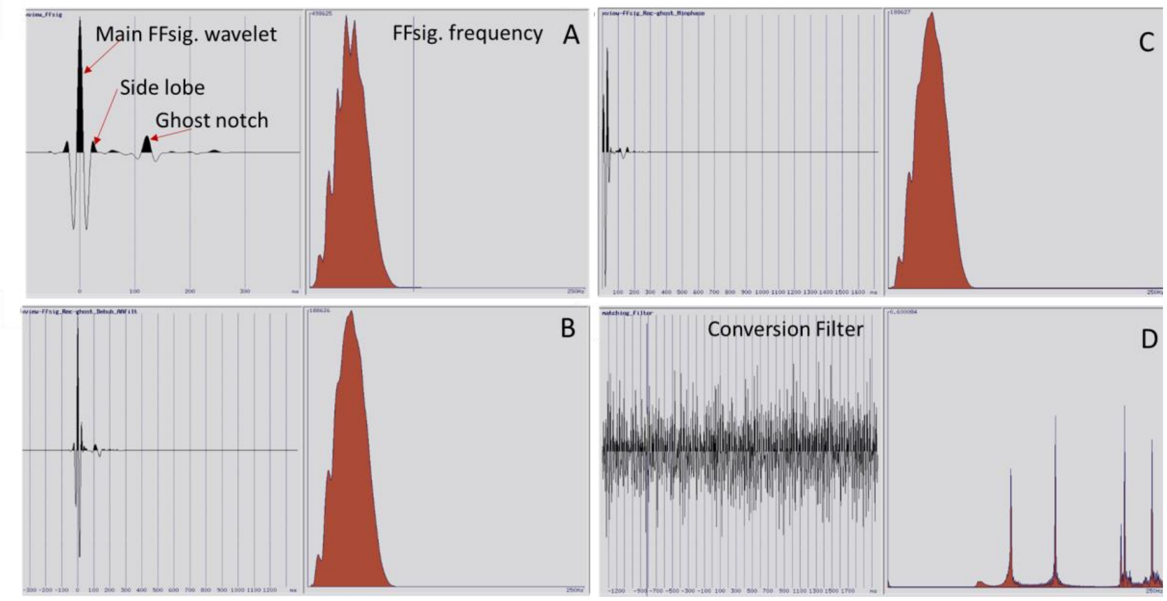

Figure 4.7: Shot source signature (far-field wavelet and frequency) estimation stages used in the process of wavelet shaping prior to deconvolution step. Modelled wavelet (a) derived from the near trace plot of a shot gather and composite far-field wavelet (b) resulting from convolution of possible bubbles, anti-aliased filter, and receiver ghost reflections. (c) Resulting minimum phase equivalent of (b). (d) Minimum phase conversion filter derived from (c). The first half of each plot is the time – amplitude wavelet plot while the second half is the frequency – amplitude plot.

minimum phase conversion filter (Figure 4.7). This filter was obtained from the minimum phase version of the far-field wavelet (Figure 4.7a) derived from the near trace data (autocorrelation and stacking applied as suggested by Bianco, 2016). The extracted far-field was convolved with an anti-aliasing filter (a low pass filter), modelled receiver ghost and bubble pulse accounting for the possible composite recorded reflection wavelet (Figure 4.7b). Far-field modelling from near trace became needful owing to the failure of some air guns in the shot array during data acquisition and subsequent deviation of the originally modelled acquisition far-field wavelet. The receiver ghost was modelled as a spike in consideration to the streamer tow depth of 8 m or 10 m depending on the line. The ensuing wavelet was converted to a minimum phase wavelet (Figure 4.7c) after which a minimum phase conversion filter (Figure

4.7d) was derived and applied to the dataset to yield a minimum phase data. This minimum phase data afterwards passed down the processing flow for hyperbolic velocity filtering (tail muting) and deconvolution in the tau-p domain. The advantage of following wavelet shaping with tau-p domain deconvolution is the repeatability (stationarity) of traces in this domain, thus ensuring optimal performance of the gapped deconvolution applied.

4.5 Tau-p processing:

Slantstack domain introduced and explained in chapter 3 has slowness (p) and intercept time (tau, τ) as coordinates. Plotting seismic traces in terms of p offers the advantage (by ensuring the repeatability of such traces) of plotting the traces in terms of horizontal velocities with which they appear to propagate (that is the slope of each energy in the $x - t$ plot) through an area of interest (Chapman, 1981). Ignoring anisotropic characteristics of any medium it therefore would be possible to segregate seismic reflections and noise based on the speed of travel in different media (Tatham, 1984). This is obtainable in the $\tau - p$ domain and its application to seismic processing has evolved in usage from considering or plotting the p-axis on only the positive or negative slowness to combining both values in a single plot. Such combination ensures both positive and negative dipping events in a shot gather are all captured in the tau-p plot (Figure 4.8).

Combined with other processes, tau-p processing of seismic reflection shot gather has been shown to effectively attenuate seismic reflection noise when mutes and/or gapped deconvolution (which utilises the stationarity of the noise and P-waves in L6a.26 data in the tau-p domain) are applied to the slant-stack gather (Dunne and Beresford, 1995; Yilmaz, 2001; Cao et al., 2003, Masoomzadeh et al., 2004, Kumar

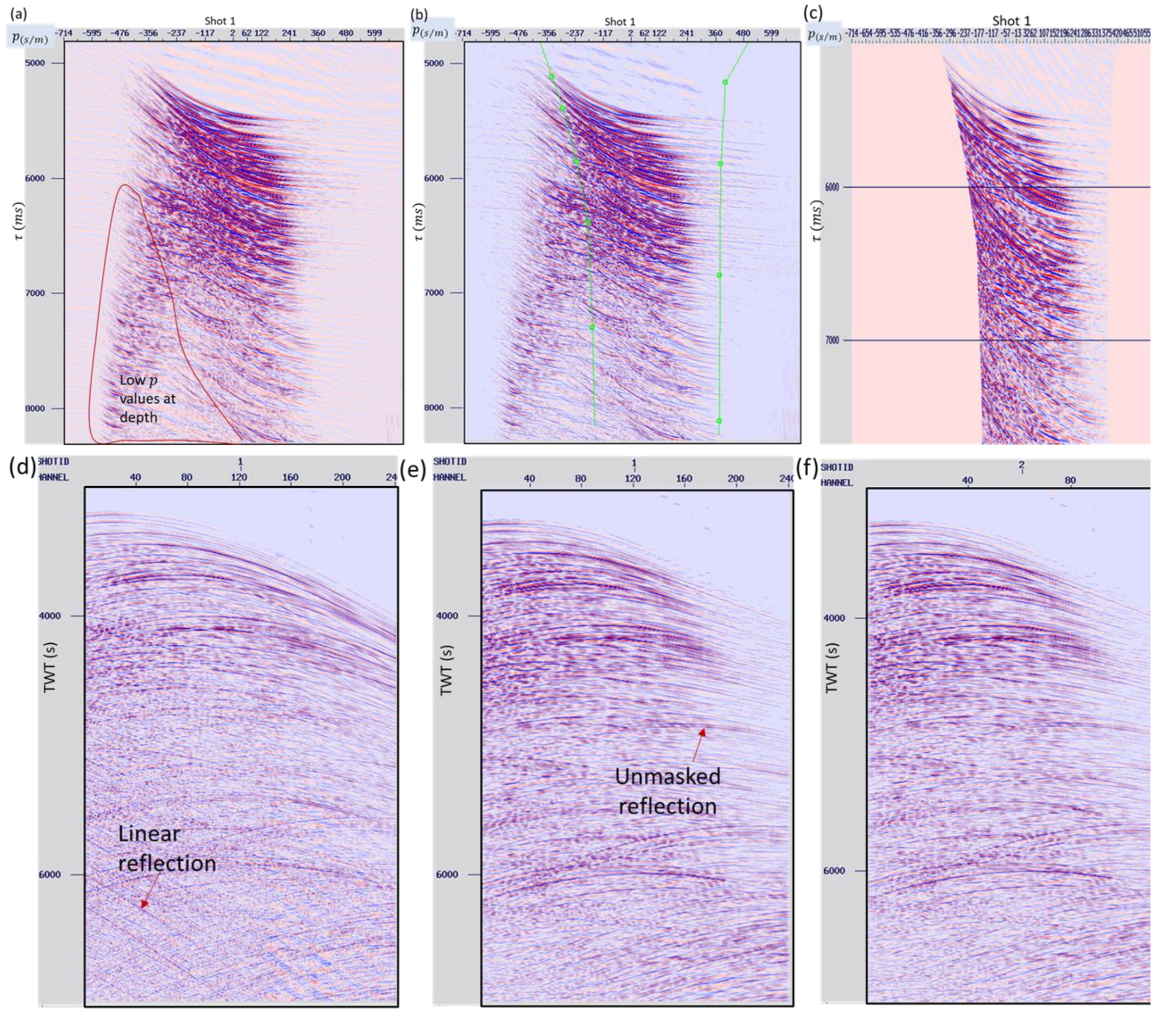

Figure 4.8: Application of velocity filtering via tail muting in the $\tau - p$ domain. (a) First Shot of line 6a.26 in the $\tau - p$ domain showing elliptical and non-elliptical reflections with low linear velocity. Defined (b) and applied (c) mute boundary on (a) muting out most of the low linear events at deep. Comparing the shot gathers (in the offset-time domain) before (d) and after (e) hyperbolic velocity filtering shows removal of most linear noise in (d) while unmasking weak reflections in (e). (f) Interpolated shot gather with first resulting shot numbered 2.

et al., 2018). This results from the slant-stack domain separating reflections according to their plane wave propagation speed, which largely depend on the medium’s linear velocity. Processing the 1320 dataset in this domain, therefore, highlights the strong presence of slow traveling linear velocity reflections (dominant at 6s and below) as a contaminant of the datasets acquired from the MAR (Figure 4.8a). The gathers shown exhibit very low p-values at deeper τ not relatable to linear velocities associated at such τ with possible geological inline P-wave reflection. As in $\tau - p$ space, such very slow linear velocity reflections are best seperated from faster velocity phases the can be suppressed by the application of a tail mute designed to remove both their negative and positive components as shown (Figure 4.8c). A comparison (Figure 4.8d and 4.8e) of the resulting shot gather (before and after slantstack muting) highlights unmasked reflections which are possible prior weak inline P-wave reflections.

A combination of hyperbolic velocity filtering and gapped deconvolution (removal of the source wavelet from the earths reflectivity) in the $\tau - p$ domain enhanced the signal to noise ratio of each resulting shot gather, especially for shots with 25m spacing geometry. The deconvolution was applied with a short window gap of 26ms and an operator length of 500ms. The short-gapped deconvolution over a long window length ensured that dominant reverberations on the shot gathers were removed.

Close inspection of the $\tau - p$ transformed shot record (Figure 4.8a) shows not readily distinct elliptical reflection boundaries from one reflection end to another. Thus, implying picking of tail mute points is critical to ensure close to geological p-values as linear velocities (interval velocities for isotropic medium) are chosen as mute points. The above procedure was also applied on all the other lines resulting in noise suppression as shown by shot gather comparison before and after on line L15a.17 (Figure 4.9).

Note that k-filtering coupled with shot interpolation and group regularization could be implemented before the tau-p processing step which would ensure transforming shot gathers having little or no spatial aliasing (for this dataset we implemented it after). Besides interpolating in the shot-channel domain, all filtering processes are in the shot domain as the seismic noises are well sorted in the CMP domain, therefore not easily identifiable and do not stack-out.

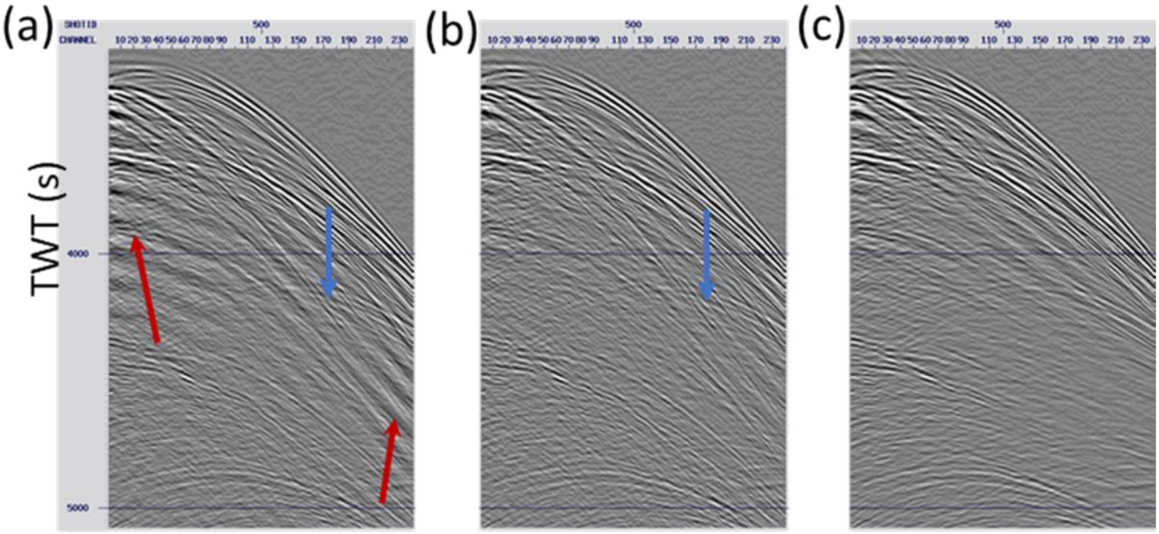

Figure 4.9: Line L15a.17 shot gather comparing the result of $\tau - p$ deconvolution and muting to the original shot gather. (a) shows the shot gather with bandpass filtering, swell noise and water refraction removal applied. The red arrows point to possible reverberations or bubbles in the data while the blue arrows point to possible diffraction tails. (b) and (c) are gather in (a) with deconvolution and deconvolution combined with velocity filtering (tail muting) in the $\tau - p$ domain. (c) shows removal of both events in (a) and (b).

4.6 Interpolation and regularization (De-aliasing):

Trace regularization is change in the original acquisition geometry of seismic traces to either a reduced, increased, or regularised geometry (Gong et al., 2016) and implemented in processing using the OFFREG module of Globe Claritas software (Claritas). Channel interval (12.5m) regularizing was regularized to 3.125m after tau-p processing enabling wavenumber (k) filtering (k-filt) to address shot gather aliasing in the frequency-wavenumber (fk) domain, reverting to the original acquisition interval afterwards. The smaller interval unwrapped aliased frequencies in the fk-plot followed by muting via k-filt preserving only the dominant frequencies.

Shot interval (25m or 50m) was reduced by half (12.5m or 25m, doubling the number of shots) through interpolating two new shots (the first numbered 2) for each in the data following trace regularization from 12.5m to 25m (after the k-filt step). Thus, increasing the group interval by dropping every other trace in a record of 240 traces

(Cary, 1999), reducing the shot fold to 120 (Figure 4.8f) while doubling the CMP fold to either 120 or 60. This aimed at further addressing spatial aliasing in the shot gather by a change of acquisition geometry. The outcome of migrating the interpolated data is commented in the result, however, interpolation attenuated the diffraction tail limbs by unwrapping aliased frequencies in the diffraction events (Smith et al., 2008; Liu and Li, 2010) and improved the resulting time and depth imaged sections. Note that k-filtering coupled with shot interpolation and group regularization could be implemented before the tau-p processing step which would ensure transforming shot gathers having little or no spatial aliasing (for this dataset we implemented it after). Besides interpolating in the shot-channel domain, all filtering processes are in the shot domain as the seismic noises are well sorted in the CMP domain, therefore not easily identifiable and do not stack-out

4.7 Velocity models and stacking:

A key challenge of imaging datasets acquired over a hard sea floor is the difficulty in obtaining velocity models from the recorded reflections. This problem is attributable to the masking of inline geologic reflections by low velocity reflections which can be observed in the resulting semblance plot of the data (red arrow Figure 4.10). The semblance velocity values show water-related velocity plots which are not rock related velocities Sub-bottom of the 1320 OCC.

To surmount this challenge, stacking velocities were computed (using python programming, see appendix A for code) from mid-oceanic crust interval velocity (for 1320 OCC) determined from refraction data (Grevemeyer et al., 2017; Peirce et al., 2019). Figure 4.11a shows Peirce et al.’s (2019) velocity model plot in the interval velocity-depth domain.

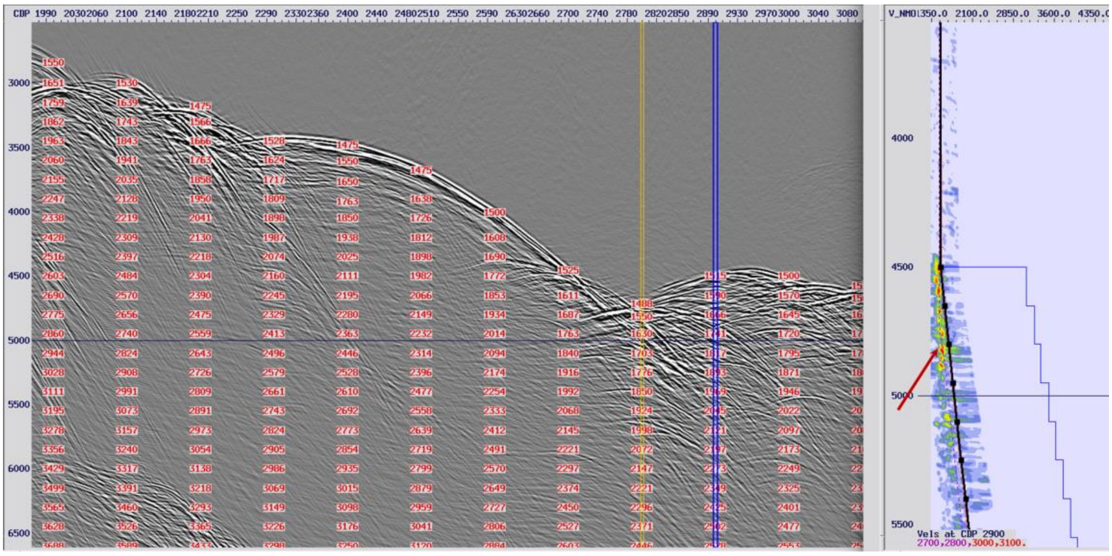

Figure 4.10: Semblance plot of L6a.26 with an initial seed model velocity in an attempt for velocity analysis. The plot shows the stacked sections (left) of the line and the estimated semblance plot (right) at the location (blue line through stack) along the line. The red arrow points at the low velocity estimates of the semblance from the data.

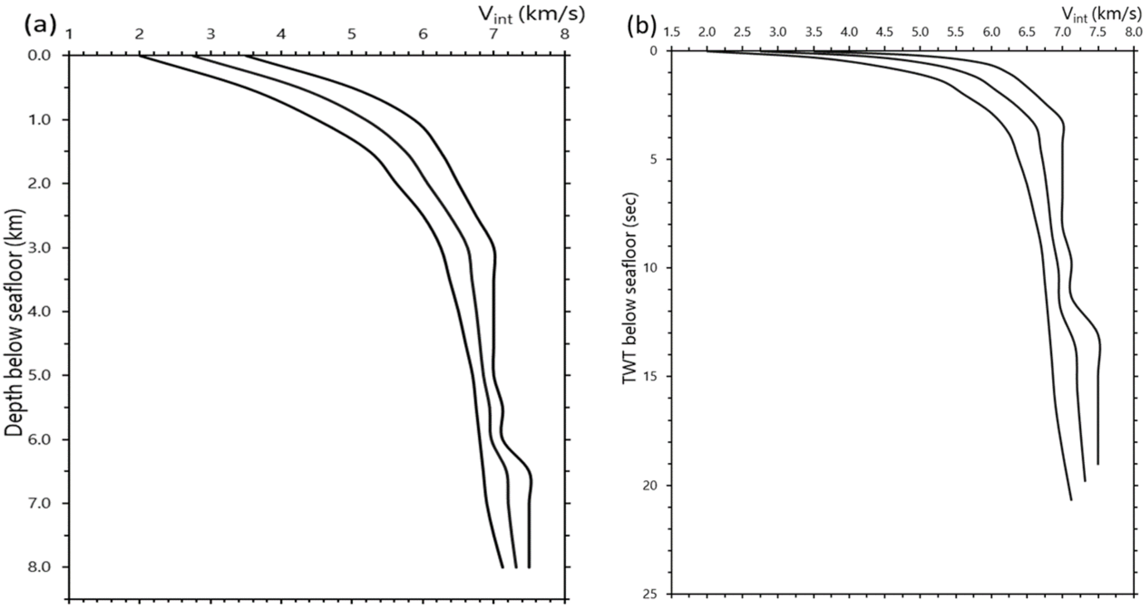

Figure 4.11: v_{int} – depth (a) of Peirce et al. (2019) and resulting v_{int} – time of (a) for seismic reflection studies of slow-spreading Mid-Atlantic ridge. The three plots are the upper (max) and lower (min) bound of the velocities with the mid-range (ave.) added. It is noted that the velocity model is a band of the possible range of values from the minimum to the maximum that oceanic rocks in a mid-ocean ridge could have. Note it does not indicate there are reversal implying there are no low velocity zones.

The top of this interval velocity-depth model was suspended from the seafloor and converted to interval velocity-time plot, see Table 2 in appendix B, (Figure 4.11b) and then to v_{rms} – time used for NMO correction and hence for stacking. A challenge encountered here is the nonexistence of a layered structure in the MOR especially in the vicinity of the detachment fault as shown by the authors of possible boundaries at depth intervals of the velocity plot on which the extraction could be hinged. Therefore, a simplified velocity model extraction was assumed as a 0.5km (simple cake model earth) layering along the v_{int} - depth plot on which the depth to time conversion was made (see Table 4.2) using the velocity two-way time equation $t = \frac{2d}{v}$. This approach was chosen as the most effective to ensure NMO correction and all imaging are implemented with velocities relatable to the MOR rock velocities. The resulting velocity model of Peirce et al., (2019), being a range of velocity values, a one-dimensional (1D or single value) velocity digitization was extracted by dividing the velocity ranges at different depths (starting from seafloor) into minimum, average, and maximum. The average was modelled into root-mean-square velocity (V_{rms}), interval velocity (V_{int}) time and cascaded V_{int} used in imaging. A key step in building these models was the extraction of seafloor horizon times from 1500m/s stacked and imaged data, below which velocity values exist. Resulting velocity models in python were converted to a multidimensional file format (netcdf5) and to SEGY prior to use. Figs. 4.12a and 4.12b are the modelled V_{rms} implemented for NMO correction and the V_{int} depth converted model applied for Kirchhoff depth migration. Applying the V_{rms} to NMO correct the CMP gathers yielded the stack section in Figure 4.13. Comparing Figure 4.13 and Figure 4.6a shows $\tau - p$ processing step ensured low velocity reflections at later times were attenuated considerably while preserving diffraction tails that might be associated with possible dipping events.

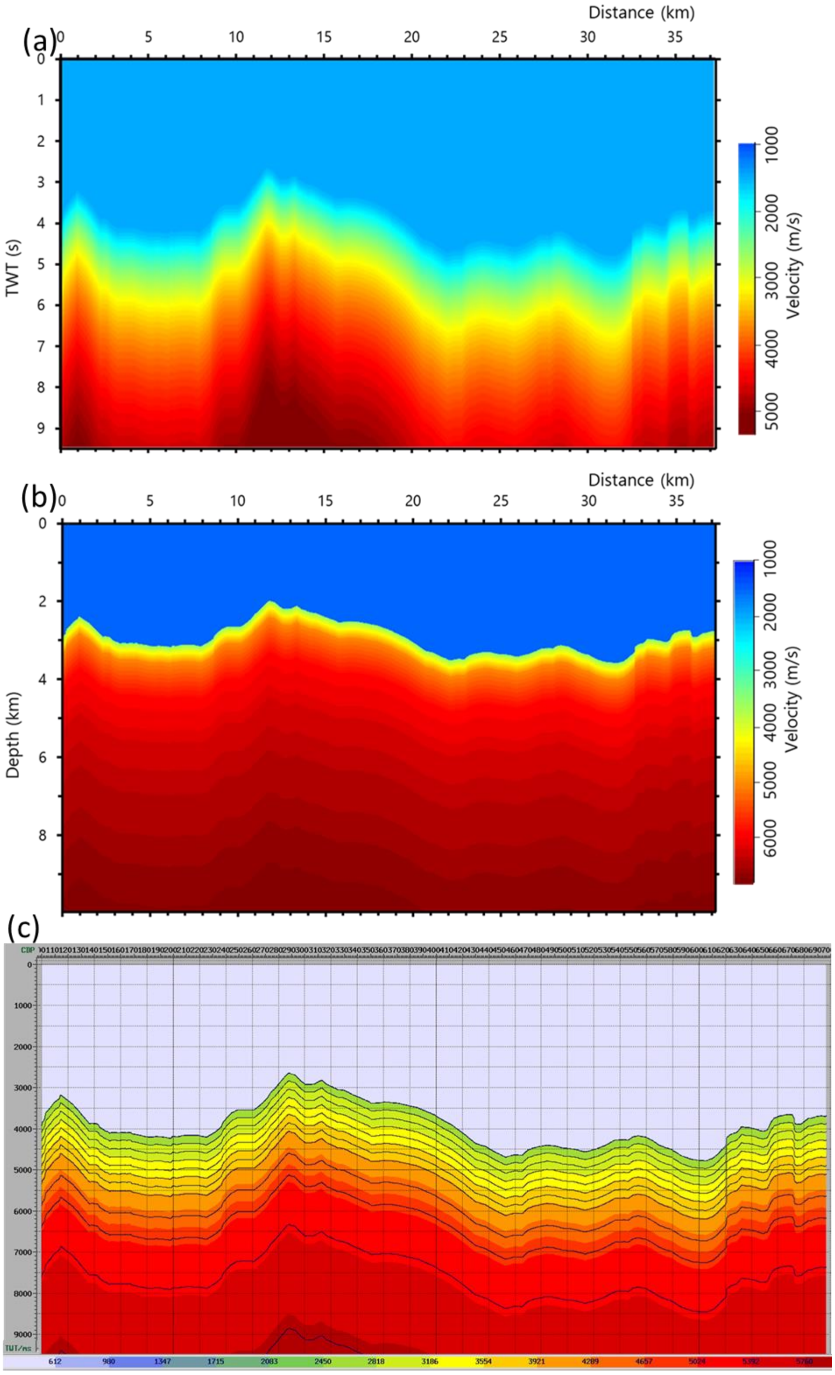

Figure 4.12: v_{rms} – time model (a), built from v_{int} – time model plot Figure 4.8b of Peirce et al., (2019,) used for NMO correction prior to stacking. (b) Dix converted v_{int} – depth model built from the v_{int} – time plot. (c) Second V_{int} - time model for cascaded FD migration. These models are built in python owing to the difficulty of running velocity analysis from the 2D dataset due to masking of P-waves by sideswipes, diffraction noise and other low velocities associated with it. The layering is not indicative of the geology, but the assumptions made prior to building the velocity model and this was smoothed out before use in imaging. The models are displayed in Madagascar and Claritas.

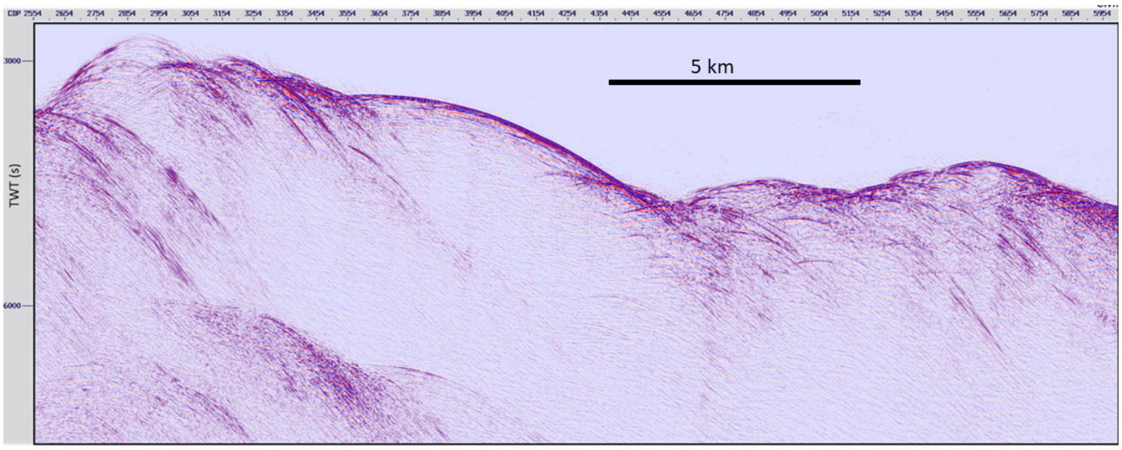

Figure 4.13: CMP stack section of line 1320 after velocity filtering of the shot-channel gathers and NMO correction of the resulting CMP gather with built v_{rms} - time model. Note that velocity filtering attenuates most of the left dipping diffraction tail when compared to the right dipping tails in Figure 4.6b.

4.8 Post-stack imaging:

4.8.1 Cascaded migration:

As outlined in Table 4.1, the time imaging sequence applied to the data set is a two-step cascaded migration approach. Cascaded migration method is an imaging routine employing more than one imaging processes, typically with some intervening process, to improve the seismic image in the time domain (Rotham et al., 1985; Larner and Beasley, 1987). The sum of the velocities used in each step of the cascaded migration process should add up to the square of the desired velocity at each travel-time. As typically the first migration is carried out with a water velocity to suppress water-borne diffractions (see below), the second migration will be with a very low velocity (close to zero) in the water column but increasing sharply deeper to values close to the overall desired velocity. This could be using same or different migration algorithms, but from a processing efficiency standpoint it makes sense to use time invariant Stolt migration for the first step followed by time and space variable velocities for the second, residual, migration. The migration algorithms used is dependent of the imaging challenge to be addressed such as under-migration. Cascaded migration also aims to combine the advantages of one migration algorithm (like speed of imaging and accuracy) with that of another (like the capability to use laterally varying velocities).

The second "residual migration" in a cascaded migration approach implements the inherent residual nature of imaging velocities in post-stack (and pre-stack although different in application and not used here) migration equations (Larner and Beasley, 1987; Stolt, 1996; Sava, 2003) to effect velocity update to an under-migrated section. Thus, cascaded migration involves remigration of an initially under-migrated data using the residual (V_{resd}) of the full velocity (V_{full}) in relation to the incorrect velocity (V_{init}) initially employed, as in the equation $V_{resd}^2 = V_{full}^2 - V_{init}^2$.

In the post-stack domain, Rothman et al., (1985) showed the initial velocity for cascaded migration could be a variable or constant velocity. However, they suggested a constant or mildly varying velocity as the initial velocity of a two-step cascaded migration is wave theoretically valid and preferred. Here the constant velocity (1480m/s) approach was used as the prime purpose was to collapse and apply de-spiking to possible residual sideswipes observed on imaged data after velocity filtering. The first migration using a constant water velocity (1480 m/s or similar) does not significantly move real sub-surface reflections but does help suppress diffractions from the rough seafloor. These diffractions having only travelled within the water column, are marked by hyperbolae characterized by water velocity, so water velocity migration collapsed them to small points that can be suppressed using a variety of techniques, particular on the basis of their amplitude.

We initially applied the above method to stacked data: the $1480\ m/s\ fk$ migration (Stolt, 1978) collapsing sideswipe diffraction hyperbola to noise bursts which can be suppressed on the basis of their amplitude: we experimented with a variety of suppression methods before settling on the use of a de-spiking algorithm. The de-spiking parameters are:

- LWINDOW: This determines the long running average sliding window for amplitude anomalies and a reference for the short-window sliding average comparison, value employed is 200 ms.
- SWINDOW: This is the short sliding average amplitude window and the window which aims to remove the spike, value of 24 ms employed was the average size of the spikes in the data. Multiples of this removes longer spikes
- FACTOR: This sets the detection window after comparing two products (Factor and LWINDOW) with SWINDOW and if shorter than SWINDOW a spike is detected. 4.0 value used.
- INTERPLEN (8 ms): Length of spike sample to be replaced if up to TAPERLEN ms long by interpolation from the spike region.
- ZEROLEN (16 ms): Length of data in ms zeroed in the centred spike.
- TAPERLEN (10 ms): Linear tapering to the zeroed window extending it.
- TSTART (300 ms): Data above time which is not muted de-spiking process.
- NTIMES (1): Number of times to repeat de-spiking on a trace

TAPERLEN (20 ms): cosine tapering applied (optional) to any zeromute applied besides de-spiking.

As this set the amplitudes in small windows around the largest amplitude anomalies to zero, we were concerned that it might both lead to the irretrievable suppression of real reflections, and to artefacts related to the abrupt amplitude cut-off. As a result, we explored carrying out the first migration before stack by working in offset ranges of which results will be presented in a paper. The imaging steps applied to the data in

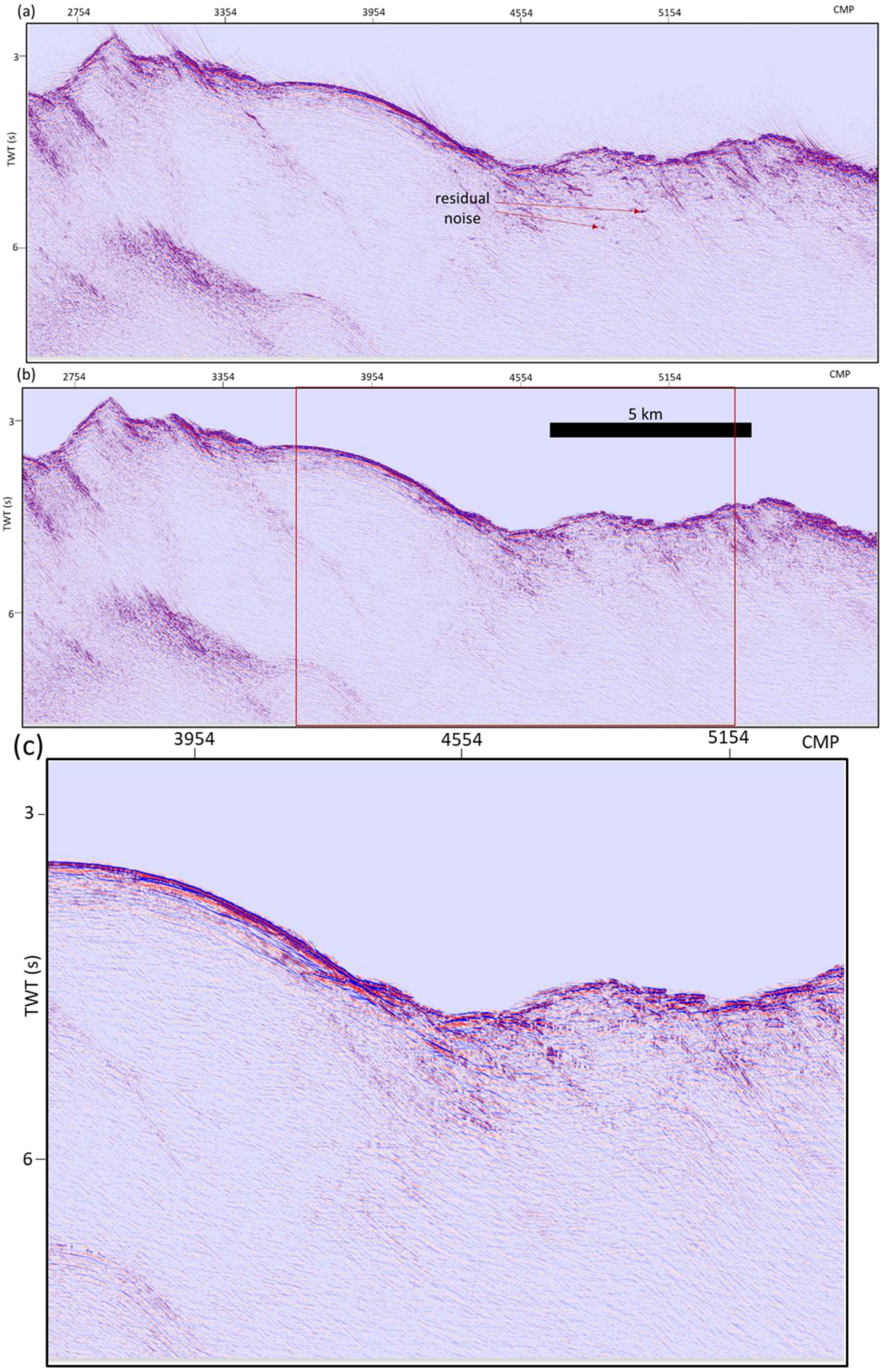

Figure 4.14: $1480\,m/s$ Stolt migrated sections of line 6a.26 (25m shot interval) showing the impact of de-spiking a Stolt imaged data to suppress residual sideswipes after velocity filtering in the $\tau - p$ domain. (a) Section without de-spiking and (b) Section with de-spiking applied. Note the improvement to the image of the seafloor and the removal of noise bursts resulting from diffraction-collapse. (c) Enlarged view of red square in (b)

the time domain include $1480\ m/s$ (used to ensure the residual velocity of water resulting after is not zero) Stolt migration, de-spiking of the Stolt migrated data, and finite difference cascaded time migration. Thus, the cascaded migration approach enabled further muting of possible residual sideswipe reflections not attenuated in the $\tau - p$ process, prior to full migration. The de-spiking process is an important step in muting out bursts in the Stolt migrated data attributable to water velocity diffractions, as such reflections smears out on fully imaged sections (Figure 4.6c). Figure 4.14 shows Stolt migrated sections without (Figure 4.14a) and with de-spiking (Figure

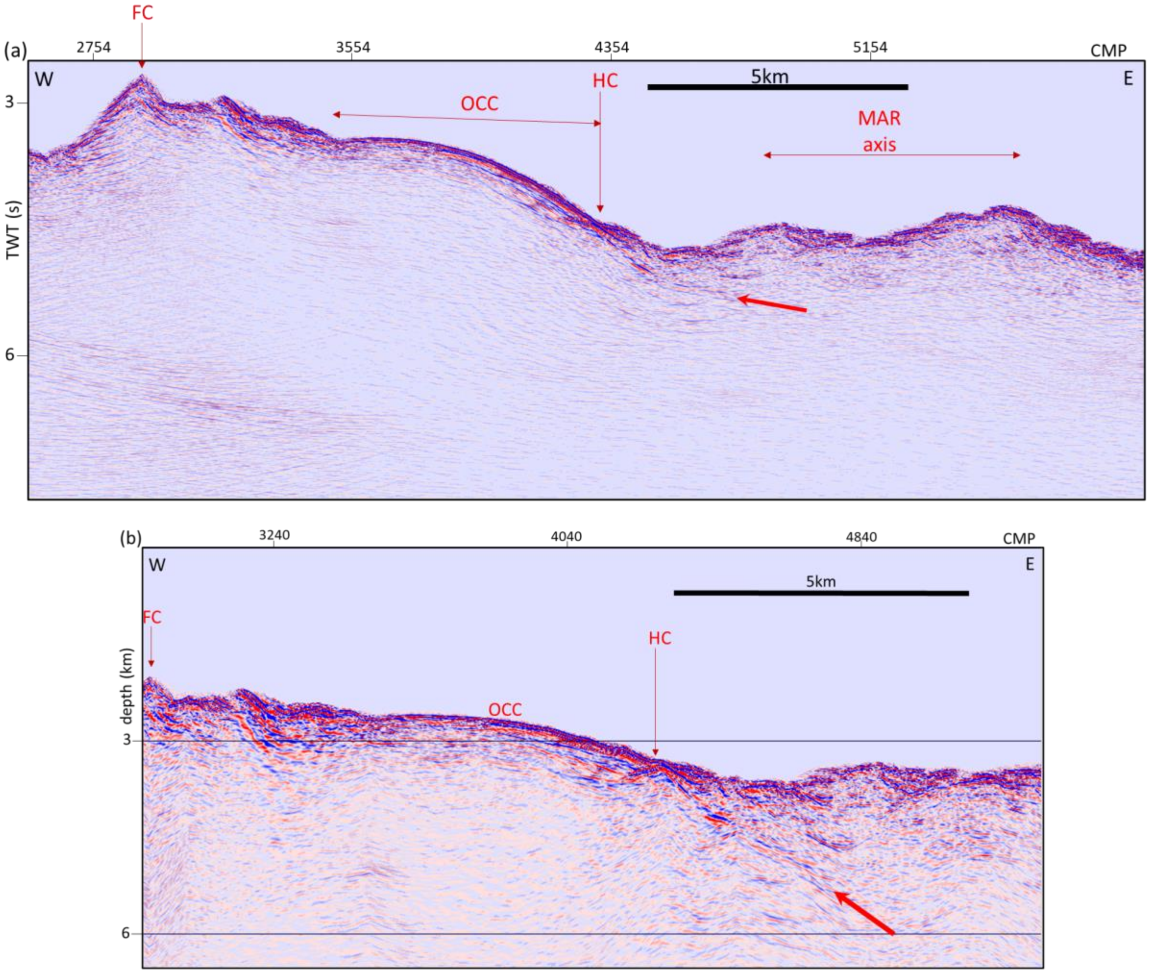

Figure 4.15: CMP imaged time and depth converted sections of line 6a.25. (a) The FD migrated time section image with the cascaded migration process applying $1480\, m/s$ *Stolt de-spike to attenuate residual sideswipe noise. In this section the red arrow points to a strong reflection from the footwall of the detachment fault. FC=footwall cut-off, HC=hanging wall cut-off, between the FC and HC is the chaotic zone. (b) Depth converted section of (a).*

4.14b) having observable pockets of data removed from the de-spiked section. However, this is a compromise made ensuring imaged sections are mostly related to reflections associated to mid-ocean rocks. To the de-spiked Stolt migrated data, finite difference (FD) migration (Figure 4.15a) was applied as the cascade of the time imaging process using the cascaded V_{int} model, and depth converted giving a preview of what the OCC structure could be at depth (Figure 4.15b). These sections show the applied processes up until now preserved mid-ocean crust related reflections while attenuating sideswipes and possible low velocity reflections. Therefore, the next imaging step applied was a depth migration process using Kirchhoff post-stack migration implemented with the full V_{int} - depth model.

4.8.2 Depth migration:

Depth migration offers considerable advantages over time migration. First the output is in depth, allowing the true geometry of the geological structures to be revealed. Second, depth migration accounts for the ray path bending / wavefront distortion that results according to Snell's Law as the seismic energy propagates to depth, and a particular issue at a hard seafloor where velocities jump from 1500 m/s to values in excess of 4000 m/s. But unlike time migration, depth migration cannot be cascaded. As a result, the post-stack depth migration procedure involved the $1480\ m/s$ modelling (de-migration) of the de-spiked Stolt migrated data in Madagascar to restore the data to an unmigrated state prior to the application of the depth imaging flow. The modelled (de-migrated data, Figure 4.16) thus are effectively the same as the unmigrated data (Figure 4.13), apart from the suppression of the side-coming reflection hyperbolae. The depth imaging process of 1320 data used the full modelled depth converted V_{int} (Figure 4.12b), a migration range of 6500 m, 5 m depth sampling

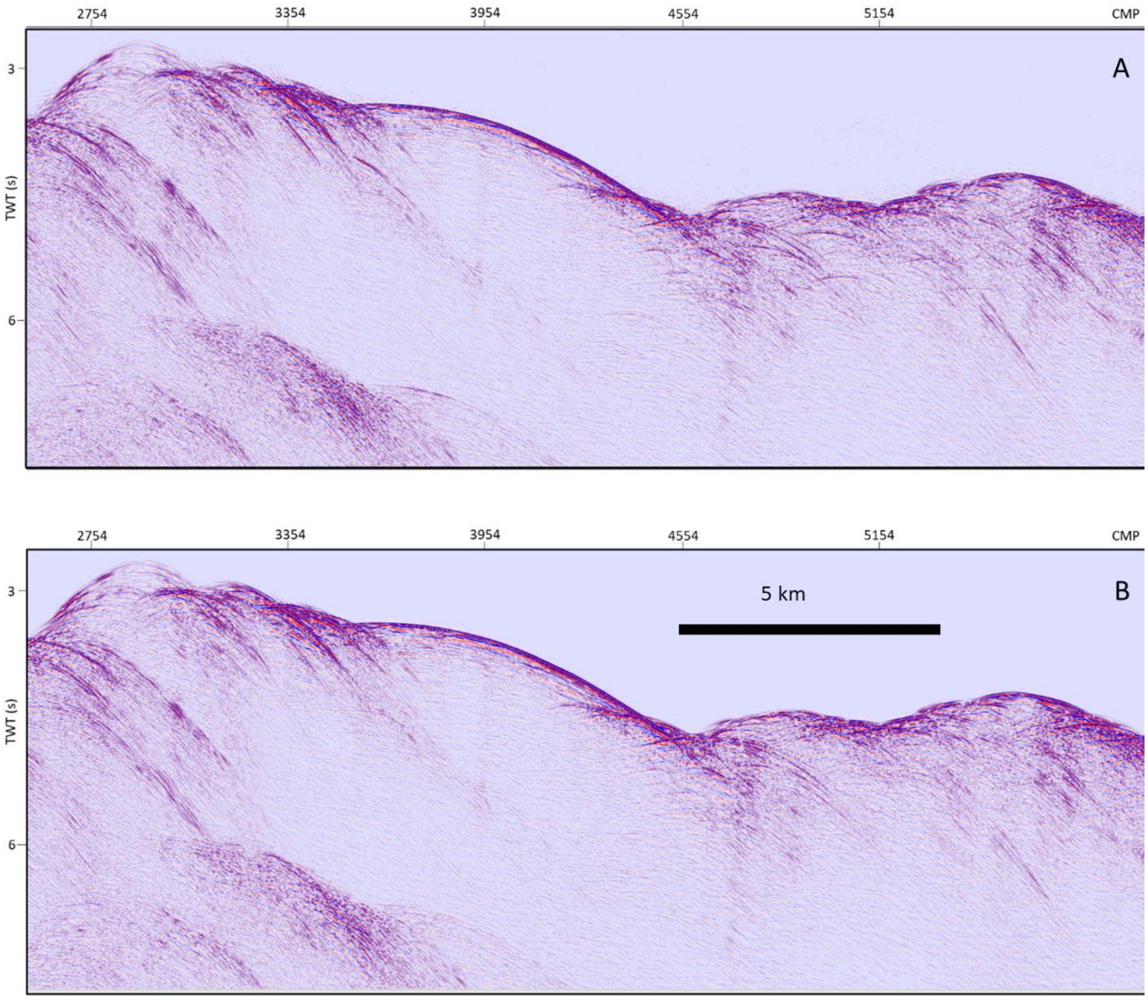

Figure 4.16: A: stack image from Figure 4.13, showing sideswipe diffraction hyperbolae from the rough seafloor. B: De-migrated data section resulting from the $1480\,m/s$ *Stolt de-spiked data. Residual noises prior in the original CMP data are better attenuated for depth imaging procedure implementation.*

interval with a 2001 sampling point and 10° migration angle from the vertical direction for the 25 m shot spaced line. Figure 4.17 shows the resulting 2D depth imaged sections of line 6a.26 for the original and interpolated geometries with the fault plane sub-ocean bottom of the OCC clearly imaged.

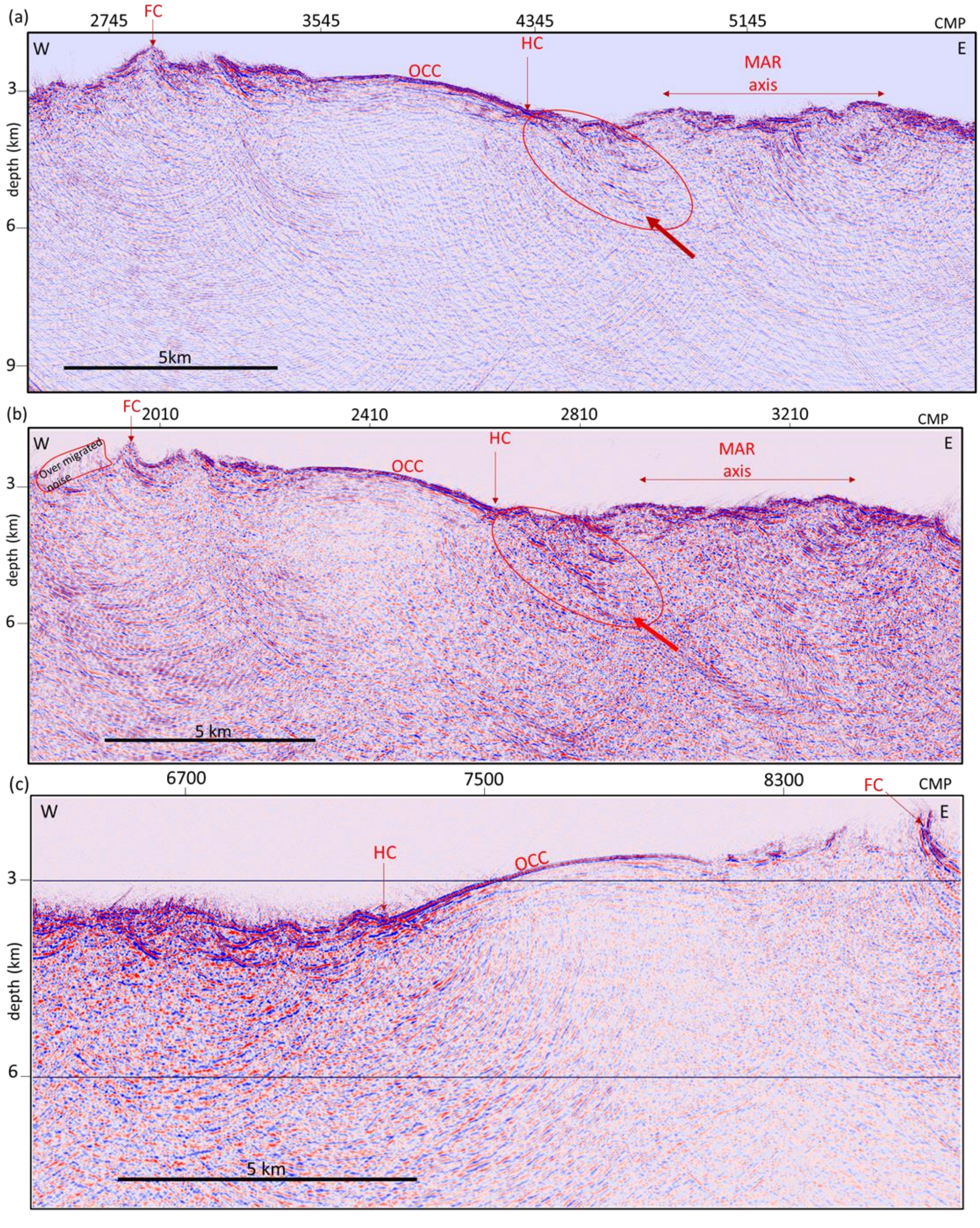

Figure 4.17: Post-stack Kirchhoff migrated (ImageK2D) sections of lines 6a.26 and 6.6. (a) Depth migration of 6a.26 with original acquisition geometry; the red arrow pointing to the footwall sub-bottom. (b) Depth section of line 6a.26 interpolated data. The red sphere highlights the difference and improvement in (b) when compared to (a), also the footwall reflection is more continuous. However, the interpolated data has more migration noise. (c) Line 6.6 (50m shot spacing) depth image with more migration noise. Key features of the imaging are visible in all sections however sections from 25m shot spacing has better resolution.

4.9 Results and discussions:

4.9.1 OCC footwall subseafloor:

The key outcome of the processing sequence applied is the imaged footwall of the detachment fault at the 1320 MAR, in time and depth. The depth migrated section (Figure 4.17) outlines the fault plane extending up to 5000m subseafloor, and other features of the detachment fault regarding its current state and formation. For instance, it shows the likelihood of a hydration system for the OCC via the fault in the chaotic

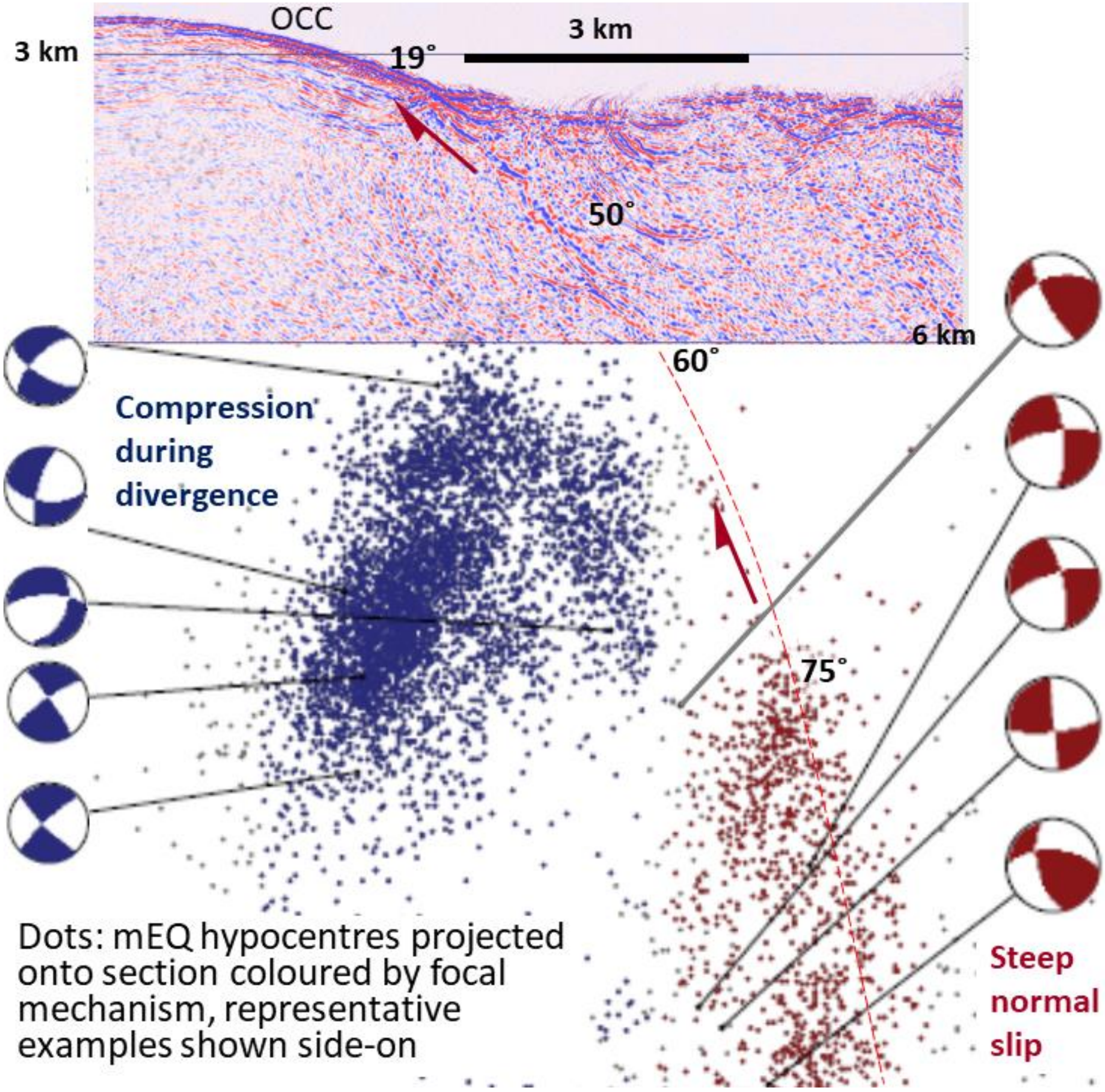
OCC
3 km
3 km
19°
50°
6 km
60°
Compression
during
divergence
75°
Dots: mEQ hypocentres projected onto section coloured by focal mechanism, representative examples shown side-on
Steep
normal
slip

Figure 4.18: Earthquake (EQ) plot from the 1320 MAR showing calculated hypocentres of the microseismicity from the detachment fault. The dash line is the elastic-plastic model deviation of the footwall subsurface. Compared to Figure 4.17 the imaged footwall conforms to this calculation by Parnell-Turner et al., 2017.

section eastward (Figure 4.17b) of the breakaway point observed by MacLeod et al., (2009); giving rise to more questions on the evolution of the 1320 OCC hydration fault system. The interpolated depth section (Figure 4.17b) shows a possible incipient rafted block (poorly resolved in Figure 4.17a) on the footwall (OCC) from the hanging-wall. This possibility is explored further in Chapter 5. However, migration smiles still existed in the sections showing that the processing sequence applied did not attenuate fully all the slow traveling events. However, it enabled imaging the detachment fault of the 1320 OCC in the depth domain.

The imaged section when compared to earthquake data and calculations (Parnell-Turner et al., 2017) from the 1320 detachment fault (Figure 4.18) validates the imaged footwall as a real geological feature falling withing the detachment fault seismic moments. It also shows a convex-up fault plane in line with the footwall flexing of large offset detachment faults as shown by Reston (2020).

4.9.2 Impact of shot spacing:

Imaging the two lines with different shot spacing (25m and 50m shot spacing) informs seismic reflection data acquisition from a hard seafloor environ may be better engaged with smaller shot interval. Comparing Figure 4.17a, and 4.17c shows better resolution of sub-bottom footwall geometry for the 25m shot interval data unlike the 50m.

The stack sections (Figure 4.6a and 4.6b) show the seismic noises present in the dataset are not attenuated by stacking (Larner et al., 1983; Calvert, 1997) either with water or near geological velocity, therefore, sorted-in in the CMP domain; thus, resulting to long diffraction tails in the section. Applying velocity filtering ensures these diffraction tails are attenuated while $1480\ m/s$ Stolt migration de-spiking removed most residuals prior to imaging (in time and depth). To further improve the resolution of imaged sections shot interval reduction and group spacing increment via interpolation was implemented improving the resolution of imaged sections (Figure 4.17b). Such resolution improvement was for the 25m interval shot data but not the 50m. Therefore, data interpolation was not continued for the 50m shot interval data. Interpolation however suggests the need to properly address spatially aliased frequencies during data acquisition and processing.

4.10 Conclusions:

One of the key questions about oceanic core complexes concerns the geometry of the controlling oceanic detachment fault (Mitchell et al., 1998). Early ideas that the fault was actually the basal detachment of a slope failure (Cann et al., 1997) had already been challenged by the plutonic and mantle nature of the footwall, and paleomagnetic data suggested that the footwall had rotated > 45˚ about an axis-parallel horizontal axis and thus that fault should root at least this angle. The distribution of earthquakes (Parnell-Turner et al., 2017) suggested that the fault was steep at depth, but as elsewhere (DeMartin et al, 2008) the exact geometry was not known.

A processing sequence which included wavelet shaping, linear slant-stack processing, $1480\, m/s$ Stolt de-spiking aimed at suppressing the seismic noises in the 1320 data from the MAR, was applied prior to imaging (time and depth). The resulting depth image of the 1320 OCC footwall subsurface (~9km deep) reveals a reflection that at the seafloor is co-linear with and aligned with the top of the corrugated surface, and which steepens smoothly to > 45˚ as it approaches the steeply dipping band of normal fault earthquakes identified by Parnell-Turner et al. (2017). This result will be discussed further in chapter 5 in the context of other images of this and other detachment faults.

Chapter 5 Seismic Interpretation:

5.1 Introduction:

The preceding chapters have introduced the core motives driving this research: the study of the development, geometry and structure of the detachment faults that produce and control oceanic core complexes (OCC) at slow spreading ridges using multi-channel seismic (MCS) data; the challenge of noise in that data resulting from the hard rough, rugged and 3D seafloor; and how we have approached attenuating such noise to image the detachment fault. This chapter presents the results of processing of three lines parallel to the spreading direction (Figure 5.1 right) in the vicinity of the 1320 and 1330 OCC and one parallel to the spreading axis (crossing both the 1320 and 1330 OCC) and interprets the images within the context of the known geology of the study area, focusing on the structure and evolution of the oceanic core complexes.

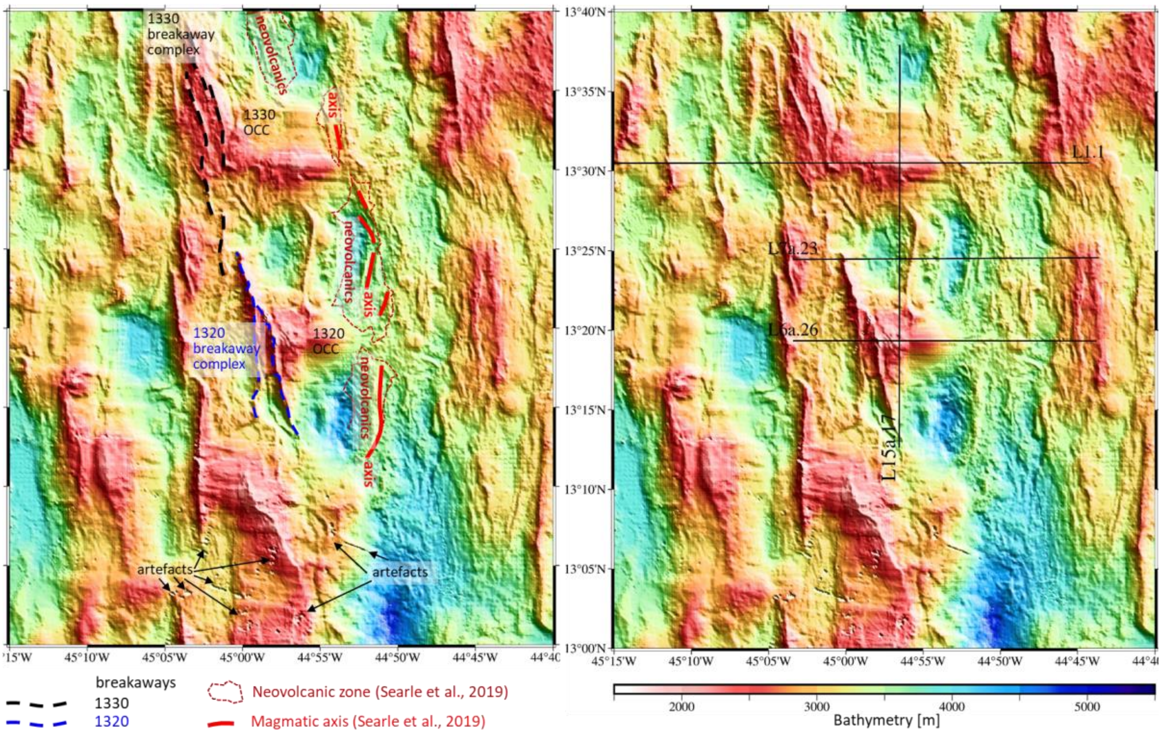
1330
breakaway
complex
neovolcanics
axis
1330
OCC
neovolcanics
axis
axis
1320
breakaway
complex
1320
OCC
neovolcanics
axis
artefacts
artefacts
13°40'N
13°35'N
13°30'N
13°25'N
13°20'N
13°15'N
13°10'N
13°05'N
13°00'N
'15'W
45°10'W
45°05'W
45°00'W
44°55'W
44°50'W
44°45'W
44°4C
breakaways
1330
1320
Neovolcanic zone (Searle et al., 2019)
Magmatic axis (Searle et al., 2019)
L1.1
L7a.23
L6a.26
L15a.17
45°15'W
45°10'W
45°05'W
45°00'W
44°55'W
44°50'W
44°45'W
44°4(
2000
3000
4000
5000
Bathymetry [m]

Figure 5.1: Bathymetric map of the study area using data collected during JC132. Location of the lines discussed are shown.

5.2 Prior knowledge of the study area:

The region of oceanic core complexes between 13˚00 and 13˚40N has been extensively investigated as outlined in Chapter 2. Here we revisit some of the key

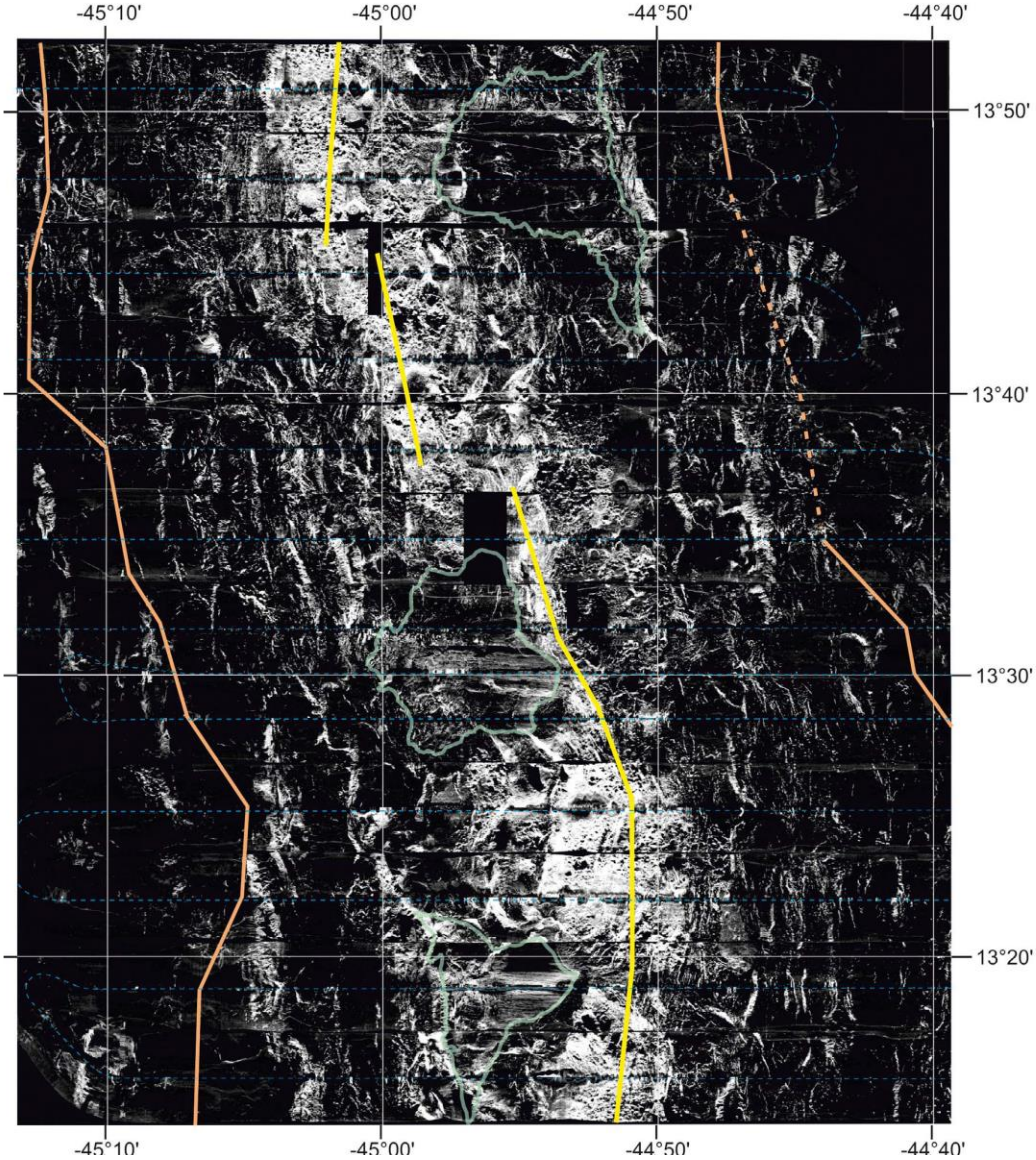

Figure 5.2: TOBI side-scan sonar mosaic of the study area (Mallows and Searle, 2012). Dashed blue lines show the TOBI tracks spaced 6 km apart. Either side of each track the acoustic illumination ("insonification") is outwards from the track and so alternates every 3 km between northward (north of the track) and southward (S of the track). OCCs are picked out in pale green, the approximate position of the spreading axis in yellow and in pale orange-pink is magnetic anomaly 2. Bright regions have high acoustic back-scatter and are a combination of hard, rough, or steep and give an idea of both the age of the seafloor (hardness, roughness: as the seafloor ages, it is buried under soft sediment reducing its backscatter) and its geological fabric (e.g., volcanics, corrugated surface).

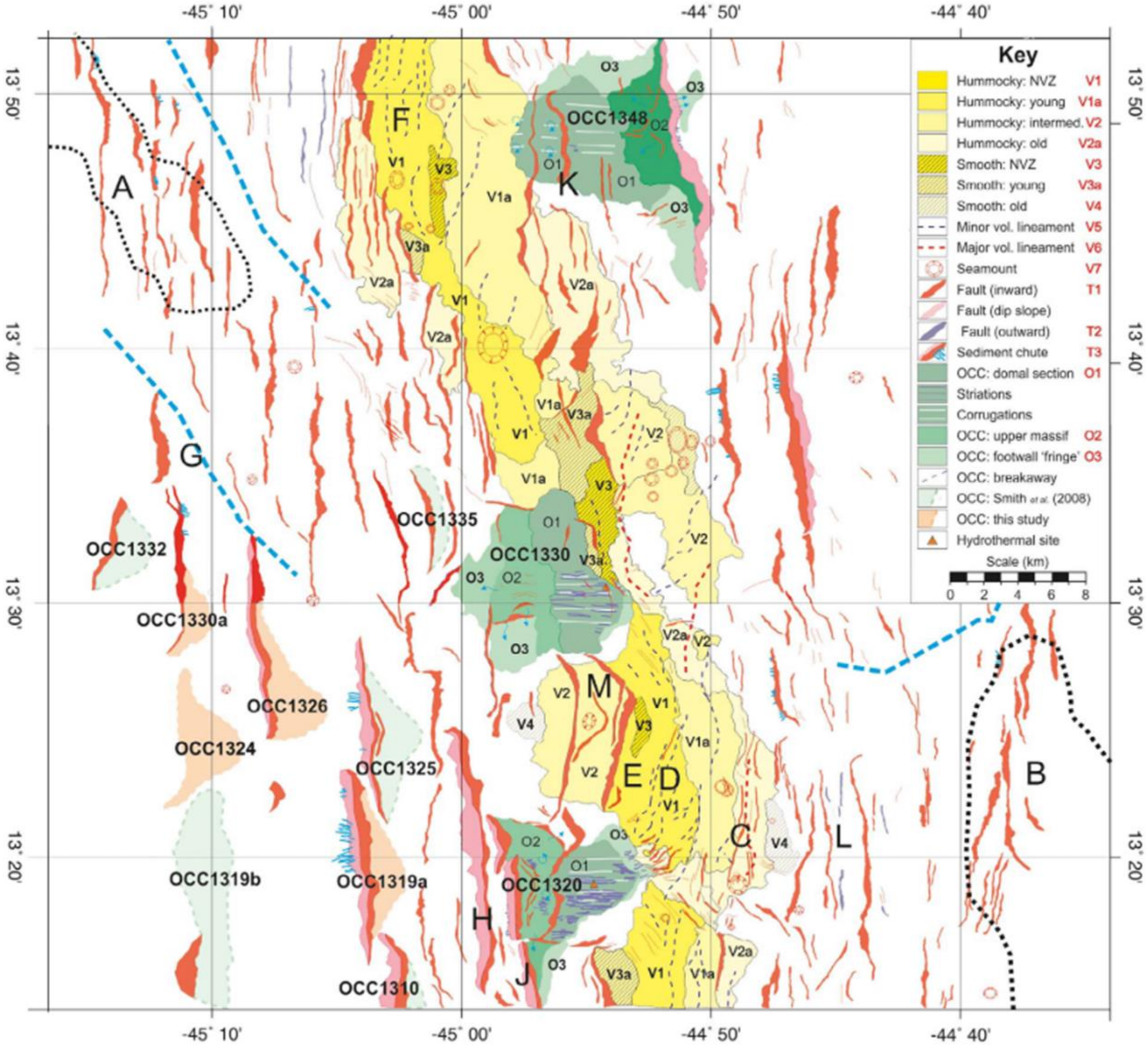
-45° 10'
-45° 00'
-44° 50'
-44° 40'
13° 50'
13° 40'
13° 30'
13° 20'
Key
Hummocky: NVZ V1
Hummocky: young V1a
Hummocky: intermed. V2
Hummocky: old V2a
Smooth: NVZ V3
Smooth: young V3a
Smooth: old V4
Minor vol. lineament V5
Major vol. lineament V6
Seamount V7
Fault (inward) T1
Fault (dip slope)
Fault (outward) T2
Sediment chute T3
OCC: domal section O1
Striations
Corrugations
OCC: upper massif O2
OCC: footwall 'fringe' O3
OCC: breakaway
OCC: Smith et al. (2008)
OCC: this study
Hydrothermal site
Scale (km)
0 2 4 6 8
A
B
C
D
E
F
G
H
J
K
L
M
OCC1348
OCC1335
OCC1332
OCC1330
OCC1330a
OCC1326
OCC1324
OCC1325
OCC1319b
OCC1319a
OCC1320
OCC1310
O1
O2
O3
V1
V1a
V2
V2a
V3
V3a
V4

Figure 5.3: Seafloor fabrics (Mallows and Searle, 2012) inferred from the side-scan sonar survey, interpreted in Figure 5.4. The interpretations and relative ages will aid interpretation of the seismic sections.

results to set the scene for the interpretation of the profiles presented here and in particular, the interpretation of the seafloor imagery (Figure 5.2) by Mallows and Searle (2012).

The TOBI deep-tow side-scan sonar survey discussed by Mallows and Searle (2012) images a band of high backscatter interpreted as rough, young volcanic seafloor. Mallows and Searle further divide this into a neo-volcanic zone (NVZ) and slightly older volcanic seafloor (Figure 5.3), describing a variety of other back-scatter fabrics that can be used for geological interpretation and also tentatively identify a

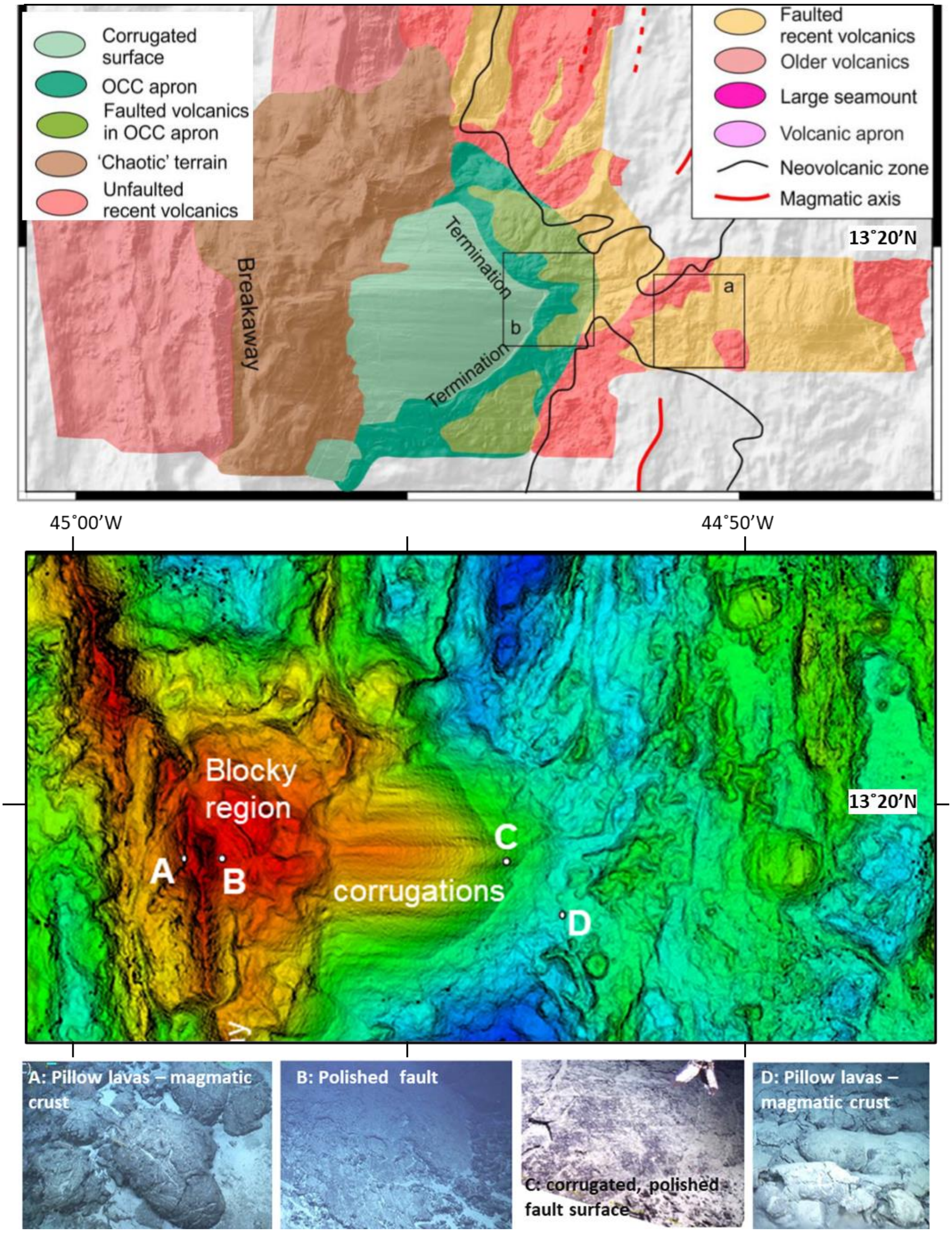
Corrugated surface
OCC apron
Faulted volcanics in OCC apron
'Chaotic' terrain
Unfaulted recent volcanics
Faulted recent volcanics
Older volcanics
Large seamount
Volcanic apron
Neovolcanic zone
Magmatic axis
Breakaway
Termination
Termination
a
b
13˚20'N
45˚00'W
44˚50'W
Blocky region
corrugations
A
B
C
D
13˚20'N
A: Pillow lavas – magmatic crust
B: Polished fault
C: corrugated, polished fault surface
D: Pillow lavas – magmatic crust

Figure 5.4: Comparison between the interpreted seafloor geology in the vicinity of the 1320 OCC (seafloor geology map: Mallows and Searle, 2012; seafloor photographs - Escartin et al., 2017) and the detailed bathymetric image. Location of Line 6.26 shown.

spreading axis. The NVZ narrows as it passes the toe of both the 1320 and the particularly the 1330 OCC supporting the idea that OCC formation is accompanied by less magmatism and that a substantial proportion of the plate divergence is by faulting and OCC exhumation. This theme is revisited when discussing the structure and evolution of the 1330 OCC.

5.3 Line 6.26 and the structure of the 1320 OCC

Line 6-26 runs EW along the axis of the 1320 OCC. As such from previous work (Mallows and Searle, 2012) we would anticipate it crossing a variety of different types of seafloors (Figure 5.4), all important geological components of the slow-spreading system (Figure 5.4). Line 6.26 runs from older volcanics in the west, across the breakaway of the 1320 oceanic detachment fault, over the so-called chaotic terrain of Mallows and Searle (2012), which is labelled as a “blocky region” in Figure 5.4 and elsewhere, over the corrugated surface, running ~parallel to the corrugations, across the "apron” (Escartin et al., 2017) and faulted volcanics within the apron, and across faulted recent volcanics. Searle et al. (2019) do not identify a “*magmatic axis”* at this latitude, but Mallows and Searle (2012) do identify a spreading axis and a band of unfaulted recent volcanics trending ~30˚ east of north and presumably erupted from a recent magmatic axis.

As described in detail in Chapter 4, the processing of line 6.26 has involved several steps (Figure 5.5):

- careful velocity filtering and deconvolution in the tau-p domain,
- downward continuation through water velocity Stolt migration to collapse diffractive energy that travelled at water velocity and so has passed

exclusively through water (where these lie beneath the seafloor, the energy has come from the side) to small energy bursts,

- the suppression of those bursts with de-spiking
- de-migration of the section, followed by Kirchhoff post-stack depth migration with the full velocity field to reveal the true geometry of the subsurface in depth (Figure 5.5).

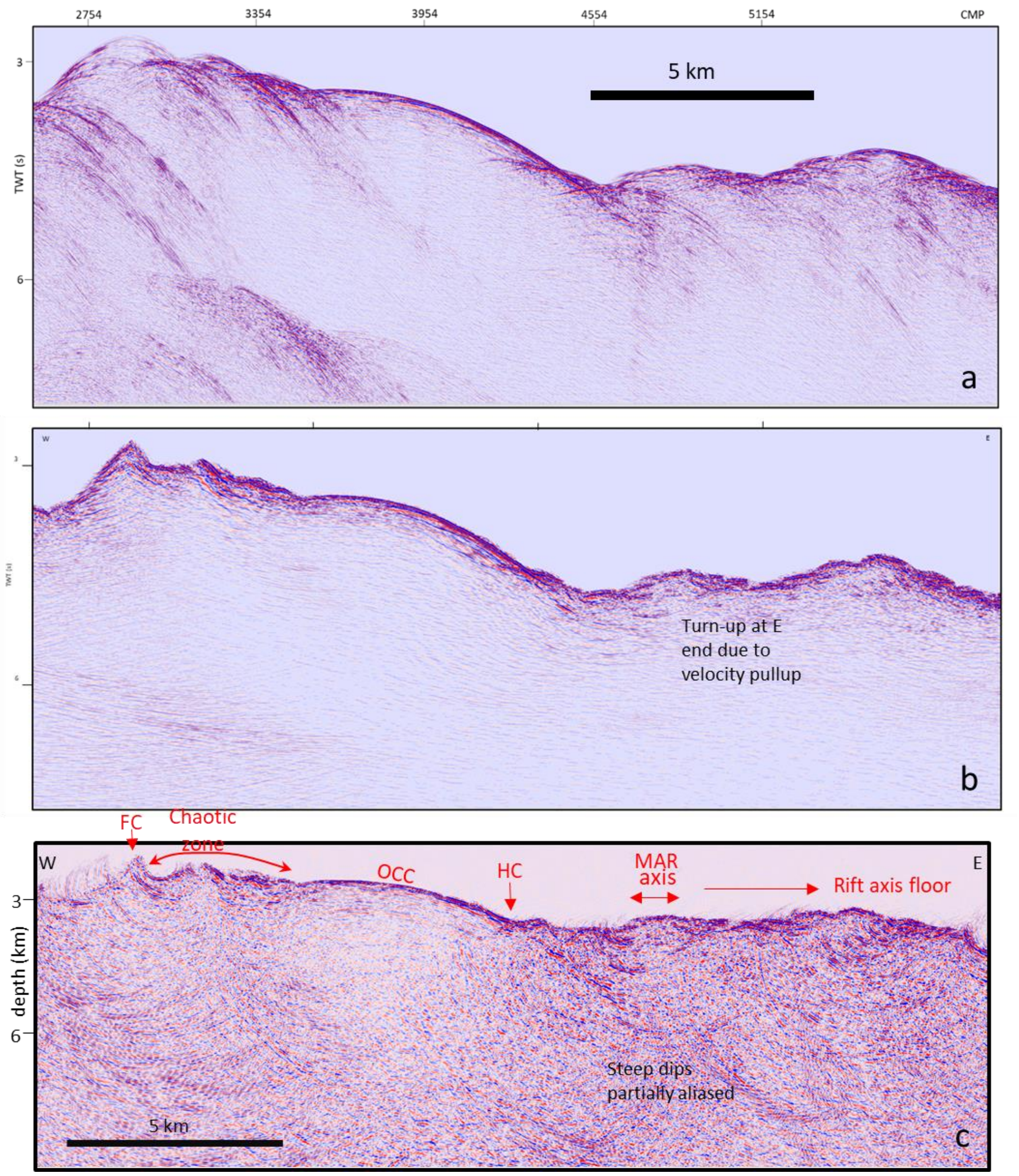

Figure 5.5: CMP stack, time and depth migrated section of line L6a.26. (a) Modelled CMP stack after de-spiking the $1480\,m/s$ Stolt migrated data and de-migration. (b) Kirchhoff migrated section of the line of the second step migration applied. (c) Interpolated geometry depth migrated section.

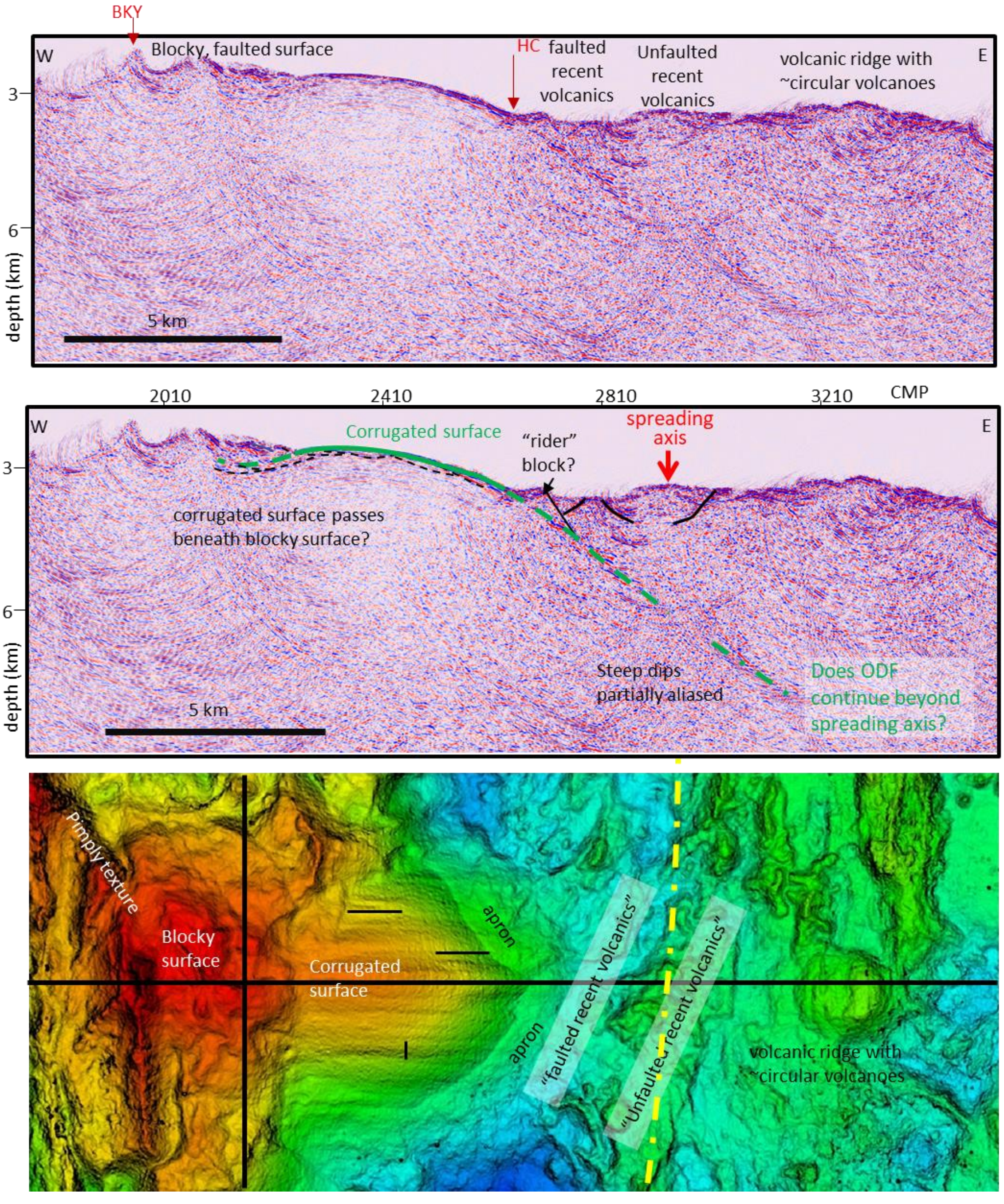

Figure 5.6: Interpretation of the depth section along the axis of the 1320 OCC. Thin black lines show the dimensions of ridges/scoops along and across the corrugations discussed in the text and in Chapter 6. HC is the hanging wall cut-off, where the oceanic detachment fault dips below the seafloor. The detachment steepens smoothly downwards, reaching a dip of ~ 45 at a depth of 6 km below the sea surface, that is ~ 3 km below the seafloor where the image worsens beneath the spreading axis: a possible continuation is shown. The continuation to depth and implications of the detachment geometry is discussed further in Chapter 6. Yellow line on the map is the spreading axis of Mallows and Searle (2012).

The depth image can be usefully compared with the seafloor geology and bathymetry (Figure 5.6). West of the breakaway (BKY) the west-dipping seafloor has a pimply texture, interpreted as volcanics such as pillow lavas and lava tubes. East of the breakaway the blocky seafloor (Mallows and Searle's chaotic zone) is interpreted as dikes and other intrusive mafic rocks. The eastern edge of the blocky surface is higher than the adjoining corrugated surface, which even partly appears to continue beneath the blocky region. This is not an obvious artefact and may indicate the complex nature of faulting: there is not a single slip surface in the chaotic region (or where corrugated), but rather a complex zone of faulting. One possibility is that the blocky zone consists of rider blocks of the upper crust that have been rafted up and out of the median valley by the detachment, consistent with the ideas of Reston and Ranero (2011) and Choi and Buck (2012) that the formation or not of rafted blocks depends on the frictional properties of the main fault so that the change from a footwall of rafted blocks to the unroofed slip surface might represent a change from high friction, anisotropic lavas and dikes to lower friction serpentinites. More detail of the blocky surface will be revealed by the N-S profile 15.17 discussed below.

The corrugated surface is also thought to be the expression of a fault zone rather than a single surface: Parnell-Turner and others (2018) suggest that the corrugated surface is the surface expression of an anastomosing fault zone in which various fault strands, formed by strain weakening but abandoned during subsequent strain hardening, separate low-strain lenses. In this model, the spacing of the corrugations normal to the slip direction might represent lateral dimensions of the lenses and the length of individual corrugations, identifiable as ridges and elongated scoops, the length of the lenses in the transport direction, and the height of the corrugations the thickness of the lenses. The lenses that can be tentatively identified on the depth

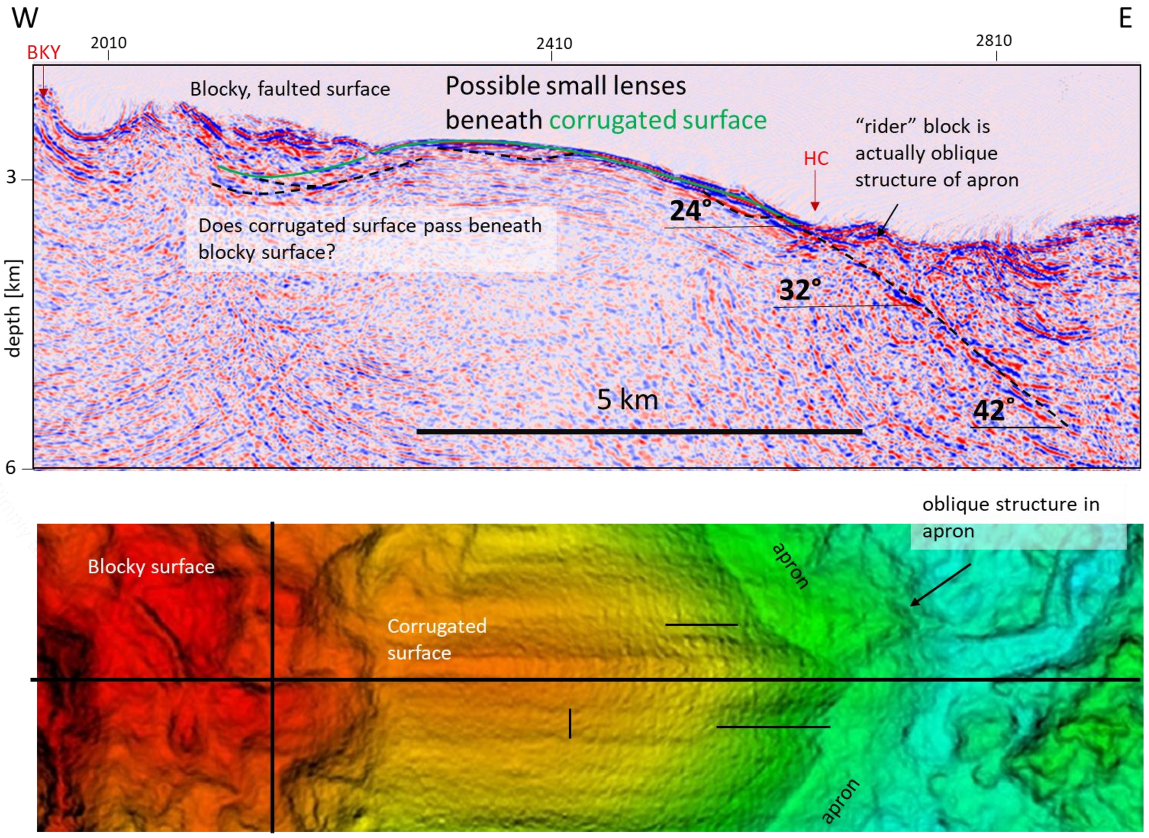
W
E
BKY
2010
2410
2810
3
6
depth [km]
Blocky, faulted surface
Possible small lenses
beneath corrugated surface
"rider" block is
actually oblique
structure of apron
HC
24°
32°
42°
Does corrugated surface pass beneath
blocky surface?
5 km
oblique structure in
apron
Blocky surface
Corrugated
surface
apron
apron

Figure 5.7: Detail of the depth image and of the corresponding bathymetry highlighting the oblique ridge within the apron giving rise to the appearance of an incipient rider block and the details of possible anastomosing patterns in the 1320 detachment of comparable size to the ridge and scoop highlighted in the bathymetry by the and horizontal (E-W along the corrugations) black lines. Also shown is a vertical line (N-S, across the corrugations), showing the typical dimensions of the larger corrugations.

migration of Line 6.26 (Figures 5.6 and 5.7) show length scale that are similar to the corrugation parallel ridges and scoops highlighted in the bathymetry of Figure 5.7., evidence for such lenses can be seen on other lines and can be compared to the length of ridges and scoops (thin black horizontal lines) and the width of the corrugations (vertical line) on the bathymetric image.

The convex-up shape of the corrugated surface is very clear and can be traced into the sub-surface where it passes beneath the hanging wall, represented initially by a strongly deformed and broken-up "apron" of volcanics. Within the apron is an apparent “rider block”, bounded by a steep west-dipping fault rooting on the 1320 detachment. Such rider blocks are a feature of one type of rolling hinge model in which the flexing main fault rotates to sufficiently low angle to lock up, causing a shortcut fault to cut up through the hanging wall from the still active detachment root zone, transferring a slice of the hanging wall to the footwall as a rider or rafted block. However, such blocks are not present on the 1320 OCC (except possible in the upper crustal blocky domain), suggesting that the imaged block is a 3D artefact. The apparent continuation of the west-dipping top surface of the rider block through the east-dipping main detachment supports this suggestion and inspection of the bathymetry shows an oblique ridge within the apron at this location: the fault bounding the ridge block is an oblique coming reflection from apron. Instead of locking up to produce such a rider block, it appears that the detachment approaches the seafloor as a still active fault, as discussed further in Chapter 6.

The “apron” of the 1320 OCC is another component of the detachment fault still speculative in nature, as to its formative process, having Escartin et al., (2017) suggesting this occurred as a holding centre for shed rubbles on the hanging wall. This implies there should be a distinct seafloor rubble boundary in the vicinity of the hanging wall-cutoff. However, depth imaging (Figure 5.6) shows the hanging wall as a single unit having east (synthetic) and west (antithetic) dipping minor faults cutting the seafloor with the apron as not having a distinguishing amplitude suggestive of shed materials. Therefore, unroofing of the OCC appears as a complex process in this zone in which the OCC develops as a single unit which terminates in the volcanic axis of the MAR as suggested by MacLeod et al., (2009).

5.4 Result of processing other Lines:

The processing sequence detailed in Chapter 4 allowed the production of clean time and depth images of line 6-26 across the 1320 OCC (Figure 5.5). The same basic procedure (prestack filtering and deconvolution in the tau-p domain, NMO correction with a smoothed geological velocity model, stack, water velocity migration, de-spiking, de-migration to revert to as zero-offset section and finally either time or depth migration with the full velocity field) has been applied to ridge-parallel profile 15a.17 and on spreading parallel profiles 1.1 and 7.23. In each case the first number refers to the location and is generally the order in which the first profile along that line was collected and the second number the actual sequence of the processed line in the shooting order. So geographic lines such as 6 that were shot twice with different shot intervals are represented by both 6.6 and 6.26.

5.4.1 Line 1-1:

This profile was the first acquired and used a 20s shot interval, requiring careful interpolation before migration. As a result, the depth migration was less stable, so results are presented as the time section resulting from water velocity Stolt migration, de-spiking and a second cascaded time migration to full RMS velocity (Figure 5.8).

Line 1.1 images several interesting features. First, the breakaway is well-defined and moving east into the oceanic core complex, the terrain is less blocky and chaotic than at 1320. In contrast to the 1320 OCC, the 1330 corrugated surface does not appear structurally deeper than the top of the blocky surface and lens-like features can be observed beneath both, with similar length-scales to those observed on Line 6.26, suggesting that the detachment developed as an anastomosing fault zone over much of its length. At the hanging wall cut-off, the corrugated surface is cut by

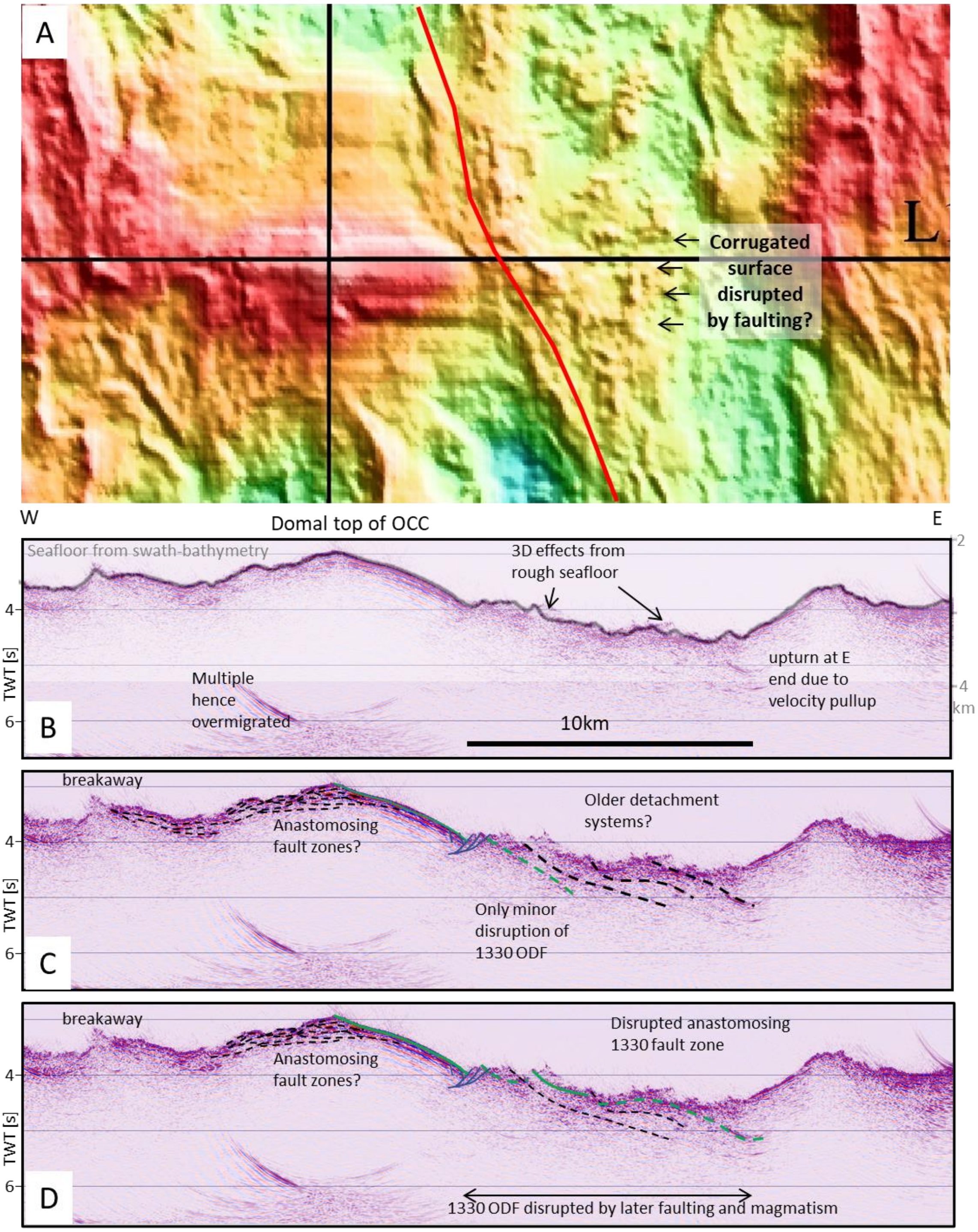

Figure 5.8: Cascaded time migration of Profile 1.1. Top location relative to bathymetric features. B: uninterpreted, with overlay of the bathymetric profile along the line to highlight local 3D effects. C: Possible interpretation in which the 1330 oceanic detachment fault (green) rooted close to the current hanging wall cut-off; D: alternative interpretation in which the detachment (green) roots further east and has been intensely disrupted by faulting and magmatism as the spreading axis propagates across the tip of the OCC.

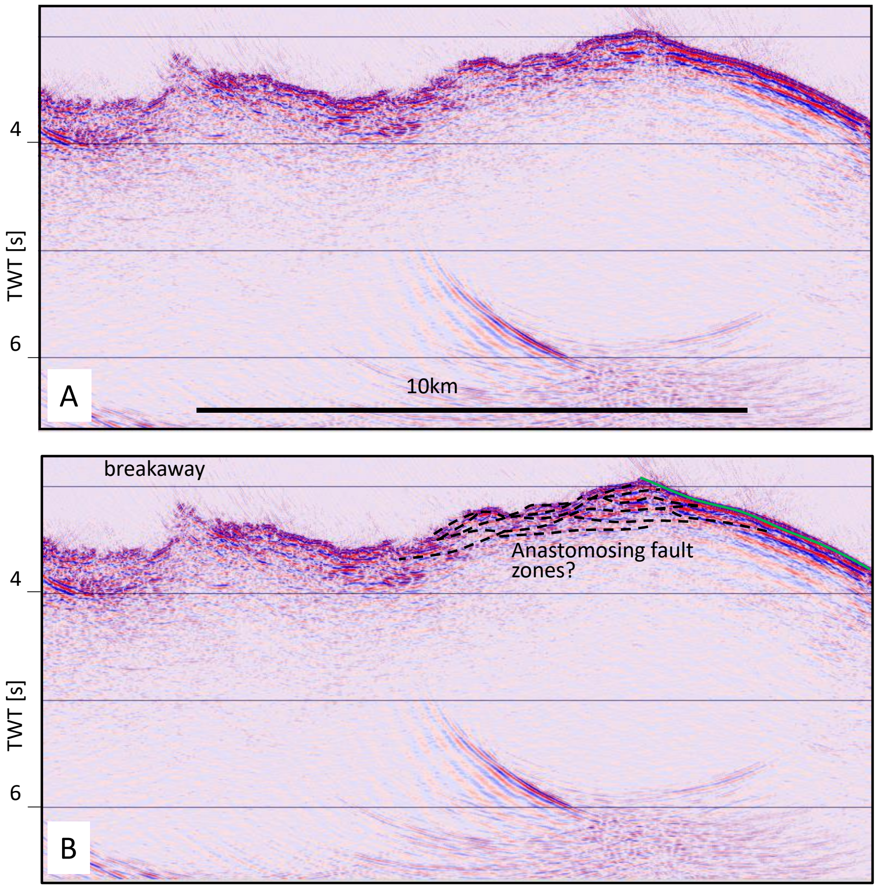

Figure 5.9: Detail of the possible anastomosing geometry of the 1330 oceanic detachment fault near the crest of the OCC dome. The length scale and thickness are similar to that observed along line 6.26 along the 1320 OCC.

outward- (west-) dipping faults. Further east the interpretation becomes less clear. One possibility is that the detachment is only slightly affected by later faulting and roots within a few km of the HC. However, further east the faulting appears dominantly east-dipping, suggesting that it formed on the west side of the spreading axis.

Figure 5.10 is a closer look at the faulted region just east of the HC. If there is only minor disruption of the original OCC (B), the dominance of east-dipping faults east of the axis needs explaining. One possibility is that the 1330 ODF roots further east (C), the underlying west-dipping fabric may be part of 1330 anastomosing fault zone, including earlier slip surfaces long abandoned as part of the fault zone's evolution. In support of this idea is the presence of a smoother east-facing portion of seafloor, the western edge of which closely matches the eastern edge of the main corrugated surface, and which looks as if it might have been rifted off the main OCC. Furthermore, weak corrugations may be present well to the east of the OCC, suggesting the presence of a broad extended, probably intruded the corrugated surface, partly covered in rubble and later lavas.

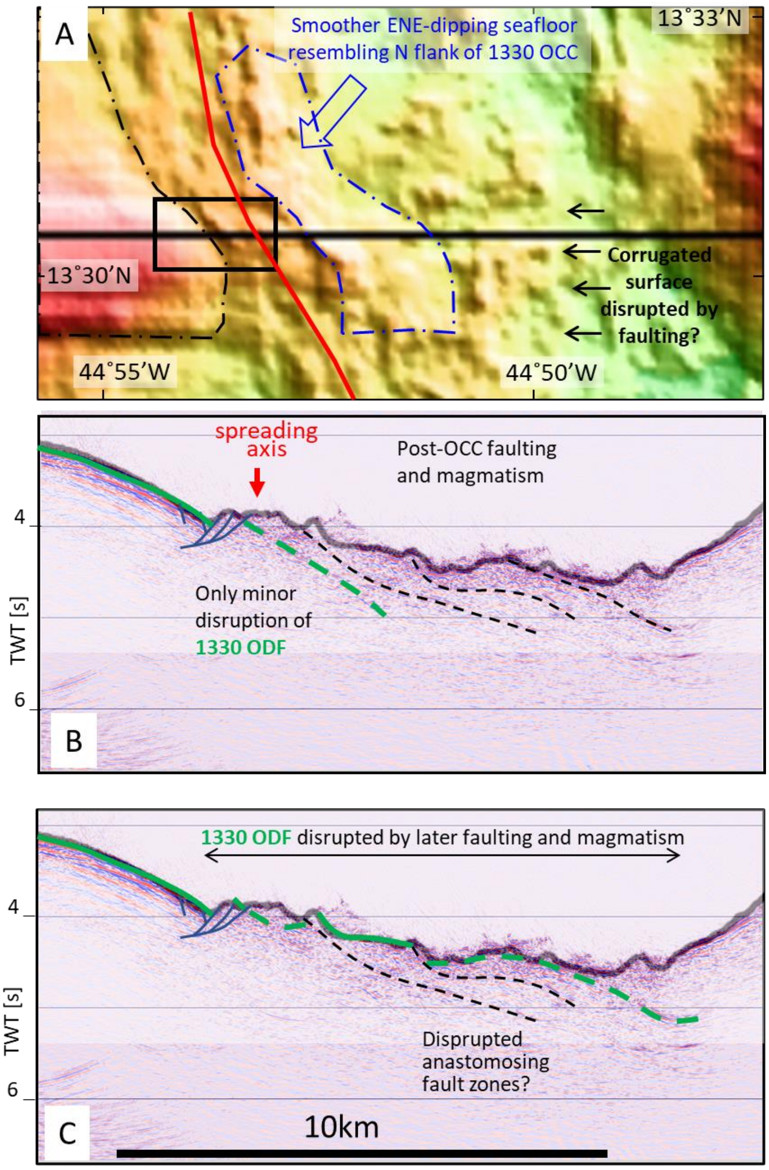
A
Smoother ENE-dipping seafloor resembling N flank of 1330 OCC
13˚33'N
13˚30'N
Corrugated surface disrupted by faulting?
44˚55'W
44˚50'W
spreading axis
Post-OCC faulting and magmatism
Only minor disruption of 1330 ODF
4
6
TWT [s]
B
1330 ODF disrupted by later faulting and magmatism
4
6
TWT [s]
Disprupted anastomosing fault zones?
C
10km

Figure 5.10: Detail of Line 1.1 (B, C) just east of the corrugated surface, and of the corresponding bathymetry (A). Spreading axis of Mallows & Searle (2012) in red. Black box shows area of Figure 5.11 (Escartin et al., 2017). See text for discussion.

The proposed piece of the 1330 OCC is considerably larger than that identified by Escartin et al. (2017) on the basis of detailed near-bottom swath bathymetry (Figure 5.11) and ROV sampling: the Escartin slice shows up in Figure 5.10 as a diagonal feature in the middle of the box showing the extent of Figure 5.11 and is about 200m across in the E-W direction (and is the footwall to the westernmost west-dipping fault that cuts

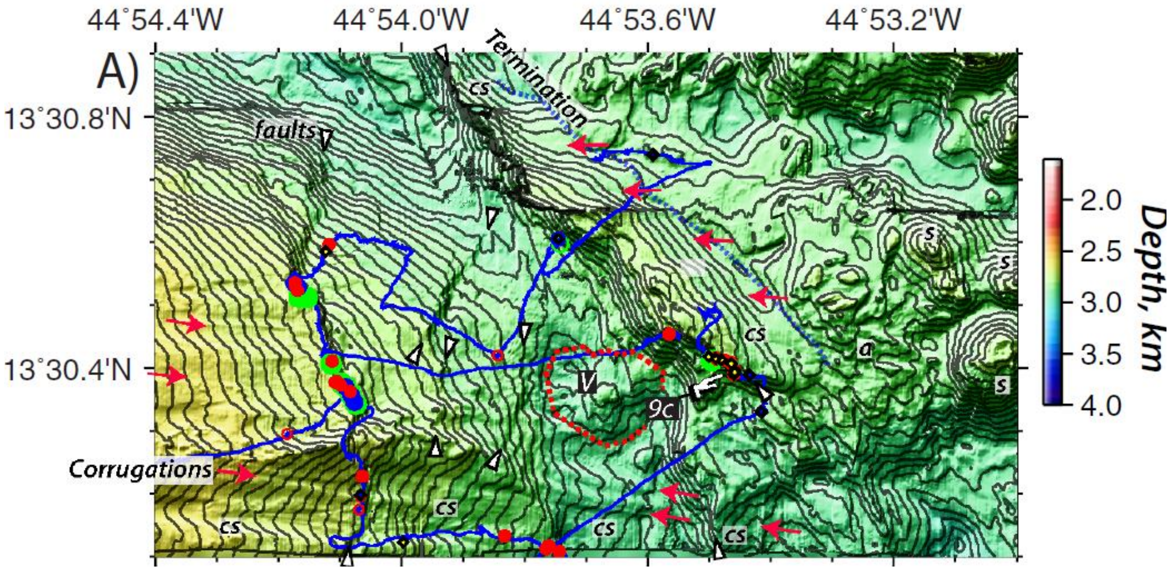

Figure 5.11: Detail of the bathymetry at the toe (hanging wall cutoff) of the 1330 OCC (Escartin et al., 2017) showing the same detached block tentatively identified on the seismic image in Figure 5.10.

across the 1330 toe) but the one inferred here is about ten times as wide and considerably further east. This larger block is more reminiscent of that described by Reston et al., (2002) from 5˚S, interpreted as the result of a ridge jump or more likely a propagation event.

The formation of a slice of the 1330 OCC has implications for the evolution of that and other oceanic core complexes, which are explored further in Chapter 6.

5.4.2 Line 15a.17:

Line 15a.17 was acquired parallel to the ridge axis and across the two OCCs (1320 and 1330) of interest in the Mid-Atlantic area. The purpose of the profile was to investigate the internal structure of the OCC along axis, including of the controlling oceanic detachment, and to determine the lateral extent and geometry of the oceanic detachment faults controlling the formation of the 1320 and1330 OCC. Of particular interest would be any demonstrable spatial linkages between them (Reston and

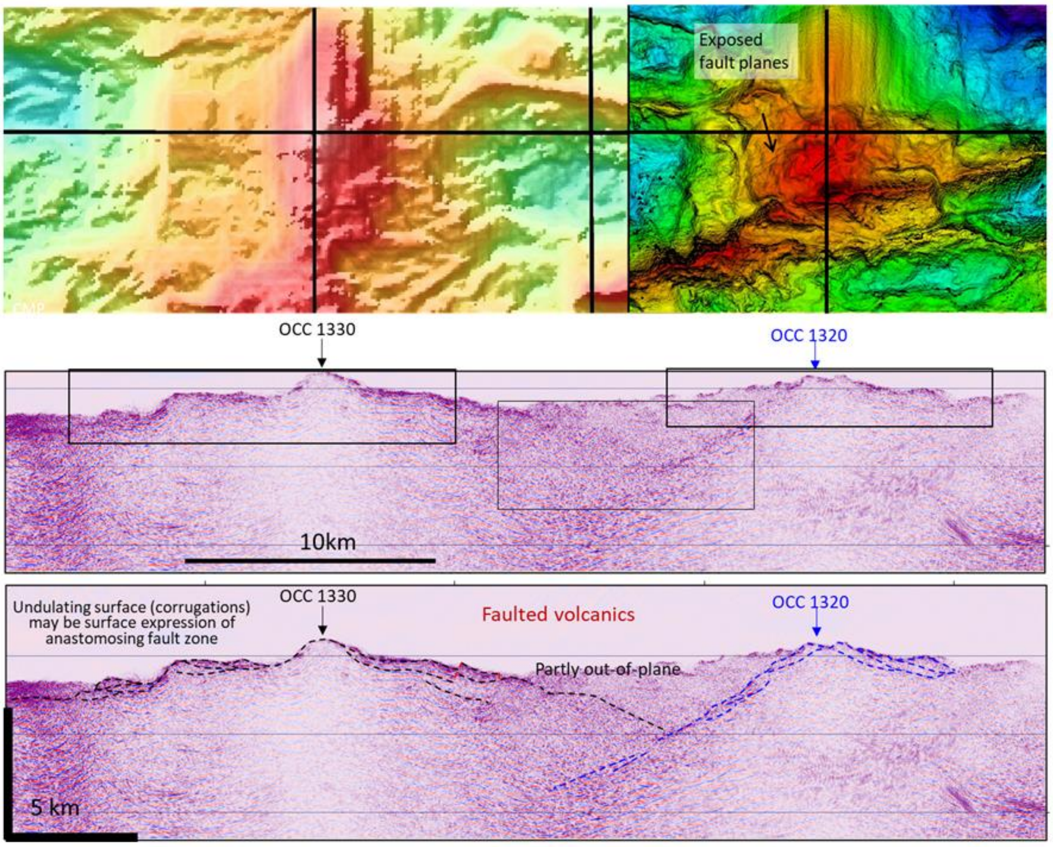

Figure 5.12: Depth migrated image along the N-S profile 15-17. Top: bathymetry, showing that the profile crosses both the 1330 OCC (left) and the 1320 OCC, and thus can test whether the OCC are linked in some way. The profile crosses the corrugated surface of the 1330 OCC: weak reflections that do not parallel the top of the surface may be lenses within an anastomosing fault zone: some of the reflections correspond to steps in the seafloor expressed as corrugations. The profile crosses the blocky surface of the 1320 OCC. Reflections from the N flank of the 1320 OCC appear to pass below the S-dipping reflections coming from the S-flank of the 1330 OCC.

Ranero, 2011), perhaps indicating that the exposed detachments are part of a laterally more extensive detachment system, or whether oceanic detachment faults are of limited lateral extent, requiring some form of lateral ramp or a transition to more magmatic spreading in the region between the OCC.

In general, a similar processing scheme to Line 6.26 was followed, resulting in a final depth migration. The results are interesting (Figure 5.12). First, the corrugated surface of the 1330 OCC appears almost stepped in the depth image, with each step

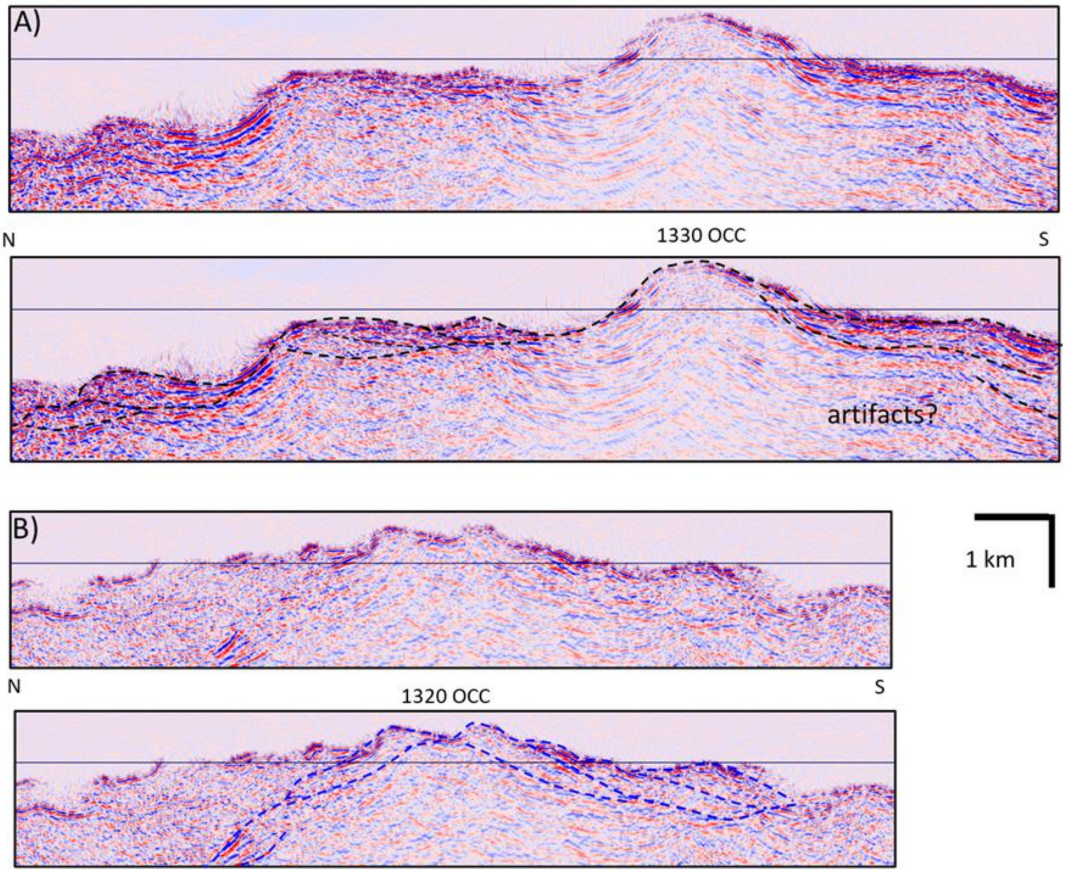

Figure 5.13: Details of the lenses tentatively identified within the footwall of detachments imaged on profile 15-17. These may be lenses within an anastomosing fault zone: some of the reflections correspond to steps in the seafloor expressed as corrugations. The lenses are short enough in the isochron direction (perpendicular to slip) for the largest to be clearly resolved and control the apparent step-like topography. As depth below the seafloor increases, the anastomosing become increasingly less clear.

tentatively related to the lens-like pattern imaged beneath the seafloor. These are interpreted as the lenses of anastomosing fault zones (Figure 5.12, 5.13, 5.14) that have been postulated to control the corrugations of the corrugated surface. This interpretation is explored further in Chapter 6.

Between the 1330 and 1320 OCC, the depth image shows a pronounced dipping band of reflections that can be traced northward from the northern flank of the 1320 OCC to a depth of at least 6 km (below sea surface, ~ 3 km below seafloor) and possibly deeper. This band cuts across the path of a less distinct but still visible band of south-

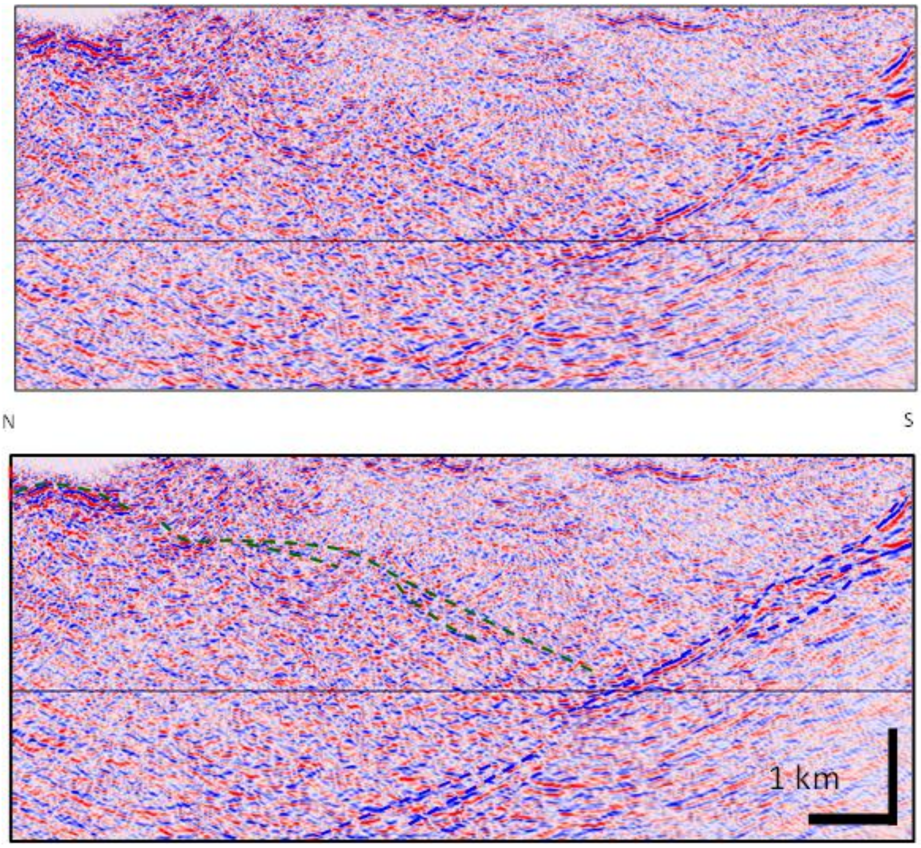

Figure 5.14: Detail of N-S profile 15-17 showing the relationship between reflections from the 1330 OCC (dark green) and those from the 1320 OCC, both of which can be tentatively interpreted as anastomosing at depth. Reflections from the N flank of the 1320 OCC appear to pass below the S-dipping reflections coming from the S-flank of the 1330 OCC. One possible interpretation is that the younger 1320 ODF partly cut across the older 1330 ODF inactive and cut by later faults. However, the 3D geometry of the surface needs to be determined.

dipping reflections that mark the continuation of the corrugated surface on the southern flank of the 1330 OCC (Figure 5.12, 5.14). If these dipping bands of reflections do represent the lateral continuation of the 1320 and 1330 detachments respectively, the geometry would suggest that the detachments are linked in some way, to be discussed in Chapter 6. However first it is necessary to demonstrate that the dipping bands are not from out of the plane of section.

The true dip and geometry of reflections can be revealed at the intersection of seismic lines: Line 7.23 crosses 15.17 ~midway between the 1320 OCC (line 6-26) and the 1330 OCC (line 1-1). True correlation should be carried out with unmigrated,

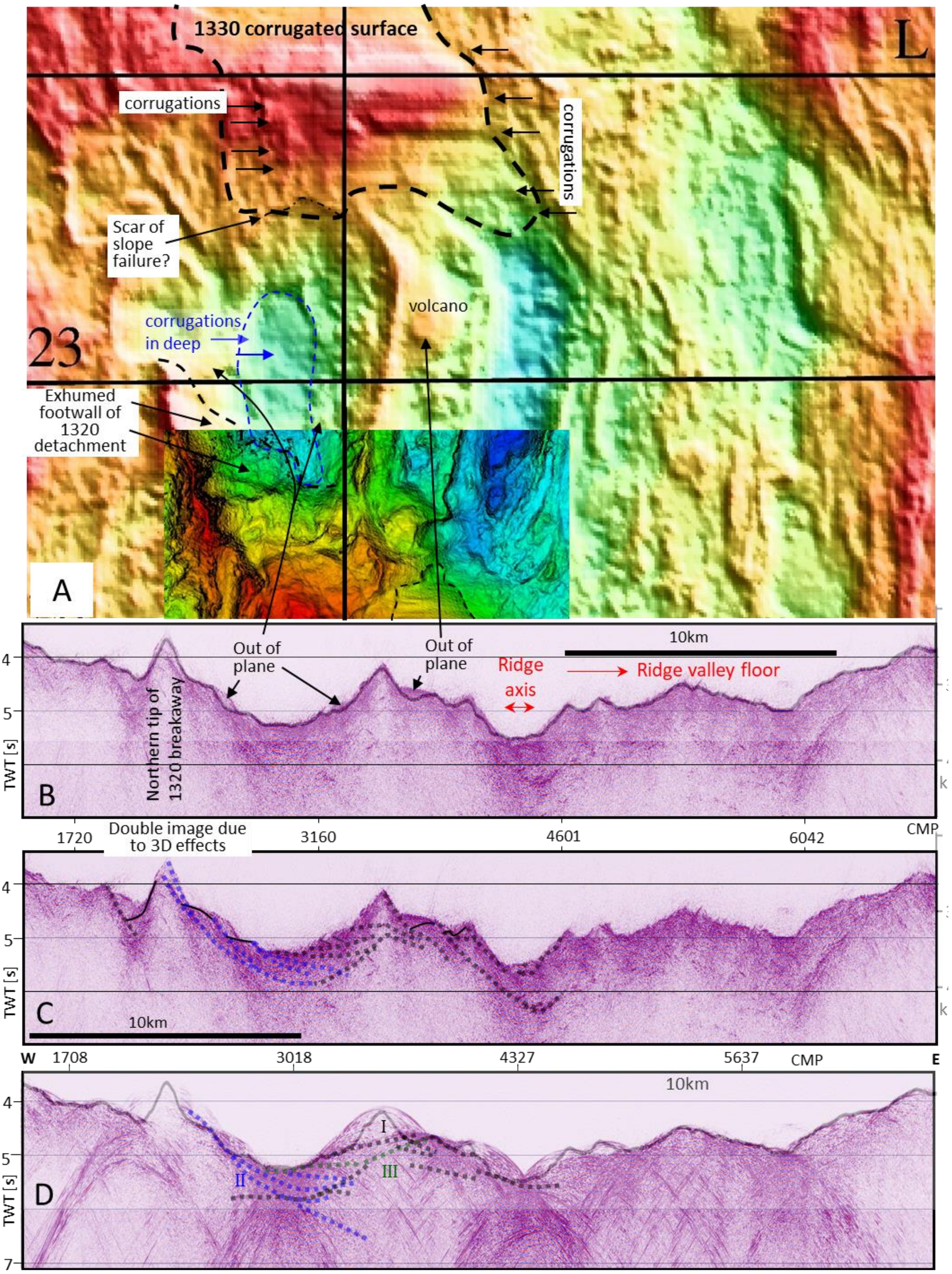

Figure 5.15: Line 7.23: A: bathymetry, B: uninterpreted time migration, with overlay of bathymetric profile to highlight regions of partly out-of-plane reflections. C: interpretation: key reflections marked by broken lines: those in blue are associated with the 1320 breakaway ridge. D: same general features identified on the stack section for correlation with features on line 15-17.

stack sections (Figure 5.15), as these approximate zero-offset sections on which traces at the line of intersection should ideally be identical. [In practice the directivity resulting from the source and streamer arrays and through the CMP method mean that amplitudes tend to differ]. Migrations including depth migrations should not be used as the process of migration moves dipping reflections only within the line of section with consequently different behaviour on intersecting lines. [3D migrations migrate dipping reflections within a volume and so are ideal but require 3D datasets].

5.4.3 Line 7.23:

This line was acquired in the west-east direction parallel to the spreading direction and runs about midway between the 1330 and 1320 detachment faults and traverses the MAR axis (Figure 5.15). The main aim of it, as others, was to understand the extent of the detachment faults including their connectivity. Crucially this profile provides some 3D control on the geometry of the key structures imaged on the N-S line 15.17. As Line 7.23 lies halfway between 6.26 (the 1320 OCC) and line 1.1 (the 1330 OCC), it might image features (e.g., the detachment fault) associated with both, one, or neither OCC. The image quality resulting from depth migration was poor so the main focus will be on the time migration and the stack, the former providing a basic overview, if in time and hence velocity-distorted, of the main tectonic features, and the latter providing the key 3D control on the dipping reflections coming off the 1320 and 1330 OCC. The northern tip of the breakaway of the 1320 ODF is clipped by the line but to the south of the line, east of the breakaway and west of line 15.17 a pronounced break of slope (thin broken black line in Figure 5.15A) marks where the 1320 footwall dips beneath the seafloor: its lateral extent is thus unclear from the bathymetry.

In a 2D world the seafloor would be perfectly imaged on the seismic but overlaying the migrated image on the bathymetry along the profile (extracted from the grid file) shows that there are some 3D effects. The northern tip of the 1320 breakaway is marked by a sharp basement high on the bathymetric profile (Figure 5.15), but the three-dimensionality of the breakaway ridge (it is both oblique to the profile and slightly higher to the south of the profile) means it is imaged twice, as a peak within a peak. The seafloor steps down to the east but again a slight local mismatch with the bathymetric profile indicates some obliquity in reflections from the seafloor (Figure 5.15). However, the base of a ~flat-bottomed deep coincides exactly on the seismic and on the bathymetry. Just north of the profile the base of the deep appears corrugated: as this occurs NE of the 1320 breakaway, such corrugations may rather come from the 1330 OCC to the north: on the bathymetric data (Figure 5.16 A), the 1330 corrugated surface can be traced almost halfway to line 7.23 and almost to the depth of the corrugated deep but appears to have been affected by slope failure in the intervening region. As line 15.17 passes just east of the flat-bottomed corrugated deep, it might be expected that the 1330 detachment can be traced close to the floor of the deep.

Given the direct association between the double-image peak and the 1320 breakaway, a starting point for the interpretation of this line is the identification of features coming off that high which may be part of the 1320 fault system. These are marked as thick blue, semi-transparent dotted lines in Figure 5.16 C; other reflections are in grey. The same, or at least similar features have been interpreted on the stack section (Figure 5.16 C).

The next step is to correlate with the reflections identified for the intersecting N-S line 15.17. For clarity reflections from line 7.23 are shown thick and dotted, those from

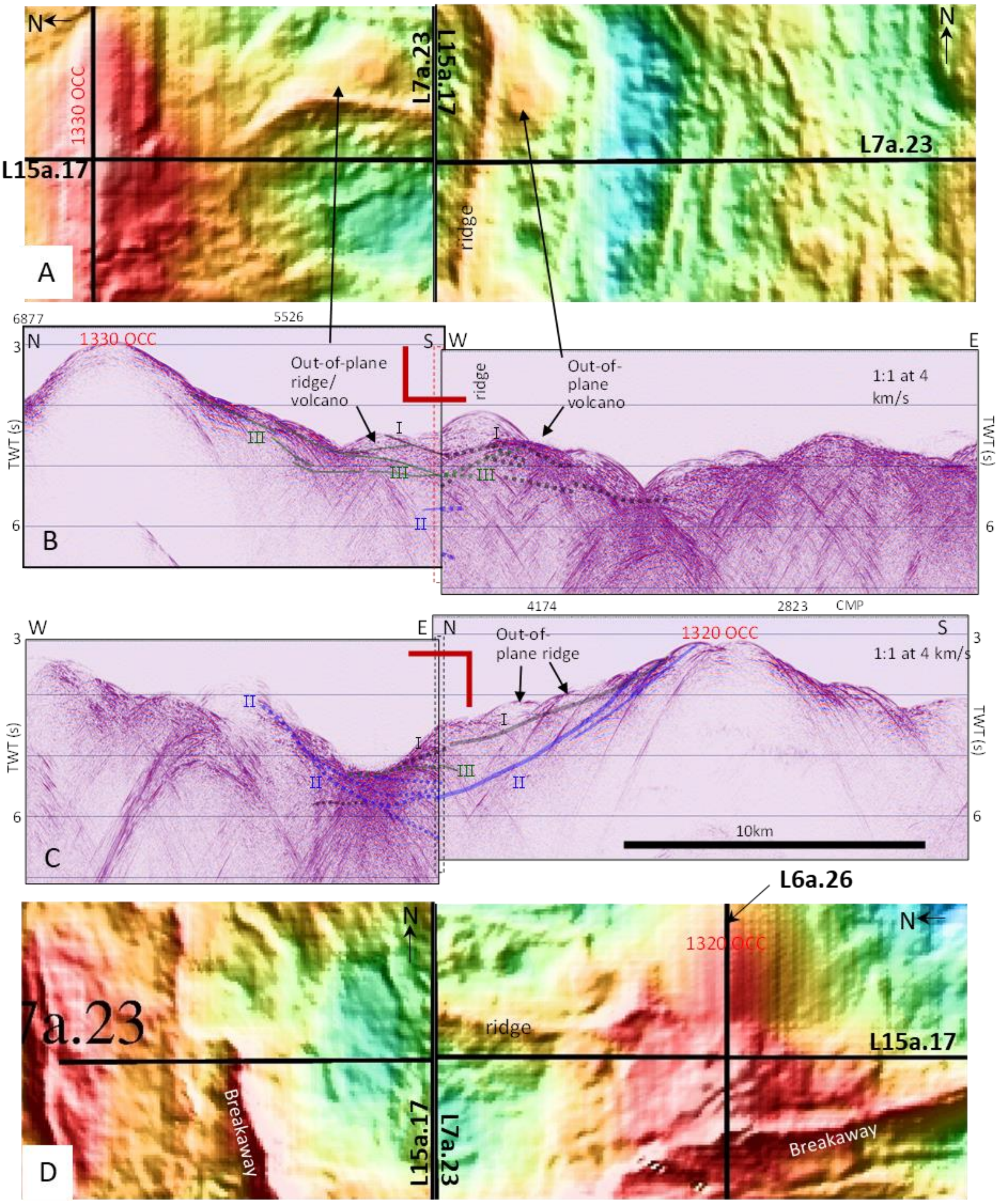

Figure 5.16: Correlation between profiles 7-23 and 15-17. The features associated with both the 1330 OCC (green colours, B) and the 1320 high (blue colours, C) correlate with gently-dipping to sub-horizontal features on the intersecting profile, suggesting that neither comes markedly from out of the plane of section and thus that the 1320 detachment cuts beneath and across the 1330 detachment as inferred previously. Grey lines on selected profile are the seafloor from the bathymetry.

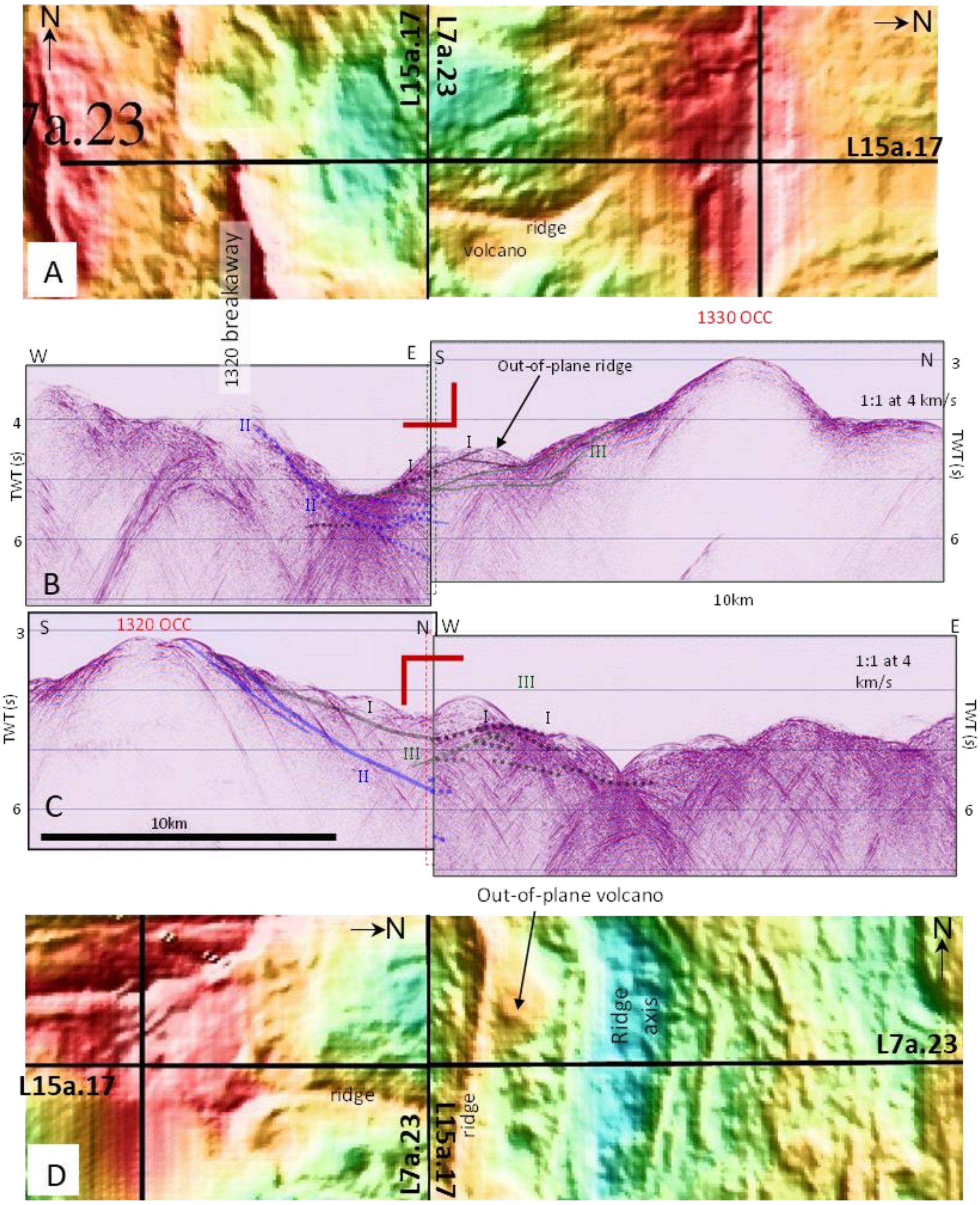
N
L15a.17
L7a.23
→N
7a.23
L15a.17
ridge
volcano
A
1320 breakaway
1330 OCC
W
E
S
Out-of-plane ridge
N
3
1:1 at 4 km/s
4
II
I
I
III
TWT (s)
II
6
B
10km
3
S
1320 OCC
N
W
E
1:1 at 4 km/s
III
I
I
I
III
II
6
C
10km
Out-of-plane volcano
→N
N
Ridge axis
L7a.23
L15a.17
ridge
ridge
L7a.23
L15a.17
D

Figure 5.17: Correlation between profiles 7-23 and 15-17. The features associated with both the 1330 OCC (B, green colours) and the 1320 high (C, blue colours) correlate with gently-dipping to sub-horizontal features on the intersecting profile, suggesting that neither comes markedly from out of the plane of section and thus that the 1320 detachment cuts beneath and across the 1330 detachment as inferred previously. Grey lines on selected profile are the seafloor from the bathymetry.

15.17 are shown thinner and unbroken. As some stop near the intersection, both are carried a short way across the divide. For both lines, reflections that can be associated with the 1320 OCC are shown in blue and those associated with the 1330 OCC are shown in dark green (Figure 5.17).

To ensure that the correlations are as clear as possible, the intersection is shown with both possible pairings: the northern portion of 15.17 with the eastern portion of 7.23 and the western portion of 7.23 with the southern portion of 15.17 (Figure 5.17) and the western portion of 7.23 with the northern portion of 15.17 and the southern portion of 15.17 with the eastern portion of 7.23 (Figure 5.17).

Three main features can be correlated. Feature I is the shallowest, appearing beneath a series of diffraction apexes which can themselves be correlated with bathymetric features out of the plane of section: a north-south trending ridge just east of 15.17, a volcano just east of that ridge and just north of 7.23 (Figure 5.16 A). Comparison with the bathymetry (Figure 5.15 A and 5.16 B) shows that I is actually the reflection from the seafloor ~beneath the sail-line. The deeper features II and III are thus below the seafloor and within the basement. On both 15.17 and 7.23, II can be traced up towards the 1320 OCC (Figure 5.16 and 5.17): the breakaway on 7.23 and the blocky or chaotic zone on 15.17. Thus, II is interpreted as the part of the 1320 detachment system but cannot be traced far both east and north of the line intersection. Feature III occurs between I and II and on 15.17 can be traced south from the flank of the 1330 dome. III thus appears to be the slip surface of the 1330 OCC, likely corrugated. At the intersection with 7.23, III can be traced west to floor the flat-bottomed deep that exhibits corrugations, supporting the interpretation of those corrugations as part of the 1330 detachment system, and continues towards the east-dipping II reflections coming down from the 1320 breakaway. Thus, III appears to stop at the underlying 1320 detachment, feature II.

5.5 Conclusions:

Despite the noise problems described in Chapter 3, the results presented here have shown that useful images can be obtained at slow spreading ridges. In particular, key results include: the deep geometry of the 1320 oceanic detachment fault is convex up in nature going from ~24° at the seafloor to ~42° at ~6 km depth; the internal structure of both the 1320 and the 1330 fault zones show anastomosis with identifiable scales as corrugations on bathymetric map could be a natural occurrence for OCC development; the spatial relationship between the detachment systems show two OCCs one diving deeper (1320) and the other partially exhumed (1330); the temporal evolution, abandonment of the 1330 oceanic core complex and associated detachment dissection by the spreading axis. Lastly these results are relatable to real subsurface reflections. Discussions on these results are made in the light of previous work in the next chapter to address the key questions posed in Chapters 2 and 3.

Chapter 6 Discussion and Conclusions

Oceanic core complexes (OCC) and the oceanic detachment faults (ODF) that appear to control their formation (Chapter 2) are so widespread at slow-spreading ridges that it has been estimated up to 50% of such spreading involves slip unroofing deep crustal and/or mantle rocks (Escartin et al., 2008). The previous chapters have detailed the gaps in our knowledge of slow seafloor spreading in general and about OCC and ODFs in particular (Chapter 2), gaps that are exacerbated by challenges associated with seismic imaging (e.g., Peirce et al., 2006; Chapter 3). Chapter 4 described the 2D seismic processing methods applied to reduce noise and the imaging of deep structures from a slow spreading segment of the MAR. An interpretation of the resulting imaged section of lines both parallel to the slip direction and parallel to the spreading axis was presented in Chapter 5. In this final chapter we present a discussion of how the issues raised in Chapters 2 and 3 have been addressed, and how in combination with the interpretations made in Chapter 5 the results bridge the key gaps in our understanding of slow-spreading. The key questions once again are:

1. How can we suppress the side-coming scattered energy that is so-problematic at slow-spreading ridges and so produce the best image of oceanic detachment faults?
2. What is the true geometry of the detachment from the surface (fault trace) to depth?
3. What are the implications of this geometry for the mechanics of the fault?
4. What is the internal structure of the detachment: is the corrugated surface the two-dimensional representation of a 3D anastomosing fault zone?

5. What is the lateral extent of the detachment? Specifically, are the 1320 and 1330 detachments part of one undulating structure, in places beneath a series of fault blocks or if not, how do they interact?

6.1 Suppression of side-coming scattered energy to better image faulting.

One reasons that these questions have remained unanswered is the poor quality of seismic imagery that has been available at mid-ocean ridges and the consequent failure to resolve the geometry, internal structure, and lateral continuity of the key detachment faults. Much of the problem is caused by the presence of side-coming scattered noise, as detailed in Chapter 3. This noise appears on the stack section as convex-up diffractions (Figure 6.1A), which smear out into smiles on migration (Figure 6.1B). As phase screen modelling showed most of this noise comes from the seafloor, it has travelled exclusively at water velocity (~1480 m/s) and so can be collapsed to small energy bursts by migrating with that velocity (Figure 6.1C). These energy bursts can then be suppressed on the basis of their localization (limited lateral extent and short duration) and amplitude by treating them as noise spikes and applying a de-spiking algorithm (Figure 6.1D). Removing the migration (by “modelling” also known as de-migration) recreated a stack section without the diffractions (Figure 6.2B), allowing subsequent full velocity time migration via a cascaded migration (Figure 6.2C) or (following de-migration) either full velocity time or depth migration (Figure 6.2D). As detailed in Chapter 4, other key processing steps included velocity filtering and deconvolution in the tau-p domain. Thus:

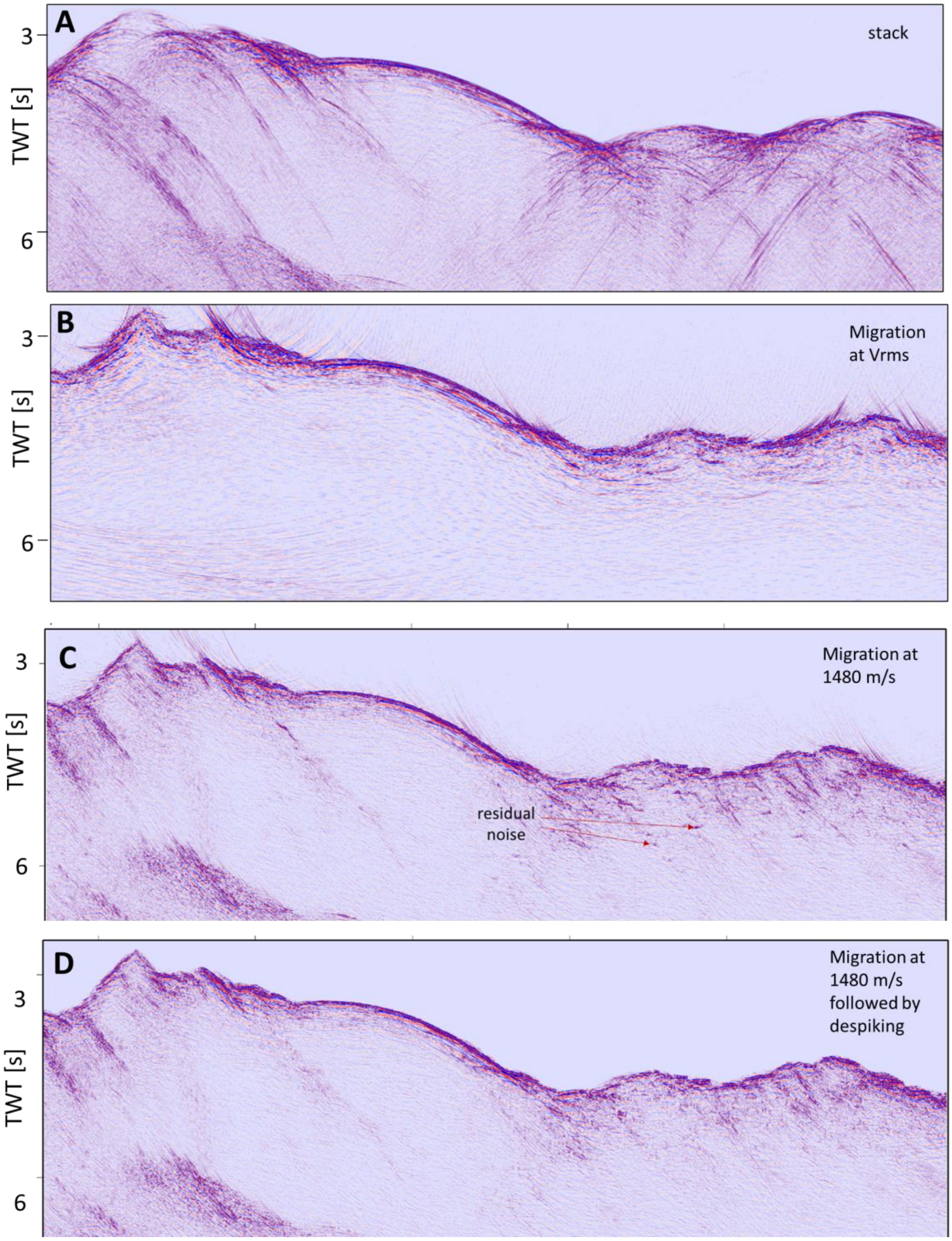

Figure 6.1: Key steps in seismic processing illustrated by profile 6.26. A: CMP stacked section, showing pronounced convex-up diffractive energy, much with apexes below the seafloor. Phase screen modelling of the acoustic response of the 2D seafloor showed that much of this energy comes from the seafloor out of the plane of section. B: migration with full V_{rms} of the stack in A produced smeared out migrations smiles from the side-coming seafloor diffractions, obscuring any real sub-surface features. C: migration of the stack with water velocity (1480 m/s) collapses the diffractions to localised energy bursts which could be suppressed with de-spiking (D). The processing sequence continues in Figure 6.2

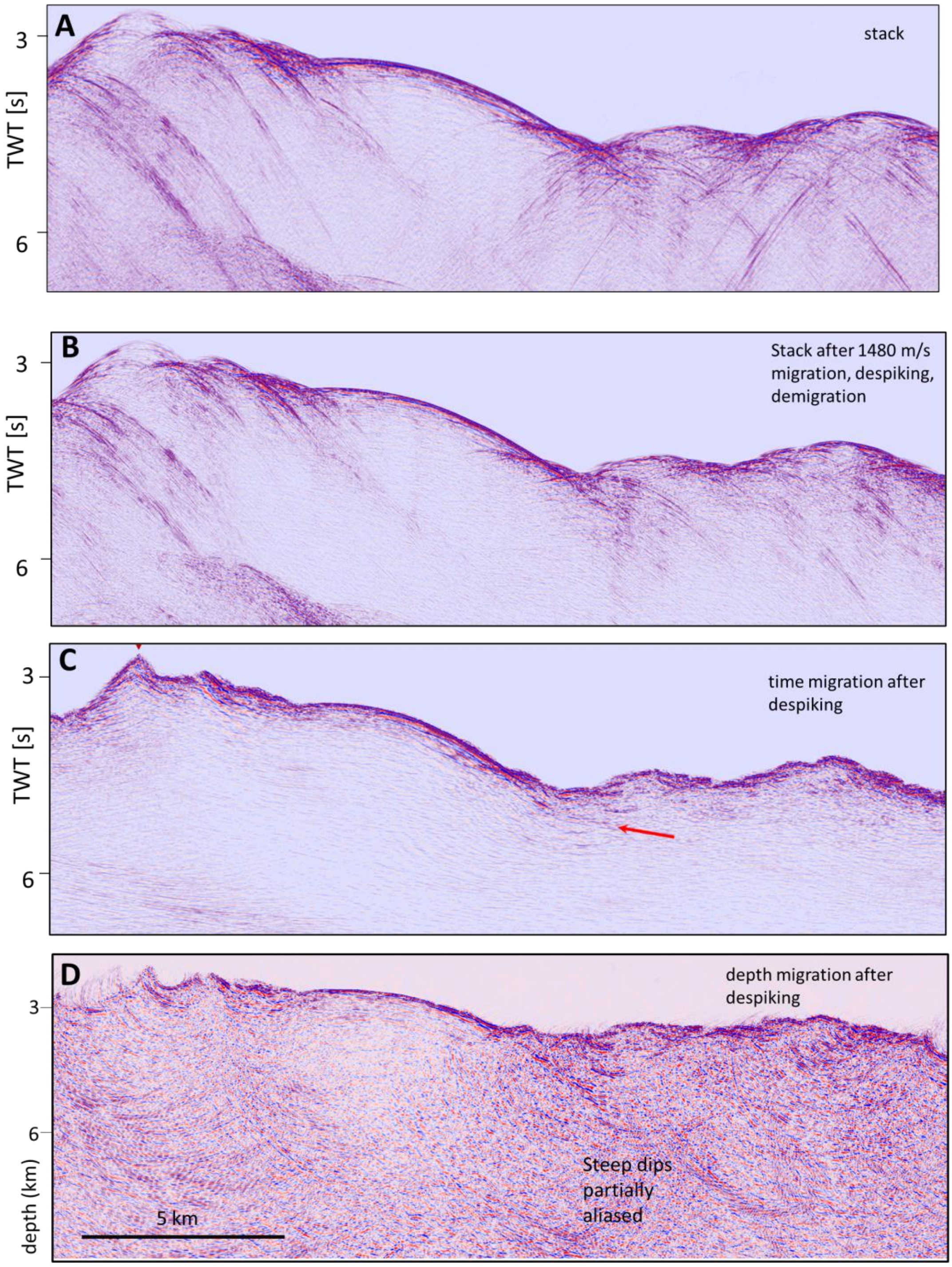

Figure 6.2: Key steps in seismic processing illustrated by profile 6.26, continued. A: CMP stacked section, showing pronounced convex-up diffractive energy coming from the seafloor out of the plane of section. B: stack section produced by de-migration of de-spiked section in Figure 6.1D. Compared to the stack in A, the diffractive energy has been largely suppressed. C: Full time migration after de-spiking. The same result can be obtained by migrating the image in B using full V_{rms} *velocities or by a cascaded migration of the section in Figure 6.1D using reduced velocities. D: Depth migration of B using* V_{rms} *velocities, revealing the true geometry of the 1320 oceanic detachment fault.*

Conclusion 1: imaging of slow spread crust can be improved by suppressing side-coming diffractive energy through water velocity migration and de-spiking, and by both velocity filtering and deconvolution in the tau-p domain.

6.2 Geometry of the detachment:

The question of how and even whether OCC-forming oceanic detachment faults root at depth has been asked since OCCs were first identified (Cann et al., 1997) and has a bearing on the geological processes leading to the formation of OCC and that contribute to slow seafloor spreading. Cann et al., (1997) considered two possibilities: that the detachment soles out in the rift valley as a large landslip or rooted to depth. Mitchell et al., (1998) wondered if the detachment rooted as a convex-up, steep (high angle) structure or a gentle (low angle) fault.

Results obtained via depth imaging show the slow spreading detachment fault plane below the seafloor steepens smoothly with depth from ~19° at the edge of the exhumed footwall, to 24° just beneath the deformed hanging wall “apron”, to ~38° at a depth of ~5km below the seafloor, to values approaching 60° where the reflection image is lost. But extrapolating the geometry links with the observed distribution of normal fault seismicity mapped by Parnell-Turner et al. (2017, 2021, Figure 6.3D). Together the reflection image and the earthquake distribution provide the most complete image of an oceanic detachment geometry yet, confirming that they are strongly convex-up structures, rooting at steep angles beneath the spreading axis (Mitchell et al., 1998). This geometry is entirely consistent with the flexural rotation of a steeply rooting normal fault, as described by the rolling hinge model (Chapter 2; Lavier et al., 2000) commonly invoked for their formation of oceanic core complexes.

Conclusion 2: depth migration shows that the active 1320 detachment dips beneath the deforming hanging wall at ~20˚, steepening steadily downwards to dip at > 60˚ ~ 3km below the seafloor, and projecting towards the band of microearthquakes at greater depth even steeper dips where it is seismically active (Figure 6.3).

6.3 Detachment mechanics

The markedly convex-up detachment geometry has implications for the properties of the fault. Faults form by the fracturing and displacement along a planar surface, a process accompanied by a dramatic drop in the inherent strength of the rock (cohesion) and the formation of fault rocks, generally of lower friction than the intact rock. Mohr-Coulomb theory (Choi and Buck, 2012) predicts that for typical intact rock properties (friction coefficients between 0.6 and 0.85), normal faults should form at 60-70°, but the loss of cohesion and reduction in friction allows further slip to occur over wider range of angles. As normal faults are expected to flex to lower angle as offset on them increases (Choi and Buck, 2012), the ability of the fault to slip at angles lower than that of formation is critically important in allowing the fault to continue to slip without locking up.

The minimum angle at which a normal fault might slip for a variety of rock and fault properties was explored by Choi and Buck (2012) for Mohr-Coulomb behaviour and expanded by Reston (2020) to include Griffiths behaviour (cracking and fissuring) at depths shallow enough for the horizontal stress to become tensile. The results (Figure 6.4) show that as depth increases, the lowest angle at which a fault can slip without locking up also decreases for all faults with 20% or less of the intact cohesion, as might

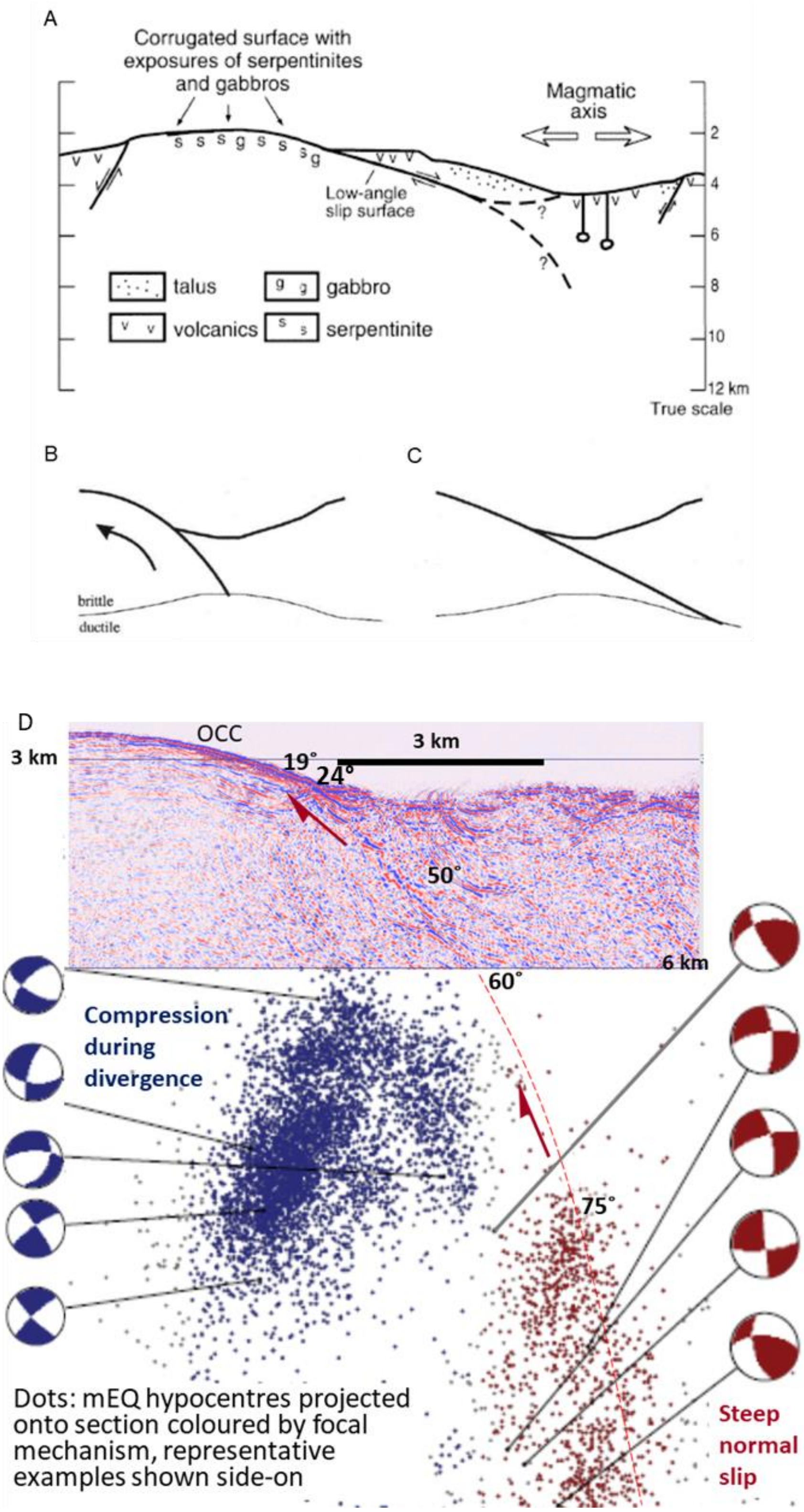
A
Corrugated surface with exposures of serpentinites and gabbros
Magmatic axis
Low-angle slip surface
?
?
talus
gabbro
volcanics
serpentinite
2
4
6
8
10
12 km
True scale
B
brittle
ductile
C
D
OCC
3 km
3 km
19°
24°
50°
6 km
60°
75°
Compression during divergence
Steep normal slip
Dots: mEQ hypocentres projected onto section coloured by focal mechanism, representative examples shown side-on

Figure 6.3: Geometry of an OCC as proposed by Cann et al., (1997), Mitchell et al., (1998) and depth imaged from 2D MCS from the MAR. The geometries of ODF have been suggested prior to now and this includes as a failed plane (A) and as a steep angled (B) or low angled (C) normal fault at depth. (D) Depth image of the 1320 ODF OCC superimposed on microearthquakes (Parnell-Turner et al., 2017).

be expected. Only hypothetical faults with cohesion significantly more than 20% of the intact rock behave otherwise.

The ability of a fault to slip at lower angles near the surface is especially relevant for oceanic detachment faults which are thought to form as steep structures and flexurally rotate to low angle during slip and footwall exhumation (Choi and Buck, 2012). The geometry of the 1320 detachment revealed by processing to depth migration (Figure 6.4) and projecting to the band of earthquake hypocentres and corresponding slip planes identified by Parnell-Turner et al., (2017) is everywhere

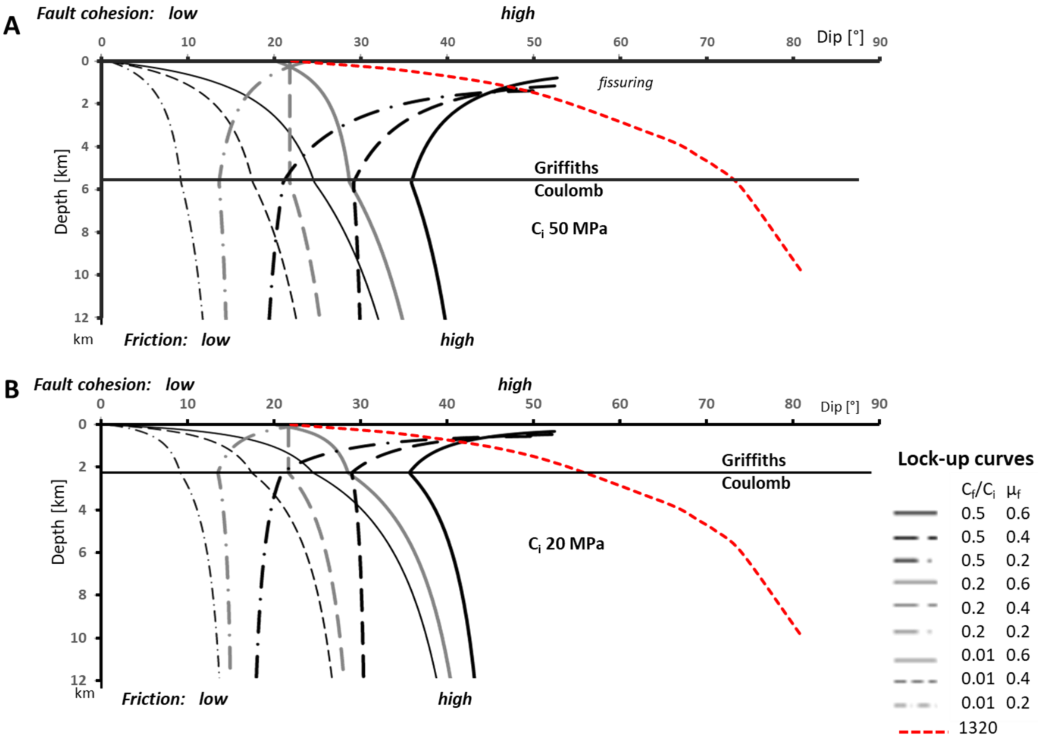

Figure 6.4: Geometry of 1320 ODF vs lock-up angles from Reston (2020). The grey and black lines show the minimum angles at which faults with the specified properties can slip as a function of depth. These lock-up angles generally decrease upwards, except for those faults that might have a high cohesion (thick black solid, broken and dot-dash lines). The dip of the 1320 detachment as imaged on the seismic (red lines) increases from low to high angle with depth, and is to the right of (steeper than) the minimum slip angle for most faults (thin and grey lines), which that the 1320 detachment should be able to slip unless it has a cohesion more than 20% of the intact rock. C_i*= cohesion of intact rock (50 MPa in the top figure, 20 MPa in the lower figure),* C_f*= cohesion of faulted rock. Unfaulted friction coefficient* (μ)*=0.75 which most strongly affects the lock-up angle below the horizontal line which marks a transition from Griffiths to Coulomb behaviour.*

steeper than the lock-up angle (the angle at which the normal fault can no longer slip) of low or very low cohesion faults with a variety of friction coefficients (Reston, 2020). The implication is that the 1320 detachment would be able to continue slipping for a wide range of fault properties, and would not need to have particularly low friction as is commonly supposed.

Conclusion 3: The observed geometry is consistent with a wide range of fault properties under Mohr-Coulomb (Choi and Buck, 2012) and/or Mohr-Griffith conditions (Reston, 2020) and does not require unusually low friction fault rocks.

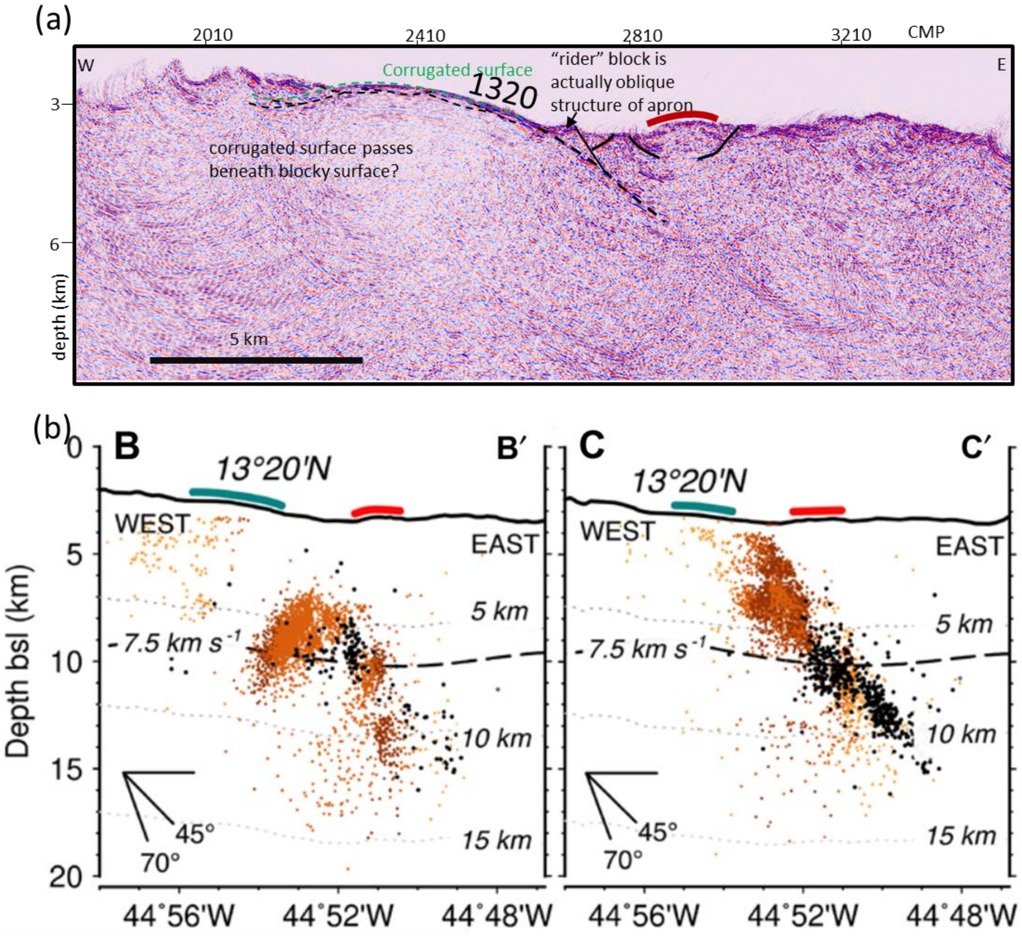

Figure 6.5: 1320 ODF depth (a) and micro-earthquake sections (b, Parnell-Turner et al., 2021). Comparing (a) and (b) it is observed the micro-seismicity slip surface aligns with the OCC from the seafloor on the depth section though the micro-earthquake is deeper than the imaged ODF plane. (b) left is closest to line 6.26 while the right side is to the south. Thick red lines indicate the position of the ridge axis on imaged section and micro-earthquake data.

The depth image of the ODF (Figure 6.5) appears to be missing directly beneath the spreading axis. This might be interpreted as indicating that the fault has been obscured by intrusions, but there is very little volcanic activity observed in this part of the spreading axis (Escartin et al., 2017). Furthermore, the micro-earthquake distribution (Parnell-Turner, 2021) suggests that brittle faulting continues along a steeply east-dipping band beneath the spreading axis: indeed, the fault may be considered the geometry of the spreading axis as it separates the plates. The loss of image might rather represent a loss of signal with depth, a loss of reflected signal as the fault becomes steeper, or the effects of scattering and poor signal penetration through shallow volcanic rocks.

6.4 Detachment internal structure:

Parnell-Turner et al. (2018) proposed that the corrugated structure of the exhumed footwall of OCCs is the expression of an anastomosing fault zone (Figure 6.6a) in which strain / slip is concentrated in bands that separate lower-strain lenses within a broad zone of deformation. As outlined in Chapter 2, fault anastomosis is thought to develop from a combination of initial strain weakening followed by strain hardening. Initially, the rock weakens with moderate strain, causing slip to focus where the rock is more deformed, forming a “fault core” within a lower strain “damage zone” (strain weakening, strain focusing). However, for some lithologies, with further slip the fault core may become stronger (strain hardening) and more resistant to slip than the surrounding lower-strain zones. The core is then abandoned and slip refocuses elsewhere within the damage zone. Repeated cycles produce bands of successive fault cores separated by lenses of low strain damage zone rocks.

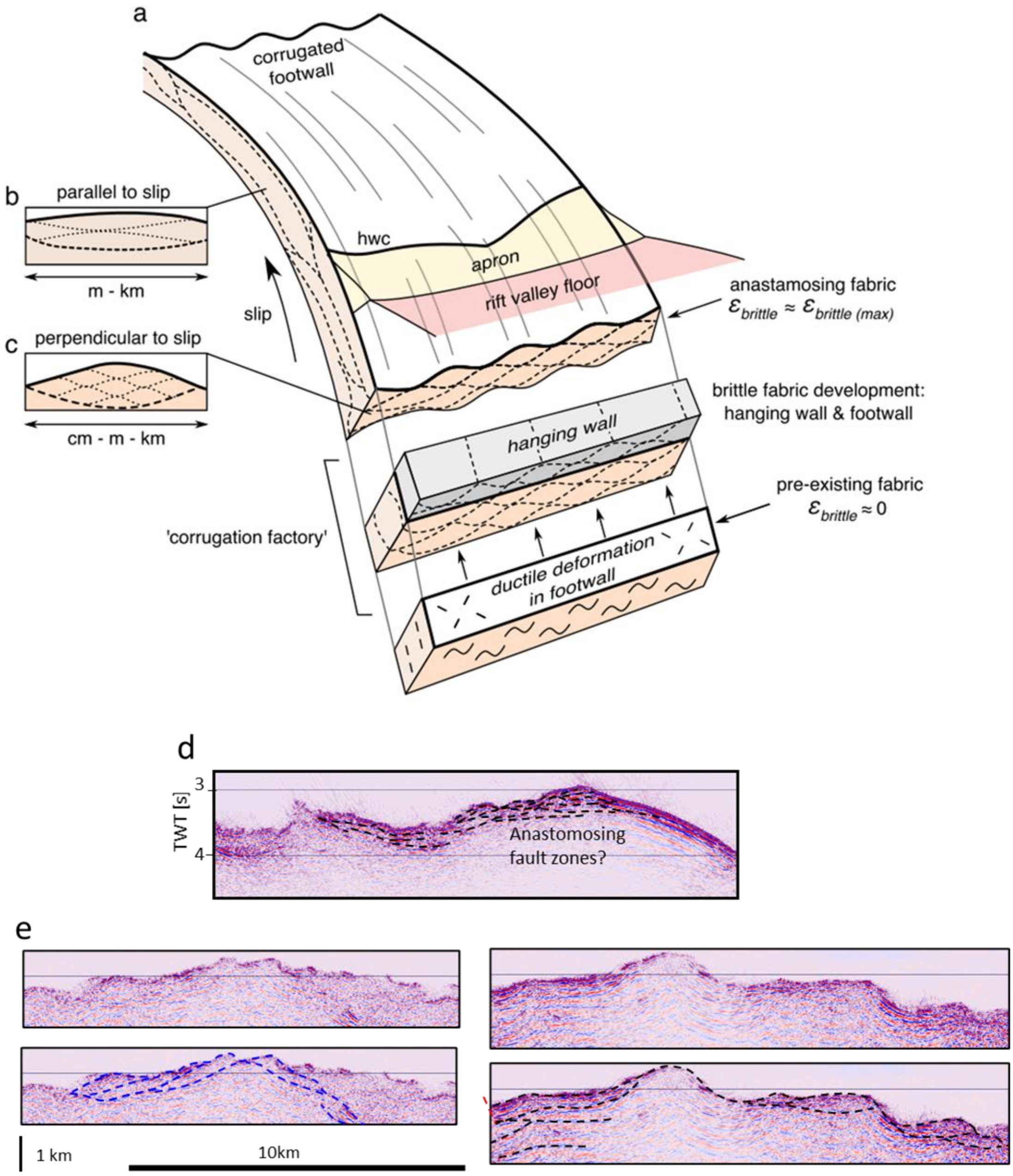
a
corrugated footwall
b
parallel to slip
m - km
slip
c
perpendicular to slip
cm - m - km
hwc
apron
rift valley floor
anastamosing fabric
$\varepsilon_{brittle} \approx \varepsilon_{brittle\ (max)}$
brittle fabric development: hanging wall & footwall
hanging wall
'corrugation factory'
pre-existing fabric
$\varepsilon_{brittle} \approx 0$
ductile deformation in footwall
d
TWT [s]
3
4
Anastomosing fault zones?
e
1 km
10km

Figure 6.6: Perspective view (Parnell-Turner et al., 2018) and sections showing the internal structure of OCCs (1320 and 1330) pointing to anastomosis in the footwall. (a) Core complex cartoon showing how footwall anastomosis play a role in the formation of observed corrugation on the slip surface. (b) and (c) Slip and axis direction of the fault veins of rock anastomosis. (d) and (e) Section through the anastomosing fault zones in the slip and strike direction respectively, expressed where exposed as corrugated surface. In the axis-parallel (strike) direction only lenses corresponding to the largest scale of corrugations are clearly resolved and control the apparent step-like topography. As depth below the seafloor increases, the anastomosing become increasingly less clear and may include some reverberations.

Possible anastomosing fault networks were imaged at both the 1320 and 1330 OCC on lines running both in the spreading direction and parallel to the spreading axis (Figure 6.6). These networks of faults are observed mostly in the shallow subsurface of the detachment faults (Figure 6.7d and e) and seem to relate to the geometry of the corrugated surfaces seen at the seafloor. The fault zone lenses resolved in the isochron direction (parallel to the spreading axis and so perpendicular to slip) appear to control the step-like topography of the corrugated surface. As depth below seafloor increases the anastomosing pattern becomes increasingly less clear (Figure 6.6d and e), perhaps related to the thickness of the fault zone.

The image of line 6.26 seems to show that the corrugated surface at the top of the exhumed footwall projects beneath the blocky faulted surface closer to the breakaway (Figure 6.5). Here it is important to remember that the corrugated slip surface exposed at the top of the footwall is only the latest fault strand, the one that was active as the footwall was pulled up and out from beneath the hanging wall. If the corrugated surface projects below the blocky surface, it implies that the active slip surface, which would have been forming and being abandoned within the damage zone due to cycles of weakening then hardening with increasing strain, locally moved deeper into the footwall as extension and exhumation proceeded.

To show the relation between the lenses within the shallow footwall observed on the depth images to the largest wavelength corrugations observed on the high-resolution bathymetry of the OCC 1320, a direct measure was taken both on section and map in the slip direction. The horizontal dimensions of anastomosing lenses measured on the depth section vary from 1-2 km which overlaps the range of the larger visible corrugations (0.8 - 1.4 km) on the bathymetric image. The lens geometries imaged may thus correspond to the same anastomosing process that is seen as corrugation in the bathymetry (Parnell-Turner et al., 2017). Although the lengths of the lenses on the depth section in the slip direction and those parallel to the axis are similar, while Parnell-Turner et al.'s predicted that they should be longer in the slip direction than in the isochron direction, the near equivalence in lens length on sections along slip (from line 6.26) and axis (line 15.17) directions may arise from the limit of lateral seismic resolution: put simply we see all the lenses in the slip direction but only the largest in the isochron direction.

> **Conclusion 4:** The corrugated surface appears to represent the two-dimensional representation of a 3D anastomosing fault zone consisting of a series of interlinked slip surfaces separating lens-shaped lower strain zones. The largest lenses are imaged on the seismic profiles. As anastomosing fault zones are thought to develop through initial strain softening followed by strain hardening, the implication is that the rocks concerned display these properties, and thus that corrugated surfaces may preferentially develop in some oceanic lithologies than others. The smooth seafloor of exhumed peridotites at the Southwest Indian Ridge (Cannat et al., 2008; Reston, 2018) may not have undergone this weakening/hardening sequence.

6.5 Lateral continuity of oceanic detachment faults:

A final question is whether oceanic core complexes are simply where the footwall of laterally more continuous detachment systems are exposed and that elsewhere they are present but covered by small, rafted blocks. As described in Chapter 2, Line L15a.17 was acquired to investigate the lateral extent and linkage between the two OCCs (1320 and 1330) in the north-south direction (parallel to the spreading axis) as such linkage was a key controversy in the understanding of the tectonics of ODFs and OCCs in proximity. One end member view is that oceanic core complexes are the exposed portions of a much larger single detachment (Figure 6.7A; Escartin et al., 2008; Reston and Ranero, 2011). The alternative view is that OCC are the exhumed footwall of laterally restricted oceanic detachment faults which are separated by regions of more magmatic spreading Figure 6.7B – Parnell-Turner et al., 2021). In either model, the detachment may be short-lived as variations in magma supply cause control the proportion of the divergence that is taken up by magmatism (M number: a value of 0.5 may optimise the lifespan of an ODF – Tucholke et al., 2008) and hence the migration of the detachment root (MacLeod, et al., 2010; Reston, 2018).

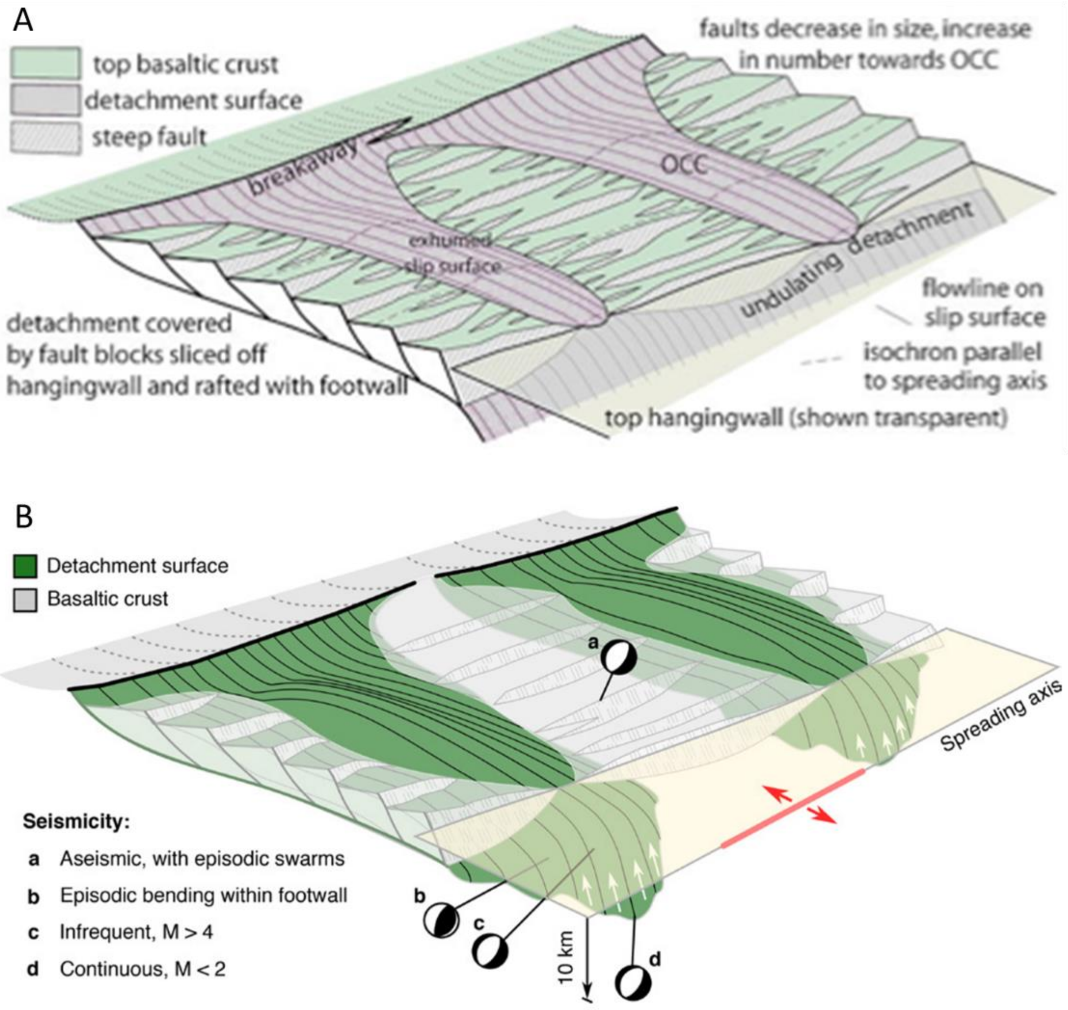
A
top basaltic crust
detachment surface
steep fault
faults decrease in size, increase in number towards OCC
breakaway
OCC
exhumed slip surface
undulating detachment
flowline on slip surface
isochron parallel to spreading axis
detachment covered by fault blocks sliced off hangingwall and rafted with footwall
top hangingwall (shown transparent)
B
Detachment surface
Basaltic crust
Spreading axis
Seismicity:
a Aseismic, with episodic swarms
b Episodic bending within footwall
c Infrequent, M > 4
d Continuous, M < 2
10 km
a
b
c
d

Figure 6.7: Perspective views of ODFs by (A) Escartín et al. (2008) and Reston & Ranero (2011) and (B) Parnell-Turner et al., (2021). (A) ODFs are considered as a large single geologic entity with a surface expression resulting in unroofing of deep oceanic or mantle rocks during slip to form OCCs. (B) ODFs are depicted as isolated geologic entities having an aseismic zone separation.

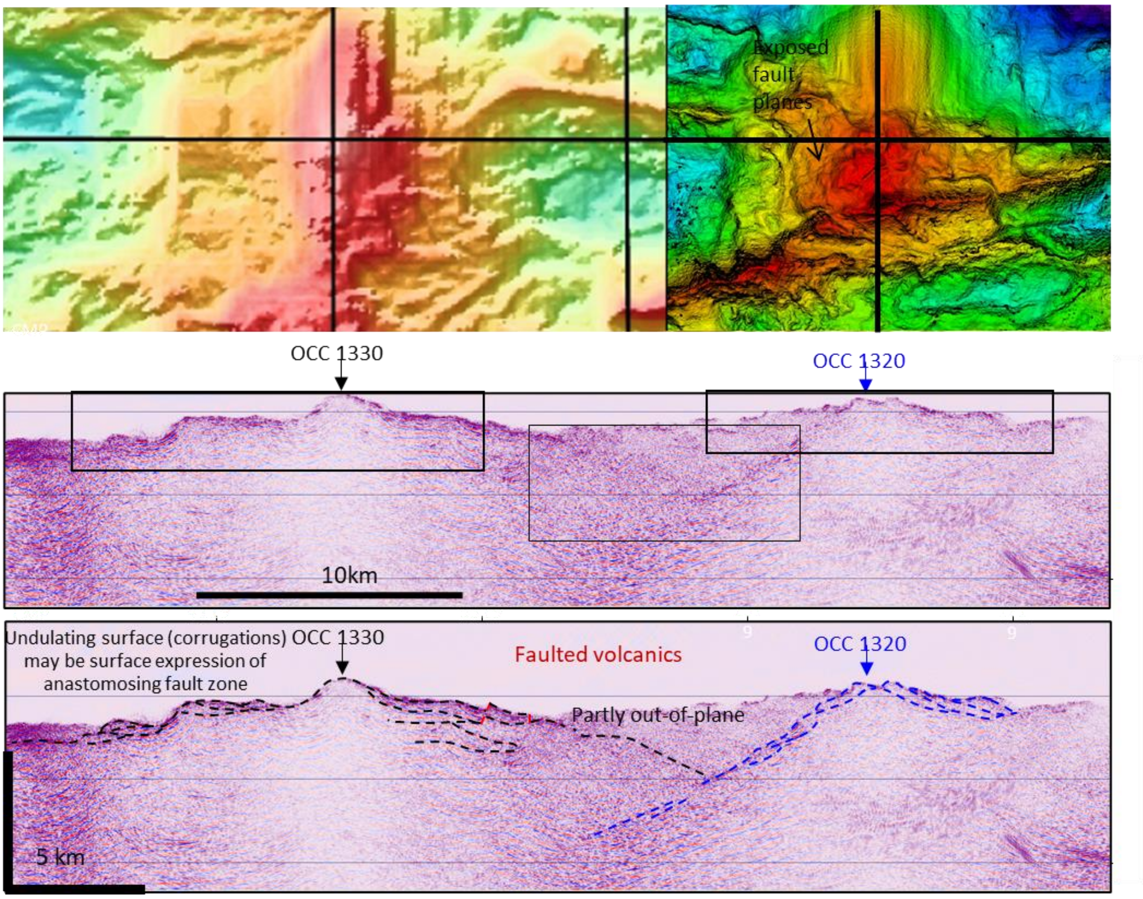

Figure 6.8: Interpreted depth imaged section along axis direction aimed to substantiate if the closely position OCCs in the MAR are single unite of a very large ODF or if they are two distinct ODFs in close proximity. Our interpretation shows these ODFs are isolated as at present but could have been linked at some point in time.

In the 13N regions, although the 1330 and 1320 OCC are within ~ 10 km of each other, seafloor imagery (Escartin et al., 2017) shows that the 1330 OCC is being broken up by faulting and seismic activity (Parnell-Turner, 2021) show that the root of the 1330 ODF is inactive. In contrast, the 1320 OCC is intact and the root of the 1320 ODF is still active. These observations mean that currently the two structures cannot at present share a common root.

The seismic image of line 15.17 images bands of anastomosing reflections, interpreted as the anastomosing ODFs associated with the 1320 and 1330 OCCs dipping away from each domal massif. Between the two OCCs, the 1320 ODF dips more steeply and cuts across at ~ 3km below the seafloor the 1330 ODF, continuing to a depth of > 5km below the seafloor. These cross-cutting relationships are consistent with the 1320 ODF being active more recently than the 1330 ODF and thus with both the seismicity and the seafloor observations (Fig 6.8). The geometry is remarkably similar to that of the same detachment as traced by seismicity (Parnell-Turner et al., 2021) ~ along the ridge axis (Fig 6.9), although there the whole structure is deeper. The same axis-parallel seismicity also highlights that the 1330 detachment is not active.

Thus the 1320 and the 1330 do not form a single continuous surface but together they extend across the gap between the two OCCs, suggesting that detachment faulting has been important between the OCC. It is also possible that the two ODF

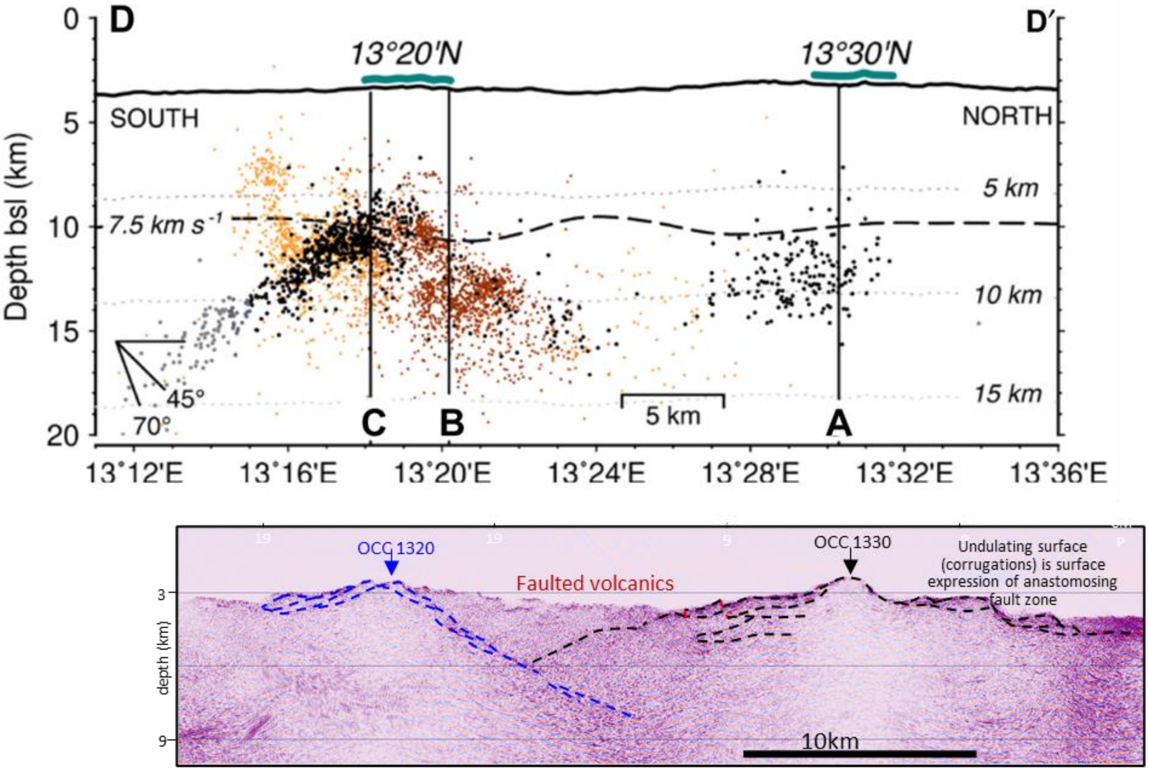

Figure 6.9: Along axis micro-earthquake (top - Parnell-Turner et al., 2021) and imaged depth section (bottom - line 15.17) of the 1320 ODF footwall (OCC). Even though the two sections cross the two OCC at different longitudes (the micro-earthquake section ~along the spreading axis and the seismic line 15.17 ~ten km further west and thus over the OCCS in the footwall of the detachment they show similar geometries for 1320 detachment.

may have formed a single surface in the past before the 1330 one became inactive. Thus, elements of both parts of Figure 6.7 may be correct.

So, the final conclusions are:

- **Conclusion 5:** Both the 1320 and 1330 ODF can be traced to depth on either side of the respective OCC. In the region between the two OCC, the 1320 oceanic detachment appears to cut across the 1330 ODF and continues to depth, consistent with slip on the 1320 ODF continuing more recently than that of the 1330 ODF.
- **Conclusion 6:** The 1320 and 1330 ODF do not currently form a single, simple undulating surface as postulated by Reston and Ranero (2011), but do appear to have been linked, possibly as part of a larger system of fault zones and to extend across the gap between their surface expressions, the OCC.

6.6 Conclusions and future work:

At the start of this thesis several questions were posed. Those questions have all been answered. The chief conclusions are:

1. imaging of slow spread crust can be achieved by suppressing side-coming diffractive energy through water velocity migration and de-spiking, and by both velocity filtering and deconvolution in the tau-p domain.
2. depth migration shows that the active 1320 detachment dips beneath the deforming hanging wall at ~20˚, steepening steadily downwards to dip at > 60˚ ~3km below the seafloor, and projecting towards the band of microearthquakes at greater depth even steeper dips where it is seismically active (Figure 6.3).

3. The observed geometry is consistent with a wide range of fault properties under Mohr-Coulomb (Choi and Buck, 2012) and/or Mohr-Griffith conditions (Reston, 2020) and does not require unusually low friction fault rocks.
4. The corrugated surface appears to represent the two-dimensional representation of a 3D anastomosing fault zone consisting of a series of interlinked slip surface separating lens-shaped lower strain zones. The largest lenses are imaged on the seismic profiles. As anastomosing fault zones are thought to develop through initial strain softening followed by strain hardening, the implication is that the rocks concerned display these properties.
5. Both the 1320 and 1330 ODF can be traced to depth on either side of the respective OCC. In the region between the two OCC, the 1320 oceanic detachment appears to cut across the 1330 ODF and continues to depth beneath it, consistent with slip on the 1320 ODF continuing more recently than that of the 1330 ODF.
6. The 1320 and 1330 ODF do not currently form a single, simple undulating surface as postulated by Reston and Ranero (2011), but do appear to have been linked, possibly as part of a larger system of fault zones and to extend across the gap between their surface expressions, the OCC.

Future work should test these conclusions for other oceanic core complexes, and to apply the imaging methods to other rugged deep marine settings such as convergent margins. These could include the following:

- Applying the processing sequence outlined here to any seismic line acquired for the study of other OCCs, such as the Kane, Atlantic Massif, TAG and Rainbow, to re-test the applicability of the key processing steps to suppress noise and enhance P-wave from such fields. Were applicable new data with shorter shooting interval is needed to compare the impact of varying the shot geometry to further understand how such impacts the resolution of the seismic data for imaging. Current works on some of these OCCs still leave room for further constraining of their geometries.

- A study using high resolution 3D seismic for the 3D visualisation of the corrugated surface and its anastomosing fault zone enabling the update or development of comprehensive 3D models of oceanic detachment faults sub-seabed, including the extent of the anastomosis.
- Having applied the tau-p process for velocity filtering of the data set further work would be to extract and build velocity models directly from such data in the tau-p domain for comparison with seismic refraction derived velocity models. This would involve tau-p NMO analysis and imaging.
- Furthermore, deep seismic data imaging would be required to revalidate and identify any or possible transition zones in the vicinity of OCCs and environs as inferred from refraction data.
- Most deep sea 2D seismic data sets are inundated with side-coming event, owing the existence of canyons and ridges, therefore would definitely be improved by applying the processing sequence used in this thesis.

References

Al-Chalabi, M. 1994. Seismic velocities-a critique. First Break Vol 12 No. 12

Al-Yahya, K. M., Kelamis, P. G., and Mueller, R. E. 2005. Suppressing noise by prestack hyperbolic velocity filtering and poststack partial K-L transform. SEG Technical Program Expanded Abstracts, pg. 1626-1628

Anderson, R. G., and McMechan, G. A. 2002. Noise-adaptive filtering of seismic shot records. Geophysics, Vol. 53, No. 5, pg. 638-649

Bansal, R., and Imhof, M. G. 2005. Diffraction enhancement in prestack seismic data. Geophysics, Vol. 70, No. 3, pg. 73-80

Basak, R. L., Rana, K. S., Rao, K., Gangaiah, A., and Chandrasekaran, C. R. 2012. Removal of noises using Tau-P transformation - an indigenous tool for noise attenuation in shallow seismic data. 9th Biennial International Conference & Exposition on Petroleum Geophysics

Bécel, A., Shillington, D. J., Nedimović, M, R., Webb, S. C., and Kuehn, H. 2015. Origin of dipping structures in fast-spreading oceanic lower crust offshore Alaska imaged by multichannel seismic data. Earth and Planetary Science Letters, Vol. 424, pg. 26-37.

Benoliel,S.D., Schneider, W. A, and Shurtleff, R. N. 1987. Frequency wavenumber approach of the tau-p transform: some application in seismic data processing. Geophysics Prospecting, Vol. 35, No. 5

Bianco, E. 2016. Tutorial: Wavelet estimation for well ties. The Leading Edge, Vol. 35, No. 6, pg. 541-543. http://library.seg.org/doi/10.1190/tle35060541.1

Blackman, D. K., and Collins, J. A. 2010. Lower crustal variability and the crust/mantle transition at the Atlantis Massif oceanic core complex.Geophysical Research Letters, Vol. 37, No. 24, pg. 1-5.

Blackman, D. K., Cann, J. R., Janssen, B, Smith, D. K. 1998. Origin of extensional core complexes: Evidence from the Mid-Atlantic Ridge at Atlantis Fracture Zone. Journal of Geophysical Research: Solid Earth, Vol. 103, No. B9, pg. 21315-21333

Bonnemains, D., Escartín, J., Mevel, C., Andréani, M., and Verlaguet, A. 2017. Perversive silicification and hanging wall overplating along the 1320'N oceanic detachment fault (Mid-Atlantic Ridge). Geochemistry, Geophysics, Geosystems. Vol. 18, pg. 1810-1823

Bönnemann, C., and Buttkus, B. 1999. Estimation of seismic velocities from deep reflections in the τ-p domain. Pure and Applied Geophysics, Vol. 156, No. 1-2, pg. 279-301

Bown, J., and White, R. S. 1994. Variation with spreading rate of oceanic crustal thickness and geochemistry. Earth and Planetary Science Letters, Vol. 19, No. 121, pg. 435-449

Buck, W. R., Lavier, L. L., and Poliakov, A. N. B. 2005. Modes of faulting at mid-ocean ridges. Nature, Vol. 434, No.7034, pg. 719-723

Buck, W.R., 1988. Flexural rotation of normal faults. *Tectonics*, *7*(5), pp.959-973.

Buttkus, B., and Bönnemann, C. 1999. Enhancement of deep seismic reflections in pre-stack data by adaptive filtering. Pure and Applied Geophysics, 156, 1-2, pg. 253-278

Calvert, A. J. 1995. Seismic evidence for a magma chamber beneath the slow-spreading Mid-Atlantic Ridge. Nature, Vol. 377, No. 6548, pg. 410-414.

Calvert, A. J. 1997. Backscattered coherent noise and seismic reflection imaging of the oceanic crust: An example from the rift valley of the Mid-Atlantic Ridge at 23°N. Journal of Geophysical Research: Solid Earth, Vol. 102, No. B3, pg. 5119-5133

Canales, J. P. 2010. Small-scale structure of the Kane oceanic core complex, Mid-Atlantic Ridge 23°30′N, from waveform tomography of multichannel seismic data. Geophysical Research Letters. Vol. 37, No. 21, pg. 1-6.

Canales, J. P., Tucholke, B. E., and Collins, J. A. 2004. Seismic reflection imaging of an oceanic detachment fault: Atlantis megamullion (Mid-Atlantic Ridge, 30°10′N). Earth and Planetary Science Letter, Vol. 222, No. 2, pg. 543-560

Cann, C, R., Blackman, C. K., Smith, D. K., McAllister, E., Janssen, B., Mello, S., Avgerinos, E., Pascoe, A. R., and Escartín, J. 1997. Corrugated slip surfaces formed at ridge-transform intersections on the Mid-Atlantic Ridge. Nature, 385, pg. 329-332

Cann, J. R., Smith, D. K., Escartin, J., and Scohouten, H. 2015. Tectonic evolution of 200 km of Mid-Atlantic Ridge over 10 million years: Interplay of volcanism and faulting. Geochemistry, Geophysics and Geosystems, 2303-2321

Cannat, M. 1996. How thick is the magmatic crust at slow spreading oceanic ridges? Journal of Geophysical Research: Solid Earth, Vol 101, 2847-2857

Cannat, M., Mevel, C., Maia, M., Deplus, C., Durand, C., Gente, P., Agrinie, P., Belarouchi, A., Dubuisson, G., Humler, E., and Reynolds, J. 1995. Thin crust, ultramafic exposures, and rugged faulting patterns at the Mid-Atlantic Ridge (22°-24°N). Geology, Vol. 23, No. 1, pg. 49-52

Cao, Z.N., Bancroft, J.C., Brown, R.J. and Xaio, C.M., 2003. Radon transform and multiple attenuation. *CREWES Research Report*, *15*.

Carbotte, S. M., Marjanović, M., Carton, H., Mutter, J. C., Canales, J., Nedimović, M. R., Han, S, and Perfit, M. R. 2013. Fine-scale segmentation of the crustal magma reservoir beneath the East Pacific Rise. Nature Geoscience, Vol. 6, No. 10, pg. 866-870.

Carbotte, S. M., Smith, D. K., Cannat, M., and Klein, E. M. 2016. Tectonic and magmatic segmentation of the Global Ocean Ridge System: A synthesis of observations. Geological Society Special Publication, Vol. 420, No. 1, pg. 249-295.

Cary, P. W. 1999. Generalized Sampling and “Beyond Nyquist” Imaging. CREWES Report 11

Chambers, R., Jakubowicz, H., Lamer, K. L., and Yang, M. 1984 Suppression of backscattered coherent noise by prestack partial migration. SEG Annual Meeting.

Chapman, C. H. 1981. Generalized Radon transforms and slant stacks. Geophysical Journal of the Royal Astronomical Society, Vol. 66, No. 2, pg. 445-453

Choi, E., and Buck, W. R. 2012. Constraints on the strength of faults from the geometry of rider blocks in continental and oceanic core complexes. Journal of Geophysical Research: Solid Earth, Vol. 117, No. 4, pg. 1-14

Choi, E., Buck, W. R., Lavier, L. L., and Petersen K. D. 2013. Using core complex geometry to constrain fault strength. Geophysical Research Letters, Vol. 40, No. 15, pg. 3863-3867

Christie, P.A.F., Hughes, V.J. and Kennett, B.L.N., 1983. Velocity filtering of seismic reflection data. *First Break*, *1*(3).

Collettini, C. 2011. The mechanical paradox of low-angle normal faults: Current understanding and open questions. Tectonophysics Elsevier B.V., Vol. 510, No. 3-4, pg. 253-268. doi.org/10.1016/j.tecto.2011.07.015

Collettini, C., and Sibson, R. H. 2001. Normal faults, normal friction? Geology, Vol. 29, No. 10, pg. 927-930

Collier, J. S., Dañobeitia, J. J., Canales, J. P., Dalwood, R., Gadd, S., Hayward, N., Henstock, T., Krastel, S., Peirce, C., and Watts, A. 1997. Evidence for asymmetric accretion and low-angle, planar faults in slow-spreading oceanic crust. Geology, Vol. 25, no. 12, pg. 1075-1078

Cormier, M. H, https://www.gebco.net/about_us/presentations_and_publications/documents/cen_conf_abstract_cormier.pdf

Cowie, P. A., Underhill, J. R., Behn, M. D., Lin, J., and Gill, C. E. (2005). Spatio-temporal Evolution of Strain Accumulation Derived from Multi-Scale Observations of Late Jurassic Rifting in the Northern North Sea: A Critical Test of Models for Lithospheric Extension. *Earth Planet. Sci. Lett.* 234 (3-4), 401–419.

Craig, T, J., and Parnell-Turner, R. 2017. Depth-varying seismogenesis on an oceanic detachment fault at 13°20′N on the Mid-Atlantic Ridge. Earth and Planetary Science Letters, Elsevier B.V., Vol. 479, pg. 60-70.

DeMartin, B. J., Reves-Sohn, R. A., Canales, J. P., and Humphris, S. E. 2007. Kinematics and geometry of active detachment faulting beneath the Trans-Atlantic geotraverse (TAG) hydrothermal field on the Mid-Atlantic Ridge. Geology, Vol. 35, No. 8, 711-714

Deping, S., Luping, G., Ying, X., and Pei, L. 2006. Use of low-frequency signals to improve imaging quality under high-velocity basalt. Applied Geophysics, Vol. 3, No. 2, pg. 112-119

Deregowski, S. M. 1990. Common-offset migrations and velocity analysis. First Break, Vol. 8, No. 6, pg. 225-234

Donati, M. S., and Martin, N. W. 1995. Seismic reconstruction using a 3D tau-p transform. CREWES Research Reports, 7

Dondurur, D., 2018. *Acquisition and Processing of Marine Seismic Data*. Elsevier, Netherland: Candice Janco., ISBN 978-0-12-811490-2.

Drummond, B. J., Hobbs, R. W., and Goleby, B. R. 2004. The effects of out-of-plane seismic energy on reflections in crustal-scale 2D seismic sections. Tectonophysics, Vol. 388. No. 1-4, pg. 213-224

Duarte, J. C., and Schellart, W. C. 2019. Plate Boundaries and Natural Hazards. Geophysical Monograph 1-10

Dunn, R. A., Arai, R., Eason, D. E., Canales, J. P., and Sohn, R. A. 2017. Three-Dimensional Seismic Structure of the Mid-Atlantic Ridge: An Investigation of Tectonic, Magmatic, and Hydrothermal Processes in the Rainbow Area. Journal of Geophysical Research: Solid Earth, Vol. 122, No. 12, pg. 9580-9602.

Dunne, J. and Beresford, G. 1997. Processing through to stack in the t-p domain. Exploration Geophysics, Vol. 28, No. 3

Dunne, J., and Beresford, G. 1995. A review of the τ-p transform, its implementation and its applications in seismic processing. Exploration Geophysics, Vol. 26, No. 1, pg. 19-36

Dunne, J., and Beresford, G. 1997. Processing through to stack in the t-p domain. Exploration Geophysics, Vol. 28, No. 3, pg. 341-347

Elboth, T., and Hermansen, D. 2008. Attenuation of noise in marine seismic data. SEG Technical Program Expanded Abstracts, pg. 3312-3316

Elboth, T., Qaisrani, H., and Hertweck, T. 2008. De-noising seismic data in the time-frequency domain. SEG Technical Program Expanded Abstracts, Pg. 2622-2626

Escartin, J., Mevel, C., Petersen, S., Bonnemains, D., Cannat, M., Andreani, M., Augustin, N., Bezos, A., Chavagnac, V., Choi, Y., Godard, M., Haaga, K., Hamelin, C., Ildefonse, B., Jamieson, J., John, B., Leleu, T., MacLeod, C. J., Massot-Campos, M., Nomikou, P., Olive, J. A., Paquet, M., Rommevaux, C., Steinfuhrer, A., Rothenbeck, M., Tominaga, M., Triebe, L., Campos, R., Gracias, N., and Garcia, R. 2017. Tectonic structure, evolution, and the nature of oceanic core complexes and their detachment fault zones (1320Nand 1330N, Mid Atlantic Ridge). Geochemistry, Geophysics, Geosystems, Vol. 18, pg. 1580-1593.

Escartín, J., Smith, D. K., Cann, J., Schouten, H., Langmuir, C. H., and Escrig, S. 2008. Central role of detachment faults in accretion of slow-spreading oceanic lithosphere. Nature, Vol. 455, No. 7214, pg. 790-794.

Fang, W., Yan, J., Sun, J., and Guan, L. 2004. Anti-aliasing by interpolation in pre-stack wave-equation migration. Journal of Geophysics and Engineering, Vol. 1, No. 2, pg. 153-159

Faulkner, D.R., Lewis, A.C. and Rutter, E.H., 2003. On the internal structure and mechanics of large strike-slip fault zones: field observations of the Carboneras fault in southeastern Spain. *Tectonophysics*, *367*(3-4), pp.235-251.

Fertig, J., Thomas, M., and Thomas, R. 1999. How to remedy non-optimal seismic data by seismic processing. Pure and Applied Geophysics, 156, issue 1-2, pg. 345-370

Fomel, S. 2003. Time-migration velocity analysis by velocity continuation, Geophysics, Vol. 68, No. 5, pg. 1662-1672

Fomel, S. 2003. Velocity continuation and the anatomy of residual prestack time migration. Geophysics, Vol. 68, No. 5, pg. 1650-1661

Fomel, S., Landa, E., and Turhan Taner, M. 2007. Post-stack velocity analysis by separation and imaging of seismic diffractions. Society of Exploration Geophysicists - SEG International Exposition and 76tth Annual Meeting, Vol. 72, No. 6, pg. 2559-2563

Fossen, H. 2012. *Structural Geology*. Cambridge: Cambridge University Press. doi:10.1017/CBO9780511777806

Garabito, G., Schots, H., Ferreira, D., and Caldeira, J. 2015. Regularization of 2D seismic data by using the CRS stacking operator: Application in real low-fold land data. Sociedade Brasileira de Geofísica, pg. 1114-1116

Garcés, M. and Gee, J.S., 2007. Paleomagnetic evidence of large footwall rotations associated with low-angle faults at the Mid-Atlantic Ridge. *Geology*, *35*(3), pp.279-282.

Gavotti, P.E., and Lawton, D. C. 2013. Seismic processing workflow for supressing coherent noise while retaining low-frequency signal. CREWES Research Report, 25, pg 1-16

Gong, X., Yu, S., and Wang, S. 2016. Prestack seismic data regularization using a time-variant anisotropic Radon transform. Journal of Geophysics and Engineering, IOP Publishing, Vol. 13, No. 4, pg. 462-469. doi.org/10.1088/1742-2132/13/4/462

Gray S. H. 2013. Spatial sampling, migration aliasing, and migrated amplitudes. Geophysics, Vol. 78, No. 3, pg. S157-S164

Gray, S. H. 2016. Seismic imaging. Encyclopedia of Exploration Geophysics, pg. 1-16

Gray, S. H., Etgen, J., Dellinger, J., and Whitmore, D. 2001. Seismic migration problems and solutions, Geophysics, Vol. 66, No. 5, pg. 1622-1640. http://library.seg.org/doi/10.1190/1.1487107

Grevemeyer, I., Hayman, N. W., Lange, D., Peirce, C., Papenberg, C., Van Avendonk, H. J.A., Schmid, F., de La Peña, L. G.,and Dannowsk, A. 2019. Constraining the maximum depth of brittle deformation at slow-and ultraslow-spreading ridges using microseismicity. Geology

Grevemeyer, I., Ranero, C. R., and Ivandic, M. 2018. Structure of oceanic crust and serpentinization at subduction trenches. Geosphere, Vol. 14, No. 2, pg. 395-418

Grevemeyer, I., Reston, T. J., and Moeller, S. 2013. Microseismicity of the Mid-Atlantic Ridge at 7°S-8°15′S and at the Logatchev Massif oceanic core complex at 14°40′N-14°50′N. Geochemistry, Geophysics, Geosystems, Vol. 14, No. 9, pg. 3532-3554.

Gu, Y. J., and Sacchi, M. 2009. Radon transform methods and their applications in mapping mantle reflectivity structure. Surveys in Geophysics, Vol. 30, No. 4-5. Pg. 327-354

Gülünay, N. 2003. Seismic trace interpolation in the Fourier transform domain. Geophysics, Vol. 68, No. 1, pg. 355-369

Hale, D., and Claerbout, J.F. 1983. Butterworth dip filters. *Geophysics*, *48*(8), pp.1033-1038.

Harding, A. J., Arnulf, A. F., and Blackman, D, K. 2016. Velocity structure near IODP Hole U1309D, Atlantis Massif, from waveform inversion of streamer data and borehole measurements. Geochemistry, Geophysics, Geosystems, pg. 1990-2014

Hargreaves, N., and Wombell, R. 2004. Multiple diffractions and coherent noise in marine seismic data. SEG Technical Program Expanded Abstracts, pg. 1325-1328

Hasselgren, E., and Clowes, R. M. 1995. Crustal structure of northern Juan de Fuca plate from multichannel reflection data. Journal of Geophysical Research, 100, pg. 6469-6486

Hatton, L., Worthington, M. H., and Makin, J. 1986. Seismic data processing: theory and practise. Merlin Profiles Ltd.

Henstock, T. J., White, R. S., and McBride, J. H. 1995. The OCEAN study area: tectonic history from magnetic anomaly data and seismic reflectivity. Journal of Geophysical Research, Vol. 100, No. B10.

Henstock, T. J., Woods, A. W., and White, R. S. 1993. The accretion of oceanic crust by episodic sill intrusion. Vol. 98, No. B3, Pg. 4143-4161.

Herman, M., Syahmi Hashim, H., Abdul Latif, A., and Ghosh, D, P. 2017. Application of FK Filtering for Coherent Noise Removal in High Frequency Shallow Marine Data. IOP Conference Series: Earth and Environmental Science, Vol. 88, No. 1

Hobbs, R. W., Drummond, B. J. and Goleby, B. R. 2006. The effects of three-dimensional structure on two-dimensional images of crustal seismic sections and on the interpretation of shear zone morphology. Geophysical Journal International, Vol. 164, No. 3, pg. 490-500

Huseyin, O., and Ruhi, S. 1990. Efficient multichannel filtering of seismic data. Geophysical Prospecting.

JAKUBOWICZ, H. 1990. a Simple Efficient Method of Dip-Moveout Correction. Geophysical Prospecting, Vol. 38, No. 3, pg. 221-245.

Jones, G. D., Barton, P. J., and Singh, S. C. 2007. Velocity images from stacking depth-slowness seismic wavefields. Geophysical Journal International, Vol. 168, No. 2, pg. 583-592.

Karson, J. A., Klein, E. M., Hurst, S. D., Lee, C. E., Rivizzigno, P. A., Curewitz, D., Morris, A. R., and Hess Deep '99 Scientific Party. 2006. Structure of uppermost fast-spread oceanic crust exposed at the Hess Deep Rift: Implications for subaxial processes at the East Pacific Rise. Geochemistry, Geophysics, Geosystems, Vol. 7, No. 6.

Katsumata, K., Sato, T., Kasahara, J., Hirata, N., Hino, R., Takahashi, N., Sekine, M., Miura, S., Koresawa, S., and Wada, N. 2001. Microearthquake seismicity and focal mechanisms at the Rodriguez Triple Junction in the Indian Ocean using ocean bottom seismometers. Journal of Geophysical Research: Solid Earth. Vol. 106, No. B12.

Kearey, P., Klepeis, K. A., and Vine, F. J. 2009. Global Tectonics. Pure and Applied Geophysics, third edition, Wiley-Blackwell; ISBN: 978-1-4051-0777-8.

Kelamis, P. G., and Mitchelf, A. R. 1989. Slant-stack processing'. First Break Vol 7, No 2,

Kelemen, P. B., Koga, K., and Shimizu, N. 1997. Geochemistry of gabbro sills in the crust-mantle transition zone of the Oman ophiolite : implications for the origin of the oceanic lower crust. Earth and Planetary Science Letters, Vol. 146, pg. 475-488

Kent, G. M., Detrick, R. S., Swift, S. A., Collins, J. A., and Kim, I. I. 1997. Evidence from Hole 504B for the origin of dipping events in oceanic crustal reflection profiles as out-of-plane scattering from basement topography. Geology, Vol. 25, No. 2, pg. 131-134.

Kent, G. M., Kim, I. I., Harding, A. J., Detrick, R. S., and Orcutt, J. A. 1996. Suppression of sea - floor-scattered energy using a dip - moveout approach—Application to the mid-ocean ridge environment" GEOPHYSICS, Vol. 61, pg. 821-834.

Ker, S., Marsset, B., Garziglia, S., Le Gonidec, Y., Gibert, D., Voisset, M., and Adamy, J. 2010. High-resolution seismic imaging in deep sea from a joint deep-towed/OBH reflection experiment: Application to a Mass Transport Complex offshore Nigeria. Geophysical Journal International, Vol. 182, No. 3, pg. 1524-1542.

Kim, I., and Orcut, J. A. 1991. Kirchhoff-Helmholtz modeling of sea-floor scattering in a mid-atlantic ridge (23° N) seismic reflection profile. SEG Technical Program Expanded Abstracts.

King, G. A., Leong, T. K., and Flinchbaugh, B. E. 1984. The Role of Interpolation in Seismic Resolution. SEG Technical Program Expanded Abstracts, pg. 1-2.

Klinkby, L. and Pedersen, M. W. 1998. Attenuation of near-surface diffracted energy in deep seismic data by DMO correction. Tectonophysics, Elsevier Science B.V., Vol. 286, No. 1-4, pg. 155-159 doi.org/10.1016/S0040-1951(97)00261-8.

Korger, E. I. M. and Schlindwein, V. 2014. Seismicity and structure of the 85°E volcanic complex at the ultraslow spreading gakkel ridge from local earthquake tomography. Geophysical Journal International, Vol. 196, No. 1, pg. 539-551.

Kroode, F., Bergler, S., Corsten, C., Maag, Jan W. D., Strijbos, F., and Tijhof, H. 2013. Broadband seismic data — The importance of low frequencies. Geophysics, Vol. 78, No. 2.

Kumar, J., Bell, M., Salem, M., Martin, T., and Fairhead, S. 2018. Mode conversion noise attenuation, modelling and removal : case studies from Cyprus and Egypt. First Break, Vol. 36, pg. 113-120.

Kumar, L., and Sinha, D. P. 2008. From CMP to CRS - An Overview of Stacking Techniques of Seismic Data. 7th Biennial International Conference on Petroleum Geophysics, pg. 414 – 419.

Lafond, C., Jones, I. F., Bridson, M., Houllevigue, H., Kerdraon, Y., and Peliganga, J., 2003. Imaging deepwater salt bodies in West Africa. Leading Edge, Vol. 22, No. 9, pg. 893-896.

Landa, E., Belfer, I., and Keydar, S. 1999. Multiple attenuation in the parabolic τ-p domain using wavefront characteristics of multiple generating primaries. Geophysics, Vol. 64, No. 6, pg. 1806-1815.

Lăpădat, A., Imber, J., Yielding, G., Iacopini, D., McCaffrey, K.J., Long, J.J. and Jones, R.R., 2017. Occurrence and development of folding related to normal faulting within a mechanically heterogeneous sedimentary sequence: a case study from Inner Moray Firth, UK. *Geological Society, London, Special Publications*, *439*(1), pp.373-394.

Larner, K., Chambers, R., Yang, M., Lynn, W., and Wai, W. 1983. Coherent noise in marine seismic data. Geophysics, Vol. 48, No. 7, pg. 854-886.

Lavier, L. L., Buck W. R., and Poliakov A. N. B. 2000. Factors controlling normal fault offset in an ideal brittle layer. Journal of Geophysical Research: Solid Earth, Vol. 105, No. B10, pg. 23431-23442.

Lavier, L. L., Buck, W. R., and Poliakov, A. N. B. 1999. Self-consistent rolling-hinge model for the evolution of large-offset low-angle normal faults. Geology, Vol. 27, No. 12, pg. 1127-1130.

Liang, G., Liu, Q., Gu, X., and Han, L. 1990. Signal-to-Noise Enhancement of seismic data by Hyperbolic Transform Filtering. SEG Technical Program Expanded Abstracts, pg. 1629-1632.

Lin, J., and Phipps Morgan, J. 1992. The spreading rate dependence of three-dimensional mid-ocean ridge gravity structure. Geophysical Research Letters, Vol. 19, No. 1, pg. 105-112.

Lindsey, J. P. 1989. The Fresnel zone and its interpetive significance. The Leading Edge, Vol. 8, No.10, pg. 33-39.

Liu, B., and Li, G. 2010. De-aliasing high resolution tau-p transform and its application to wave fields separation. Proceedings - 2010 International Conference on Computational and Information Sciences, ICCIS, IEEE. Vol. 4, Pg. 997-1000.

Lizarralde, D., Gaherty, J. B., Collins, J. A, Hirth, G., and Kim, S. D. 2004. Spreading-rate dependence of melt extraction at mid-ocean ridges from mantle seismic refraction data. Nature, Vol. 432, No. 7018, pg. 744-747.

Longshaw, S. K., Sunderland, J., and Horn, I. 2008. Mode conversion and multiples. SEG Technical Program Expanded Abstracts.

MacLeod, C. J., Searle, R. C., Murton, B. J., Casey, J. F., Mallows, C., Unsworth, S. C., Achenbach, K. L., and Harris, M. 2009. Life cycle of oceanic core complexes. Earth and Planetary Science Letters, Vol. 287, No. 3-4, pg. 333-344.

Mallows, C., and Searle, R. C. 2012. A geophysical study of oceanic core complexes and surrounding terrain, Mid-Atlantic Ridge 13°N-14°N. Geochemistry, Geophysics, Geosystems, Vol. 13, No. 1, pg. 1-27.

Mancktelow, N.S. and Pavlis, T.L., 1994. Fold-fault relationships in low-angle detachment systems. *Tectonics*, *13*(3), pp.668-685.

Marino, I. K., Cetale Santos, M. A., and Silva, C. G. 2013. Processing of high-resolution, shallow seismic profiles, Guanabara Bay - Rio de Janeiro state, Brazil. Revista Brasileira de Geofisica, Vol. 31. No. 4, pg. 579-594.

Marjanović, M., Carbotte, S. M., Carton, H, Nedimović, M. R., Mutter, J. C., and Canales, J. 2014. A multi-sill magma plumbing system beneath the axis of the East Pacific Rise. Nature Geoscience, Vol. 7, No. 11, pg. 825-829.

Masoomzadeh, H., Barton, P. and Singh, S., 2004. Non-stretch imaging in the tau-p domain: exploiting long-o set arrivals for sub-basalt imaging. *74th Ann. Int. Mtg., Soc. of Exp. Geoph., Expanded Abstracts, SP-P2*.

Masoomzadeh, H., Barton, P.J., and Singh, S.C. 2005. Advanced processing of long-offset seismic data for sub-basalt imaging in the Faeroe-Shetland Basin. *SEG Technical Program Expanded Abstracts 2005* (pp. 417-420). Society of Exploration Geophysicists.

Milkereit, B. 2005. Migration of noisy Crustal seismic data. Journal of Geophysical research, Vol. 92, No. B8, pg. 7916-7930.

Mitchell, A. R., and Kelamis, P. G. 2002. Efficient tau- p hyperbolic velocity filtering. Geophysics, Vol. 55, No. 5, pg. 619-625.

Mitchell. G, Escartín, J., and Allerton, S. 1998. Detachment Faults at Mid-Ocean Ridges, Garner Interest. Transactions American Geophysical Union, Eos, Vol. 79, No. 10.

Morris, A., Gee, J. S., Pressling, N., John, B. E., MacLeod, C. J., Grimes, C. B., and Searle, R. C. 2009. Footwall rotation in an oceanic core complex quantified using reoriented Integrated Ocean Drilling Program core samples. Earth and Planetary Science Letters, Elsevier B.V., Vol. 287, No. 1-2, pg. 217-228.

Muller, M. R., Minshull, T. A., and White, R, S. 1999. Segmentation and melt supply at the Southwest Indian Ridge. Geology, Vol. 27, No. 10, pg. 867-870.

Müller, R. D., Sdrolias, M., Gaina, C., and Roest, W. R. 2008. Age, spreading rates, and spreading asymmetry of the world's ocean crust. Geochemistry, Geophysics, Geosystems, Vol. 9 (4), pg. 1-19.

Murton, B. J., and Rona, P. A. 2015. Carlsberg Ridge and Mid-Atlantic Ridge: Comparison of slow spreading centre analogues. Deep-Sea Research Part II: Topical Studies in Oceanography, Vol. 121, pg. 71-84.

Mutter, J. C., 1992. Seismic imaging of sea-floor spreading. Science, Vol. 258.

Mutter, J. C., and Karson, J. A. 1992. Structural processes at slow-spreading ridges. Science, Vol. 257, No. 5070, pg. 627-634.

Newmant, P. 1983. Seismic response to sea-floor diffractors. First Break.

Noponen, I., and Keeney, J. 1986. Attenuation of waterborne coherent noise by application of hyperbolic velocity filtering during the tau- p transform. Geophysics, Vol. 51, No. 1, pg. 20-33.

Ogilvie, J. S., and Purnell, G. W. 1996. Effects of salt-related mode conversions on subsalt prospecting. Geophysics, Vol. 61, No. 2. Pg. 331-348.

Olive, J. A., Parnell-Turner, R., Escartín, J., Smith, D. K., and Petersen, S. 2019. Controls on the seafloor exposure of detachment fault surfaces. Earth and Planetary Science Letters, Elsevier B.V., Vol. 506, pg. 381-387.

Ourabah, A., Keggin, J., Brooks, C., Ellis, D. and Etgen*, J., 2015. Seismic acquisition, what really matters?. In *SEG Technical Program Expanded Abstracts 2015* (pp. 6-11). Society of Exploration Geophysicists.

Panjaitan, R. J. T., Agustine, E. Rosandi, Y., and Nainggolan, T. B. 2019. FK-filter and radon transform methods comparative study on 2D pre-stack migration gather of Kangean Waters data. Earth and Environmental Science, IOP Conference Series, Vol. 311, No. 1.

Parnell-Turner, R., Escartín, J., Olive, J. A., Smith, D. K., and Petersen, S. 2018. Genesis of corrugated fault surfaces by strain localization recorded at oceanic detachments. Earth and Planetary Science Letters, Elsevier B.V., Vol. 498, pg. 116-128.

Parnell-Turner, R., Schouten, H., and Smith, D. K. 2016. Tectonic structure of the Mid-Atlantic Ridge near 16°30’ N. Geochemistry Geophysics Geosystems, Vol. 17, pg. 1312-1338.

Parnell-Turner, R., Sohn, R. A., Peirce, C., Reston, T. J., MacLeod, C. J., Searle, R. C., and Simão, N. M. 2021. Seismicity trends and detachment fault structure at 13°N, Mid-Atlantic Ridge, Geology, Vol. 49, No. 3, pg. 320-324.

Parnell-Turner, R., Sohn, R. A., Peirce, C., Reston, T. J., MacLeod C. J., Searle, R. C., and Simão, N. M. 2017. Oceanic detachment faults generate compression in extension. Geology, Vol. 45, No.10, pg. 923-926.

Peirce, C., Reveley, G., Robinson, A. H., Funnell, M. J., Searle, R. C., Simão, N. M., MacLeod, C. J., and Reston, T. J. 2019. Constraints on crustal structure of adjacent OCCs and segment boundaries at 13°N on the Mid-Atlantic Ridge. Geophysical Journal International, Vol. 217, No. 2, pg. 988-1010.

Peirce, C., Robinson, A., Funnell, M., Searle, R., MacLeod, C., and Reston, T. 2020. Magmatism versus serpentinization – crustal structure along the 13 ° N segment at the Mid-Atlantic Ridge. Geophysical J. Int., pg.981-1001.

Peirce, C., Sinha, M., Topping, S., and Gill, C. 2007. Morphology and genesis of slow-spreading ridges - Seabed scattering and seismic imaging within the oceanic crust. Geophysical Journal International, Vol. 168, No.1, pg. 59-89.

Phipps Morgan, J. 1987. Melt migration beneth mid-oceanic spreading centers. Geophysical Research Letters. Vol. 14, No. 12, pg. 1238-1241.

Phipps Morgan, J., and Chen, J. Y. 1993. Dependence of ridge-axis morphology on magma supply and spreading rate. Letters to Nature 364, pg. 706-708.

Phipps Morgan, J., and Chen, J. Y. 1993. The Genesis of Oceanic Crust: Magma Injection, Hydrothermal Circulation, and Crustal Flow. Journal of Geophysical Research, Vol. 98, pg. 6283-6297.

Phipps Morgan, J., Parmentier, E. M., and Lin, J. 1987. Mechanisms for the Origin of Mid-Ocean Ridge Axial Topography: implication for the thermal and mechanical structure of accreting plate boundaries. Journal of Geophysical Research, Vol. 92, No. 7 12823–12836.

Planert, L., Flueh, E. R., and Reston, T. J. 2009. Along- and across-axis variations in crustal thickness and structure at the Mid-Atlantic Ridge at 5°S obtained from wide-angle seismic tomography: Implications for ridge segmentation. Journal of Geophysical Research: Solid Earth, Vol. 114, No. 9, pg. 1-20.

Planert, L., Flueh, E. R., Tilmann, F., Grevemeyer, I., and Reston, T. J. 2010. Crustal structure of a rifted oceanic core complex and its conjugate side at the MAR at 5°S: Implications for melt extraction during detachment faulting and core complex formation. Geophysical Journal International, Vol. 181, No. 1, pg. 113-126.

Radon, J., 1917. On the determination of functions from their integrals along certain manifolds. *Ber. Verh, Sachs Akad Wiss.*, *69*, pp.262-277.

Raju, K. K., Abhay, V., and Samudrala, K. 2015. Slow Spreading Ridges of the Indian Ocean : An Overview of Marine Geophysical Investigations. Journal of the Indian Geophysical Union, Vol. 19, No. 2, pg. 137-159.

Reston, T. 2020. On the rotation and frictional lock-up of normal faults: Explaining the dip distribution of normal fault earthquakes and resolving the low-angle normal fault paradox. Tectonophysics, Elsevier, 790, 228550. doi.org/10.1016/j.tecto.2020.228550.

Reston, T. J. 2018. Flipping detachments: The kinematics of ultraslow spreading ridges. Earth and Planetary Science Letters, Elsevier B.V., Vol. 503, pg. 144-157..

Reston, T. J., and McDermott, K. G. 2011. Successive detachment faults and mantle unroofing at magma-poor rifted margins. Geology, Vol. 39, No. 11, pg. 1071-1074.

Reston, T. J., and Peirce, C., 2016. The Role and Extent of Detachment Faulting at Slow-Spreading Mid-Ocean Ridges. RRS James Cook JC132 cruise report.

Reston, T. J., and Ranero, C. R. 2011. The 3-D geometry of detachment faulting at mid-ocean ridges. Geochemistry, Geophysics, Geosystems, Vol. 12, No.7, pg. 1-19.

Reston, T. J., Ranero, C. R., and Belykh, I. 1999. The structure of Cretaceous oceanic crust of the NW Pacific: Constraints on processes at fast spreading centers. Journal of Geophysical Research: Solid Earth, Vol. 104 No. B1 pg. 2156-2202.

Reston, T. J., Ranero, C. R., Ruoff, O., Perez-Gussinye, M., and Dañobeitia, J. J. 2004. Geometry of extensional faults developed at slow-spreading centres from pre-stack depth migration of seismic reflection data in the Central Atlantic (Canary Basin). Geophysical Journal International, Vol. 159, No. 2, pg. 591-606.

Rocca, F., and Salvado, L., 1982. Residual migration. SEG Technical Program Expanded Abstracts, pg. 4-7.

Rothman, D.l H., Levin, S. A., and Hoccaf, F. 1985. Residual migration: Applications and limitations. Geophysical SEG, Vol. 50, No. 1, pg. 110-126.

Sauter, D., Cannat, M., Rouméjon, S., Andreani, M., Birot, D., Bronner, A., Brunelli, D., Carlut, J., Delacour, A., Guyader, V., MacLeod, C. J., Manatschal, G., Mendel, V., Ménez, B., Pasini, V., Ruellan, E., and Searle, R. 2013. Continuous exhumation of mantle-derived rocks at the Southwest Indian Ridge for 11 million years. Nature Geoscience, Vol. 6, No. 4, pg. 314-320. http://dx.doi.org/10.1038/ngeo1771.

Sava, P. 2000. Prestack Stolt residual migration for migration velocity analysis. SEG Technical Program Expanded Abstracts.

Sava, P. C. 2003. Prestack residual migration in the frequency domain. Geophysics, Vol. 68, No. 2, pg. 634-640.

Searle, R. C., MacLeod, C. J., Peirce, C., Reston, T. J. 2019. The Mid-Atlantic Ridge Near 13°20′N: High-Resolution Magnetic and Bathymetry Imaging. Geochemistry, Geophysics, Geosystems, 20, 1, 295-313.

Simão, N. M., Peirce, C., Funnell, M. J., Robinson, A. H., Searle, R. C., Macleod, C. J., and Reston, T. J. 2020. 3-D P-wave velocity structure of oceanic core complexes at 13°N on the Mid-Atlantic Ridge. Geophysical Journal International.

Sinton, J. M., and Detrick, R. S. 1992. Mid-Ocean Ridge Magma Chambers. Journal of Geophysical Research, Vol. 97, pg. 197-216.

Smith, D. K., Escartín, J., Schouten, H., and Cann, J. R. 2008, Fault rotation and core complex formation: Significant processes in seafloor formation at slow-spreading mid-ocean ridges (Mid-Atlantic Ridge, 13°-15°N). Geochemistry, Geophysics, Geosystems, Vol. 9, No. 3

Smith, P., Jones, I. F., King, D., Sangvai, P., Biswal, A., and Mathur, M. 2008. Deep water pre-processing: East Coast India. First Break, Vol. 26, No. 5, pg. 101-107.

Soleimani, M., and Rafiei, M. 2016. Imaging seismic data in complex structures by introducing the partial diffraction surface stack method. Studia Geophysical et Geodaetica, Vol. 60, No. 4, pg. 644-661.

Spencer, J. E. 1999. Geologic continuous casting below continental and deep-sea detachment faults and at the striated extrusion of Sacsayhuaman, Peru. Geology, Vol. 27, No. 4, pg. 327-330.

Spencer, J. E. 2000. Possible origin and significance of extension-parallel drainages in Arizona's metamorphic core complexes. Bulletin of the Geological Society of America, Vol. 112, No. 5, pg. 727-735.

Spitzer, R., Nitsche, F. O., and Green, A. G. 2001. Reducing source-generated noise in shallow seismic data using linear and hyperbolic τ- p transformations. Geophysics, Vol. 66, No. 5, pg. 1612-1621.

Stewart, P. G., Jones, I. F., and Hardy, P. B. 2007. Solutions for Deep Water Imaging. SPG, GeoHorizons, P8-22.

Stoffa, P. L., 1981. Tau-p: An Alternative Domain for filtering, velocity analysis and imaging. Geophysics, SEG, Pg. 551-554.

Stoffa, P. L., Buhl, P., Diebold, J. B., and Wenzel, F. 1981. Direct mapping of seismic data to the domain of intercept time and ray parameter - a plane-wave decomposition. Geophysics, Vol. 46, No. 3, pg. 255-267.

Stolt, R. H. 2002. A prestack residual time migration operator. Geophysics, Vol. 61, No. 2, pg. 605-607.

Sun, J., Fomel, S., and Ying, L. 2016. Low-rank one-step wave extrapolation for reverse time migration. Geophysics, Vol. 81, No. 1, pg. S39-S54.

Tatham, R. H. 1984. Multidimensional Filtering of Seismic Data. Proceedings of the IEEE, Vol. 72, No. 10, pg. 1357-1369.

Tatham, R. H., and Goolsbee, D. V. 1984. Separation of S-wave and P-wave reflections offshore western Florida. Geophysics, Vol. 49, No. 5. Pg. 421-422.

Tatham, R. H., Keeney, J., Walker, C. D. T., Goolsbee, D., Wiley, J., Massell, W. F., and Parry Petty-Ray, M. 1982. Application of the tau-p trasform (slant-stack) in processing seismic reflection data. SEG Technical Program Expanded Abstracts, pg. 3-4.

Thore, P., and Juliard, C. 1999. Fresnel zone effect on seismic velocity resolution. Geophysics, Vol. 64, No.2, pg. 593-603.

Tieman, H. J. 1997. Improving plane-wave decomposition and migration. Geophysics, Vol. 62, No. 1, pg. 195-205.

Tilmann, F., Flueh, E., Planert, L., Reston, T., and Weinrebe, W. 2004. Microearthquake seismicity of the Mid-Atlantic Ridge at 5°S: A view of tectonic extension. Journal of Geophysical Research: Solid Earth, Vol. 109, No. 6

Tsai, C. J. 1984. An analysis leading to the reduction of scattered noise on deep marine seismic records. Geophysics, Vol. 49, No. 1, pg. 17-26.

Tsai, C. J. 1985. Method To Analyze and Verify Deep Crustal Reflections Offshore Costa Rica. Geophysics, Vol. 50, No. 2, pg. 196-206.

Tucholke, B. E., and Lin, J. 1994. A geological model for the structure of ridge segments in slow spreading ocean crust. Journal of Geophysical Research, Vol. 99, No. B6.

Tucholke, B. E., Behn, M. D., Buck, W. R., and Lin, J. 2008. Role of melt supply in oceanic detachment faulting and formation of megamullions. Geology, Vol. 36, No. 6, pg. 455-458.

Tucholke, B. E., Lin, J., and Kleinrock, M. C. 1998. Megamullions and mullion structure defining oceanic metamorphic core complexes on the Mid-Atlantic Ridge. Journal of Geophysical Research: Solid Earth, Vol. 103, No. B5, pg. 9857-9866.

Turner, G. 1990. Aliasing in the tau-p transform and the removal of spatially aliased coherent noise. Geophysics, Vol. 55, No. 11, pg. 1496-1503.

van der Baan, M. 2004. Processing of anisotropic data in the τ-p domain: I—Geometric spreading and moveout corrections. Geophysics, Vol. 69, No. 3, pg. 719-730. http://library.seg.org/doi/10.1190/1.1759458.

Wapenaar C. P. A., Verschuur, D. J., and Hermann, P. 1992. Amplitude preprocessing of single and multicomponent seismic data. Geophysics, Vol. 57, No. 9.

Wernicke, B. 1981. *Low-angle normal faults in the Basin and Range Province: nappe tectonics in an extending orogen.* Nature, 291 (5817). pp. 645-648. ISSN 0028-0836. doi:10.1038/291645a0.

Wolfe, C. J., Purdy, G. M., Toomey, D. R., and Solomon, S. C. 1995. Microearthquake characteristics and crustal velocity structure at 29°N on the Mid-Atlantic Ridge: the architecture of a slow spreading segment. Journal of Geophysical Research, Vol. 100, No. B12.

Wood, L. C., Heiser, R. C., Treitel, S., and Riley, P. L. 1978. the Debubbling of Marine Source. Geophysics, Vol. 43, No. 4, pg. 715-729.

Woodburn, N., Hardwick, A., Masoomzadeh, H., and Travis, T. 2014. Improved signal processing for sub-basalt imaging. Geological Society, London, Special Publications, 397, 163–171.

www.sercel.com/about/Pages/what-is-geophysics.aspx

Xiao, C. M., Bancroft, J. C., Brown, R. J., and Nancy, Z. 2003. Multiple suppression: A literature review, CREWES Research Report, 15, pg. 1-17.

Xu, M., Canales, J., Tucholke, B. E., and DuBois, D. L. 2009. Heterogeneous seismic velocity structure of the upper lithosphere at Kane oceanic core complex, Mid-Atlantic Ridge, Geochemistry, Geophysics, Geosystems, Vol. 10, No. 10.

Xu, M., Zhao, X., and Canales, J. 2020. Structural Variability Within the Kane Oceanic Core Complex from Full Waveform Inversion and Reverse Time Migration of Streamer Data. Geophysical Research Letters, Vol. 47, No. 7.

Xu, M., Zhao, X., and Canales, J. P. 2020. Structural Variability Within the Kane Oceanic Core Complex from Full Waveform Inversion and Reverse Time Migration of Streamer Data. Geophysical Research Letters, Vol. 47, No.7.

Yilmaz, O. 1987. Seismic Data Processing. Society of Exploration Geophysicists, Investigations in Geophysics, Vol. 2.

Yilmaz, O. 2001. Seismic data analysis: Processing, inversion, and interpretation of seismic data. Society of Exploration Geophysicists, Investigations in Geophysics, Vol 1 & 2.

Yin, A., & Dunn, J.F. 1992. Structural and stratigraphic development of the Whipple-Chemehuevi detachment fault system, south-eastern California: Implications for the geometrical evolution of domal and basinal low-angle normal faults. *Geological Society of America Bulletin, 104*, 659-674.

Yu, Z., Li, J., Liang, Y., Han, X., Zhang, J., and Zhu, L. 2013. Distribution of large-scale detachment faults on mid-ocean ridges in relation to spreading rates. Acta Oceanologica Sinica, Vol. 32, No. 12, pg. 109-117.

Zhang, K., Cheng, J., Ma, Z., and Zhang, W. 2006. Pre-stack time migration and velocity analysis methods with common scatter-point gathers. Journal of Geophysics and Engineering, Vol. 3, No. 3, pg. 283-289.

Zheng, Ye., and Stewart, R. R. 1993. Directional filtering and side-swipe imaging. CREWES Research Report, 5.

Appendix A: Python code for velocity model implementation and conversion to NETCDF file.

```
from __future__ import division
import numpy as np
import matplotlib.pyplot as plt
"""Enter the file path for seafloor horizon times digitized from data set fro
line of interest"""
seafloor_HorTime = np.loadtxt('F:\Documents\L19-21_plots\L6a.26_sfHoriz_Stolt_CDPtimes.txt')
depth_time = seafloor_HorTime/1000
"""
Seafloor horizon times is in micro seconds therefore the division by 1000.
These times are at each cdp. Therefore its length will give the number of CDPs.
TO generalise the script more a request for sampling time interval of interest
will be asked. 0.008 for Claritas vel files or 0.002 for other vel file.
"""
s_time = input("Enter 0.008 for a CLaritas vel file or 0.002 for others:  ")
Velocities = []
'''list of all velocities for use in the velocity file'''
def tm1(t1):  # time relating to TWT (Peirce etal 2019) definition for the first cdp depth from grid file
    t1 = np.arange(0, 0.235294118, float(s_time)) #0.008)
    return t1
def vel1(v1):
    v1 = np.linspace(2750., 4250., len(tm1(1)))
    return v1
Velocities.extend(list(vel1(1)))
def tm2(t2): #Time definiotion for the subsequent part of velocity plot
    t2 = np.arange(0.24, 0.620836286, float(s_time))
    return t2
def vel2(v2):
    v2 = np.linspace(4269.94680851, 5187.5, len(tm2(2)))
    return v2
Velocities.extend(list(vel2(2)))
def tm3(t3): #last part of velocity time plot
```

```
    t3 = np.arange(0.624, 1.142575417, float(s_time))
    return t3
def vel3(v3):
    v3 = np.linspace(5196.2890625, 5750., len(tm3(3)))
    return v3
Velocities.extend(list(vel3(3)))
def tm4(t4): #last part of velocity time plot
    t4 = np.arange(1.144, 1.802369231, float(s_time))
    return t4
def vel4(v4):
    v4 = np.linspace(5753.81097561, 6062.5, len(tm4(4)))
    return v4
Velocities.extend(list(vel4(4)))
def tm5(t5): #last part of velocity time plot
    t5 = np.arange(1.808, 2.586682957, float(s_time))
    return t5
def vel5(v5):
    v5 = np.linspace(6065.72164948, 6375., len(tm5(5)))
    return v5
Velocities.extend(list(vel5(5)))
def tm6(t6): #last part of velocity time plot
    t6 = np.arange(2.592, 3.492343334, float(s_time))
    return t6
def vel6(v6):
    v6 = np.linspace(6377.23214286, 6625., len(tm6(6)))
    return v6
Velocities.extend(list(vel6(6)))
def tm7(t7): #last part of velocity time plot
    t7 = np.arange(3.496, 4.539072306, float(s_time))
    return t7
def vel7(v7):
    v7 = np.linspace(6625.48076923, 6687.5, len(tm7(7)))
    return v7
Velocities.extend(list(vel7(7)))
```

```
def tm8(t8): #last part of velocity time plot
   t8 = np.arange(4.544, 5.724257491, float(s_time))
   return t8
def vel8(v8):
   v8 = np.linspace(6687.92517007, 6750., len(tm8(8)))
   return v8
Velocities.extend(list(vel8(8)))
def tm9(t9): #last part of velocity time plot
   t9 = np.arange(5.728, 7.047786903, float(s_time))
   return t9
def vel9(v9):
   v9 = np.linspace(6750.30487805, 6800., len(tm9(9)))
   return v9
Velocities.extend(list(vel9(9)))
def tm10(t10): #last part of velocity time plot
   t10 = np.arange(7.048, 8.507640918, float(s_time))
   return t10
def vel10(v10):
   v10 = np.linspace(6800.27472527, 6850., len(tm10(10)))
   return v10
Velocities.extend(list(vel10(10)))
count5 = 0
no_cdp = len(depth_time)
line_name = input("Enter the Line name to do ideal velocity model for :  ")
line_total_time = input("Enter the total time in seconds for line of interest:   ")
no_vel = int((float(line_total_time))/(float(s_time))) + 1
mat_vel_cdp = np.ones((no_vel , no_cdp))

for CDPpoint in range(no_cdp): #total CDPpoint extracted from the seismic data
   count1 = 0 # count import os.pathfor totaltime in sesimc data at 0.002 smaple rate
   count2 = 0
   count3 = 0
   count4 = 0
```

```
    totaltime = [0]
    modelvel = [1500]
    vel = 1500
    while totaltime[count1] <= float(line_total_time) :
        if totaltime[count1] <= depth_time[count5] :
            vel = 1500
        else:
            vel = Velocities[count2]
            count2 += 1
        num = totaltime[count1] + float(s_time)
        totaltime.append(num)
        modelvel.append(vel)
        mat_vel_cdp[count3][count5] *= modelvel[count4]
        count1 += 1
        count3 += 1
        count4 += 1
    count5 += 1

plt.figure(figsize=[20, 10], dpi=(70))
plt.imshow(mat_vel_cdp, interpolation='nearest',origin='lower', extent=[1000,5972,0,9500])
plt.xlabel('CDP')
plt.ylabel('Time (s)')
plt.gca().invert_yaxis()
plt.gca().xaxis.tick_top()
plt.colorbar()
plt.show()

'''new matrix generation for the interval velocity matrix using a list method
and appending these in the full matrix. The velocities for the matrix is
extendeded in a list from all the velocities-time function above'''
save_path = 'F:/Documents/Seafloor_HorizonNETCDF/Pierce_etal_velocity_models/'+
str(line_name)+'_VintMatrix_cdp_'+ str(s_time)+'.txt' #008.txt'

"""
```

```
## Save_path give the location the appended filename will be written to this could be any location of
choice
"""

np.savetxt(str(save_path), mat_vel_cdp, fmt='%2f')
"""
### Converting matrix to netCDF4 file for read into Claritas
"""
save_path = 'F:/Documents/Seafloor_HorizonNETCDF/Pierce_etal_velocity_models/'+ str(line_name)
+'_Intvel_model_arrays'+ str(s_time)+ '.nc'
## save_path will replace the filename which should be the first object in Dataset
from netCDF4 import Dataset
model_grp = Dataset(str(save_path) , 'w', format='NETCDF3_CLASSIC')
model_grp.Title = "2-D earth model"

Vint_model_array = mat_vel_cdp.copy()
cdp_ndim = no_cdp # size of the matrix column
time_ndim = no_vel  # size of the matrix row
cdp_dim = 6.25 * no_cdp
time_dim = float(s_time) * no_vel

"""Dimension (instead and cdp = ELevation while time = Distance)"""
model_grp.createDimension('Elevation', time_ndim)
model_grp.createDimension('Distance', cdp_ndim)
velocity = model_grp.createVariable('Velocity', 'f4', ('Elevation', 'Distance',))
velocity.Units = "m/s"
velocity.X_Limits_and_increment = 1000.000, float(cdp_ndim + 1000),  1.000
velocity.X_name = "CDP"
velocity.X_units = ""
velocity.Z_Limits_and_increment = 0.000, float((float(s_time)) * no_vel), float(s_time)
velocity.Z_name = "Time"
velocity.Z_units = "ms"
velocity.V_name = "Velocity"
velocity.V_units = "m/s"
```

```
# Data
cdp_range = np.linspace(0, cdp_dim, cdp_ndim)
time_range = np.linspace(0, time_dim, time_ndim)
Vint_model_array_transpose = Vint_model_array.transpose()
velocity[:,:] = Vint_model_array_transpose.reshape(time_ndim,cdp_ndim)
model_grp.close()

#
'''Conversion of mat_vel_cdp Vint to model_vrms Vrms'''
#
import math as mat
import numpy as np
model_vrms = np.ones(((no_vel ), no_cdp))
model_vint = mat_vel_cdp.copy()
count1 = 0
time_dim = float(line_total_time)
for cdp_point in range(no_cdp):
   count2 = 0
   total_time = 0.0
   vel_time_sum = 0.0
   vel_num = 0.0
   while total_time <= time_dim:
      int_time = float(s_time)
      vel_dino = model_vint[count2][count1]
      vel_dino_sqr = (model_vint[count2][count1]) ** 2
      vel_sqr_time = vel_dino_sqr * int_time
      vel_time_sum +=  vel_sqr_time
      vel_num += int_time
      total_time += float(s_time)    #0.008
      vel_sqrt = vel_time_sum/vel_num
      model_vrms[count2][count1] = mat.sqrt(vel_sqrt)
      count2 += 1
   count1 += 1
np.savetxt(str(line_name) +'model_Vrms_'+ str(s_time)+ '.txt', model_vrms, fmt='%2f')
```

```
"""Converting model_vrms matrix to netCDF4 file for read into Claritas"""
from netCDF4 import Dataset
save_path = 'F:/Documents/Seafloor_HorizonNETCDF/Pierce_etal_velocity_models/'+ str(line_name)
+'_model_Vrms_arrays_'+ str(s_time)+ '.nc'

model_vrms_grp = Dataset(str(save_path), 'w', format='NETCDF3_CLASSIC')
model_vrms_grp.Title = "2-D earth model Vrms"
model_vrms_array = model_vrms.copy()
cdp_ndim = no_cdp # size of the matrix column
time_ndim = (no_vel) # size of the matrix row
model_vrms_grp.createDimension('Elevation', time_ndim)
model_vrms_grp.createDimension('Distance', cdp_ndim )
#variables
velocity = model_vrms_grp.createVariable('Velocity', 'f4', ('Elevation', 'Distance',))
velocity.Units = "m/s"
velocity.X_Limits_and_increment = 1000.000, float(cdp_ndim + 1000),  1.000
velocity.X_name = "CDP"
velocity.X_units = ""
velocity.Z_Limits_and_increment = 0.000, float(float(s_time) * no_vel), float(s_time)
velocity.Z_name = "Time"
velocity.Z_units = "ms"
velocity.V_name = "Velocity"
velocity.V_units = "m/s"
# Data
cdp_range = np.linspace(0, cdp_dim, cdp_ndim)
time_range = np.linspace(0, time_dim, time_ndim)
model_vrms_array_transpose = model_vrms_array.transpose()
velocity[:,:] = model_vrms_array_transpose.reshape(time_ndim,cdp_ndim)
model_vrms_grp.close()




##
```

```
"""Cascaded migration velocity flow calculated from intertval velocity for FDMIG"""
##

second_mig_Intvel = np.ones((no_vel,no_cdp))
stolt_mig_vel = (np.ones((no_vel,no_cdp))) * 1480
count1 = 0
count2 = 0
while count1 !=  no_vel:
    mat_vel_element = (mat_vel_cdp[count1][count2]) ** 2 #cascaded Velocity elemnet from interval
velocity
    stolt_vel = 1480 ** 2
    second_mig_intvel_elem = mat_vel_element - stolt_vel
    second_mig_Intvel[count1][count2] = mat.sqrt(second_mig_intvel_elem)
    count1 += 1
    if count1 == no_vel:
        count2 += 1
        count1 = 0
    if count2 == no_cdp:
        break

"""##converting second cascade model Vint to netCDF4 for read into Claritas"""

from netCDF4 import Dataset
save_path = 'F:/Documents/Seafloor_HorizonNETCDF/Pierce_etal_velocity_models/'+ str(line_name)
+'_model_SecCascade-IntVel_arrays_'+ str(s_time)+ '.nc'

model_Sec_Intvel_grp = Dataset(str(save_path), 'w', format='NETCDF3_CLASSIC')
model_Sec_Intvel_grp.Title = "2-D earth model second cacade InterVel"
Sec_mig_Intvel_model_array = second_mig_Intvel.copy()
cdp_ndim = no_cdp  # size of the matrix column
time_ndim = (no_vel) # size of the matrix row
cdp_dim = 6.25 * no_cdp
time_dim = float(s_time) * no_vel
```

```
""" Dimension (instead and cdp = ELevation while time = Distance)"""
model_Sec_Intvel_grp.createDimension('Elevation', time_ndim)
model_Sec_Intvel_grp.createDimension('Distance', cdp_ndim)



#variables
velocity = model_Sec_Intvel_grp.createVariable('Velocity', 'f4', ('Elevation', 'Distance',))
velocity.Units = "m/s"
velocity.X_Limits_and_increment = 1000.000, float(cdp_ndim + 1000),  1.000
#velocity.X_Limits_and_increment = 1000.000, 5667,  1.000
velocity.X_name = "CDP"
velocity.X_units = ""
velocity.Z_Limits_and_increment = 0.000, float(float(s_time) * no_vel), float(s_time)
velocity.Z_name = "Time"
velocity.Z_units = "ms"
velocity.V_name = "Velocity"
velocity.V_units = "m/s"

# Data
cdp_range = np.linspace(0, cdp_dim, cdp_ndim)
time_range = np.linspace(0, time_dim, time_ndim)
Sec_mig_Intvel_model_array_transpose = Sec_mig_Intvel_model_array.transpose()
velocity[:,:] = Sec_mig_Intvel_model_array_transpose.reshape(time_ndim,cdp_ndim)
model_Sec_Intvel_grp.close()
```

***Appendix B:** Digitised velocity values for velocity building*

Table 2: V_{int} (km/s), and depth (km), first and second column extracted from Peirce et al seismic refraction model (Figure 4.11a) of a Slow spreading area and converted to time (s) third column then replotted, Figure 4.11b. (2a) Maximum V_{int} and depth values (Figure 4.11a) while the last two columns are the time conversion and plotting (Figure 4.11b) values. (2b) Minimum V_{int} and depth values (Figure 4.11a) while the last two columns are the time conversion and plotting (Figure 4.11b) values. (2c) Average V_{int} and depth values and corresponding time conversion and plot values.

Table 2a

Max V_{int} (km/s)	Depth (km)	TWT (s) for depth intervals at Max V_{int}	TWT (s) plotted for Max V_{int}
3.5	0	0	0
5	0.5	0.2	0.2
5.875	1	0.340425532	0.540425532
6.25	1.5	0.48	1.020425532
6.5	2	0.615384615	1.635810147
6.75	2.5	0.740740741	2.376550888
7	3	0.857142857	3.233693745
7	3.5	1	4.233693745
7	4	1.142857143	5.376550888
7	4.5	1.285714286	6.662265174
7	5	1.428571429	8.090836602
7.125	5.5	1.543859649	9.634696251
7.125	6	1.684210526	11.31890678
7.5	6.5	1.733333333	13.05224011
7.5	7	1.866666667	14.91890678
7.5	7.5	2	16.91890678
7.5	8	2.133333333	19.05224011

Table 2b:

Min V_{int} (km/s)	Depth (km)	TWT (sec) for depth intervals for Min V_{int}	TWT time plotted for Min V_{int}
2	0	0	0
3.5	0.5	0.285714286	0.285714286
4.5	1	0.444444444	0.73015873
5.25	1.5	0.571428571	1.301587302
5.625	2	0.711111111	2.012698413
6	2.5	0.833333333	2.846031746
6.25	3	0.96	3.806031746
6.375	3.5	1.098039216	4.904070962
6.5	4	1.230769231	6.134840192
6.6	4.5	1.363636364	7.498476556
6.7	5	1.492537313	8.99101387
6.75	5.5	1.62962963	10.6206435
6.8	6	1.764705882	12.38534938
6.85	6.5	1.897810219	14.2831596
6.9	7	2.028985507	16.31214511
7	7.5	2.142857143	18.45500225
7.125	8	2.245614035	20.70061629

Table 2c:

Ave. Min and Max V_{int}	Depth (km)	TWT for depth interval for Ave. V_{int}	TWT plotted for Ave. V_{int}
2.75	0	0	0
4.25	0.5	0.235294118	0.235294118
5.1875	1	0.385542169	0.620836286
5.75	1.5	0.52173913	1.142575417
6.0625	2	0.659793814	1.802369231
6.375	2.5	0.784313725	2.586682957
6.625	3	0.905660377	3.492343334
6.6875	3.5	1.046728972	4.539072306
6.75	4	1.185185185	5.724257491
6.8	4.5	1.323529412	7.047786903
6.85	5	1.459854015	8.507640918
6.9375	5.5	1.585585586	10.0932265
6.9625	6	1.723518851	11.81674535
7.175	6.5	1.81184669	13.62859204
7.2	7	1.944444444	15.57303649
7.25	7.5	2.068965517	17.64200201
7.3125	8	2.188034188	19.83003619

***Appendix C**: Claritas de-spiking values.*

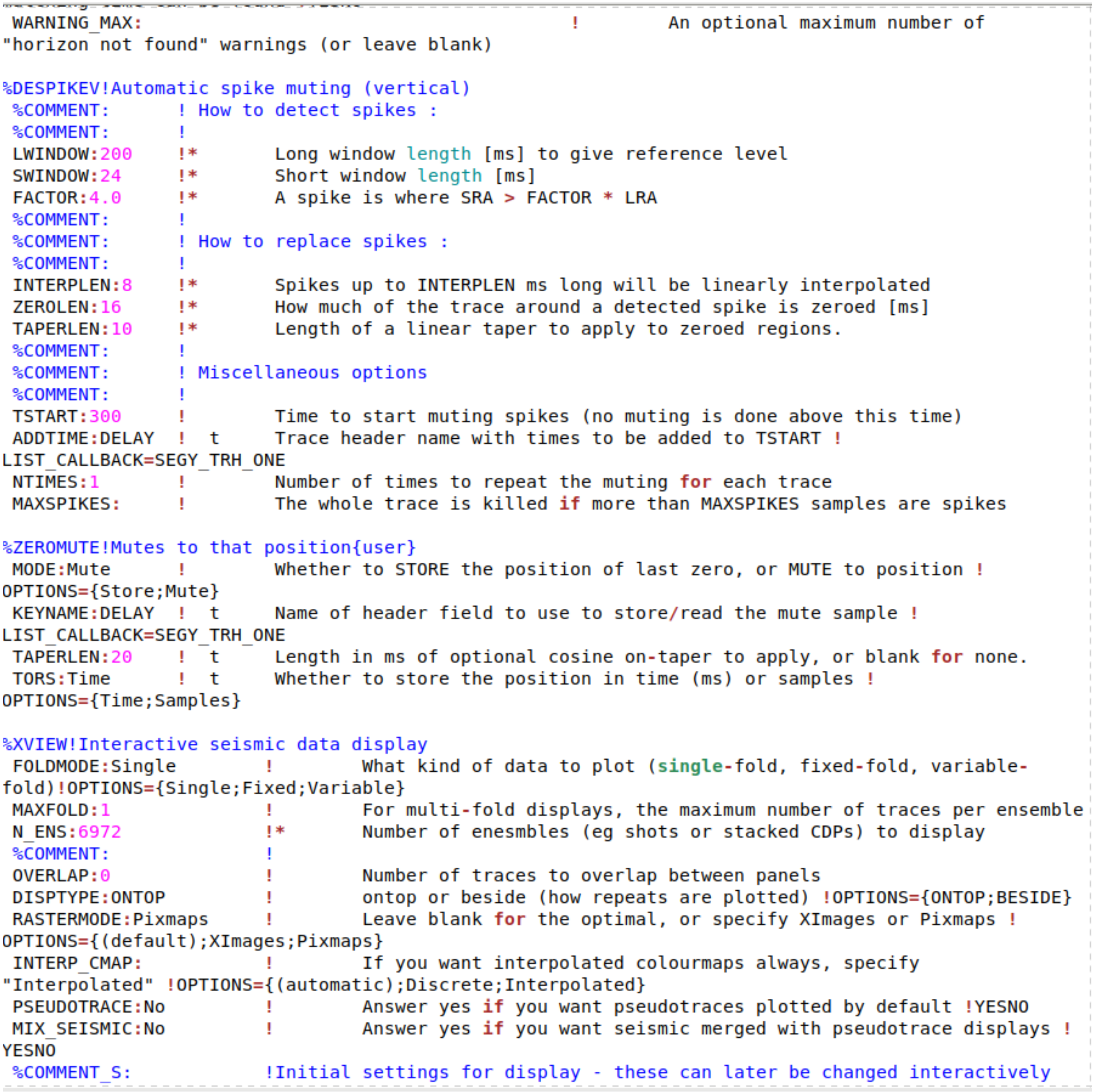

```
 WARNING_MAX:                                    !        An optional maximum number of
"horizon not found" warnings (or leave blank)

%DESPIKEV!Automatic spike muting (vertical)
 %COMMENT:      ! How to detect spikes :
 %COMMENT:      !
 LWINDOW:200    !*       Long window length [ms] to give reference level
 SWINDOW:24     !*       Short window length [ms]
 FACTOR:4.0     !*       A spike is where SRA > FACTOR * LRA
 %COMMENT:      !
 %COMMENT:      ! How to replace spikes :
 %COMMENT:      !
 INTERPLEN:8    !*       Spikes up to INTERPLEN ms long will be linearly interpolated
 ZEROLEN:16     !*       How much of the trace around a detected spike is zeroed [ms]
 TAPERLEN:10    !*       Length of a linear taper to apply to zeroed regions.
 %COMMENT:      !
 %COMMENT:      ! Miscellaneous options
 %COMMENT:      !
 TSTART:300     !        Time to start muting spikes (no muting is done above this time)
 ADDTIME:DELAY  !  t     Trace header name with times to be added to TSTART !
LIST_CALLBACK=SEGY_TRH_ONE
 NTIMES:1       !        Number of times to repeat the muting for each trace
 MAXSPIKES:     !        The whole trace is killed if more than MAXSPIKES samples are spikes

%ZEROMUTE!Mutes to that position{user}
 MODE:Mute      !        Whether to STORE the position of last zero, or MUTE to position !
OPTIONS={Store;Mute}
 KEYNAME:DELAY  !  t     Name of header field to use to store/read the mute sample !
LIST_CALLBACK=SEGY_TRH_ONE
 TAPERLEN:20    !  t     Length in ms of optional cosine on-taper to apply, or blank for none.
 TORS:Time      !  t     Whether to store the position in time (ms) or samples !
OPTIONS={Time;Samples}

%XVIEW!Interactive seismic data display
 FOLDMODE:Single        !        What kind of data to plot (single-fold, fixed-fold, variable-
fold)!OPTIONS={Single;Fixed;Variable}
 MAXFOLD:1              !        For multi-fold displays, the maximum number of traces per ensemble
 N_ENS:6972             !*       Number of enesmbles (eg shots or stacked CDPs) to display
 %COMMENT:              !
 OVERLAP:0              !        Number of traces to overlap between panels
 DISPTYPE:ONTOP         !        ontop or beside (how repeats are plotted) !OPTIONS={ONTOP;BESIDE}
 RASTERMODE:Pixmaps     !        Leave blank for the optimal, or specify XImages or Pixmaps !
OPTIONS={(default);XImages;Pixmaps}
 INTERP_CMAP:           !        If you want interpolated colourmaps always, specify
"Interpolated" !OPTIONS={(automatic);Discrete;Interpolated}
 PSEUDOTRACE:No         !        Answer yes if you want pseudotraces plotted by default !YESNO
 MIX_SEISMIC:No         !        Answer yes if you want seismic merged with pseudotrace displays !
YESNO
 %COMMENT_S:            !Initial settings for display - these can later be changed interactively
```

Figure C: This is a snapshot from Claritas showing the applied de-spiking parameters for the Stolt de-spiking process.